

Improving Capabilities in Modeling Aircraft Noise Sources

Vieira, A.E.

DOI

[10.4233/uuid:806e1965-8320-4a40-b0fc-0b060ac62799](https://doi.org/10.4233/uuid:806e1965-8320-4a40-b0fc-0b060ac62799)

Publication date

2021

Document Version

Final published version

Citation (APA)

Vieira, A. E. (2021). *Improving Capabilities in Modeling Aircraft Noise Sources*. [Dissertation (TU Delft), Delft University of Technology]. <https://doi.org/10.4233/uuid:806e1965-8320-4a40-b0fc-0b060ac62799>

Important note

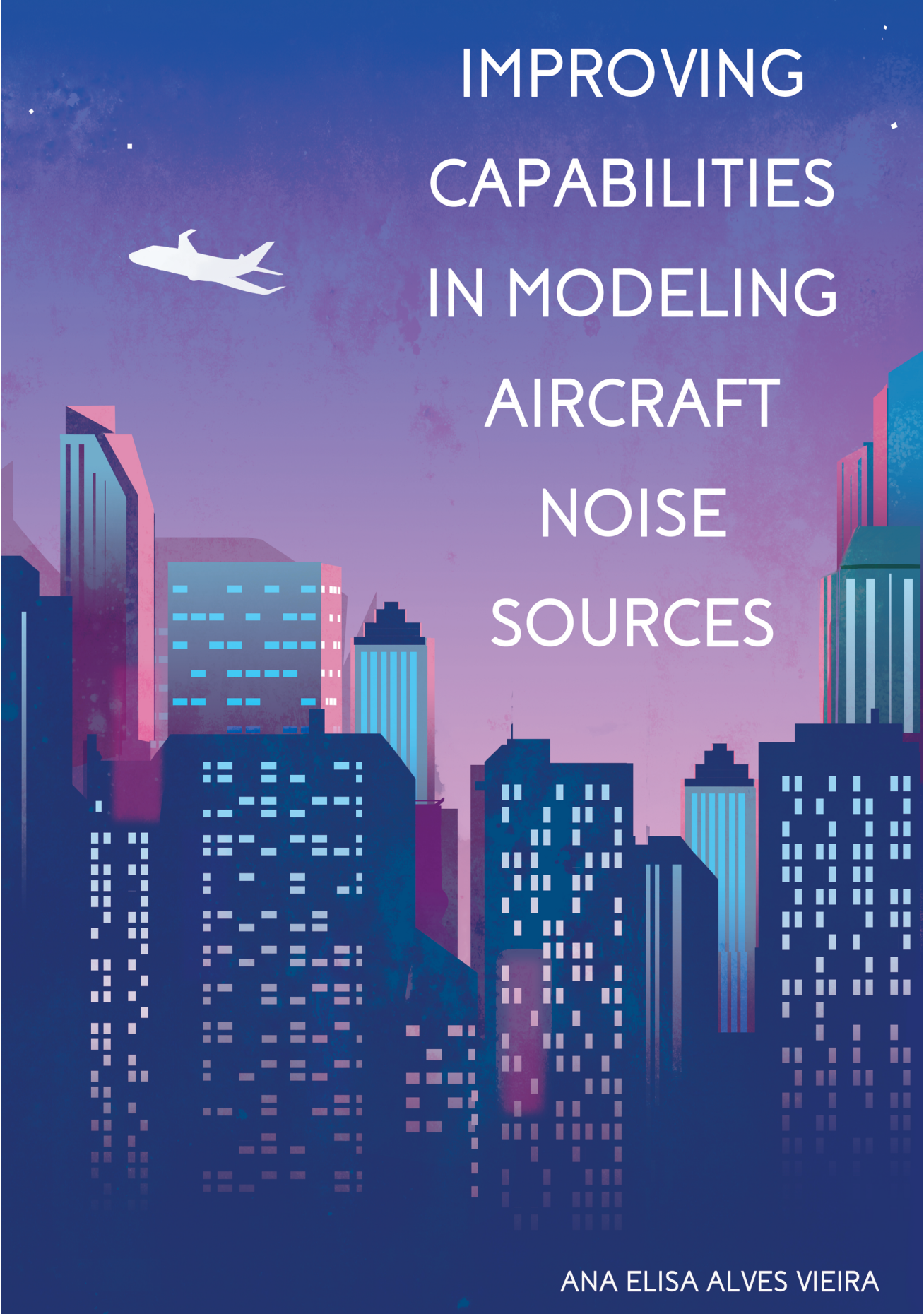
To cite this publication, please use the final published version (if applicable).
Please check the document version above.

Copyright

Other than for strictly personal use, it is not permitted to download, forward or distribute the text or part of it, without the consent of the author(s) and/or copyright holder(s), unless the work is under an open content license such as Creative Commons.

Takedown policy

Please contact us and provide details if you believe this document breaches copyrights.
We will remove access to the work immediately and investigate your claim.



IMPROVING
CAPABILITIES
IN MODELING
AIRCRAFT
NOISE
SOURCES

ANA ELISA ALVES VIEIRA

Improving capabilities in modeling aircraft noise sources

Improving capabilities in modeling aircraft noise sources

Proefschrift

ter verkrijging van de graad van doctor
aan de Technische Universiteit Delft,
op gezag van de Rector Magnificus Prof. dr. ir. T.H.J.J. van der Hagen,
voorzitter van het College voor Promoties,
in het openbaar te verdedigen op wednesday 16 june 2021 om 15:00 uur

door

Ana Elisa ALVES VIEIRA

Master of Science in Aerospace Engineering,
Instituto Superior Técnico, Lissabon, Portugal,
geboren te Viana do Castelo, Portugal.

Dit proefschrift is goedgekeurd door de

promotor: Prof. dr. D.G. Simons

promotor: Prof. dr. ir. M. Snellen

Samenstelling promotiecommissie:

Rector Magnificus,	voorzitter
Prof. dr. D.G. Simons,	Technische Universiteit Delft, promotor
Prof. dr. ir. M. Snellen,	Technische Universiteit Delft, promotor

Onafhankelijke leden:

Prof. dr. ir. C.H. Venner	Universiteit Twente
Prof.dr. ir. L.L.M. Veldhuis	Technische Universiteit Delft
Prof. dr. ir. M. Voskuil,	Nederlandse Defensie Academie
Prof. dr. ir. J.M. Hoekstra,	Technische Universiteit Delft

Overige leden:

Dr. ir. L. Bertsch,	Deutsches Zentrum für Luft- und Raumfahrt, Duitsland
---------------------	---

Keywords: Noise Shielding, Aircraft Annoyance, Sound Quality Metrics, Semi-empirical Noise Models, Aircraft noise.

Printed by: IPSKAMP printing

Front & Back: Future scenario of a silent night undisturbed by an aircraft flyover.

Copyright © 2021 by A. Vieira

ISBN 000-00-0000-000-0

An electronic version of this dissertation is available at
<http://repository.tudelft.nl/>.

*O caos é uma ordem por decifrar
Chaos is merely order waiting to be deciphered.*

José Saramago

Contents

Summary	ix
Samenvatting	xi
Nomenclature	xiii
Acronyms	xxv
1 Introduction	1
1.1 Impact of aircraft noise	1
1.2 Low noise aircraft	3
1.3 Calculation and assessment of aircraft noise	4
1.3.1 Methods to estimate aircraft noise.	4
1.3.2 Noise metrics to determine annoyance	6
1.4 Research Objectives	6
1.5 Thesis Outline	7
2 Theory	9
2.1 Noise sources in conventional aircraft	10
2.1.1 Engine noise	13
2.1.2 Airframe noise	19
2.2 Propeller noise	23
2.3 Noise shielding prediction.	29
2.3.1 Overview	29
2.3.2 Noise shielding for sharp-edge objects	34
2.3.3 Modification for curved edges	38
2.3.4 Modification for different noise source types.	39
2.3.5 Comparison of different noise shielding methods: validation cases	40
2.4 Acoustic Imaging	44
2.5 Noise metrics	46
2.5.1 Limitations of traditional metrics	46
2.5.2 Sound quality metrics	52
2.5.3 Psychoacoustic Annoyance Metrics	60
3 Engine noise shielding for aircraft under operating conditions	61
3.1 Experimental Setup	62
3.2 Assumptions	63
3.3 Comparison of noise shielding predictions and measurements for the Fokker 70	65
3.4 Discussion of the assumptions.	68

4	Noise shielding of propeller noise by a wing	75
4.1	Experimental setup at the anechoic room	76
4.2	Noise shielding of an omni-directional noise source	78
4.3	Noise shielding of a propeller by a wing	83
4.4	Conclusions	92
5	Influence of noise shielding in low noise aircraft	93
5.1	Methodology	94
5.2	Reference vehicle	96
5.3	Noise assessment of the low noise aircraft	99
5.3.1	Optimal engine position	100
5.3.2	Noise impact for departure	102
5.3.3	Noise impact for landing	104
5.4	Discussion.	105
5.5	Acknowledgment	107
6	Sound Quality Metrics of aircraft under operating conditions	109
6.1	Experimental Setup	110
6.2	Experimental assessment of the Sound Quality metrics.	112
6.3	Correlation of the SQM with the aircraft design.	117
6.4	Accounting for the variability of the SQM within aircraft type .	120
6.5	Comparison of EPNL with PA_{mod}	125
6.6	Discussion.	128
7	Engine and airframe noise during landing and take-off	131
7.1	Sensitivity Analysis	132
7.1.1	Take-off	132
7.1.2	Approach	138
7.1.3	Summary	140
7.2	Comparison of semi-empirical noise models with flyover data .	140
7.2.1	Airbus A320.	142
7.2.2	Boeing B777.	146
7.2.3	Airbus A330.	147
7.2.4	Summary	147
8	Summary and Outlook	153
8.1	Summary	153
8.2	Outlook	156
A	Appendix A - Green's function	159
B	Appendix B - Method of the stationary phase	161
C	Appendix C - Evaluation of the line segment in the uniform theory of diffraction	163
D	Appendix D - Determination of the tone correction for the Tone Corrected Perceived Noise Level	165

E Appendix E - Flyover measurements of the F70 compared with predictions	169
References	173
Acknowledgements	185
Curriculum Vitæ	187
List of Publications	189

Summary

Today's globalized world depends on civil air transportation, which has been continuously growing over the last decades. Nevertheless, the sustainability of this expansion is a challenge due to environmental problems. Along with greenhouse gas emissions, noise represents a severe hazard for human health, and consequently, noise regulations limit the airport capacity and impose night curfews.

Noise is therefore an important design driver for future aircraft, and accurate noise predictions are essential at an early design stage. The total noise emission of an aircraft poses a complex problem, as the distinct components emit noise with different characteristics. High fidelity methods are computationally demanding and time-consuming at an early design phase and less complex solutions, such as semi-empirical methods, are often considered to be more suitable. This thesis focuses on aspects that can improve noise predictions for a new generation of silent aircraft.

The concept of noise shielding is present in many future aircraft designs, in which engine noise is partially shielded by the airframe, resulting in a noise reduction on the ground. The noise shielding predictions presented in this work use a theory based on the Kirchhoff integral and the Modified Theory of Physical Optics. This method was extended to consider other noise source radiation patterns than the monopole and to calculate the creeping rays originated by smooth edges.

Experiments in the wind tunnel were used to validate these methods and showed that the values of noise shielding are strongly dependent on the source directivity and the shape of the obstacle.

Flyover measurements of rear engined aircraft were compared with predictions of noise shielding. The good agreement obtained considering a sharp-edged wing in the predictions was further improved by considering the curvature of the leading edge.

A low-noise variation of the Boeing 747-400 is explored using noise shielding predictions, and the optimal engine positions were found to be different when considering the wing leading edge as sharp and with a curvature. This analysis shows how the design of an aircraft is affected by the approximations adopted in the noise shielding predictions, therefore also affecting its performance.

For conventional aircraft, the noise emission is commonly estimated using semi-empirical methods. These models are based on experimental data and require detailed input of the aircraft geometry and engine settings. This work uses experimental data to test the limitations of such empirical methods during take-off and landing.

The efforts to reduce aircraft noise are only meaningful when resulting in a decrease of annoyance. Traditional metrics such as the Effective Perceived Noise Level are used to assess the annoyance caused by aircraft flyovers but do not provide information about the sound characteristics, such as tonal content and fast and slow

amplitude oscillations. Sound quality metrics provide a more complete characterization of a sound and can be combined in psychoacoustics annoyance metrics. Flyover measurements of different aircraft types during take-off and landing were used to investigate the correlation between the sound quality metrics and the aircraft geometry and propulsion system. Strong correlations were found between the sound quality metrics and a number of aircraft characteristics, indicating that psychoacoustic metrics can be used to drive the design process, similarly to existing methods that apply traditional metrics for the same purpose. The variability of the sound quality metrics and psychoacoustic annoyance within the same aircraft type was also investigated. This variability was attributed to the aircraft operating conditions.

Samenvatting

De huidige geglobaliseerde wereld is afhankelijk van civiele luchtvaart, een sector die de afgelopen decennia voortdurend is gegroeid. De duurzaamheid van deze uitbreiding is een uitdaging vanwege milieuproblemen. Naast de uitstoot van broeikasgassen vormt lawaai een ernstig gevaar voor de menselijke gezondheid, en als gevolg daarvan worden geluidsvoorschriften opgesteld die de luchthavencapaciteit beperken en een nachtklok instellen.

Geluid is dus een belangrijke drijfveer voor het ontwerp van toekomstige vliegtuigen en nauwkeurige geluidsvoorspellingen zijn essentieel in een vroege ontwerp-fase. De totale geluidsemisatie van een vliegtuig vormt een complex probleem, omdat de verschillende onderdelen geluid uitstoten met andere eigenschappen. High-fidelity-methoden vereisen veel rekenkracht en zijn tijdrovend in een vroege ontwerp-fase, en dus worden minder complexe oplossingen, zoals semi-empirische methoden, vaak als geschikter beschouwd. Dit proefschrift richt zich op aspecten die geluidsvoorspellingen kunnen verbeteren voor een nieuwe generatie stille vliegtuigen.

Het concept van geluidsafscherming is in veel toekomstige vliegtuigontwerpen. Hierbij wordt het motorgeluid gedeeltelijk afgeschermd door de romp, wat resulteert in een geluidsreductie op de grond. De voorspellingen voor het afschermen van geluid die in dit werk worden gepresenteerd, gebruiken een theorie die is gebaseerd op de Kirchhoff-integraal en de Modified Theory of Physical Optics. Deze methode werd uitgebreid om, naast de monopool, andere stralingspatronen van geluidsbronnen in aanmerking te nemen en om de kruipende stralen te berekenen die worden veroorzaakt door gladde randen.

Experimenten in de windtunnel werden gebruikt om deze methoden te valideren en deze toonden aan dat de waarden van geluidsafscherming sterk afhankelijk zijn van het stralingspatroon van de bron en de vorm van het obstakel.

Geluidsmetingen van overvliegende vliegtuigen met de motor richting de staart, werden vergeleken met voorspellingen van geluidsafscherming. Een goede overeenkomst werd verkregen als een scherpgerande vleugel in de voorspellingen werd gebruikt. De voorspellingen werden verder verbeterd door rekening te houden met de kromming van de voorrand.

Een geluidsarme variant van de Boeing 747-400 wordt onderzocht met behulp van voorspellingen voor het afschermen van geluid, en de optimale motorposities bleken anders te zijn wanneer de vleugelvoorrand werd beschouwd als scherp dan met een kromming. Deze analyse laat zien hoe het ontwerp van een vliegtuig wordt beïnvloed door de benaderingen die worden gedaan in de voorspellingen voor geluidsafscherming, wat dus ook de prestaties ervan beïnvloedt.

Voor conventionele vliegtuigen wordt de geluidsemisatie doorgaans geschat met behulp van semi-empirische methoden. Deze modellen zijn gebaseerd op experi-

mentele gegevens en vereisen gedetailleerde invoer van de vliegtuiggeometrie en instellingen van de motoren. Dit werk maakt gebruik van experimentele gegevens om de beperkingen van dergelijke empirische methoden tijdens het opstijgen en landen te testen.

De inspanningen om vliegtuiglawaai te verminderen hebben alleen zin als ze leiden tot een vermindering van de hinder. Traditionele maatstaven zoals het Effected Perceived Noise Level worden gebruikt om de hinder te beoordelen die wordt veroorzaakt door vliegtuigen, maar bieden geen informatie over de geluidskarakteristieken, zoals de aanwezigheid van tonen of snelle en langzame amplitude-oscillaties. Metrieken over geluidskwaliteit bieden een completere karakterisering van een geluidsfragment en kunnen worden gecombineerd tot psychoakoestische hinder waardes. Geluidsmetingen van verschillende vliegtuigtypen tijdens het opstijgen en landen werden gebruikt om de correlatie tussen de meetwaarden van de metrieken over geluidskwaliteit en de vliegtuiggeometrie en het voortstuwings-systeem van het vliegtuig te onderzoeken. Er werden sterke correlaties gevonden tussen metrieken over geluidskwaliteit en een aantal vliegtuigkenmerken, wat erop wijst dat psychoakoestische meetwaarden kunnen worden gebruikt om het ontwerpproces aan te sturen, zoals er ook bestaande methoden zijn die traditionele metrieken toepassen voor hetzelfde doel. De variabiliteit van de metrieken over geluidskwaliteit en psychoakoestische hinder binnen hetzelfde vliegtuigtype werd ook onderzocht. Deze variabiliteit werd toegeschreven aan de operationele condities van het vliegtuig.

Nomenclature

Latin Symbols

a	Local radius of the curvature
a_0	Transmission between a free field and a peripheral hearing system
a_i	Power coefficient relating the acoustic power with the flow speed
A	Area
A_{EK}	Amplitude of the secondary neural excitation of a frequency
A_f	Amplitude function of the diffraction line integral
Ai	Airy function
A_n	Jet nozzle area
A_s	Scaling coefficient depending on the jet region used in Stone's model
A_{tt}	Noise attenuation
A_w	Wing area
B	Empirical term in correlation of noise components at high velocity
b	Span
B	Source power estimate/beamformer output for a given scan point
c_0	Speed of sound
c_K	Calibration constant used in the tonality calculation
c_S	Calibration constant used in the sharpness calculation
C	Tone correction
\mathbf{C}	Cross-spectral matrix
CBW	Critical bandwidth
C_{FS}	Constant equal to 0.249 used in the fluctuation strength calculation

C_s	Scaling coefficient used in the jet noise calculation according to Stone's model
d	Distance between two monopoles composing a dipole
d_{array}	Distance between the microphone array and the noise source
d_j	Characteristic diameter
d_{object}	Distance between the noise source and the obstacle
D_e	Effective aperture of the array
D_f	Directivity function
D_{fan}	Fan diameter
D_m	Diffraction coefficients
D_w	Wheel diameter
e	Unit direction vector of a line segment
e_i	Specific excitation time function
E	Function dependent on the amplitude function and the derivatives of the phase function
E_{GR}	Masking intensity of the broadband noise surrounding selected tones
E_{HS}	Intensity at the threshold of hearing
f	Frequency
f_c	Central frequency
f_{mod}	Modulation frequency
f_T	Frequency of test tone
f_e	External force density
F	Fresnel integral
\mathcal{F}	Factor for the amplitude function
F_1	Function dependent on the tip Mach number, used to calculate fan noise in Heidmann's model
F_2	Function dependent on the rotor-stator spacing, used to calculate fan noise in Heidmann's model

F_3	Directivity correction used to calculate fan noise in Heidmann's model
F_4	Spectrum shape used to calculate fan noise in Heidmann's model
F_f	Spectrum falloff for combustor noise
F_m	Masking factor
FS	Fluctuation strength
F_t	Difference between the original and the corrected value of sound pressure level
g	Phase function of the diffraction line integral
g_R	Calibration factors used in the roughness calculation
g_s	Weighting function for the sharpness calculation
G	Green's function
G_i	Constant taking into account the effect of the aircraft component in Fink's method
\mathbf{h}	Steering vector
$h_{BP,i}$	Weighted excitation envelop
h_n	Steering vector for a n^{th} element of the microphone array
h_{source}	Height of the source relative to the ground of the anechoic room
H	Absolute altitude
H_i	Weighting function to model the bandpass characteristics of overlapping critical bands
i^2	Imaginary unit, -1
I	Identity operator
\mathbf{I}	Unit tensor
I_{jet}	Sound intensity generated by the jet
I_Γ	Diffraction line integral of a straight segment Γ
k	Wavenumber
k_c	Convection coefficient

K	Tonality
K_i	Empirical constant in Fink's method
l	Azimuthal number
l_{strut}	Length of the strut
L_A	A-weighted sound pressure level
$L_{\text{Aeq,T}}$	Equivalent A-weighted sound level for multiple flight events
L_b	Base level of the fan
L_c	Characteristic length
L_{DEN}	Day-evening night average level
L_E	Excitation level
$L_{i,o}$	Length between the inner/outer jet exhaust plane
L_k	Sound pressure level of a k^{th} tonal component
L_N	Loudness level
L_p	Sound pressure level value
L_{pr}	Sound pressure level value relative to the maximum value
L_T	Level of test tone
L_{TQ}	Threshold in quiet
m	Mass source term
m_i^*	Effective degree of modulation
\dot{m}_f	Mass flow rate across the fan
\dot{m}_{ref}	Empirical reference value of the mass flow rate across the fan
M	Mach number
M_c	Convective Mach number
M_{DP}	Fan rotor tip Mach number at design point
M_t	Tip Mach number
MTR	Design Mach tip
\mathbf{n}	Normal vector to the aperture

n_c	Constant used in Stone's model
n_{\max}	Maximum noy value
n_{tot}	Overall noy value
n_{wheel}	Number of wheels
N	Loudness
N'	Unmasked specific loudness
\bar{N}	Weighted first momentum of unmasked specific loudness
\mathcal{N}	Fresnel's number
N_1	Rotational speed of the fan relate to its maximum value, in percentage
$N_{1,c,b}$	Cutback rotational speed
N_B	Number of fan blades
N_{est}	Values of Effective Perceived Noise Level in a linear scale
N_{Gr}	Loudness of a sound without the tones
N_{spec}	Specific loudness
N_V	Number of stator vanes
p	Acoustic pressure
p_0	Reference sound pressure
\mathbf{p}_o	Position of an observer for the formulation of the Boundary Element Method
p_d	Diffracted acoustic field
p_{GO}	Undisturbed incident acoustic field
p_i	Incident acoustic field
\mathbf{p}_m	$N \times 1$ vector containing the Fourier transform of the recorded pressure at each microphone
p_s	Scattered acoustic field
\mathbf{P}	Fluid stress tensor

PA	Value of annoyance as determined by the psychoacoustics annoyance model
PA_{mod}	Value of annoyance as determined by the modified psychoacoustic annoyance model
\mathcal{P}_j	Noise penalty depending on the time period
\mathbf{q}	Position of a source for the formulation of the Boundary Element Method
Q_0	Volume velocity
q_m	m^{th} root of the first derivative of the Airy function
\mathbf{r}	Vector from the location of a point of the aperture to the receiver position
r_i	Specific roughness
$r_{t,0}$	Distance between the scan point and the center of the array
$r_{t,n}$	Distance between the scan point and microphone n
\mathbf{r}_p	Vector between two points in a curve, corresponding to the grazing incidence of two rays, from the source and the observer to the curve
\mathbf{R}	Vector from the noise source to the receiver position
R	Roughness
R^2	Correlation coefficient squared
s	Slope of the spectrum in 1/3-octave bands
s^*	Stationary phase point
s_a	Start point of a segment of the aperture contour
s_b	End point of a segment of the aperture contour
s_t	Slope used in the excitation level calculation
S	Sharpness
S_f	Spectral function in Fink's method
S_t	Strouhal number
t	Time variation

T	Temperature
T_1	Time interval of 1 second
T_{10}	Normalization time of 10 seconds
T_j	Total temperature in a jet region j
t_d	Detour parameter used in the uniform theory of diffraction
t_c	Arc between two points of the curvature, corresponding to the grazing incidence of two rays, from the source and the observer to the curve
u_{jet}	Jet velocity
U	Unit step function
UOSPL	Unrefracted Sound Pressure Level
v_{cruise}	Cruise velocity
V_{Gr}	Total ground speed
V_{mix}	Airflow velocity of the jet region
w_1	Bandwidth weighting function for tonality
w_2	Frequency weighting function for tonality
w_3	Prominence weighting function for tonality
w_{Gr}	Weighting function to account for broadband noise effects on tonality
w_t	Total weighting function for tonality
x	Position of the receiver
x_0	Position at the center of the array
x_{fdc}	Engine position in relation to the nose of the aircraft
x_s	Position of the sound source
x_t	Scan point
y	Vector of a line segment
y_0	Initial point of a segment of the aperture contour
z	Critical band number

z_{bf} Perpendicular distance of the planar array to the scan points

Greek Symbols

α_D	Attenuation factor of a diffuse sound field
α_m	Decay coefficients
α_s	Empirical scaling coefficient
β	Fraction of volume
γ_i	Constants used in the calculation of the psychoacoustic annoyance model ($i = 1, \dots, 5$)
Γ	Straight segment of the aperture contour
δ	Path difference of the distance between source and observer with and without the obstacle
δ_{co}	Cut-off correction
δ_{ij}	Kronecker delta
δ_i^*	Dimensionless thickness of the boundary layer of component i
Δ	Difference
Δl	Rayleigh criterion
ΔL	Masking depth
ΔL_i	Sound pressure level excess
ΔS_j	Panel i of the surface S
ΔT_f	Total temperature rise across the fan
ΔT_{ref}	Empirical reference value of the temperature rise across the fan
ϵ_ξ	Shadow indicator for the detour parameter ξ
θ	Polar angle between the source and the receiver positions
$\bar{\theta}$	Angle between the path from the inlet symmetry axis to the observer
θ_s	Polar angle between the noise source and a segment of the aperture contour
θ_{flap}	Flap deflection angle

λ	Wavelength
λ_F	Wing aspect ratio
Λ	Wing sweep
μ	Dynamics viscosity
ξ	Detour parameter introduced to eliminate the singularity of the diffraction line integral
ϵ_t	Shadow indicator for the detour parameter t
ζ	Non-dimensional value in Stone's method
ϖ	Domain of integration for the formulation of the Boundary Element Method
ρ	Fluid density
ρ_f	Original fluid density
ρ_m	Mass density of a fraction of volume
$\rho\mathbf{q}$	Vector from the source position to a point at the aperture
Π	Acoustic power
\mathbf{v}	Flow velocity
σ	Aperture in a screen
$\bar{\sigma}$	Screen
$\boldsymbol{\tau}$	Viscous stress tensor
ϕ	Azimuth angle
ϕ_{fan}	Fan rotor diameter
ϕ_{jet}	Jet diameter
φ	Acoustic potential
ω	Angular velocity
ω_{FR}	Term that includes the effect of roughness and fluctuation strength in the psychoacoustic annoyance model
ω_{S}	Term that includes the effect of sharpness in the psychoacoustic annoyance model

ω_T Term that includes the effect of tonality in the psychoacoustic annoyance model

Subscripts

0	Referring to ambient conditions
3	Value at the combustor
4	Value at the exit of the combustor
5	Value exceeded 5 % of the time signal
8	Values at the exit of the turbine
<i>a</i>	Referring to the start point of a segment in the aperture contour
<i>b</i>	Referring to the end point of a segment in the aperture contour
<i>c</i>	Referring to convective
comb	Referring to combustion
<i>d</i>	Referring to design conditions
dipole	Referring to a dipole directivity
<i>e</i>	Referring to effective
eow	Referring to engines over the wings
experimental	Referring to a value obtained experimentally
flap	Referring to the flaps
<i>h</i>	Referring to the horizontal tail
inner	Referring to an inner condition across the turbofan stages
ISA	Referring to standard conditions
multi-source	Referring to a multi-source
no shielding	Referring to a situation in which the incident field is not disturbed by the presence of an obstacle
outer	Referring to an outer condition across the turbofan stages
prediction	Referring to a predicted value
rr	Referring to the reference aircraft

ref	Reference values
shielding	Referring to a situation in which the incident field is disturbed by the presence of an obstacle
tot	Referring to a total value
v	Referring to the vertical tail
w	Referring to the wing

Superscripts

*	Complex conjugate transpose
'	Acoustic variable
~	Root mean square of a value
aperture	Referring to a value in the aperture
GTD	Referring to the Geometrical Theory of Diffraction
object	Referring to a value on the object/obstacle surface

Other

$\mathbb{E}(\cdot)$	Expectation operator
∇	Gradient operator

Acronyms

ACARE	Advisory Council for Aeronautics Research in Europe
ADS-B	Automatic Dependent Surveillance-Broadcast
AGL	Above Ground Level
ANOPP	NASA Aircraft Noise Prediction Program
BEM	Boundary Element Method
BPF	Blade Passage Frequency
BPR	Bypass Ratio
BWB	Blended Wing Body
BSM	Barrier Shielding Method
BSN	Buzz-saw Noise
CAA	Computational Aeroacoustics
CDA	Continuous Descent Approach
CFD	Computational Fluid Dynamics
CSM	Cross-Spectral Matrix
DIM	Diffraction Integral Method
DLR	Deutsches Zentrum für Luft-und Raumfahrt (German Aerospace Center)
DNS	Direct Noise Simulation
DNW	Deutsch-Niederländische Windkanäle (German-Dutch Wind Tunnel)
EASA	European Union Aviation Safety Agency
ECAC	European Civil Aviation Conference
EPNL	Effective Perceived Noise Level

ESM	Equivalent Source Method
FAA	Federal Aviation Administration
FlipNA	Flightpaths for Noise Analysis
FSC	Fast Scattering Code
GSP	Gas Turbine Simulation Program
GTD	Geometrical Theory of Diffraction
<i>GTlab</i>	Gas Turbine Laboratory
HLD	High Lift Devices
ICAO	International Civil Aviation Organization
IFFT	Inverse Fast Fourier Transform
LES	Large Eddy Simulation
MLG	Main Landing Gear
MLW	Maximum Landing Weight
MOB	Multidisciplinary Optimisation of a Blended Wing Body
MTOW	Maximum Take-off Weight
MTPO	Modified Theory of Physical Optics
NASA	National Aeronautics and Space Administration
NLG	Nose Landing Gear
NPD	Noise-Power-Distance
NRM	Nederlands Reken Model (Dutch Aircraft Noise Model)
NWB	Niedergeschwindigkeits-Windkanal Braunschweig (Low-Speed Wind Braunschweig)
OSPWL	Overall Power Level
OSPL	Overall Sound Pressure Level
PANAM	Parametric Aircraft Noise Analysis Model
PDE	Partial Differential Equation
PNL	Perceived Noise Level

PNLT	Tone Corrected Perceived Noise Level
PO	Physical Optics
<i>PrADO</i>	Preliminary Aircraft Design and Optimization
PSD	Power Spectral Density
RMS	Root Mean Square
RSS	Rotor Stator Spacing
SEL	Sound Exposure Level
SPL	Sound Pressure Level
SPW	Sound Power Level
SQM	Sound Quality Metrics
SRA	Strategic Research Agenda
TAS	True Air Speed
TSFC	Thrust-Specific Fuel Consumption

1

Introduction

This introduction gives an overview of the current noise reduction challenges of aviation and explains the contribution of this research work to the present state-of-the-art. A brief historical perspective of aircraft noise evolution is presented, along with its impact on the community and available assessment methods.

1.1. Impact of aircraft noise

Civil aviation plays an important role in the world economy and globalization. Air traffic has been continuously rising together with the passenger growth rate since its early days in the 1960s [1]. The European Union Aviation Safety Agency (EASA) estimates an average annual growth rate of 1.5 % of the total number of flights in the countries of the European Union and European Trade Association between 2017 and 2040 [2]. Also the Federal Aviation Administration (FAA) estimates a continuous increase of air traffic, at an average annual growth rate of 2 % of the domestic and 3 % of the international market for the period between 2019 and 2039 [3].

Despite the importance of civil aviation in modern life, it has a negative impact on the environment [4, 5] and human health [6, 7] due to greenhouse gas and noise emissions. The prolonged exposure of urban areas close to airports to high levels of noise is associated with sleep disorders and cardiovascular diseases [8]. In addition, recent evidence suggests that community's tolerance to aircraft noise has decreased over time [9, 10].

This reality is reflected in the noise target established in the Strategic Research Agenda (SRA) [11] of the Advisory Council for Aeronautics Research in Europe (ACARE), which aims at a reduction of 10 dB per aircraft operation in 2020 relative to typical aircraft of 2000. According to the International Civil Aviation Organization (ICAO) Balanced Approach concept [12], noise reduction targets should be achieved combining novel technologies, optimized operational procedures and effective metrics for perceived annoyance, in a combined effort of industry and airports.

The first action towards more silent aircraft dates back to the 1970s, with the in-

crease of engines bypass ratio [13], which drastically reduced the jet contribution to the total noise emission and decreased the perceived noise level by 20 dB throughout the decades, as depicted in Figure 1.1. The acoustic treatment of the engine ducts with liners [14], which applies the principle of the Helmholtz resonator to damp frequencies of interest, also proved to be an effective technology in reducing engine noise.

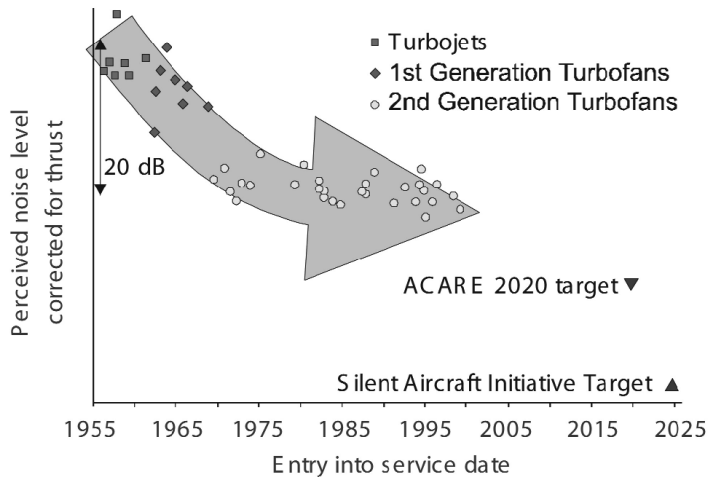


Figure 1.1: Evolution of engine noise [13].

As engine noise decreased, airframe noise sources, such as high-lift devices and the landing gear, became more important during landing [15]. A balanced approach to reduce airframe noise without negatively affecting the aerodynamic performance of the high-lift devices and the landing gear proved to be a difficult task [16]. Side-edge fences and flow transparent edge replacements [17] (using porous metal foams) showed promising results in reducing the noise generated by flap side edges but such materials are still not approved for aircraft applications. Slat covers are another example of technology with potential to reduce airframe noise [18]. Most of these airframe noise reduction technologies were tested in wind tunnel facilities and more recently also in flight demonstrations [19].

The referred noise reduction technologies, together with noise abatement trajectories [20, 21], contribute to mitigate the noise impact of flight operations. The Continuous Descent Approaches (CDAs) are already in use at some airports to minimize the impact of individual aircraft during approach [22]. During CDAs the noise footprint on ground is reduced by maximizing the cruise phase, which is followed by a vertically optimized route. Most optimized approach and take-off trajectories consider single event flights, but recent studies already analyze concepts of multi-event trajectory optimization [23].

1.2. Low noise aircraft

Despite all the efforts towards more silent flight operations around airports, the noise reduction targets for 2050 are far from being met. The prospect of a continuous growth of the number of passengers along with a more critical perception of noise and its effects on human health anticipate increasingly strict noise regulations. It is therefore questionable whether noise emissions of conventional aircraft can still be significantly further decreased.

Due to such constraints, unconventional aircraft are increasingly seen as alternatives capable to meet noise regulations' targets. The Blended Wing Body (BWB) aircraft is perhaps the first concept that comes to mind, due to its distinct airframe. This concept is being considered as an option for long range operations since the early 2000s due to its aerodynamic efficiency, low noise emissions and reduced direct operating costs [24]. The different variations of the BWB aircraft include disruptive technologies such as distributed propulsion (positioned at the rear fuselage) and laminar flow technology. BWB concepts are more silent than conventional wing and tube aircraft because they do not require flaps and a tailplane, and engine noise is significantly shielded by the airframe [25]. These features make the BWB aircraft an attractive concept for the industry, and many joint initiatives explored different variations of this concept, as illustrated in the examples of Figure 1.2. Nevertheless, several challenges still remain, such as stability and control problems and interactions between the airframe and the propulsion system.

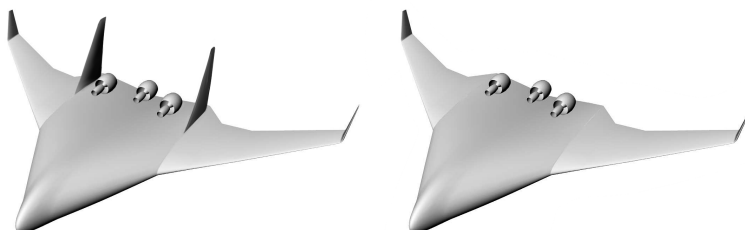


Figure 1.2: BWB aircraft variations investigated in the scope of the Multidisciplinary Optimisation of a Blended Wing Body (MOB) project [26].

Other unconventional aircraft, such as delta, truss-braced and strut-braced configurations, were also investigated as low noise alternatives to conventional commercial aircraft [27]. The Low Noise Aircraft of the German Aerospace Center (DLR), represented in Figure 1.3, is an example of an unconventional aircraft that does imply such a drastic design change compared to today's aircraft as the BWB does. In this concept the engines are mounted above the forward swept wings, relying on noise shielding for reducing engine noise, as in the case of the BWB. The vertical tail plane is replaced by double fins (also to take advantage of engine noise shielding), the wings are moved backwards to minimize cabin noise and the canard configuration stabilizes the model [28].



Figure 1.3: Top view of a scale model of DLR's Low Noise Aircraft in the Low-speed wind tunnel Braunschweig (NWB) operated by the foundation Deutsch-Niederländischer Windkanal (DNW) [29].

Less drastic design modifications, such as tube and wing aircraft with rear mounted engines, also showed good prospects in decreasing community noise [30], and are more likely to be adopted by the industry over the coming decades than disruptive concepts. These configurations rely on engine noise shielding and make use of airframe noise reduction technologies to decrease the noise footprint on the ground.

1.3. Calculation and assessment of aircraft noise

Aircraft are complex noise sources, composed of engine and airframe noise components, which change with different operational conditions. Therefore, the noise signature of an aircraft is different for distinct flight phases, for example engine noise is dominant for take-off but has an equivalent contribution to airframe noise during approach [15]. Different methods are used to predict aircraft noise depending on the level of detail and accuracy required. Ultimately, reducing individual noise sources is only meaningful if community annoyance is decreased. Psychoacoustic surveys show that the negative response towards a sound (annoyance) is determined not only considering its intensity and duration, but it is also affected by the frequency and tonal content [31].

A brief description of the methods used to calculate aircraft noise and to assess annoyance is given below. A more detailed review of the traditional and psychoacoustic metrics used to determine annoyance can be found in Section 2.5.

1.3.1. Methods to estimate aircraft noise

When investigating a phenomenon, the first natural step is to study it experimentally. Wind tunnels are widely used to study the aerodynamics and acoustic properties of aircraft components or scaled models. These facilities can be characterized according to their flow regime (low-speed, transonic and supersonic), duct circuit (open or closed), size (high-speed wind tunnels are normally smaller due to the

amount of power used to operate them) and application (e.g. climate and icing tunnels) [32].

The background noise of the test section in open jet wind tunnels has been reduced since the 1960s [33], allowing for more precise aeroacoustic measurements. Also the noise generated by the fan/compressor used to generate the airflow was optimized throughout the last decades.

Wind tunnel facilities are a controlled environment, and therefore, the acoustic measurements are precise and replicable. However, it is not possible to test a full size aircraft in a wind tunnel. Field measurements using microphone arrays are used to assess aircraft noise under operating conditions. Several corrections should be performed when evaluating the measured data, such as the atmospheric attenuation and the Doppler effect, as the aircraft is a moving source. Also noise reflections and unexpected background noise sources have to be taken into consideration.

The data from wind tunnels and field measurements is used to validate predictions but also to develop empirical models. Predicting aircraft noise for different operating conditions is essential to make design choices, as testing scale-models in wind tunnels is expensive and time consuming.

Concerning modeling approaches, different methods can be used to estimate aircraft noise with distinct accuracy and computational time. High-fidelity methods denominated computational aeroacoustics (CAA), provide accurate and detailed analysis but are computationally expensive. CAA methods can be divided in three categories: comprehensive CAA, hybrid CAA and large eddy simulation [34]. In comprehensive CAA the flow generation and near-field propagation are solved computationally. In hybrid CAA, the nonlinear flow is solved at the source and propagated to the far-field using an acoustic theory, for instance the Lighthill's analogy [35]. Many CAA hybrid methods were developed for flow simulations, such as the combination of direct noise simulation (DNS) or large eddy simulation (LES) with the acoustic analogy [36].

On the other side of the spectrum, best practice methods are used to estimate noise of conventional aircraft with minimum computational time, in order to calculate noise contours around airports. Unlike CAA methods, best practice methods include many approximations and a limited number of input parameters such as the engine thrust and distance to the observer to determine the noise level. The methods are typically based on experimental data, i.e., they are empirical. This data is usually provided by the manufacturers and obtained during the certification process. Examples of best practice methods are models based on Noise-Power-Distance (NPD) tables, in agreement with Document 29 of ECAC (European Civil Aviation Conference) [37]. The noise levels determined with NPD tables for an observer on the ground have to be corrected for lateral attenuation, bank angle and flight profile height. The Netherlands Reken Model (NRM) - Dutch Aircraft Noise Model, used for estimating community noise around Amsterdam Airport Schiphol, is an example of a best practice approach.

Semi-empirical methods use empirical data from measurements but are physics based and often parametric [37]. In these models engine noise is separated from airframe noise, and the different noise components such as the fan, turbine, high-

lift devices and landing gear are also often estimated. PANAM (Parametric Aircraft Noise Analysis Module) [38] and ANOPP (NASA Aircraft Noise Prediction Program) [39, 40] are well-known parametric semi-empirical tools suitable to be integrated in multi-disciplinary aircraft design frameworks.

1.3.2. Noise metrics to determine annoyance

The impact of aircraft noise on communities is determined using different metrics that take into account signal characteristics such as intensity, frequency content and duration. Common metrics to assess the impact of single flyover events are the A-weighted Sound Pressure Level (dBA) and the Sound Exposure Level (SEL). The A-weighting metric was created to approximate the human hearing response to noise, which perceives high frequencies as more disturbing than frequencies below 500 Hz. The A-weighting metric approximates the 40 phon equal loudness curve [41]. The Sound Exposure Level takes into consideration the duration of the signal in dBA, and it is widely used to assess aircraft noise.

The Effective Perceived Noise Level (EPNL) metric is used for certification purposes and includes weighting of tonal elements based on psychoacoustics tests [42]. Also the day-evening-night average level (L_{DEN}) is used for certification, but for multi-events over time, distributing different weights for daytime and nighttime flights.

Complex metrics such as the EPNL provide a good estimate of annoyance compared with more simplistic metrics such as the A-weighted Sound Pressure Level, but do not give detailed information about the noise characteristics responsible for a more or less annoying sound. Attributes such as tonality, sharpness, roughness and fluctuation strength provide more information about a sound than traditional metrics. Together with loudness, those are called sound quality metrics (SQM) and can be combined using psychoacoustics metrics [43] to determine annoyance.

1.4. Research Objectives

The previous sections highlighted the need for lower aircraft noise emissions in order to protect the welfare of communities around airports, and indicated possible solutions. Innovative low-noise aircraft concepts and metrics capable of identifying the most annoying noise characteristics to the human ear are two possible approaches to minimize the noise impact.

The four research objectives of this thesis, described below, explore aspects with the potential to improve current aircraft noise predictions:

1. Development and validation of a noise shielding prediction tool suitable to be used for low-noise aircraft concepts, i.e. accurate, flexible and time-efficient.
2. Explore the potential of a low-noise version of the B747-400 aircraft, with over the wing engines.
3. Investigate the suitability of psychoacoustics metrics (using flyover measurements) in the design of new aircraft.

4. Comparison of flyover measurements with engine and airframe noise predictions using parametric semi-empirical methods. The limitations of such methods are assessed and a sensitivity analysis is performed to understand which parameters might be neglected or approximated when not available.

1.5. Thesis Outline

Engine noise shielding, referred in Objective 1, is explored from Chapter 2 to Chapter 5. The methods used to calculate noise shielding are described in Chapter 2, for shielding objects with sharp and round edges, and considering different noise source directivities. Noise shielding predictions are compared with flyover measurements of the Fokker 70 in Chapter 3. Measurements of noise shielding in the controlled environment of a wind tunnel are presented and compared with predictions in Chapter 4. These experiments explore the effect of different obstacles and noise sources on the values of noise attenuation. Improvements of the predictions are made based on the findings of this measurement campaign.

Chapter 5 explores a low-noise variation of the Boeing 747-400, with over the wing engines, using noise shielding predictions (Objective 2). The optimal position of the engines was found based on Sound Exposure Level noise contours. This application case assessed the potential of noise shielding in reducing aircraft noise, for a non-disruptive design.

Traditional metrics and the sound quality metrics were used to assess aircraft noise during take-off and landing in Chapter 6, which addresses Objective 3. Flyover measurements recorded at Schiphol airport were used to verify the variability of such metrics for aircraft with similar operating conditions and whether these metrics can be correlated with the aircraft characteristics and be used to drive the design of new concepts.

To investigate Objective 4, a set of take-off and landing flyover measurements was used for the comparison with predictions of engine and airframe noise using semi-empirical methods in Chapter 7. The limitations of such methods were assessed and a sensitivity analysis was performed to understand which input parameters might be neglected when not available.

Finally, Chapter 8 summarizes what was achieved in this research work and gives suggestions for future research topics.

2

Theory

In this chapter a description of the theoretical concepts necessary for a better understanding of the following chapters is given. The different noise sources on-board of conventional aircraft are described as well as the methods used to calculate them. In addition, a focus is put on propeller noise, due to its importance for unconventional aircraft designs. A substantial part of this thesis is dedicated to noise shielding and, therefore, this chapter also gives a comprehensive overview of this topic and describes the method adopted in this work. Finally, the subject of aircraft noise metrics is addressed in detail.

A part of this chapter have been published in The Journal of the Acoustical Society of America, **143**, 1 (2018) [44] and in The Journal of the Acoustical Society of America, **146**, 2 (2019) [45].

2.1. Noise sources in conventional aircraft

The total noise emitted by an aircraft is the result of different noise sources, which are divided into two main categories: airframe and engine noise. As the name indicates, engine noise originates from the propulsion system and airframe noise is generated by the interaction between an unsteady turbulent flow and airframe components such as the landing gear, fuselage and high-lift devices. Figure 2.1 shows the most relevant noise sources on aircraft.

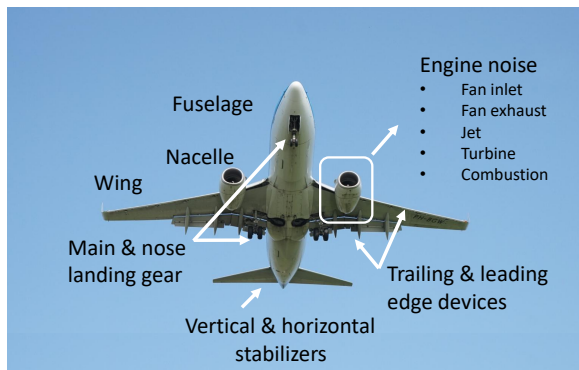


Figure 2.1: Different sources of aircraft noise.

The spectral characteristics depend on the component, i.e., the high and low frequency content varies for the different components. Also the sound directivity varies for different components. As an example, Figure 2.2 shows the directivity of the most relevant noise sources on a modern turbofan engine with a high bypass ratio. Both inlet and exhaust fan noise are represented, along with jet noise, compressor, turbine and combustion noise, each component with a distinct radiation directivity associated. Figure 2.2 only illustrates the noise directivity with respect to the polar emission angle, but the directivity can also vary in the azimuthal direction. Figure 2.3 defines the polar (θ) and azimuthal (ϕ) emission angles.

The engines and airframe contribution to total noise varies with the aircraft operating conditions. The noise emission of conventional turbofan aircraft during take-off is dominated by engine noise. However, for landing, the contribution of airframe and engine noise is approximately equivalent [47]. The landing gear is the most relevant source of airframe noise during landing, and the fan dominates engine noise.

In addition to the individual noise components, installation and interaction effects also contribute to total noise. Reflection of jet noise on the wing surface [48] and shielding of engine noise by the airframe [44] are examples of installation effects. Noise reflection of under the wing engines can significantly contribute to an increase of total noise, whereas the noise generated by rear-mounted engines can be partially shielded by the airframe, resulting in a decrease of total noise on the

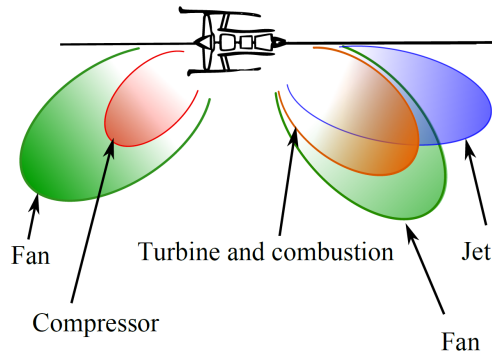


Figure 2.2: Sound directivity of different engine noise components [46].

ground. The latter is particularly important for innovative low-noise designs, and it will be further explored in this work. Examples of interaction effects are the interference of the main landing gear in the flow around the flaps or the effect of the spoiler deflection on the flow around the slat and flap.

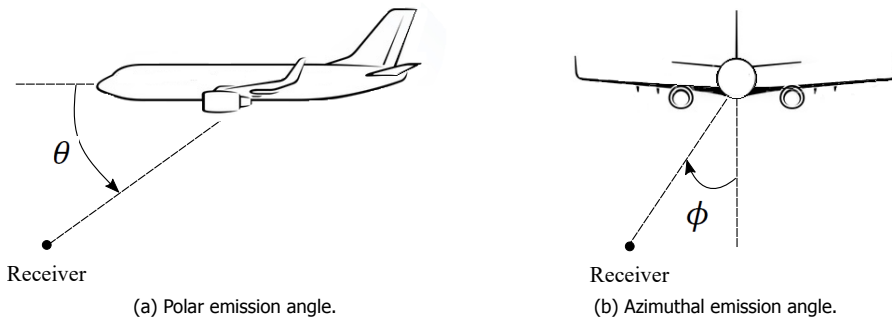


Figure 2.3: Polar and azimuthal emission angles.

Reducing aircraft noise is a complex task, requiring an in-depth knowledge of the different components. Some noise sources, such as the jet and flaps, are well understood by the scientific community but others, e.g. the spoilers and speed brakes, are still far from being fully addressed [47]. Aircraft noise can be assessed by different approaches, depending on the required level of accuracy.

Best-practice methods use experimental data to estimate the noise impact on ground. The methods based on the Noise-Power-Distance (NPD) tables are examples of such methods. They use noise certification data to estimate the noise levels on the ground, according to the weight class and flight profile of the aircraft. Another example is FLULA [49], a tool developed by the Swiss Federal Laboratories for Materials Testing and Research (EMPA). This model is based on measurements of

the noise radiation directivity patterns of commercial and military aircraft flyovers.

Despite the practicality of best-practice methods in estimating noise contours around airports, no information about the individual noise components is used. High fidelity methods and physics-based models require very detailed input data and are computationally expensive, and therefore unpractical for aircraft conceptual design within a multidisciplinary framework.

Parametric semi-empirical models are another possible approach to calculate aircraft noise. These methods determine the noise generated by the different components separately, based both on experimental data and approximations of physics-based models. This approach is therefore more accurate and flexible than best-practice methods and, on the other hand, less complex to implement and computationally expensive than high-fidelity and physics-based methods. Well-known examples of tools using semi-empirical models are NASA's ANOPP [39, 50] and DLR's PANAM [38].

ANOPP development started in the 1970s and it has been continuously updated as aircraft evolved. This tool uses Fink's approach [51] to calculate airframe noise, the method of Stone [52] for determining jet noise and the method of Heidmann [53] to predict fan noise. The latter was updated for modern turbofan engines with high values of bypass ratio using experimental data [54]. A new version of ANOPP was recently released and renamed as ANOPP2 [55]. ANOPP2 features both the parametric semi-empirical models of the early version of ANOPP and high-fidelity and physics-based models [56], allowing for the simulation of unconventional aircraft such as blended wing body configurations.

PANAM, similarly to ANOPP, applies Stone's method to calculate jet noise and uses a modified version of Heidmann's method, based on experimental data, to calculate fan noise. Airframe noise is calculated using the method developed by Dobrzynski et al [57, 58].

This thesis uses semi-empirical methods to predict aircraft noise. The most relevant airframe noise components (main and nose landing gear, wings, vertical and horizontal stabilizers, slats and flaps) are calculated with Fink's approach. Jet noise is determined using Stone's model and fan noise with Heidmann's model. In addition, combustion noise is also estimated using the same approach as ANOPP [59, 60].

The calculation of airframe noise requires detailed information about the aircraft dimensions, e.g. the wing span, the tire diameters of the main and nose landing gear and the flap area. This information is relatively easy to obtain. On the contrary, engine noise predictions require input data such as the jet velocity, fan rotational speed, and values of mass flow rate, temperature and pressure across the different engine stages, which needs to be determined for the aircraft operating conditions.

Typically, programs such as the Gas Turbine Simulation Program (GSP) [61] are used to obtain the input data required for the engine noise predictions. GSP was developed by NLR and TU Delft and calculates the gas turbine performance for a reference design point, steady off-design and transient simulations.

The models used to calculate the different noise components are presented in the following subsections.

2.1.1. Engine noise

Most commercial aircraft are equipped with turbofan engines due to their high thrust to weight ratio and fuel efficiency. The turbofan has four main stages that work together to accelerate the incoming flow in order to produce thrust: intake, compression, combustion and exhaust. These stages comprise five engine parts, illustrated in Figure 2.4: the fan, the compressor, the combustor, the turbine and the nozzle. The engine noise model used in this work includes fan, jet and combustion noise.

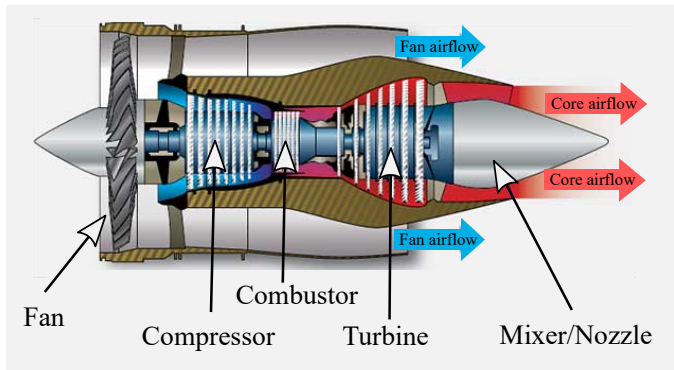


Figure 2.4: Turbofan engine stages (adapted from [62]).

In a turbofan engine, the fan collects the incoming airflow and conducts a part of it to the engine core. The other portion of the airflow is moved around the outside of the engine core, creating additional thrust and cooling the engine. This is denominated bypass air, and in modern engines with high values of bypass ratio this plays an important role in the total thrust. In the compressor, the stators (stationary blades) and the rotors (driven blades) pressurize the air, ensuring that it is ignited at the combustor with the correct pressure and temperature. The fuel is ejected at the combustor and the mixture air-fuel expands rapidly and it is forced to exit to the exhaust. The energy of the expanding gas due to the combustion is transferred into rotation energy by a coaxial shaft connected to the turbine. Finally, a high velocity jet exits the nozzle, generating thrust.

Fan noise

The fan is the first stage of a turbofan engine and the most important source of engine noise, due to the strong presence of fan noise both during landing and take-off. Fan noise presents tonal and broadband components. Heidmann's model predicts the free-field noise from the fan, considering five noise mechanisms:

- Discrete tones from the inlet;
- Broadband noise from the inlet;
- Combined tones from the inlet (buzz-saw noise);

- Discrete tones from the exhaust;
- Broadband noise from the exhaust.

The discrete tones from the inlet are generated by the rotor-stator interaction, due to the lift fluctuations on rotor blades and stator vanes, caused by the wakes generated by the rotor and inlet guide vanes hitting the stator. This disrupts the pressure field distribution in a periodic pattern, dependent on the number of fan blades and the fan rotational speed. The fundamental frequency of this pattern is known as the Blade Passage Frequency (BPF), which is given by

$$\text{BPF} = \frac{N_B \text{RPM}_{\text{fan}}}{60}, \quad (2.1)$$

where N_B is the number of fan blades and RPM_{fan} is the rotational speed of the fan in rotations per minute. The multiples of the BPF are denominated as harmonics.

The discrete tones from the exhaust are generated by the same noise mechanism as the tones produced by the inlet but propagate from the engine bypass exhaust.

Inlet and exhaust broadband noise are generated by unsteady flow and turbulence in blade wakes and boundary layers. Combination tones, also referred to as buzz-saw noise (BSN), are generated when the tip Mach number is under supersonic regime. The shock waves propagate upstream and coalesce in the inlet duct, generating a periodic pattern at every engine rotation, i.e., occur at multiples of the shaft speed. These tones are called buzz-saw noise tones and are characteristic of aircraft noise during take-off.

Heidmann's model predicts the noise level, spectrum shape and directivity of the five fan noise components mentioned above. Fan noise does not vary with the azimuthal direction. The main equation comprising each of the five noise mechanisms is given by

$$\text{SPL}(\theta, f) = L_b + F_1(M_t) + F_2(\text{RSS}) + F_3(\theta) + F_4(f). \quad (2.2)$$

The functions $F_{1,2,3,4}$ can be found in [53]. Function F_1 depends on the tip Mach number (M_t), F_2 takes into account the rotor-stator spacing (RSS), F_3 contains a directivity correction for polar emission angle and F_4 represents the spectrum shape, dependent on the frequency f . The value RSS is given in percentage, relative to the chord of the fan blades. The variable L_b is calculated using the expression,

$$L_b = 20 \log_{10} \left(\frac{\Delta T_f}{\Delta T_{\text{ref}}} \right) + 10 \log_{10} \left(\frac{\dot{m}_f}{\dot{m}_{\text{ref}}} \right), \quad (2.3)$$

where \dot{m}_f is the mass flow rate across the fan and ΔT_f is the temperature rise. The variables \dot{m}_{ref} and ΔT_{ref} are empirical reference values.

The attenuation of the tones in the duct is taken into account by considering a tone cut-off correction δ_{co} based on the studies of Tyler and Sofrin [63], given by

$$\delta_{\text{co}} = \frac{M_t}{\left| 1 - \frac{N_V}{N_B} \right|}, \quad (2.4)$$

where N_V is the number of stator vanes behind the fan. The tip Mach number can be calculated using

$$M_t = \frac{\pi BPF \phi_{fan}}{N_B c_0}, \quad (2.5)$$

where ϕ_{fan} is the diameter of the fan rotor and c_0 is the speed of sound.

An empirical correction is used to account for the lining treatment at the inlet and the exhaust [64]. Acoustic lining is a treatment of the engine duct, which allows the attenuation of sound at specific frequencies, due to perforations that act as Helmholtz resonators.

Table 2.1 summarizes the input data required for the fan noise predictions according to Heidmann's method.

Table 2.1: Input data required for the fan noise predictions using Heidmann's model.

ϕ_{fan}	[m]	Fan rotor diameter
N_B	[-]	Number of rotor blades
N_V	[-]	Number of stator vanes
M_{DP}	[-]	Fan rotor tip Mach number at design point
RSS	[%]	Rotor-stator spacing
BPF	[Hz]	Blade Passage Frequency
ΔT_f	[K]	Total temperature rise across the fan
\dot{m}_f	[kg/s]	Mass flow rate across the fan
N_1	[rpm]	Rotational speed of the fan

Jet noise

Jet noise is one of the most important noise sources for departure, but its importance has decreased since the 1960s. Back then, aircraft were powered by turbofan engines with lower values of bypass ratio than modern engines. Lower values of bypass ratio result in higher values of jet velocity, which is strongly correlated with noise generation.

Lighthill's acoustic power law [65, 66] was one of the first studies about jet noise. This law considers that a turbulent jet generates a sound with intensity I , proportional to the eighth power of the jet velocity,

$$I_{jet} \sim \frac{\rho \phi_{jet}^2 u_{jet}^8}{|R|^2 c_0^5}, \quad (2.6)$$

where ϕ_{jet} is the jet diameter, u_{jet} is the jet velocity, ρ is the medium density and $|R|$ is the distance between the noise source and a receiver. Since $I = p'^2 / \rho c_0$, the

far-field acoustic pressure fluctuation p' is approximately given by

$$p'_{\text{jet}} \sim \frac{\rho \phi_{\text{jet}} u_{\text{jet}}^4}{|R| c_0^2}. \quad (2.7)$$

Other authors, such as Curle [67] and Ffowcs-Williams & Hawkings [68] found that the sound intensity of the jet depends on the 5th and the 6th power of the jet velocity and formulated different approaches to determine jet noise. However, these methods require computationally expensive CFD calculations to determine the input data.

As an alternative, this work uses Stone's model, which determines mixing noise and shock induced noise produced by the jet. Mixing noise is generated by high velocity jets mixing with the ambient air, and also due to the interaction of the jet exiting the primary and secondary nozzles. The phenomena of jet mixing noise are illustrated in Figure 2.5. Mixing noise has a broadband nature that peaks at low frequencies, around 100-200Hz.

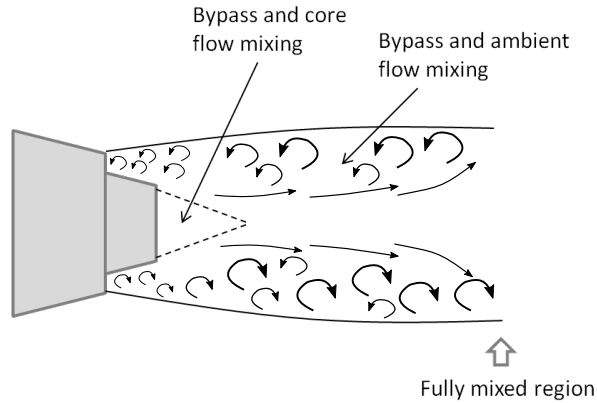


Figure 2.5: Jet mixing noise.

The method developed by Stone consisted in finding correlations between noise measurements of different engines and Lighthill's acoustic power law. A correlation between the sound intensity and the 8th power of the jet velocity could be found for large scale turbulence further upstream of the engine nozzle, but the same was not observed for other regions. Other works, such as Curle's [67] also found a lower dependence of noise intensity on jet velocity than the 8th power.

The first step of the method consists in determining the Overall Sound Pressure Level (OSPL) at the polar angle of 90° and then applying frequency-dependent directivity patterns. The OSPL is defined as the sum of the intensities corresponding to the discrete Sound Pressure Level (SPL) values per frequency of the noise spectrum. The SPL quantifies the variation in pressure originating from a sound wave relative to a the reference sound pressure p_0 of 20 μ Pa (considered as the threshold of human hearing) in logarithmic scale .

The method of Stone [52] includes the effect of forward flight, chevrons and defines three mixing zones. Two shear layers, one at the bypass airflow mixing with the ambient flow and another generated by the mixing between the bypass and core airflow, induce sound waves due to the difference of flow velocity.

The outer shear layer (between the bypass and ambient flow) generates transitional scale noise and the inner shear layer (interaction of the bypass and core flow) generates small scale turbulence, i.e., high-frequency noise. A third noise source is generated upstream of the engine exhaust, in a fully mixed region, where large scale turbulence is present, i.e., low frequency noise. This low frequency noise dominates jet noise. Shock noise is not considered because the aircraft analyzed in this work do not operate supersonic.

The unrefracted OSPL of each jet mixing noise source is given by the expression

$$\begin{aligned} \text{UOSPL} = & A_s + 10 \log_{10} \left[\left(\frac{\rho_0}{\rho_{\text{ISA}}} \right)^2 \left(\frac{c_0}{c_{\text{ISA}}} \right)^4 \right] + 10 \log_{10} \left(\frac{A_n}{|\mathbf{R}|^2} \right) + 10\zeta \log_{10} \left(\frac{\rho_e}{\rho_0} \right) \\ & + 10 \log_{10} \left[\frac{\left(\frac{v_e}{c_0} \right)^N}{1 + \mathcal{B} \left(\frac{v_e}{c_0} \right)^{N-3}} \right] - 5k_c \log_{10} \left[(1 + M_c \cos \theta)^2 + (\alpha_s M_c)^2 \right]. \end{aligned} \quad (2.8)$$

Here UOSPL is the unrefracted OSPL of the jet mixing component and the variables c_{ISA} and ρ_{ISA} are the speed of sound and the air density at standard conditions, respectively. The variable A_n corresponds to the nozzle area, k_c is the convection coefficient, α_s is an empirical scaling coefficient and \mathcal{B} is a dimensionless empirical term. The variable A_s is a scaling coefficient that depends on the region of the jet, ζ is a non-dimensional value that depends on the outflow velocity and ρ_e is the mass density in a region of the jet. N is the velocity power coefficient, which is 8 for large mixing noise and 7.5 for other regions of the jet. The values of the constants can be consulted in [69]. The effective velocity, v_e is calculated as follows,

$$v_e = V_{\text{mix}} \sqrt{1 - M \left(\frac{c_0}{V_{\text{mix}}} \right)}, \quad (2.9)$$

where V_{mix} is the flow velocity of the jet region. The convective Mach number M_c of Equation (2.8), is calculated using

$$M_c = n_c \left[\left(\frac{V_{\text{mix}}}{c_0} \right) - M \right], \quad (2.10)$$

where n_c is a constant that depends of the region of the jet (large, small or transitional turbulence) and it is determined based on the inner and outer jet velocity and on the engine having a single or dual nozzle. The quantities ρ_e and V_{mix} also depend on the region of the jet, and are determined based on the inner and outer jet temperature, velocity and mass flow rate. Similarly to the variable n_c , the value

of V_{mix} also changes for a engine with a single or dual nozzle. Expressions for these quantities can be found in [69].

The sound pressure level can be obtained at a distant point using look-up tables function of the UOSPL and the Strouhal number (S_t),

$$S_t = \frac{f d_j}{v_e} \left(\frac{T_j}{T_0} \right)^{0.4+(1+\cos\bar{\theta})}, \quad (2.11)$$

where d_j is the characteristic diameter, T_j is the stagnation temperature in the jet region and $\bar{\theta}$ is the angle between the engine inlet symmetry axis and the observer.

Table 2.2 shows the input data required for the calculation of the three components of jet mixing noise.

Table 2.2: Input data required for the jet mixing noise predictions using Stones's model.

\dot{m}_{inner}	[kg/s]	Jet inner mass flow rate
\dot{m}_{outer}	[kg/s]	Jet outer mass flow rate
T_{inner}	[K]	Total jet inner temperature
T_{outer}	[K]	Total jet outer temperature
V_{inner}	[m/s]	Inner jet velocity
V_{outer}	[m/s]	Outer jet velocity
A_{inner}	[m ²]	Inner jet area
A_{outer}	[m ²]	Outer jet area
$L_{i,o}$	[m]	Length between the inner/outer jet exhaust plane

Combustion Noise

The contribution of the combustor to the overall aircraft noise has gained importance over the last decades due to the reduction of jet and fan noise. Combustion noise has a broadband nature and can be classified as direct and indirect. Direct combustion noise occurs due to the effect of the expansion of the gas mixture on the surrounding gas, producing sound waves. Indirect combustion noise is generated by the convection of non-uniformities through the pressure gradients in the turbine, and consequently creating entropy fluctuations that generate acoustic waves. For that reason this type of noise is also denominated entropy noise.

The general formulation of the method used to calculate combustion noise in

this work [60] is given by

$$\text{OAPWL} = 10 \log_{10} \left(\frac{\dot{m}_3 c_0^2}{\Pi_{\text{ref}}} \right) + 10 \log_{10} \left\{ \left(\frac{T_4 - T_3}{T_3} \right)^2 \left(\frac{p_3}{p_0} \right)^2 \left[\frac{(T_4 - T_8)_d}{T_0} \right]^{-4} \right\} - 60.5, \quad (2.12)$$

where OAPWL is the overall power level, \dot{m}_3 is the combustor mass flow rate, Π_{ref} is the reference power of 10^{-12} W , $(T_4 - T_3)$ is the total temperature rise in the combustor, p_3 is the combustor inlet total pressure and $(T_4 - T_8)_d$ is the engine design point total temperature extraction by the turbines. When this parameter is unavailable, the value at take-off can be used instead.

The Sound Pressure Level is calculated applying the spectrum falloff for combustor noise, $F_{f,\text{comb}}$, which peaks at 400 Hz (values listed in the literature for 1/3-octave bands), followed by a far-field directivity correction, $D_{f,\text{comb}}$, also listed in the literature [60]. This results in the following expression,

$$\text{SPL}_{\text{comb}}(f, \theta) = \text{OPWL} + F_{f,\text{comb}} + D_{f,\text{comb}} + 10 \log_{10} \left(\frac{\Pi_{\text{ref}} \rho_0 c_0}{4\pi p_{\text{ref}}^2} \right), \quad (2.13)$$

considering a distance from the noise source to the observer of 1 m. Table 2.3 summarizes the input variables necessary to calculate combustion noise.

Table 2.3: Input data required for the combustion noise predictions.

MTR	[-]	Design tip mach number
p_3	[Pa]	Total pressure at the inlet of the combustor
T_3	[K]	Total temperature at the inlet of the combustor
\dot{m}_3	[kg/s]	Mass flow rate at the inlet of the combustor
T_4	[K]	Total temperature at the outlet of the combustor
T_8	[K]	Total temperature at the exit of the turbine

2.1.2. Airframe noise

Airframe noise is generated by the interaction of the airflow with the aircraft structure and has a broadband nature. The noise produced by the landing gear and the high lift surfaces are examples of relevant airframe noise sources during landing as revealed by acoustic imaging with a microphone array. The plots of Figure 2.6 show the main noise sources of two different aircraft types during landing. The Fokker 70, in Figure 2.6a, clearly shows two comparable noise sources located at the engines and at the nose landing gear (NLG), whereas the Airbus A380 shows a strong source at the location of the main landing gear (MLG). This trend was observed for other aircraft as well, which shows the importance of landing gear noise, and consequently of airframe noise, during landing [70].

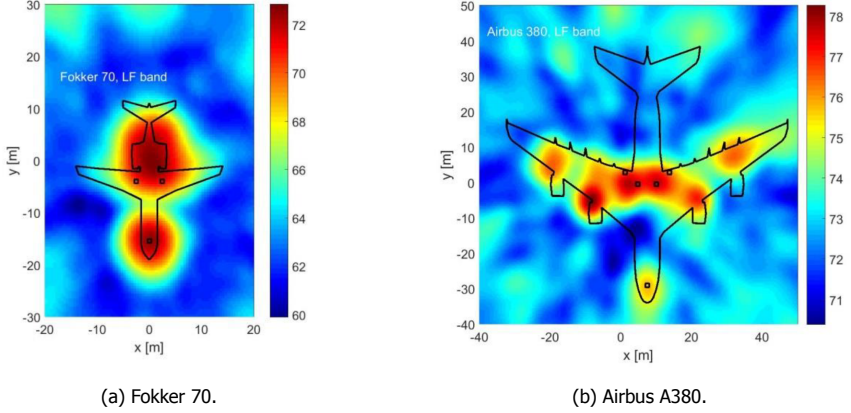


Figure 2.6: Beamforming plots of landing flyovers for frequencies between 1500 and 4500 Hz [70].

In this work, the noise in the far-field of each airframe component i is calculated using

$$p_i^2 = \frac{\Pi_i F_i(S_t) D_{f,i}(\theta, \phi)}{4\pi |\mathbf{R}|^2 (1 - M_0 \cos \theta)^4 \rho_0 c_0}, \quad (2.14)$$

where D_f is the directivity function and F is the spectral function, which depends on the Strouhal number S_t

$$S_t = (1 - M_0 \cos \theta) \frac{f L_c}{M_0 c_0}. \quad (2.15)$$

Here L_c is the characteristic dimension of the airframe component. The variable Π_i is the acoustic power, given by

$$\Pi_i = K_i (M_0)^{a_i} G_i \rho_0^3 c_0^3 b_w^2, \quad (2.16)$$

where K_i is an empirical constant, a_i is a power coefficient relating the acoustic power with the flow speed, b_w is the span, and G_i takes into account the effect of the airframe component and thus differs depending on the component.

This work calculates the noise generated by the clean wing and tail configurations, flap trailing edge noise, slat leading edge noise and landing gear noise.

Clean trailing edge noise

For a clean wing or tail configuration, according to Fink's model, the convection of the turbulent boundary layer past the trailing edge generates noise, as represented in Figure 2.7. It is assumed that this type of airframe noise has the directivity of a dipole (see Section 2.2) and the spectral function is determined empirically.

The acoustic power from the trailing edge of a conventional wing is calculated as follows,

$$\Pi_w = 4.464 \times 10^{-5} M_0^5 \delta_w^* c_0^3 b_w^2, \quad (2.17)$$

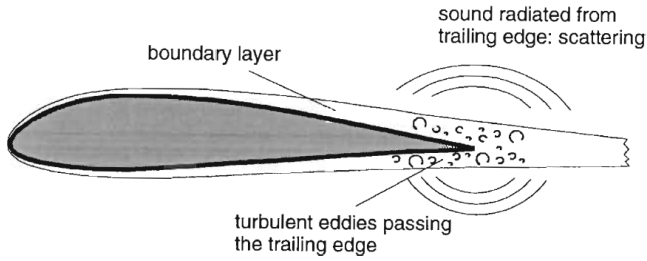


Figure 2.7: Noise generation in a clean airfoil [71].

where δ_w^* is the dimensionless thickness of the boundary layer

$$\delta_w^* = 0.37 \frac{A_w}{b_w^2} \left(\frac{\rho_0 M c_0 A_w}{\mu_0 b_w} \right)^{-0.2}. \quad (2.18)$$

Here μ_0 is the ambient dynamic viscosity and A_w is the wing area.

Equations (2.17) and (2.18) can be used for the wing and both the horizontal and vertical tail planes, replacing the corresponding geometric parameters such as the span and the area. The directivity of the wing and the horizontal tail is given by Equation (2.19). Equation (2.20) gives the directivity expression for the vertical tail,

$$D_{w,h}(\theta, \phi) = 4 \cos^2 \left(\frac{\theta}{2} \right) \cos^2 \phi, \quad (2.19)$$

$$D_v(\theta, \phi) = 4 \cos^2 \left(\frac{\theta}{2} \right) \sin^2 \phi. \quad (2.20)$$

The empirical spectral function is different for rectangular and delta wings, and it is given by Equation (2.21) and Equation (2.22), respectively.

$$F_{\text{rectangular wing}}(S_t) = 0.613(10 S_t)^4 [(10 S_t)^{1.5} + 0.5]^{-4}, \quad (2.21)$$

$$F_{\text{delta wing}}(S_t) = 0.485(10 S_t)^4 [(10 S_t)^{1.35} + 0.5]^{-4}. \quad (2.22)$$

Slat noise

When the slats are deployed, these mechanisms contribute significantly to airframe noise. This increment of noise is caused by the trailing edge noise generated by the slat itself but also by its interaction with the wing boundary layer. The first noise mechanism is considered to have an equal acoustic power contribution as the clean wing but with a different spectral function,

$$F_{\text{slat}} = 0.613(2.19 S_t)^4 [(2.19 S_t)^{1.5} + 0.5]^{-4}. \quad (2.23)$$

To account for the second noise mechanism, the acoustic power radiated from the trailing edge with the slat deployed is considered to be the double of the clean wing configuration.

Flap noise

Airframe noise increases when the flaps are deployed due to their interaction with the surrounding turbulent flow. The noise generated by the flaps increases with the deflection angle. Fink's model assumes the same empirical constant for single and double slotted flaps and another for tripled slotted flaps. The acoustic power for single/double and tripled slotted flaps are expressed by Equation (2.24) and Equation (2.25), respectively

$$\Pi_{1-2\text{ slots}} = 2.787 \times 10^{-4} M_0^6 \frac{A_{\text{flap}}}{b_w^2} \sin^2 \Theta_{\text{flap}} \rho_0 c_0^3 b_w^2, \quad (2.24)$$

$$\Pi_{3\text{ slots}} = 3.509 \times 10^{-4} M_0^6 \frac{A_{\text{flap}}}{b_w^2} \sin^2 \Theta_{\text{flap}} \rho_0 c_0^3 b_w^2. \quad (2.25)$$

Here Θ_{flap} is the deflection angle of the flaps. The empirical directivity function for flap noise is given by

$$D_{f,\text{flap}}(\theta, \phi) = 3(\sin \Theta_{\text{flap}} \cos \theta + \cos \Theta_{\text{flap}} \sin \theta \cos \phi)^2. \quad (2.26)$$

Landing gear noise

For predicting landing gear noise, Fink assumes two primary noise sources: the strut of the gear and the wheels. This means that other sources of noise such as the interaction between the gear and the fuselage are not considered.

The model of Fink uses two distinct equations to estimate the acoustic power of landing gear depending on the number of wheels. For landing gears with one or two wheels, a typical configuration of a nose landing gear, the acoustic power function is given by

$$\Pi_{1-2\text{ wheels}} = 4.349 \times 10^{-4} M_0^6 n_{\text{wheels}} \left(\frac{d_{\text{wheels}}}{b_w} \right)^2 \rho_0 c_0^3 b_w^2, \quad (2.27)$$

and for gears with four or more wheels, typically the main landing gear, the acoustic power function is expressed as

$$\Pi_{\geq 4\text{ wheels}} = 3.414 \times 10^{-4} M_0^6 n_{\text{wheels}} \left(\frac{d_{\text{wheels}}}{b_w} \right)^2 \rho_0 c_0^3 b_w^2. \quad (2.28)$$

In Equation (2.27) and Equation (2.28) n_{wheels} is the number of wheels of the gear and d_{wheels} is the diameter of the wheels, which is normally different for the nose and the main landing gear. The contribution of the strut to landing gear noise is calculated using

$$\Pi_{\text{strut}} = 2.753 \times 10^{-4} M_0^6 \left(\frac{d_{\text{wheels}}}{b_w} \right)^2 \frac{l_{\text{strut}}}{d_{\text{wheels}}} \rho_0 c_0^3 b_w^2, \quad (2.29)$$

where l_{strut} is the length of the strut. This dimension, similarly to the diameter of the wheels, is typically different for the nose and the main landing gear. The directivity functions for the contribution of the wheels and the strut to landing gear noise are given by Equation (2.30) and Equation (2.31), respectively:

$$D_{f,\text{wheel}}(\theta, \phi) = \frac{3}{2} \sin^2 \theta, \quad (2.30)$$

$$D_{f,\text{strut}}(\theta, \phi) = 3 \sin^2 \theta \sin^2 \phi. \quad (2.31)$$

The spectrum function for landing gear noise, $F_{1.g.}$, depends on the number of wheels, and it is given by the general expression

$$F_{1.g.} = \frac{\hat{C} S_t^{c_1}}{(\hat{B} + S_t^{c_2})^{c_3}}, \quad (2.32)$$

where \hat{C} , \hat{B} , c_1 , c_2 and c_3 are constants, which differ for the wheels and strut, depending on the number of wheels, as shown in Table 2.4.

Table 2.4: Constants used in the spectrum function of landing gear noise.

Component	\hat{C}	\hat{B}	c_1	c_2	c_3
Wheel ($n_{\text{wheels}}=2$)	13.58	12.5	2	2	2.25
Wheel ($n_{\text{wheels}}=4$)	0.0577	1	2	2	1.5
Strut ($n_{\text{wheels}}=2$)	5.325	30	2	8	1
Strut ($n_{\text{wheels}}=4$)	1.28	1.06	3	2	3

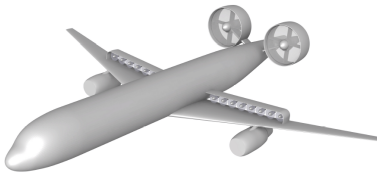
The geometry parameters required to calculate the contribution of airframe noise by Fink's method are listed in Table 2.5.

2.2. Propeller noise

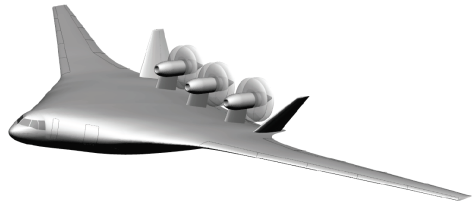
Turboprop engines are not a common design choice for medium-range commercial aircraft, but many low-noise concepts explore alternative propulsion systems to turbofan engines, such as open-rotors and distributed electric propulsion. Figure 2.8 shows two examples of those unconventional designs. These designs are more sustainable than current aircraft, presenting lower levels of greenhouse gas emissions (the open rotor is estimated to result in approximately 25% less fuel consumption than modern turbofans [72]) and take advantage of noise shielding to reduce the engine contribution to the total noise impact on ground. Ducted propellers are also a popular design choice, because the duct increases the overall thrust [73]. The effect of the duct on the noise radiation, however, is complex and highly dependent on the duct geometry and operating conditions [74].

Table 2.5: Input data required for the airframe noise predictions.

$A_{w,h,v}$	$[m^2]$	Area of the wing, horizontal and vertical tail
$b_{w,h,v}$	$[m]$	Span of the wing, horizontal and vertical tail
n_{slot}	$[-]$	Number of slots
A_{flap}	$[m^2]$	Flap area
b_{flap}	$[m]$	Flap span
$l_{MLG,NLG}$	$[m]$	Length of the strut of the MLG and NLG
$n_{MLG,NLG}$	$[-]$	Number of wheels in the MLG and NLG
$D_{MLG,NLG}$	$[-]$	Diameter of wheels in the MLG and NLG
θ_{flap}	$[\text{radians}]$	Flap deflection



(a) Distributed electric propulsion [75].



(b) Open-rotor propulsion [76].

Figure 2.8: Low-noise concepts featuring an alternative propulsion system to turbofan engines.

Other types of air vehicle, e.g. concepts of aerial taxis for a small number of passengers, are also powered by propellers or rotors. Figure 2.9 shows a ‘flying taxi’ concept of Hyundai, powered by several propellers, with capacity for 5 passengers. A realistic modelling of propeller noise is therefore of unquestionable importance to future air transportation, both for commercial aviation and urban mobility.

Rotating surfaces such as propellers, rotors and fans generate aerodynamic noise, which by definition is the sound resultant from the relative motion between a body or stream of fluid and the medium [78]. Other examples of aerodynamic noise in an aircraft besides the sound generated by rotating surfaces are jet noise and the noise generated by the landing gear and the high-lift devices.

Propeller noise is a specific case of noise generated by rotating surfaces, and it is considered as less complex than rotors and fans. Propellers have a small number of blades and the flow is in the direction of the disc plane, minimizing the interference between blades and the wake of preceding blades. Gutin performed one of the



Figure 2.9: Concept of flying taxi of Hyundai [77].

first analytical works about propeller noise [79], and considered that the thrust and torque acting on the medium were the only noise mechanisms. The model of Gutin considered a ring of discrete sources distributed over the propeller disc and showed a good agreement with experimental data. However, the equations of Gutin were an approximation and therefore not all sources of propeller noise were considered. Experimental data showed that this method underestimated the noise level of the higher harmonics when the propeller was set at a low speed.

The Lighthill's analogy using the non-homogeneous wave equation demonstrates why an approximation such as Gutin's is not sufficiently accurate to describe the complex nature of propeller noise.

Consider the inhomogeneous mass and momentum conservation equations,

$$\frac{\partial \rho}{\partial t} + \frac{\partial}{\partial x_i}(\rho v_i) = m \quad (2.33)$$

$$\frac{\partial}{\partial t}(\rho v_i) + \frac{\partial}{\partial x_i}(P_{ij} + \rho v_i v_j) = f_i + m v_i \quad (2.34)$$

where ρ is the fluid density, v_i is the flow velocity in direction i at position x at time t , m is the mass source term, f_i is an external force density and $P_{ij} = p\delta_{ij} - \sigma_{ij}$, in which δ_{ij} is the Kronecker delta and σ_{ij} the viscous stress tensor .

The mass source m is defined as a mass of density ρ_m of a fraction of volume β injected in the medium at a certain rate and therefore $m = \frac{\partial}{\partial t}(\beta \rho_m)$. The original fluid with density ρ_f is displaced by the same amount of volume as the injected mass, so $\rho = \beta \rho_m + (1 - \beta)\rho_f$. Replacing these terms and taking the time derivative of Equation (2.33) results in

$$\frac{\partial}{\partial t} \frac{\partial}{\partial x_i}(\rho v_i) = -\frac{\partial^2}{\partial t^2} \rho_f + \frac{\partial^2}{\partial t^2} \beta \rho_f. \quad (2.35)$$

Equation (2.36) results from the divergence of the momentum conservation law of Equation (2.34),

$$\frac{\partial}{\partial t} \frac{\partial}{\partial x_i} (\rho v_i) + \frac{\partial}{\partial x_i} \frac{\partial}{\partial x_j} (P_{ij} + \rho v_i v_j) = \frac{\partial}{\partial x_i} f_i. \quad (2.36)$$

The system of equations (Equation (2.35) and Equation (2.36)) is solved by eliminating the term $\frac{\partial}{\partial t} \frac{\partial}{\partial x_i} (\rho v_i)$, resulting in

$$\frac{\partial^2 \rho_f}{\partial t^2} = \frac{\partial}{\partial x_i} \frac{\partial}{\partial x_j} (P_{ij} + \rho v_i v_j) + \frac{\partial^2 \beta \rho_f}{\partial t^2} - \frac{\partial}{\partial x_i} f_i. \quad (2.37)$$

Given the small scale of the acoustic pressure, a linearization of the variables around the mean ambient condition is considered, i.e., $\rho_f = \rho_0 + \rho'$, $p = p_0 + p'$ and $v_i = v_{i,0} + v'_i$. The mean ambient conditions do not vary in time, and therefore their derivatives are equal to zero. In addition, the term $c_0^2 \nabla^2 \rho'$ is subtracted from both sides of Equation (2.37) in order to obtain the form of the Lighthill's equation,

$$\frac{\partial^2 \rho'}{\partial t^2} - c_0^2 \frac{\partial}{\partial x_i} \frac{\partial}{\partial x_j} \rho' = \frac{\partial^2 \beta \rho_f}{\partial t^2} - \frac{\partial}{\partial x_i} f_i + \frac{\partial}{\partial x_i} \frac{\partial}{\partial x_j} T_{ij}. \quad (2.38)$$

Here T_{ij} is the Lighthill's tensor [80], given by

$$T_{ij} = \rho v_i v_j - \tau_{ij} + (p' - c_0^2 \rho') \delta_{ij}. \quad (2.39)$$

Equation (2.38) identifies the different noise generation mechanisms and the corresponding type of elementary source (monopole, dipole and quadrupole, briefly described below). The term $\frac{\partial^2 \beta \rho_f}{\partial t^2}$ corresponds to the introduction of mass in the medium, and it is described by a monopole. An example of this noise generation term is the volume introduced in the medium by a moving blade. The second term of the equation, $\frac{\partial}{\partial x_i} f_i$, corresponds to the noise generated by a force distribution and has a dipole radiation. This corresponds to forces acting on the medium caused by the action of the body, and in the case of the propeller the most obvious example is the thrust. The Lighthill's tensor has a quadrupole nature and accounts for viscous forces and deviations from an isentropic behaviour and non-linear convective forces [81].

The monopole, dipole and quadrupole are denominated elementary sources and were derived by Lord Rayleigh [82]. A monopole sound field is generated by a pulsating rigid sphere of radius a and the sound wave is given by

$$p(|\mathbf{R}|, t) = i \rho_0 c_0 \frac{Q_0 k}{4\pi |\mathbf{R}|} e^{i(\omega t - k|\mathbf{R}|)}, \quad (2.40)$$

in which $\omega = 2\pi f$ is the angular frequency, $Q_0 = \pi a^2 v_0$ is volume velocity, v_0 is the velocity amplitude at the sphere's surface and k is the wavenumber $k = \omega/c_0$.

A dipole results from two monopoles of equal strength but opposite phase, separated by a distance d (small compared with the wavelength, $kd \ll 1$), and can be expressed as

$$p(|\mathbf{R}|, t, \theta) = \rho_0 c_0 \frac{Q_0 k^2}{4\pi |\mathbf{R}|} d \cos \theta e^{i(\omega t - k|\mathbf{R}|)}, \quad (2.41)$$

where θ is the angle between the dipole and the observer position.

A quadrupole is generated by two dipole sources of equal strength and opposite phase, separated by the distances d and D , and can be expressed as

$$p(|\mathbf{R}|, t, \theta) = i\rho_0 c_0 \frac{Q_0 k^3}{8\pi |\mathbf{R}|} dD \sin(2\theta) e^{i(\omega t - k|\mathbf{R}|)}. \quad (2.42)$$

The directivity pattern radiated by a monopole, dipole and quadrupole is illustrated in Figure 2.10.

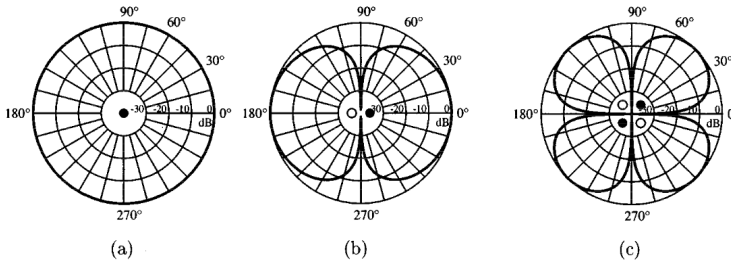


Figure 2.10: Theoretical noise pattern of a: (a) monopole, (b) dipole, (c) quadrupole [83].

Propeller noise is composed of noise sources with monopole, dipole and quadrupole directivity. For rotating surfaces, aerodynamic noise can be divided in two main categories, periodic and broadband [78], as represented in Figure 2.11.

Periodic noise describes sound with discrete frequencies, therefore rotational noise and interaction and distortion effects belong to this category. The airfoil of the propeller blades has a pressure distribution relative to the medium, which results in a thrust and a torque component (see Figure 2.12a), i.e., a force applied to the medium, equivalent to the second term of the right side of Equation (2.38). Therefore, the noise generated by the thrust and torque of the propeller has a dipole directivity.

Another periodic noise source generated by the propeller rotation comes from the volume of air displaced by the movement of the blades (phenomenon represented by the first term of the right side of Equation (2.38)). This type of noise results from a periodic insertion and removal of mass, which means it has the directivity of a monopole. The volume of air displaced depends on the blade thickness and therefore this type of noise is denominated as thickness noise.

Other examples of periodic noise sources are the blade slap, wake and field interaction (denominated as interaction effects) and amplitude and frequency mod-

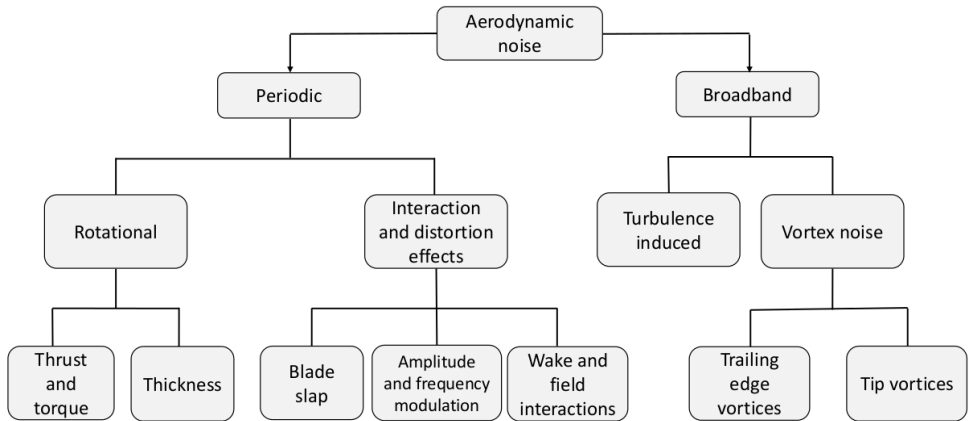


Figure 2.11: Different noise sources of propeller noise (adapted from [78]).

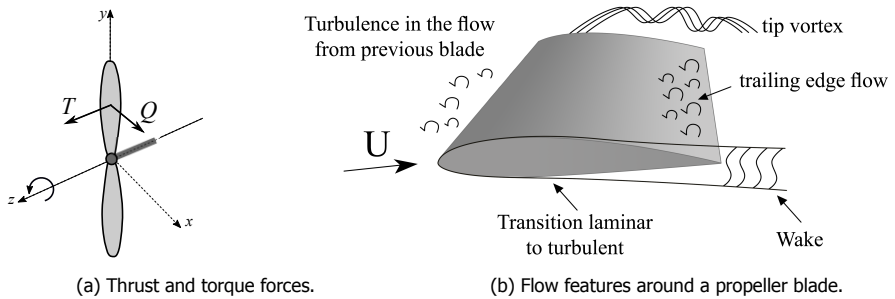


Figure 2.12: Sources of aerodynamic noise of a propeller.

ulation (distortion effects). These types of noise are generally not important for propeller noise, but can be relevant for rotor and fan noise.

Figure 2.12b shows the flow around a propeller blade, and the different mechanisms that contribute to noise. Blade slap noise arises when impulsive fluctuating forces actuate in the blade, e.g. by blade-vortex interaction. The movement of the blades passing through series of wakes generated upstream, as in the case of a fan with an upstream stator or counter rotating propellers, is an example of noise generated by the wake and field interaction. The amplitude and frequency modulation is related with distortion effects associated to the periodic advance and retreat of the noise source relative to the observer.

Broadband noise is dominated by vortex noise, which is generated by the vortices formed at the trailing edge and tip of the blades. Vortex noise has a dipole directivity [78]. Turbulence induced noise is produced in a flow field containing shear layers, and the motion of small scale turbulence produces broadband noise. This type of noise has a quadrupole directivity and it is negligible in the presence of other noise sources, however, it can be amplified when interacting with the pressure

field of the rotating blades.

In summary, rotational periodic noise (particularly the thrust and torque contributions for small propellers with modest airfoil thickness) and vortex noise are the most important types of noise generated by a propeller. These two noise types have a dipole directivity, and therefore the propeller noise radiation is commonly approximated as a dipole, as illustrated in Figure 2.13.

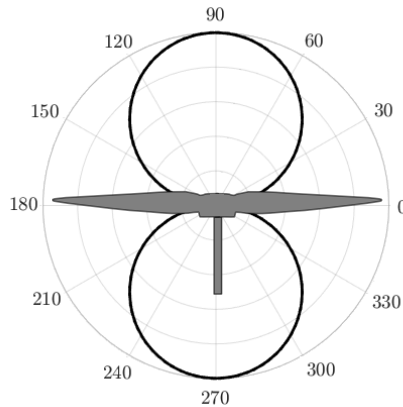


Figure 2.13: Approximation of the radiation directivity of propeller noise.

2.3. Noise shielding prediction

As discussed in previous sections, many low-noise aircraft designs present shielding of engine noise and rely on this installation effect to reduce the noise level on the ground. This section gives an overview of the different noise shielding prediction methods and presents in detail the approach used in this work. In addition, a validation effort compares results obtained with this method for simple geometries with well-established computational tools.

2.3.1. Overview

Noise shielding occurs when the incident acoustic field is modified by the presence of an obstacle between the noise source and the observer. The value of noise shielding is quantified by the ratio between the acoustic pressure received by the observer and its value if the object was not present.

When the path of a ray between the noise source and the observer passes through an obstacle, by definition, the observer is in the shadow zone, otherwise it is in the illuminated zone. Two types of rays can be generated at the observer by the presence of an obstacle: edge-diffracted and creeping rays. The edge-diffracted rays originate from sharp objects and the creeping rays from objects with a curvature, as represented in Figure 2.14, for a uniform medium.

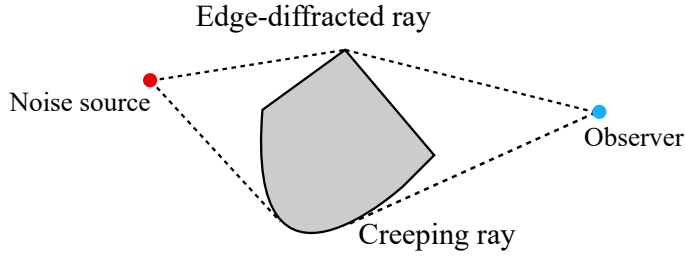


Figure 2.14: Schematic representation of creeping and sharp-edge rays.

A number of different methods is used to calculate noise shielding, for distinct types of sources and shapes of the obstacle. These methods consider different approximations and consequently the accuracy, computational time and their range of applications differ. This section provides an overview of the available methods to calculate noise shielding and their main advantages and disadvantages. The following methods are commonly used to predict noise shielding:

- Barrier Shielding Method (BSM);
- Boundary Element Method (BEM);
- Equivalent Source Method (ESM);
- Ray-tracing method;
- Kirchhoff Theory of Diffraction.

The BSM is an empirical method based on measurements of Maekawa [84], which correlates values of noise shielding in free space with the Fresnel number, for a semi-infinite rectangular plate. The Fresnel number, \mathcal{N} is given by

$$\mathcal{N} = \frac{2}{\lambda} \delta, \quad (2.43)$$

where δ is the path difference from the source to the receiver with and without the obstacle. In the example illustrated in Figure 2.15, the value of δ is given by $\delta = \pm(|\mathbf{A}| + |\mathbf{B}| - |\mathbf{d}|)$, in which the signal is positive when the direct path vector \mathbf{d} intersects the obstacle and negative otherwise. This implies that observers lie in the illuminated zone when $\mathcal{N} < 0$ and in the shadow zone when $\mathcal{N} > 0$.

The measurements of Maekawa were performed using a pulsed tone with a sufficiently short duration to allow the signal to be distinguished from the reflected sound. The values of acoustic pressure were measured at different observer positions inside the shadow zone ($\delta > 0, \mathcal{N} > 0$). Figure 2.16 shows the measurement results, which can be approximately fitted in one curve of attenuation values against the Fresnel number. Kurze [85] fitted the following equation for the shadow zone

$$\Delta L_p = 5 + 20 \log 0 \frac{\sqrt{(2\pi|\mathcal{N}|)}}{\sqrt{\tanh(2\pi|\mathcal{N}|)}} \text{ dB}, \quad (2.44)$$

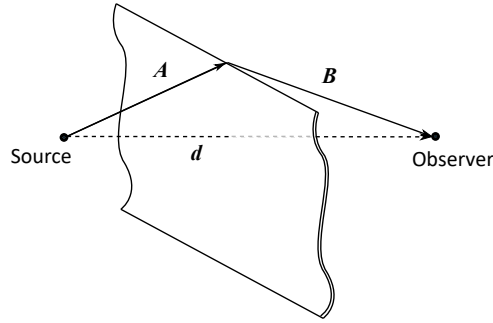


Figure 2.15: Scheme of the direct and indirect path considered by Maekawa to calculate the Fresnel's number.

in which ΔL_p is the noise shielding value in decibels. Equation (2.44) is valid for values of $\mathcal{N} \geq -0.2$, otherwise the value of attenuation is considered equal to 0 dB.

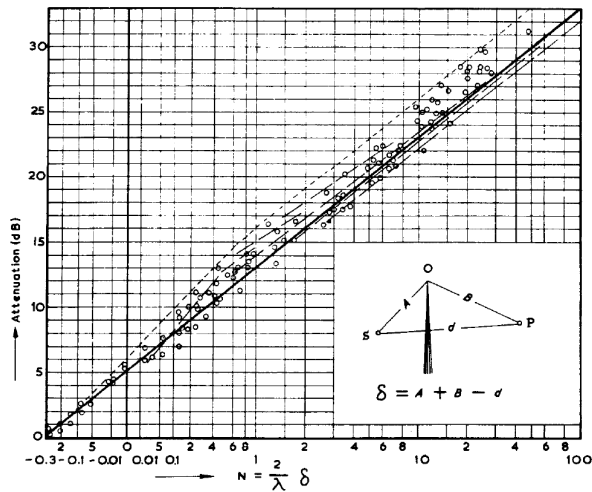


Figure 2.16: Measured values of sound attenuation by a semi-infinite thin barrier in the experiments of Maekawa [84].

Equation (2.44) calculates the noise shielding of a semi-infinite plate with one edge, but practical problems, for instance the noise shielding caused by a rectangular finite plate, can also be calculated using this empirical method. An early version of NASA's noise shielding code implemented in ANOPP [86] used this method to estimate the noise shielding of a simplified wing with no thickness, considering three sharp-edges. Equation (2.44) is applied for each edge and the total value of noise

shielding at a specific location ($\Delta L_{p,\text{tot}}$) is obtained adding the contribution of the three edges,

$$\Delta L_{p,\text{tot}} = -10 \log \sum_{i=1}^3 10^{-\Delta L_{p_i}/10}. \quad (2.45)$$

The BSM is easy to implement, not computationally expensive, and consequently it is an attractive way of roughly estimating noise shielding values. However, this method can only be applied to limited types of geometries, and it is only valid for point sources.

The BEM lies at the other extreme of the BSM because it is an accurate method but computationally expensive. In BEM, the partial differential equation (PDE) that expresses the physical problem is re-formulated as an integral equation on the boundary domain. This is an advantage relative to other methods (e.g. the finite element method), which consider the entire domain of the problem.

The BEM can be used to solve external acoustic problems, such as the case of an incident field disturbed by an obstacle (resulting in noise shielding), but also to solve interior acoustic problems and interior modal analysis [87].

A problem of noise scattering considering an obstacle with boundary S and an exterior region E , is equivalent to the solution of the Helmholtz equation,

$$\nabla^2 \varphi(\mathbf{p}) + k^2 \varphi(\mathbf{p}) = 0, \quad (\mathbf{p} \in E), \quad (2.46)$$

where $\varphi(\mathbf{p})$ is the time-independent velocity potential, k is the wave number and \mathbf{p} is the receiver position.

The Helmholtz equation is solved for each wavenumber and boundary condition. The time-dependent velocity potential $\Psi(\mathbf{p}, t)$ is obtained combining the separate solution,

$$\Psi(\mathbf{p}, t) = \text{Re} \varphi(\mathbf{p}) e^{-i\omega t}, \quad (2.47)$$

where ω is the angular frequency ($\omega = 2\pi f$ and f the frequency), t represents the time dependency. The time-dependent sound pressure $Q(\mathbf{p}, t)$ is given by

$$Q(\mathbf{p}, t) = -\rho \frac{\partial \Psi}{\partial t}(\mathbf{p}, t). \quad (2.48)$$

Integral formulations of this problem can be consulted in [88]. The BEM implementations depend on the approaches used to derive the system of linear equations. The most common approach is denominated collocation and consists of a discretization of S in panels, which together with the corresponding boundary condition are denominated as elements. The BEM is accurate but complex to implement, and becomes increasingly computationally demanding as the frequency increases, due to a more refined boundary discretization.

The Equivalent Source Method is based on the BEM, but while in the BEM the elements are located at the boundary S , in the ESM, they are located inside the boundary, and are denominated equivalent sources, as represented in Figure 2.17. The ESM has many variations such as the wave superposition method, multipole

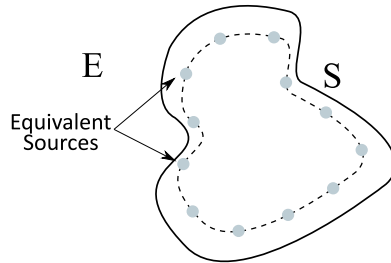


Figure 2.17: Representation of equivalent sources.

method, just to name a few examples [89]. A well-known example of a tool that makes use of the ESM is NASA's Fast Scattering Code (FSC) [90].

The main advantage of the ESM compared with the BEM is the absence of the singularity problems that arise in BEM as the distance between the noise source and the boundary approaches to zero, because in the ESM the fictitious source is inside the boundary. Also, the number of equivalent sources is not required to be the same as the surface collocation points, resulting in faster calculations.

The main problem associated with the ESM is deciding where to place the equivalent sources, and the number to consider. A suboptimal choice of the location and number of equivalent sources will decrease the accuracy of the solution. The ESM can also suffer from instability, associated with an ill-conditioned system of equations.

The ray-tracing method is a high-frequency approach, in which the Physical Optics (PO) solution is used to compute the direct and reflected rays. If the observer is in the shadow zone, the PO method is extended using the Geometrical Theory of Diffraction [91]. The rays are propagated from the source as straight lines, and have to be tracked just once and then be computed for multiple frequencies, which allows parallel computing, making this approach less time-consuming than the BEM and the ESM. However, each ray needs to be evaluated with an iterative scheme to identify the rays between the source and receiver positions, which is computationally expensive for complex geometries. Another disadvantage of this method is that only monopole sources can be considered. This method can estimate edge-diffracted and creeping rays.

The complexity of evaluating the rays for the case of aircraft noise is well explained in the work of Agarwal et al [92], in which noise shielding is computed for a flying wing aircraft using the ray-tracing method.

Finally, the Kirchhoff Theory of Diffraction is briefly explained, because it is the method adopted in this work. It is presented in detail in Section 2.3.2 to Section 2.3.4. The Kirchhoff method is less computational expensive than the BEM, the ESM and the ray-tracing method because the shielding object is not considered two or three-dimensional. Instead, the calculations consider a contour which separates the shadow and the illuminated zone.

Another advantage of the Kirchhoff method is its adaptability for noise direc-

tivities others than of a monopole. The method can also be adapted to include creeping rays.

Table 2.6 compares the different methods here presented, for the specific case of engine noise shielding by the airframe. The BSM is not suitable to this problem, because it is not adaptable to different aircraft designs and it lacks accuracy since it is an empirical model. The BEM and the ESM are both considered very accurate and adaptable methods, but their implementation is complex, computationally expensive, and therefore not suitable for an aircraft multidisciplinary design framework. The ray-tracing method is less computationally expensive than the BEM and BSM, but the limitation of the noise source directivity makes it less flexible. The Kirchhoff integral method was therefore adopted for the noise shielding calculations in this research work, since it shows the best trade-off between accuracy, computational time and flexibility.

Table 2.6: Comparison of different noise shielding methods.

Method	Accuracy	Adaptability	Implementation	Computational Time
BSM	✗	✗	✓	✓
BEM	✓	✓	✗	✗
ESM	✓	✓	✗	✗
Ray-tracing	✓	✗	✗	✗
Kirchhoff Integral	✓	✓	✓	✓

2.3.2. Noise shielding for sharp-edge objects

This section presents the noise shielding method used in this research work. The approach is based on the Kirchhoff Theory of Diffraction and the Modified Theory of Physical Optics (MTPO) [93]. The Kirchhoff Theory of Diffraction is derived from the Helmholtz equation using the Green's functions (see Appendix A), defining the scattered field in terms of a surface integral [94, 95].

Consider an arbitrary aperture σ in a screen $\bar{\sigma}$, located between a sound source placed at x_s and a receiver at position x , as represented in Figure 2.18.

The scattered field p_s and the field emitted by the source, p_i , follow the Helmholtz equation in a volume of control that does not include the screen surface and the source location, as illustrated in Figure 2.19.

The Gauss and Green theorems are applied to the referred volume of control and the system of equations, and the following approximations are applied to the boundary conditions:

- The scattered field, p_s is considered zero on the screen (i.e., the object is at rest in a non-oscillatory state);

- The scattered field p_s approximates to zero for large enough distances from the source;
- The scattered field p_s is equal to the incident field, p_i , in the aperture.

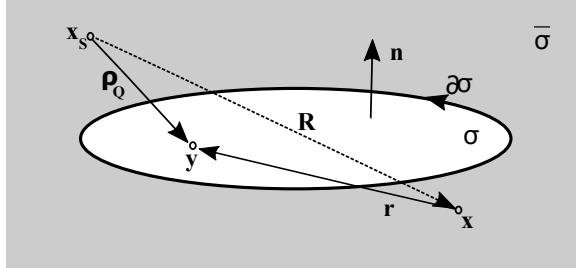


Figure 2.18: Schematic of the aperture σ in the screen $\bar{\sigma}$.

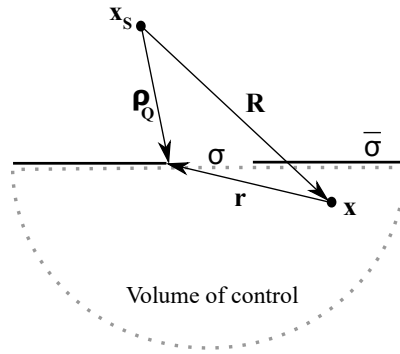


Figure 2.19: Volume of control assumed for the Kirchhoff integral method.

The pressure field at the receiver position x can then be obtained using the Kirchhoff integral over the aperture σ ,

$$p_s^{\text{aperture}} = \frac{1}{4\pi} \int_{\sigma} \left[p_i \mathbf{n} \cdot \nabla \frac{e^{ik|r|}}{|r|} - \frac{e^{ik|r|}}{|r|} \mathbf{n} \cdot \nabla p_i \right] dS, \quad (2.49)$$

where $\mathbf{r} = \mathbf{y} - \mathbf{x}$, \mathbf{y} is a point at the aperture and k is the wavenumber.

The surface integral of Equation (2.49) can be computationally expensive for large surfaces, as in the case of an aircraft, so the theory of boundary diffracted waves is applied. This theory states that the scattered field is given by the undisturbed incident field, p_{GO} and the boundary diffracted field p_d ,

$$p_s^{\text{aperture}} = p_{GO} + p_d. \quad (2.50)$$

Here $p_{GO} = p_i \chi$, where χ is a delta function equal to unity when the ray between source and receiver passes through σ and zero otherwise.

As the name indicates, in this theory the diffracted field depends only on the outline of the shielding obstacle, $\partial\sigma$, and the surface integral can be written as a line integral. Maggi and Rubinowicz derived an expression for the diffracted field p_d in terms of a line integral, considering a monopole source [96],

$$p_d = \frac{1}{4\pi} \oint_{\partial\sigma} \frac{e^{ik|\rho_Q|}}{|\rho_Q|} \frac{e^{ik|r|}}{|r|} \frac{(\rho_Q \times r) \cdot ds}{|\rho_Q||r| + \rho_Q \cdot r}. \quad (2.51)$$

Here $\rho_Q = \mathbf{y} - \mathbf{x}_s$, as represented in Figure 2.18 and Figure 2.19.

The integration contour can be discretized in straight line segments, as

$$\mathbf{y}(s) = \mathbf{y}_0 + s\mathbf{e}, \quad s_a < s < s_b, \quad (2.52)$$

where \mathbf{y}_0 is an initial arbitrary point of the contour $\partial\sigma$, \mathbf{e} is the unit direction of the line segment, and s_a and s_b are the start and end points of the segment.

Miyamoto and Wolf [96] extended the work of Maggi and Rubinowicz so that the incident field of Equation (2.51) is not limited to spherical and plane waves,

$$p_d = \frac{1}{4\pi} \oint_{\partial\sigma} p_i(|\rho_Q|) \frac{e^{ik|r|}}{|r|} \frac{(\rho_Q \times r) \cdot ds}{|\rho_Q||r| + \rho_Q \cdot r}, \quad (2.53)$$

allowing to include the noise source directivity in the term p_i .

Considering straight segments Γ of the contour $\partial\sigma$, described by Equation (2.52), the diffraction line integral can be rewritten as,

$$I_\Gamma = \frac{1}{4\pi} \int_\Gamma \frac{1}{|\rho_Q|} \frac{1}{|r|} \frac{(\rho_Q \times r) \cdot ds}{|\rho_Q||r| + \rho_Q \cdot r} e^{ik(|\rho_Q|+|r|)}, \quad (2.54)$$

and in terms of a Fourier integral,

$$I_\Gamma = \int_\Gamma A_f(s) e^{ikg(s)} ds. \quad (2.55)$$

Here $A_f(s)$ is the amplitude of the function to be integrated and $g(s)$ is the phase. The integral of Equation (2.55) is solved using the method of stationary phase, which introduces a singularity in the contribution of the end points of the straight segment. The singularity is solved using the method of uniform theory of diffraction [97]. The equations used in the method of the stationary phase can be found in Appendix B.

The uniform theory of diffraction states that the scattered field behaves like a Fresnel integral in the points connecting the different segments considered for the contour of the aperture. This theory is based on the exact solution derived by Sommerfeld to the canonical problem of plane wave diffraction by a semi-infinite plate [98]. A change of variable allows introducing a parameter denominated "detour", which together with the fundamental property of the Fresnel integral results in Equation (2.56) (this mathematical manipulation is explained in Appendix C),

$$I_{\Gamma} = \sqrt{\pi} e^{i\frac{\pi}{4}} e^{ikg(s^*)} \{E(s^*) (U(-t_d(s_a)) - U(-t_d(s_b))) + E(s_a) \text{sign}(t_d(s_a)) F[|t_d(s_a)|] - E(s_b) \text{sign}(t_d(s_b)) F[|t_d(s_b)|]\}. \quad (2.56)$$

Here s^* is the stationary phase point, t_d is the detour parameter and U is the unit step function. More details can be found in Appendix B. The Fresnel integral, F , is given by Equation (2.57) and the variable E by Equation (2.58),

$$F[x] = \frac{e^{-i(\pi/4)}}{\sqrt{\pi}} \int_x^{\infty} e^{it_d^2} dt, \quad (2.57)$$

$$E(s) = A_f(s)/h(s). \quad (2.58)$$

In Equation (2.58) $h(s)$ is a function dependent on the derivatives of the phase function $g(s)$ (expressions for the derivatives of $g(s)$ can be found in Appendix C),

$$h(s) = \begin{cases} k \frac{g'(s)}{2t_d(s)}, & \text{if } s \neq s^* \\ \sqrt{\frac{k g''(s^*)}{2}}, & \text{if } s = s^*. \end{cases} \quad (2.59)$$

The asymptotic expression of the Fresnel integral is given by,

$$\text{sign}(x) F[|x|] \simeq \frac{e^{i(\pi/4)} e^{ix^2}}{2\sqrt{\pi} x}. \quad (2.60)$$

The integral of Equation (2.56) contains a singularity when $|\rho_Q| |r| + \rho_Q \cdot r = 0$. Another detour parameter, ξ is introduced to eliminate such singularity, and the asymptotic expression of the Fresnel integral is replaced by the actual function (see Appendix C), resulting in the following expression,

$$I_{\Gamma} = 2\sqrt{\pi} \xi \text{sign}(\xi) F[|\xi|] \{E(s^*) [U(-\xi_a) - U(-\xi_b)] + E(s_a) \text{sign}(\xi_a) F[|\xi_a|] - E(s_b) \text{sign}(\xi_b) F[|\xi_b|]\}. \quad (2.61)$$

The detour parameter ξ is given by

$$\xi(s, \mathbf{P}) = \epsilon_{\xi}(\mathbf{P}) \sqrt{k[g(s) - |\mathbf{R}|]}, \quad (2.62)$$

here ϵ_{ξ} is a shadow indicator equal to 1 if the point \mathbf{P} is located in the illuminated region and -1 if in the shadow zone.

Therefore, the diffracted field through an aperture, p_d^{aperture} , is given by the sum of the individual contribution of the straight segments of the contour, Γ , calculated by Equation (2.61). The scattered field by the aperture, p_s^{aperture} can then be calculated using Equation (2.50). To obtain the scattered field due to the presence of the shielding object, p_s^{object} , is made use of the Babinet's principle [99],

$$p_s^{\text{object}} = p_i - p_s^{\text{aperture}}. \quad (2.63)$$

The value for the scattered field due to the presence of an object is then used to determine noise shielding in decibels using,

$$\Delta\text{SPL} = -20 \log_{10} \left| \frac{p_s^{\text{object}}}{p_i} \right|. \quad (2.64)$$

2.3.3. Modification for curved edges

The noise shielding method presented in the previous section can only be applied to edge-diffracted rays. In this section, the method is extended to include creeping rays, which is achieved by modifying the amplitude $A_f(s)$ of the diffracted field of Equation (2.55). The diffracted field is assumed as defined by the geometrical theory of diffraction (GTD) [100, 101] for edges with a curvature (as illustrated in Figure 2.20),

$$p_d^{\text{GTD}} = p_i e^{ik|r|} \sqrt{\frac{|r_p|}{|r|(|r_p| + |r|)}} \sum_m D_m^2(k, a_c) e^{-t_c \alpha_m} e^{ikt_c}. \quad (2.65)$$

Here t_c is the arc length between two points, P_1 and P_2 . P_1 and P_2 correspond to the grazing incidence of a ray to the curve from the source and from the observer, respectively. The variable a_c is the local radius of the curvature and r_p is the distance between P_1 and P_2 .

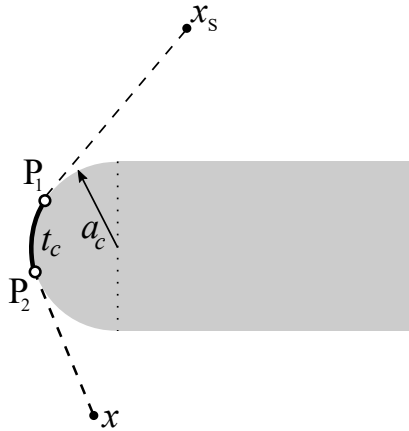


Figure 2.20: Representation of an edge with curvature and parameters used in the noise shielding calculation.

The diffraction and decay coefficients, D_m and α_m , respectively, are given by the expressions,

$$D_m^2(k, a) = \frac{e^{i\pi/12} a^{1/2}}{2^{5/6} \pi^{1/2} (ka_c)^{1/6} Ai(-q_m)^2}, \quad (2.66)$$

$$\alpha_m = \frac{1}{a_c} \left(\frac{ka_c}{2} \right)^{\frac{1}{3}} q_m e^{-i(\pi/6)}. \quad (2.67)$$

Here Ai is the Airy function and in Equation (2.67) q_m is the m^{th} root of its first derivative.

The expression of $A_f(s)$ for a curved segment is obtained considering the stationary phase point in Equation (2.56). The diffraction line integral is then compared with the p_d of the GTD, Equation (2.65), resulting in the amplitude function,

$$A_f(s) = e^{-\pi/4} \sqrt{\frac{k}{2\pi}} \sqrt{\frac{|r_p|}{|r|(|r_p| + |r|)}} \sqrt{\frac{|\rho_Q| + |r|}{|\rho_Q||r|}} \sum_m D_m^2 e^{-t_c \alpha_m} e^{ikt_c}. \quad (2.68)$$

2.3.4. Modification for different noise source types

Dipole

The noise shielding prediction method presented in Section 2.3.2 and Section 2.3.3 considered the noise source as a monopole, with the following expression for the incident field,

$$p_i(|\mathbf{R}|) = A \frac{e^{ik|\mathbf{R}|}}{|\mathbf{R}|}, \quad (2.69)$$

where A is the source strength, and it is neglected in the predictions for simplicity, because the noise shielding factors are determined by dividing the scattered acoustic pressure field by the incident field (Equation (2.64)).

A noise source with dipole directivity has the following approximate expression for the incident acoustic pressure field (see Equation (2.41)),

$$p_i(|\mathbf{R}|, \theta) = A \frac{k^2}{|\mathbf{R}|} d \cos(\theta) e^{ik|\mathbf{R}|}. \quad (2.70)$$

Here d is the distance between the two monopoles that compose the dipole so that $kd \ll 1$ and θ is the polar angle between the source and receiver positions.

The amplitude phase $A_f(s)$ (see Equation (2.55)) is therefore modified to include the dipole directivity by applying a factor $\mathcal{F}_{\text{dipole}}$,

$$A_{f,\text{dipole}}(s) = \mathcal{F}_{\text{dipole}} A_f(s), \quad (2.71)$$

where $\mathcal{F}_{\text{dipole}} = k^2 \cos(\theta_s)$. The polar angle θ_s here is the angle between the noise source and the segments I_Γ composing the contour of the aperture, and differs from θ of the incident field in Equation (2.69). The expressions of $\cos(\theta_s)$ for the contribution of the stationary phase and end points of the segment can be found in Appendix B. The value d and A can be neglected in the factor $\mathcal{F}_{\text{dipole}}$ for the same reason that the source strength A was neglected in the monopole case: the final values of noise shielding are obtained dividing the scattered field by the incident field.

Multi-source

In addition to a monopole and dipole directivity, the noise shielding method is also adapted to include multi-sources. Here a multi-source is defined as a ring of monopoles, and each monopole j is characterized by an amplitude A_0 , frequency f and phase ϕ_j ,

$$p_j = A_0 \frac{e^{ik\mathbf{R}+il\phi_j-i\omega t}}{\mathbf{R}}. \quad (2.72)$$

Here p_j is the acoustic pressure of the monopole j , t expresses the time dependence, and l is the azimuthal number that generates the azimuthal rotating modes. For the noise shielding calculations the time dependence t is neglected.

The scattered field p_{s_j} is calculated for each monopole j that compose the multi-source by modifying the amplitude phase $f(s)$,

$$A_f(s)_{\text{multi-source}} = \mathcal{F}_j A_f(s), \quad (2.73)$$

where $\mathcal{F}_j = e^{il\phi_j}$. The total scattered field p_s is obtained summing up the contributions of the total number of monopoles M composing the multi-source and the values of noise shielding are obtained using Equation (2.64), in which the incident acoustic field p_i is given by

$$p_{i_{\text{multi-source}}} = \sum_{j=1}^M p_j. \quad (2.74)$$

2.3.5. Comparison of different noise shielding methods: validation cases

This section compares the noise shielding method adopted for this research, based on the Kirchhoff integral method and the MTPO, with results of the BEM, ESM and ray-tracing method available in the literature.

The first validation case is a monopole source shielded by a flat disk, with the dimension and distance to the observers illustrated in Figure 2.21. The dimensions depend on variable a , in order to keep consistency with the nomenclature used in the literature.

Figure 2.22 shows the noise shielding values at the observer positions, considering $a=1$ m and the noise source at a frequency of 1700 Hz using the BEM and the ray-tracing method. The two plots, taken from the work of Lummer [102], are similar, which indicates that the ray-tracing method in this case is a good alternative to the BEM. The same case simulated using the MTPO-based method implemented in this work, resulted in the plot of Figure 2.23, which is similar to the two plots of Figure 2.22.

Another literature source can be used to further validate the implementation of the MTPO-based method for a flat disk. In the work of Colas et al [93] the same case of the flat disk is used to compare values of noise shielding obtained with the Diffraction Integral Method (DIM) and the ESM implemented in NASA's Fast Scattering Code [90], for a line of observers distributed along x with $y=0$ m. The results of

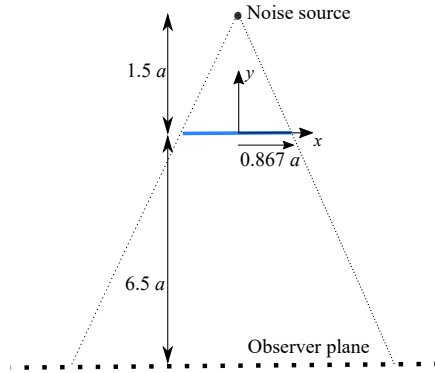


Figure 2.21: Schematic of the validation case of the flat disk.

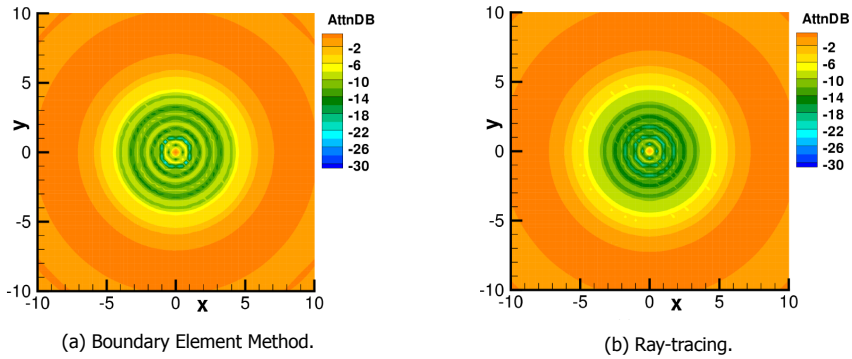


Figure 2.22: Noise shielding values below a flat disk taken from the literature [102].

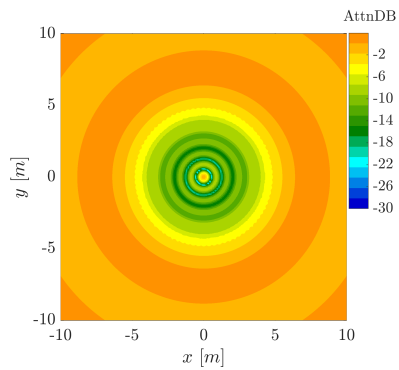
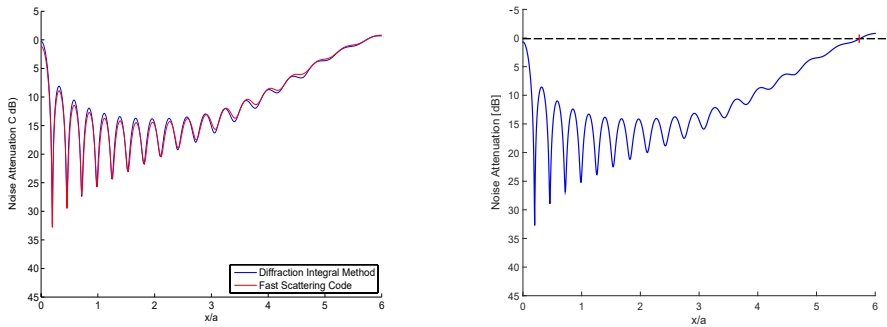


Figure 2.23: Noise shielding values below a flat disk using the MTPO-based method implemented in this work.

the two methods are shown in Figure 2.24a. In this case the frequency of the noise source is 5000 Hz ($ka = 92$ in [93], with $a=1$ m). The results of the DIM and of the Fast Scattering Code are almost coincident. The DIM is therefore a good high frequency approximation of the ESM implemented in the Fast Scattering Code [103]. The DIM has many similarities with the noise shielding method used in this work and in fact the two approaches share the same formulation until Equation (2.51) but the method used to solve the singularity ($|\rho||r| + \rho \cdot r$) differentiates them. The approach used in the DIM results in heavier computations than the MTPO-based method [104]. The plot of Figure 2.24b was obtained with the MTPO-based method implemented in this work, and as expected, it is similar to Figure 2.24a.



(a) DIM and the Fast Scattering Code results taken from [93].

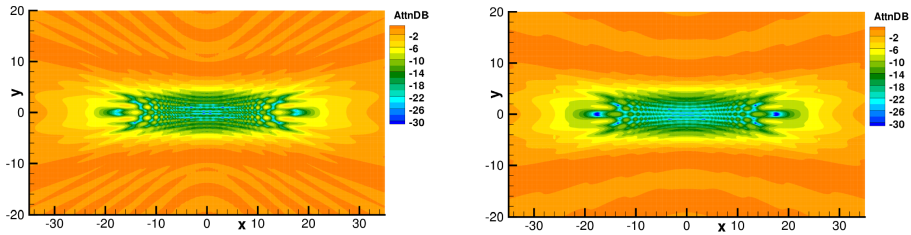
(b) MTPO-based method [44].

Figure 2.24: Noise shielding values of the disk for observers distributed along x at $y = 0$ m, using different noise shielding prediction methods. The black dashed line indicates no noise shielding and the red cross indicates the intersection of this line with the curve.

A second validation case available in the literature considers a monopole source shielded by a flat plate with a length of 10 m and width of 2 m. The distance between the plate, noise source and observers is the same as in the case of the disk (see Figure 2.21). Figure 2.25 shows the noise shielding values for a noise source at 1700 Hz, calculated using the BEM and the ray-tracing method [102]. The results have the same range of values, but the noise shielding pattern shows some differences.

The contour plot of Figure 2.26 was obtained using the noise shielding method implemented in this research work and it is similar to the plots of Figure 2.25, especially with the plot obtained using the ray-tracing method.

The flat plate simulations, together with the flat disk presented above, show that the MTPO-method is equivalent to the BEM for flat objects and also verifies its implementation. The case of the flat plate can also be compared with the Barrier Shielding Method, which is a less computationally expensive alternative and of simpler implementation than other methods. Figure 2.27 shows the noise shielding values below the flat plate using the BSM. The BSM underestimates noise shielding for some observer positions compared with the results obtained by the BEM, the ray-tracing method and the MTPO-based method. However, for most of the



(a) Boundary Element Method.

(b) Ray-tracing.

Figure 2.25: Noise shielding values below a flat plate. Results from [102].

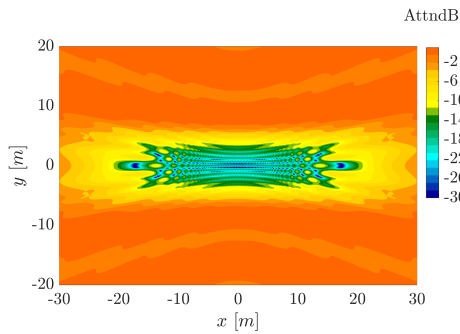


Figure 2.26: Noise shielding values below a flat plate using the MTPO-based method.

observer positions the BSM gives a good approximate value of noise shielding.

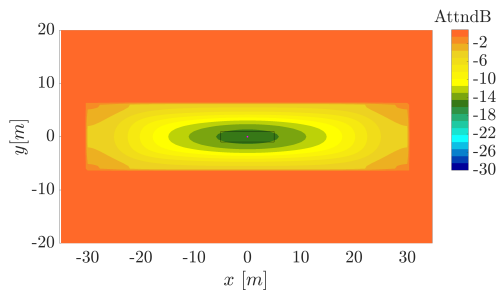


Figure 2.27: Noise shielding values below a flat plate using the Barrier Shielding Method.

Consider now observers distributed along the y -axis with $x=0$ m. Figure 2.28 displays the noise shielding values for those observer positions using both the MTPO-based method and the BSM. The BSM is an empirical method based on noise shielding measurements of a flat plate, therefore it is an approximation and is unable to capture the oscillating shielding behaviour between close observers. Neverthe-

less, this method can be used to estimate preliminary values of noise shielding for flat polygonal objects.

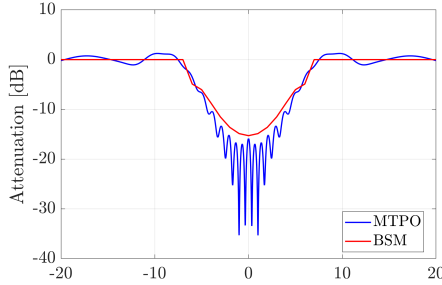


Figure 2.28: Noise shielding values below a flat plate using the Barrier Shielding Method for observers distributed along the y -axis with $x=0$ m. Also shown are the predictions obtained with the MPTO-based method.

2.4. Acoustic Imaging

Whereas in the previous sections focus was on modelling aspects, also acoustic measurements form an indispensable step in aircraft noise research. A set of microphones can be used collectively to localize and quantify sound sources through a signal processing technique denominated as beamforming. A large variety of acoustic imaging algorithms is available in literature, such as conventional beamforming [105], functional beamforming [106–108], CLEAN-SC [109] and DAMAS [110, 111], to cite a few examples. In this thesis beamforming is used to better understand the noise diffraction at the edges of an obstacle.

Conventional beamforming is a robust method, but also fast and intuitive, characteristics that makes it suitable for the analysis of noise shielding. CLEAN-SC was also considered as an option, but it was verified experimentally that for the cases considered this method was only capable to locate the strongest source on the wing edges, and for the analysis of shielding also weaker sources are of interest. This section briefly presents the method of conventional beamforming, used in this work.

Consider a set of microphone signals N represented by $\mathbf{p}_m(t) \in \mathbb{R}^{N \times 1}$. After transforming the signal to the frequency domain, $\mathbf{p}_m(\omega)$, the so-called cross spectral matrix (CSM) can be obtained,

$$\mathbf{C}(\omega) = \mathbb{E}[\mathbf{p}_m(\omega)\mathbf{p}_m^*(\omega)], \quad (2.75)$$

where $\mathbb{E}(\cdot)$ is the expectation operator and $(\cdot)^*$ the complex conjugate transpose. This means that the time signal is divided into many blocks and the CSM is calculated as an average.

The resultant beamformer output, i.e., the source power estimate for a given

scan point \mathbf{x}_t is given by

$$B(\mathbf{x}_t, \omega) = \mathbf{h}^*(\mathbf{x}_t) \mathbf{C} \mathbf{h}(\mathbf{x}_t), \quad (2.76)$$

where $\mathbf{h}(\mathbf{x}_t) \in \mathbb{C}^{N \times 1}$ is the steering vector and contains the microphone array responses of potential sources. The steering vector uses formulation III of Sarradj [112], which for the n^{th} element is given by,

$$h_n = \frac{1}{r_{t,n} r_{t,0} \sum_{n=1}^N (1/r_{t,n}^2)} e^{-i\omega(r_{t,n} - r_{t,0})/c}. \quad (2.77)$$

Here $r_{t,n} = |\mathbf{x}_t - \mathbf{x}_n|$ is the distance between the scan point and microphone n and $r_{t,0} = |\mathbf{x}_t - \mathbf{x}_0|$ is the distance between the scan point and the center of the array. A schematic of these distances is represented in Figure 2.29.

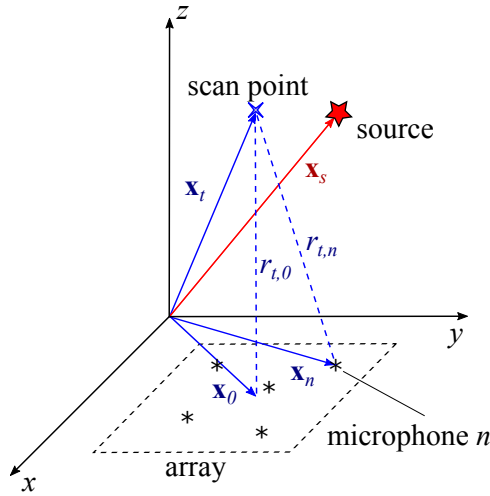


Figure 2.29: Microphone array and distances to the scan point. In this example the scan point does not coincide with the source position, i.e., $\mathbf{x}_t \neq \mathbf{x}_s$ [45].

The implementation of conventional beamforming requires the definition of a number of scan points and estimates the source powers for each point using Equation (2.76). The sound pressure level value at the centre of the array \mathbf{x}_0 can be found using

$$L_p(\mathbf{x}_t, \omega) = 20 \log_{10} \left(\frac{\sqrt{B(\mathbf{x}_t, \omega)}}{p_0} \right). \quad (2.78)$$

The levels are often depicted as a source map and the grid points usually lie in a plane. For the resultant image, high levels indicate the presence of a source $\mathbf{x}_t = \mathbf{x}_s$, whereas low levels indicate a mismatch, $\mathbf{x}_t \neq \mathbf{x}_s$.

In conventional beamforming, the capacity to distinguish two noise sources closely spaced is limited by the Rayleigh criterion [113]. For a planar microphone

array the Rayleigh criterion is given by

$$\Delta l = 1.22 c \frac{z_{\text{bf}}}{D_e f}, \quad (2.79)$$

where D_e is the effective aperture of the array, f is the frequency and z_{bf} is the perpendicular distance of the planar array to the scan plane. Therefore two noise sources are only detected individually if the distance between them is superior to Δl for the given frequency.

2.5. Noise metrics

Noise reduction is only significant when translated in a decrease of annoyance at the receivers. Annoyance is a subjective perception of noise, and therefore difficult to quantify - the objective of noise metrics is to approximate the human ear response to noise. This section gives an overview of the metrics used to assess aircraft noise, and presents the metrics adopted in this work.

2.5.1. Limitations of traditional metrics

Different metrics have been developed over the last decades with the same objective of reflecting the human response to noise. These metrics were obtained using different approaches (loudness and annoyance based) and can be used to assess a single flight event or taking into consideration many events over a time period.

Loudness is an auditory sensation that categorizes sounds from quiet to loud. The loudness level quantifies this sensation and can lead to more accurate results than estimations of the magnitude of a sound [31], which do not account for the human ear response. Therefore, loudness is a subjective perception of the acoustic pressure, unlike for example the SPL, which is the relation between the acoustic pressure of a sound and the pressure corresponding to the threshold of human hearing ($20\mu\text{Pa}$).

By definition, a sound has a loudness level in phons. This is the value in decibels of an equally loud 1kHz tone for a plane frontal incident wave. The phon unit was proposed by S. S. Stevens, a pioneer in this field [114–116].

Loudness can be experimentally determined for any sound. However, the loudness levels of pure tones at different frequencies have been measured in many laboratories and are therefore best-known and widely used. The equal-loudness contours for pure tones presented in ISO 226 (1987) and ISO 226 revisited (2003) are represented in Figure 2.30. As explained above, the equal-loudness curves are representative for the loudness of the sound pressure level in decibels at a frequency of 1 kHz.

The equal-loudness contours are obtained for a plane and frontal incident wave, however, the sound field is diffuse in many cases, i.e. situations in which the sound comes from several directions. The difference between a plane and a diffuse sound field is expressed as a frequency-dependent attenuation factor α_D . The values of this attenuation factor are shown in Figure 2.31.

At low frequencies the value of α_D is close to zero because the hearing system works as an omni-directional receiver, but it has significant values for other fre-

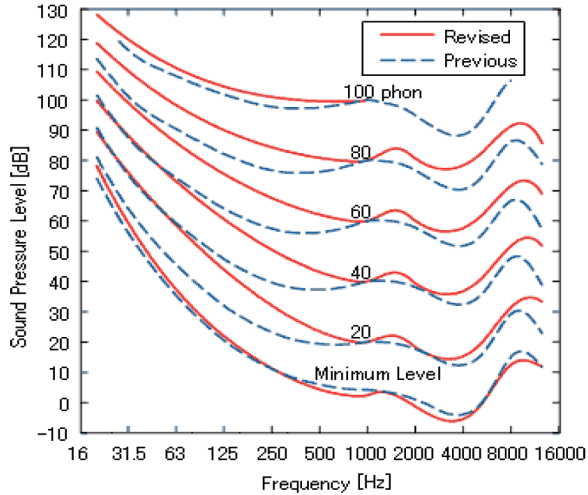


Figure 2.30: Equal-loudness levels contours presented in ISO 226 (1987) and ISO 226(2003) [43].

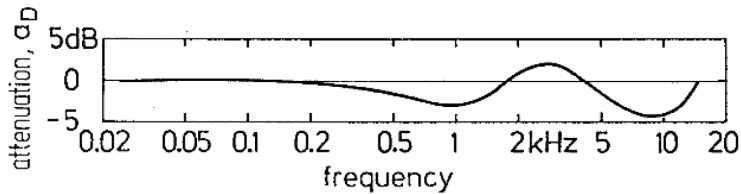


Figure 2.31: Attenuation α_D as a function of the frequency of the pure tone [31].

quencies. For instance, at 1 kHz, the value of Figure 2.31 is -3 dB, i.e., the SPL of the pure tone at that frequency in a diffuse field has to be 3 dB lower than the SPL of the tone in a plane sound field to assure an equal loudness level.

The A-weighted sound pressure level is widely used to assess the noise impact, not only of aircraft but also of rail and road traffic. This metric was developed to approximate the human hearing system reaction to the frequency content of a sound: high frequency noise is perceived as louder than low frequency noise. The A-weighting represents the equal-loudness curve of 40 phon, as shown in Figure 2.32, and it is given by the frequency-dependent expression,

$$\Delta L_A = -145.528 + 98.262 \log_{10} f - 19.509 (\log_{10} f)^2 + 0.975 (\log_{10} f)^3. \quad (2.80)$$

Another well-known loudness based metric is the C-weighted sound pressure level [118] which is based on the 100 phon equal-loudness curve. This metric is used to assess louder events than the A-weighted SPL.

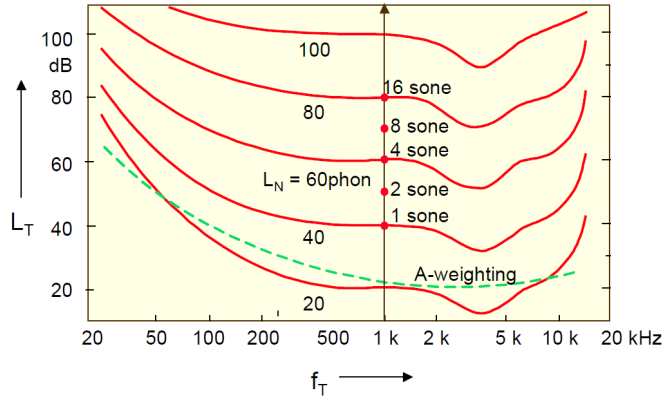


Figure 2.32: Approximation of the 40 phon equal-loudness curve used in the A-weighted SPL [117].

The Sound Exposure Level is a widely used loudness based metric to assess the annoyance of a single flight event. The time varying A-weighted sound pressure level during the event, $L_A(t)$, is integrated for the time interval in which its level is within 10 dB of the maximum value. The expression for SEL is

$$\text{SEL} = 10 \log_{10} \left[\frac{1}{T_1} \int_{t_1}^{t_2} 10^{\frac{L_A(t)}{10}} dt \right], \quad (2.81)$$

where T_1 is 1 second and t_2 and t_1 correspond to the interval of time in which $L_A(t)$ is 10 dB below the maximum value.

Community annoyance, however, depends on other factors than loudness, such as masking and critical bands. These concepts are briefly introduced below.

Masking plays a very important role in assessing annoyance, as this phenomenon is the reason why a sound can become less audible in the presence of another. The effect of masking can be quantified by determining the masking threshold, which is the minimum SPL of a test sound necessary to make it audible in the presence of a masker. The test sound is usually a sinusoidal test tone. The masking of a sound can be total, meaning that it is not audible any more, or partial.

The masking effect is not only produced when two sounds are simultaneous. The masker can be switch on after a sound impulse, being in this case denominated premasking. This premasking effect is not very strong, but the postmasking, i.e., a situation when the masker is switched off but the sound continues to be reproduced, has a relevant effect. The premasking and postmasking are also called backward and forward masking, respectively.

The masker sound, which can be a tone or narrowband noise, masks more effectively frequencies above their center frequency than those below it. Figure 2.33 shows the masking of a 2 kHz tone with a level of 40 dB by narrowband noise centered at 1 kHz. The masking narrowband sound of 80 dB is sufficient to mask the

2 kHz tone. This is an example of postmasking. The masking pattern of Figure 2.33 is valid for this specific case, and each tone or narrowband sound has its own masking pattern.

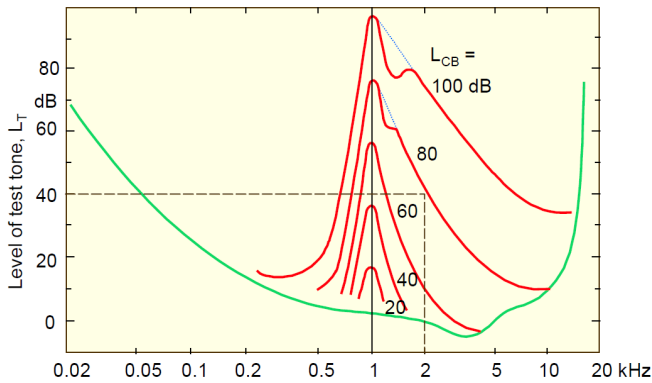


Figure 2.33: Masking of a 2 kHz tone by narrowband noise centered at 1 kHz [117].

The plot of Figure 2.34 shows the masking of the tone of 2 kHz by white noise. A tone with a SPL of 60 dB is masked by white noise with an inferior SPL, of 40 dB. Generally, high frequency sounds are masked by low frequency sounds. This is very relevant to aircraft noise, as jet noise can mask tones of the fan at high frequency.

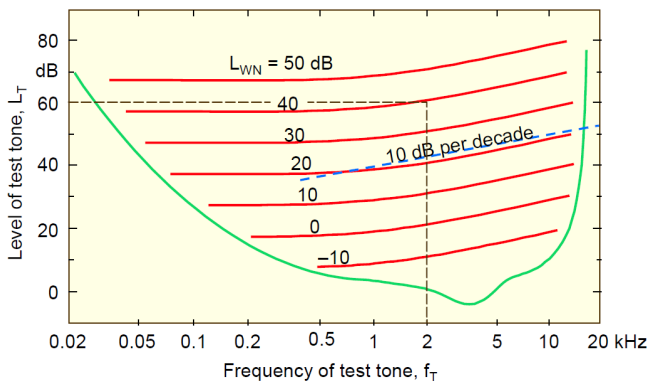


Figure 2.34: Masking of a 2 kHz tone by white noise [117].

The concept of critical bands is very important in psychoacoustics. It assumes that the human hearing system analyses a sound by a bank of filters. Figure 2.35 shows their bandwidth (denominated critical bandwidth) variation with frequency. The critical bandwidth can be approximated by the dashed green line, which means

that the critical bandwidth is kept constant from a value of 100 Hz for frequencies up to 500 Hz and increases linearly with frequency for higher values.

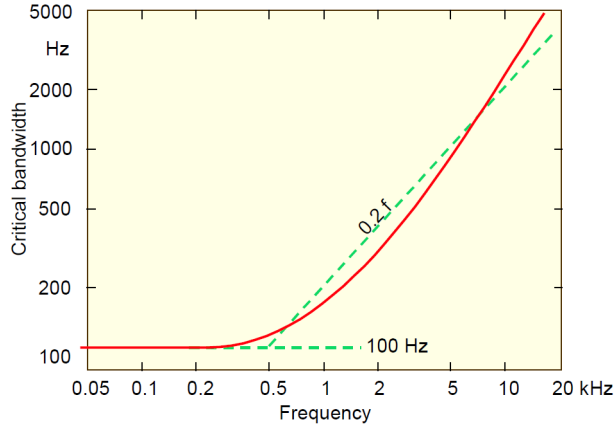


Figure 2.35: Critical bandwidth variation with frequency [117].

Two sounds within the same critical band are not heard as separate, and therefore this concept is important in the analysis of complex sounds such as aircraft noise. The unit of the critical bands is the Bark, and they range from 0 to 24. In this work, the critical band number z and the critical bandwidth CDW are calculated using Zwicker's method, described in ISO532-B and DIN 45631 [119],

$$z = 13 \arctan\left(0.76 \frac{f}{1000}\right) + 3.5 \arctan\left(\frac{f}{7500}\right)^2 \text{ Bark}, \quad (2.82)$$

$$\text{CBW} = 25 + 75 \left[1 + 1.4 \left(\frac{f_c}{1000}\right)^2\right]^{0.69} \text{ Hz}, \quad (2.83)$$

where f is the frequency and f_c the central frequency of the critical band.

The need for annoyance based metrics has been long recognized by the authorities, e.g. one of the first annoyance based metrics, the Perceived Noise Level (PNL), was developed by K. D. Kryter [120] in the 1960s under request of the Federal Aviation Authority (FAA). The PNL makes use of the equal-noisiness curves, shown in Figure 2.36. These were obtained based on subjective ratings resultant from psychoacoustic tests [121], in an analogous procedure to the method used to determine the equal-loudness curves shown in Figure 2.30.

The overall noisiness noy value n_{tot} of a sound is determined using

$$n_{tot} = n_{\max} + F_m \left[\left(\sum_{i=1}^N n_i \right) - n_{\max} \right], \quad (2.84)$$

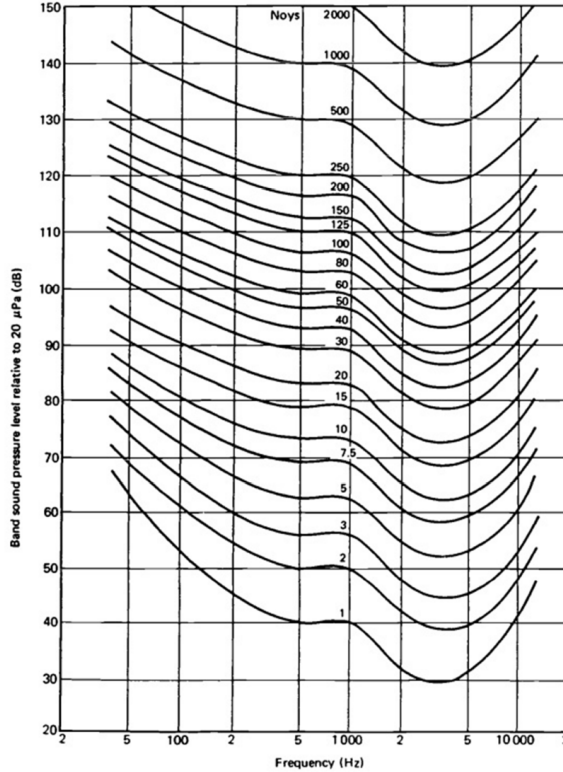


Figure 2.36: Equal-noisiness curves [122].

where n_i is the noy value of the 1/3-octave band, n_{\max} is the maximum noy value and F_m is the masking factor that has a value of 0.15 for 1/3-octave bands. The PNL (in PNdB units) is then given by,

$$\text{PNL} = 40 + 33.3 \log_{10} n_{tot}. \quad (2.85)$$

It was found that the subjects of psychoacoustics tests considered a sound as more annoying when it contained discrete tones [123]. A tonal penalty was therefore introduced in the PNL metric, resulting in the Tone Corrected Perceived Noise Level (PNTL)

$$\text{PNTL} = \text{PNL} + C, \quad (2.86)$$

where C is the tone correction. This metric, similarly to PNL, is based on 1/3-octave bands. The value C is frequency dependent and also depends on the level of the strongest protruding tone in the band, considering central frequencies from 80 Hz up to 10 000 Hz. The procedure used to determine the constant C can be found in Appendix D.

Also the effect of duration affects annoyance: it was observed that the subjects of psychoacoustics tests perceived higher values of annoyance the longer they were subjected to values close to the maximum PNLT of the flyover event.

The Effective Perceived Noise Level (EPNL), is derived from the PNLT but includes a correction factor for the flyover duration,

$$\text{EPNL} = \text{PNLTM} + \mathcal{D}. \quad (2.87)$$

Here \mathcal{D} is the time correction factor and PNLTM is the maximum value of PNLT for the flyover. The unit of EPNL is EPNLdB and the correction factor is given by

$$\mathcal{D} = 10 \log_{10} \left[\sum_{k=0}^{2d} 10^{\frac{\text{PNLT}(k)}{10}} \right] - \text{PNLTM} - 13, \quad (2.88)$$

where k is the time index and d is the time interval of the flyover in which PNLT is 10 PNLTdB below the maximum value, PNLTM.

Multiple event metrics are used to quantify the noise impact in communities close to airports. Such metrics account for various flight events during, for example, 24 hours and can attribute annoyance weights for the different periods of the day. The equivalent A-weighted sound level for multiple events, $L_{\text{Aeq,T}}$ is a widely used example of this type of metrics, and it is given by

$$L_{\text{Aeq,T}} = 10 \log_{10} \sum_{j=1}^N 10^{\frac{\text{SEL}_j}{10}} - 10 \log_{10} \Delta t, \quad (2.89)$$

where N is the number of events in the time period Δt and j is the index of the flight event.

Another multiple event metric is the day-evening-night average level, L_{DEN} , which attributes different importance to flight events depending on the time period. The L_{DEN} is given by

$$L_{\text{DEN}} = -49.4 + 10 \log_{10} \left[\sum_{j=1}^N 10^{\frac{\text{SEL}_j + \mathcal{P}_j}{10}} \right], \quad (2.90)$$

where \mathcal{P}_j is the penalty for the time period: 1 for day (7:00-19:00), 5 for evening (19:00-22:00) and 10 for night (22:00-7:00). Both $L_{\text{Aeq,T}}$ and L_{DEN} are expressed in dBA.

2.5.2. Sound quality metrics

The sound quality metrics characterize a sound in terms of loudness, tonality, roughness, sharpness and fluctuation strength. This is an alternative to traditional metrics that do not quantify the qualities of a sound separately, providing instead a total value for annoyance.

This section presents the methods used to calculate the five sound quality metrics. Since aircraft noise varies in time, the sound quality metrics are determined for the value exceeded 5 % of the flyover duration. For instance, if the flyover duration is 10 s, the value of the sound quality metric is the value exceeded for 0.5 s.

Loudness

The concept of loudness was already introduced in Section 2.5.1, together with other important definitions such as critical bands and masking. In this work, loudness is calculated based on the ISO 532-1 [124]. Loudness depends on the frequency, intensity and duration of a sound. It is expressed in phon when on a logarithmic scale and in sone when on a linear scale.

The first step of the method consists of calculating the SPL in each critical band, using the equal-loudness curves presented before in Figure 2.30. The specific loudness, i.e., the loudness in each critical band is given by

$$N_{\text{SPEC}} = 0.0635 [10^{0.025L_{\text{TQ}}(z)}] \left[\left(0.75 + 0.25 \left\{ 10^{0.1[L_{\text{E}}(z) - L_{\text{TQ}}(z)]} \right\} \right)^{0.25} - 1 \right], \quad (2.91)$$

where L_{E} is the excitation level, as calculated by Terhardt [125], and L_{TQ} the threshold in quiet. It is checked whether the specific loudness is masked by accessory loudness from other critical bands, which results in values of unmasked specific loudness N' . The total loudness is then calculated summing the values N' over the 24 critical bands,

$$N = \int_0^{24} N'(z) dz. \quad (2.92)$$

Aircraft noise varies with time and it is therefore important to account for the temporal masking, i.e., postmasking and premasking. Postmasking has more impact than premasking, as referred in Section 2.5.1, and it is accounted for in Zwicker's model.

Tonality

Tonality is one of the most important characteristics of aircraft noise. Traditional metrics such as the PNL and EPNL include tone penalties obtained through annoyance ratings given by subjects in psychoacoustic surveys. Tonality as an independent sound quality metric is implemented in this work following Aures' method [126].

Aures used a number of test sounds, pure tones and band-pass sounds with a small bandwidth of 30 Hz and a large bandwidth of 1 kHz to develop this method. These test sounds were used to assess the influence of the tonal prominence, bandwidth, frequency and loudness on the perceived tonality by the human ear relative to the overall loudness, based on psychoacoustic tests.

The first step of Aures' method consists of the identification of tonal components in the spectrum, both pure tones and narrowband sounds with smaller bandwidth than the critical band, and that protrude at least 7 dB above the adjacent narrowband noise.

Once the tones are identified, it is necessary to verify which of them are *aurally relevant*. Only those tones are considered in the tonality calculation. This is performed by calculating the SPL excess, ΔL_i , which is based on the method of Terhardt [127]. The aural relevance of the tones depends on their level, mutual masking between tones, masking of broadband noise adjacent to each tone and the level above the threshold of hearing. The SPL excess is given by the expression

$$\Delta L_i = L_i - 10 \log_{10} \left\{ \left[\sum_{k \neq i}^n A_{E_k}(f_i) \right]^2 + E_{Gr}(f_i) + E_{HS}(f_i) \right\}. \quad (2.93)$$

If ΔL_i is larger than zero, the tones are considered as aurally relevant. L_i is the SPL of the tonal component of index i , and n is the total number of tones identified in the sound. The term A_{E_k} is the amplitude of the secondary neural excitation of frequency f_i due to the k^{th} tone. This term determines the excitation that the current tone causes at other frequencies. The sum of A_{E_k} in Equation (2.93) takes therefore into account the mutual masking effect of all tonal components. This term is calculated as

$$A_{E_k}(f_i) = 10^{\frac{L_{E_k}(f_i)}{20}}, \quad (2.94)$$

where L_{E_k} is the excitation level, which is obtained by

$$L_{E_k} = L_k - s_t(z_k - z_i). \quad (2.95)$$

Here L_k is the SPL of the k^{th} tone in decibels, z_i and z_k are critical bands, and s_t is given by

$$s_t = \begin{cases} 27 & \text{dB/Bark} & f_i < f_k \\ -24 - 230f_i^{-1} + 0.20L_k & \text{dB/Bark} & f_i > f_k. \end{cases} \quad (2.96)$$

The term E_{Gr} of Equation (2.93) is the masking intensity of the broadband noise surrounding the selected tones. Its value is given by the sum of the broadband intensities surrounding tone i by 1 Bark ($z_i - 0.5$ to $z_i + 0.5$ Bark). The term E_{HS} is the intensity at the threshold of hearing,

$$E_{HS} = 3.64 \frac{f_i^{-0.8}}{1000} - 6.5 \times 10^{-0.6 \left(\frac{f_i}{1000} - 3.3 \right)^2} + 10^{-3} \left(\frac{f_i}{10000} \right)^4. \quad (2.97)$$

The values of ΔL_i aurally relevant are then used to calculate the prominence weighting function,

$$w_3(\Delta L_i) = \left(1 - e^{-\frac{\Delta L_i}{15}} \right)^{0.29}. \quad (2.98)$$

In addition, a frequency weighting function is given by

$$w_2(f_i) = \left[\sqrt{1 + 0.2 \left(\frac{f_i}{700} + \frac{700}{f_i} \right)^2} \right]^{-0.29}. \quad (2.99)$$

Finally, the bandwidth effect on tonality is taken into account using,

$$w_1(\Delta z_i) = \frac{0.13}{0.13 + \Delta z_i}. \quad (2.100)$$

The three weighting functions are then combined in an overall weighting function w_T ,

$$w_T = \sqrt{\sum_{i=1}^n [w'_1(\Delta z_i)w'_2(f_i)w'_3(\Delta L_i)]^2}, \quad (2.101)$$

where $w'_l = w_l^{1/0.29}$ for $l = 1, 2, 3$.

According to Aures' investigation, the overall weighting w_T is able to assess tonality adequately for sounds with significant tonal content, but it is not so accurate when the sound also has a strong presence of broadband noise. Therefore, another weighting function was introduced,

$$w_{Gr} = 1 - \frac{N_{Gr}}{N}, \quad (2.102)$$

where N_{Gr} is the loudness of the sound without tones.

The value of tonality is finally obtained using

$$K = c_K w_T^{0.29} w_{Gr}^{0.79}, \quad (2.103)$$

here c_K is a calibration constant equal to 1.09. The tonality is measured in t.u. (tonality units).

Sharpness

Sharpness quantifies the high frequency content of a sound, i.e., a sound is perceived as sharper when it has more high frequency content. This SQM was implemented using the method of van Bismarck [128] and its unit is the acum. A narrowband noise with width of one critical band centered at 1 kHz has 1 acum of sharpness.

This method calculates the weighted first moment of unmasked specific loudness at each critical band z ,

$$\bar{N}(z) = g_s(z)N'(z)z dz, \quad (2.104)$$

where $g_s(z)$ is a weighting function given by

$$g_s(z) = \begin{cases} 1 & 0 \leq z \leq 16 \\ 0.066e^{0.171z} & 16 < z \leq 24. \end{cases} \quad (2.105)$$

The weighting function attributes more importance to frequency content above 16 Bark (above 2700 kHz), i.e., high frequencies. The overall sharpness value is then calculated using

$$S = c_S \frac{\int_0^{24} N'(z)g_s(z)z dz}{N}, \quad (2.106)$$

where the constant c_S is 0.11.

Roughness

Roughness captures fast fluctuations in sound (50-90 Hz). One of the first models for roughness was developed by Zwicker and Fastl [31]. It was found that at low frequencies, the frequency selectivity of the hearing system was responsible for a sound being perceived as rough, but at high frequencies the limited temporal resolution was the most important factor.

The masking effect, referred in Section 2.5.1, can also vary in time, which is denominated as temporal masking. The method of Zwicker and Fastl to determine roughness is based on the temporal masking pattern, illustrated in Figure 2.37. In this plot, the envelop of a sinusoidal amplitude modulated masker is plotted in terms of sound pressure level and the temporal masking pattern is represented by the solid line. The modulation frequency, f_{mod} , and the masking depth, ΔL , are also represented in Figure 2.37. These two parameters are essential to the roughness calculation in the method of Zwicker and Fastl. The masking depth, however, is difficult to estimate and it is more practical to derive roughness from the specific loudness pattern, such as in Aures' method [129]. This work calculates roughness using an improved version of Aures' method, developed by Daniel & Weber [130].

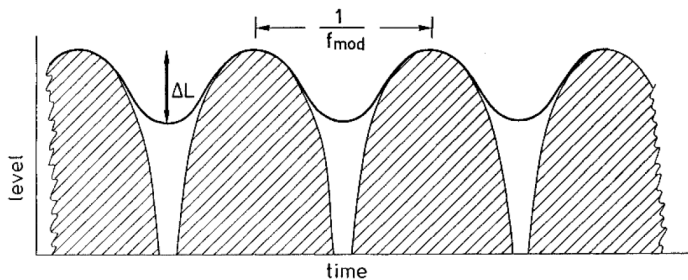


Figure 2.37: Temporal masking pattern of sinusoidally amplitude-modulated masker[31].

The first step of the method of Daniel & Weber (see Figure 2.38) consists of taking the discrete Fourier Transform (DFT) of the signal using windows of 200 ms weighted by a Blackman window. The spectrum is then multiplied by a factor α_0 , which is the transmission between a free field and the peripheral hearing system. The variation of α_0 with the critical-band rate and frequency is shown in Figure 2.39.

The next step consists of the transformation of the resultant values into an excitation pattern defined by the slopes of Equation (2.96). The specific excitations are calculated using 47 overlapping critical channels with bandwidth of 1 Bark. This results in 200 ms long specific excitation time functions $e_i(t)$. The next step applies a weighting function $H_i(f_{\text{mod}})$ to model the bandpass characteristics of the overlapping critical bands (channels). Figure 2.40 shows the basic weighting function - all the others can be derived from them, using the procedure described below.

- for $i = 1, 2, \dots, 4$ $H_1 = H_2 = H_3 = H_4,$

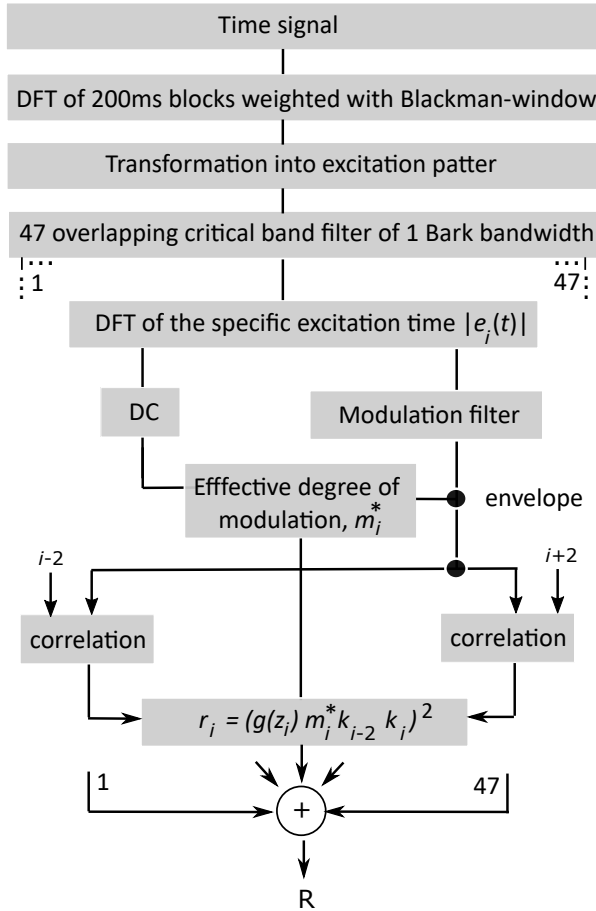


Figure 2.38: Steps necessary for the roughness calculation according to the method of Daniel & Weber. Adapted from [130].

- for $i = 6, 8, \dots, 16$ $H_{i-1} = H_i$, H_i is interpolated between H_4 and H_{16} ,
- for $i = 17, 18, \dots, 20$ $H_i = H_{16}$,
- for $i = 22, 23, \dots, 42$ $H_{i-1} = H_i$, H_i is interpolated between H_{20} and H_{42} ,
- for $i = 43, 44, \dots, 47$ $H_i = H_{42}$.

The weighted excitation envelop is then calculated using

$$h_{BP,i}(t) = \text{IFFT} \{H_i(f_{\text{mod}}) \text{FFT}(|e_i(t)|)\}. \quad (2.107)$$

The root mean square (RMS) of the $h_{BP,i}$ ($\tilde{h}_{BP,i}$) is then divided by the DC value of each original filtered signal, and the generalized modulation depth m^* is obtained

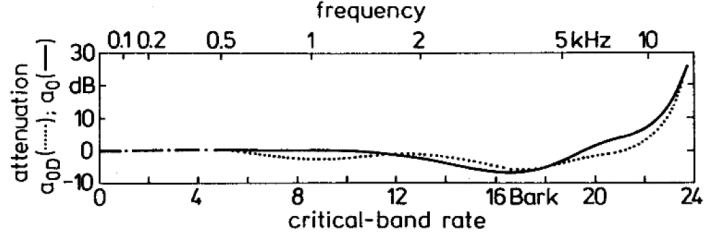


Figure 2.39: Transmission factor for the free field condition a_0 (solid line) and for the diffuse-field condition a_{0D} (dotted line) as function of critical-band rate and frequency [31].

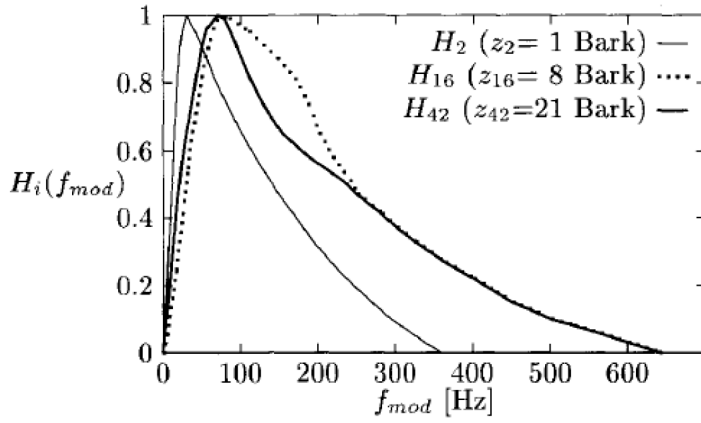


Figure 2.40: Weighting functions H_2 , H_{16} and H_{42} [130].

using,

$$m_i^* = \begin{cases} \frac{\tilde{h}_{BP,i}(t)}{h_{0,i}} & \text{if } \frac{\tilde{h}_{BP,i}(t)}{h_{0,i}} \leq 1 \\ 1 & \text{if } \frac{\tilde{h}_{BP,i}(t)}{h_{0,i}} > 1. \end{cases} \quad (2.108)$$

The specific roughness is determined using,

$$r_i = (g_R(z_i) m_i^* k_{i-2} k_i)^2, \quad (2.109)$$

where g_R are the calibration factors introduced to account for the dependency on the carrier frequency, shown in Figure 2.41. The variable k_{i-2} is the cross-correlation coefficient between envelopes of channel $i - 2$ and i , k_i is the cross-correlation coefficient between channel i and $i + 2$.

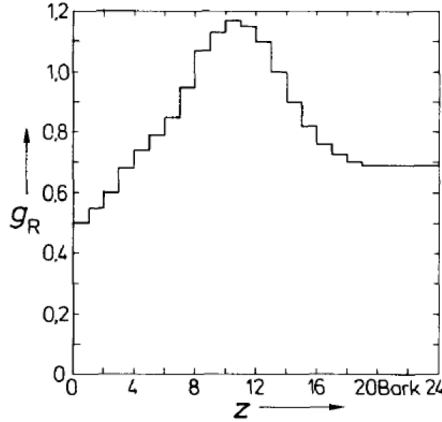


Figure 2.41: Calibration factors $g_R(z_i)$ [130].

The total roughness is finally calculated by

$$R = 0.25 \sum_{i=1}^N r_i. \quad (2.110)$$

Fluctuation Strength

The method used to calculate fluctuation strength is based on the roughness model of Daniel and Weber and was developed by Osses Vechi et al. [131]. This method uses many parameters also required for the roughness calculation since both methods assess loudness oscillations (fast for roughness and slow for fluctuation strength). Fluctuation strength is calculated using

$$FS = C_{FS} \sum_{i=1}^N (m_i^*)^{p_m} |k_{i-2} k_i|^{p_k} [g_{FS}(z_i)]^{p_g}, \quad (2.111)$$

where $C_{FS} = 0.249$, $p_m = p_k = 1.7$ and $p_g = 1$ are constants used to fit the experimental data and g_{FS} are calibration factors. The variables m_i^* , k_{i-2} and k_i are determined in the process of calculating roughness (m_i^* is the effective degree of modulation and k_{i-2} and k_i are the correlations between channels - channels overlapping critical bands).

The fluctuation strength is not an important metric to assess aircraft noise, as the perception of low frequency oscillations is associated with wind and background noise present in the measurements. Nevertheless, this SQM was determined because it is required to the psychoacoustic annoyance metrics, presented in the next subsection.

2.5.3. Psychoacoustic Annoyance Metrics

The sound characteristics, given by the five sound quality metrics previously presented, define the subjective perception of noise. Despite the high correlation of loudness with annoyance [132], this sound quality metric alone is insufficient to estimate annoyance, as sounds with equal loudness are perceived as distinct when other sound quality metrics present different values [133]. The model of Zwicker and Fastl, the so-called Psychoacoustic Annoyance (PA) model, takes into consideration the loudness, sharpness, fluctuation strength and roughness of a sound. The PA model is given by the expression,

$$PA = N_5 \left(1 + \sqrt{\omega_S^2 + \omega_{FR}^2} \right), \quad (2.112)$$

where N_5 is the value of loudness exceeded 5% of the time signal considered. The term ω_S accounts for sharpness and the term ω_{FR} adds the influence of roughness and fluctuation strength. These terms are calculated using

$$\omega_S = \begin{cases} 0.25(S - 1.75) \log_{10}(N_5 + 10), & S > 1.75 \\ 0, & S < 1.75 \end{cases} \quad (2.113)$$

$$\omega_{FS} = \frac{2.18}{N_5^{0.4}} (0.4FS + 0.6R). \quad (2.114)$$

The PA model does not account for tonality, which is an important characteristic of aircraft noise. The study of More [43] showed the importance of tonality in perceived annoyance using auralization of aircraft noise and psychoacoustic surveys, which were used to obtain a modified version of the PA model (PA_{mod}) given by

$$PA_{\text{mod}} = N_5 \left(1 + \sqrt{\gamma_0 + \gamma_1 \omega_S^2 + \gamma_2 \omega_{FR}^2 + \gamma_3 \omega_T^2} \right). \quad (2.115)$$

The term ω_T in Equation (2.115) is calculated using,

$$\omega_T^2 = (e^{-\gamma_4 N_5})^2 (e^{-\gamma_5 K_5})^2. \quad (2.116)$$

In Equations (2.115) and (2.116), $\gamma_{0,1,\dots,5}$ are empirical coefficients with the values of Table 2.7, obtained through subjective annoyance ratings.

Table 2.7: Values of the constants γ used in the modified psychoacoustic annoyance metric, PA_{mod} .

γ_0	γ_1	γ_2	γ_3	γ_4	γ_5
-0.16	11.48	0.84	1.25	0.29	5.49

The work of More showed a good correlation between the annoyance ratings of aircraft noise and PA_{mod} , with a coefficient of determination R^2 equal to 0.93. Therefore, PA_{mod} is the psychoacoustic annoyance metric adopted in this work.

3

Engine noise shielding for aircraft under operating conditions

Most commercial transport aircraft are tube-and-wing equipped with turbofan engines under the wings. Consequently, no shielding of engine noise occurs, which hinders the comparison of noise shielding predictions of aircraft under operational conditions with experimental data. However, this chapter presents the comparison of noise shielding predictions with flyovers measurements of the Fokker 70, one of the few aircraft models with engines mounted over the wings operating at civil airports.

A part of this work have been published in The Journal of the Acoustical Society of America, **143**, 1 (2018) [44] and in The Journal of Aircraft, **57**, 6 (2020) [134].

3.1. Experimental Setup

The experimental campaign took place at Amsterdam Airport Schiphol, in a location 1240 m to the South of the threshold of the Aalsmeerbaan runway (36R), as shown in Figure 3.1. This runway is mainly used for landing and during this campaign 115 landing flyovers were recorded using a 32 microphone array distributed in a spiral configuration (see Figure 3.2), with a diameter of 1.7 m. The measurements were taken in days with similar weather conditions and low wind.

The sampling frequency of the recordings is 40 kHz, and the filters of the data acquisition system cut off frequencies below 45 Hz and above 11 200 Hz. The microphones are mounted in a wooden plate covered with foam to reduce reflections. An acoustic camera was incorporated in the center of the microphone array, at a fixed angle, facing up, allowing the synchronization of the acoustic data with the video footage of the flyover. The optical camera is a Datavision UI-1220LE [135] with a Kowa LM4NCL lens, and the sampling frequency is 30 Hz. The microphones contained in the array are of the type PUI Audio POM-2735P-R [136] with a sensitivity of -35 ± 2 dB. More details about the microphone array can be found in [137].



Figure 3.1: Microphone array location, at 1240 m to the South from the Aalsmeerbaan runway, at Amsterdam Airport Schiphol.

The aircraft trajectory and velocity were determined in order to take into account the noise propagation in the atmosphere and the Doppler effect [138] in the analysis of the acoustic data. Those parameters can be obtained using frames of the acoustic camera or from the Automatic Dependent Surveillance-Broadcast (ADS-B). The ADS-B system uses the onboard Inertial Navigation System and the Global Navigation Satellite system to send the attitude and position of the aircraft to the ground for surveillance purposes. However, this is a modern system and not

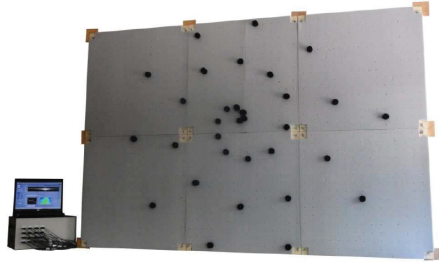


Figure 3.2: 32-microphone array and data acquisition system used in the experimental campaign.

all aircraft have ADS-B transponders.

The experimental campaign resulted in a total of 115 landing flyovers, of which 20 of the Fokker 70.

3.2. Assumptions

The comparison between predictions of noise shielding and the shielding estimated from the F70 flyover measurements is made under a number of assumptions:

- The aircraft velocity is constant for the duration of the flyover recorded by the acoustic camera.
- The aircraft follows a constant trajectory, aligned with the center of the acoustic array.
- The noise spectrum is extracted from experimental data at the overhead time and propagated back to the noise source position, and assumed to be representative for all other source locations.
- The engine directivity is modelled as a monopole.

During landing the aircraft must follow the Instrument Landing System (ILS), which results in very regular trajectories and therefore all the flyovers of the F70 present similar flight operating conditions and engine settings. Figure 3.3 shows the variability of the F70 height from the ground and velocity at the overhead time for the 20 flyovers recorded. The average height and velocity of the 20 landing flyovers is 66 m and 73 m/s, respectively. These values are used as input for the predictions.

The contour which separates the shadow zone from the illuminated zone of the F70, used for the noise shielding predictions, is represented in Figure 3.4. This contour is divided in 600 points connecting line segments, as described in Section 2.3.2. This contour discretization combined with the number of observers and frequencies of the noise spectrum results in expensive computational simulations. To reduce the simulation time, the noise spectrum is approximated and divided in 1/3-octave

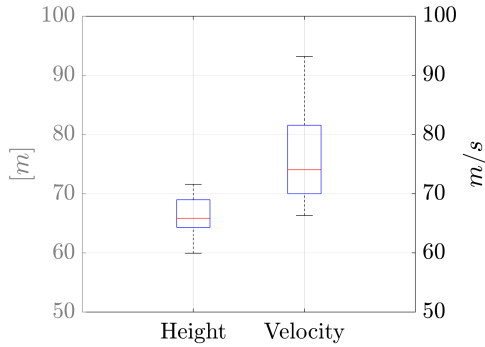


Figure 3.3: Variability of the velocity and height of the F70 at the overhead time.

bands, as represented in Figure 3.5. The influence of these approximations are discussed in Section 3.4

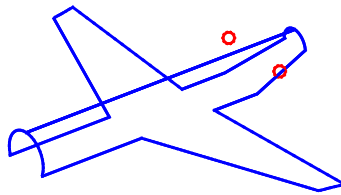


Figure 3.4: Limit shadow-light and noise source positions used in the noise shielding predictions of the F70.

3.3. Comparison of noise shielding predictions and measurements for the Fokker 70

This section compares predictions of noise shielding with measurements, using the approximations mentioned in the previous section. Using the minimum of information available, a preliminary prediction considers a sharp leading edge and that the aircraft is horizontal in relation to the acoustic array, i.e., at an attitude angle of 0° . These assumptions result in the contour plot of Figure 3.6a, which shows the values of noise shielding for a wide area of observer positions on the ground (the aircraft is at position $x = 200$ m and centered on the y -axis). The area with higher values of shielding has the shape of the wings and it is projected to the front of the aircraft, due to the rear position of the engines.

In Figure 3.6b the contour of noise shielding includes the effect of the creeping rays, i.e., the curvature of the leading edge is considered in the predictions. The values of noise shielding are slightly reduced when compared to Figure 3.6a.

The flyover measurements took place at a fixed position, aligned with the landing

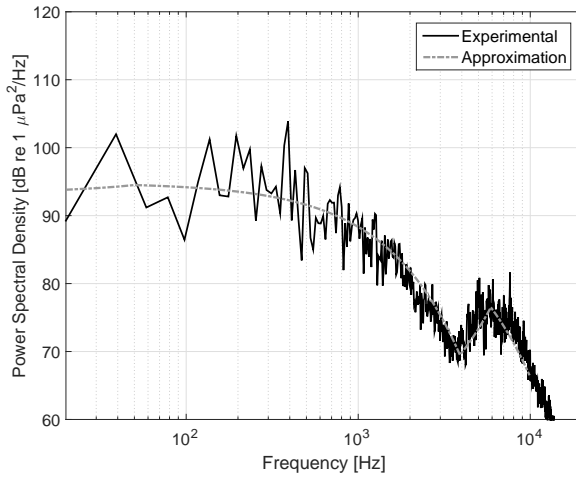
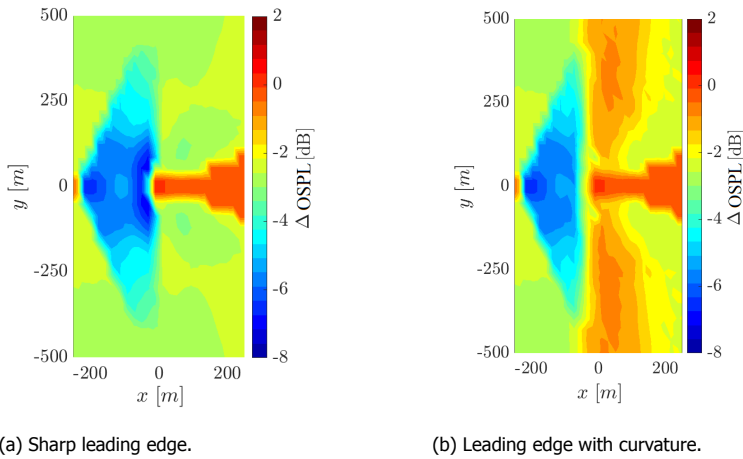


Figure 3.5: Measured frequency spectrum of the F70 engine (black line) and approximation used in the predictions (gray line) .



(a) Sharp leading edge.

(b) Leading edge with curvature.

Figure 3.6: Noise shielding prediction on the ground for a grid of observer positions. The aircraft is at the position $x = 200$ m and $y = 0$ m.

trajectory of the aircraft. Therefore the predicted and experimental values of noise shielding cannot be compared for all the observers of Figures 3.6a and 3.6b, and are limited by positions located at $y = 0$ m.

Predictions and measurements are compared in terms of Overall Sound Pressure Level (OSPL) during the flyover. As a first step, the measured OSPL for all flyovers (not only the F70) were normalized by subtracting the maximum value.

From a noise breakdown [70] it was found that the engine noise is dominant for all measurements, i.e., the OSPL values reflect engine noise. By comparing the measured OSPL curves of the F70 with those of aircraft without shielding, as shown in Figure 3.7, the F70 curve was found to be consistently below the curves of other aircraft for part of the flyover. This is an indication of noise shielding. Notice that the McDonnell Douglas 81 (MD81), also represented in Figure 3.7, is below the curves of aircraft with no noise shielding. This aircraft, similarly to the F70, has rear mounted engines, and therefore also shows evidence of noise shielding. The F70 was the only aircraft type used for the comparison with predictions because only a reduced number of MD81 flyover measurements was available.

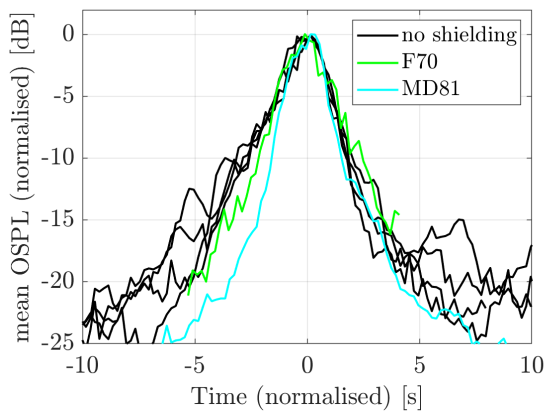


Figure 3.7: Measured OSPL (normalized and averaged over the 32 microphone array) as a function of time for flyovers (landing) of a variety of aircraft types.

Figure 3.8 shows the measured OSPL over time (black line) for four different F70 flyovers, with the OSPL values normalized by the maximum value and the time normalized by the overhead time. The blue line represents the OSPL prediction of the unshielded engines based on the noise spectrum measured at the overhead time. This curve should coincide with the measurements, except for the part where noise shielding, occurs. In that case the OSPL of the experimental curve should be lower than the OSPL of the unshielded engine.

In the plots of Figure 3.8 a third curve represents the OSPL prediction considering engine noise shielding (green line), and modeling the leading edge as sharp. Finally, the dashed red line represents the OSPL prediction with noise shielding and considering a curved leading edge.

The four curves of OSPL coincide except for a time window of approximately 2.5s before the overhead (a time period between -5 to -2.5 s). In this time period engine noise is being shielded by the wings for an observer aligned with the landing trajectory. For the four flyovers presented, predictions are overestimating noise shielding, both considering a sharp and a curved leading edge. However, the measured OSPL presents significant variability.

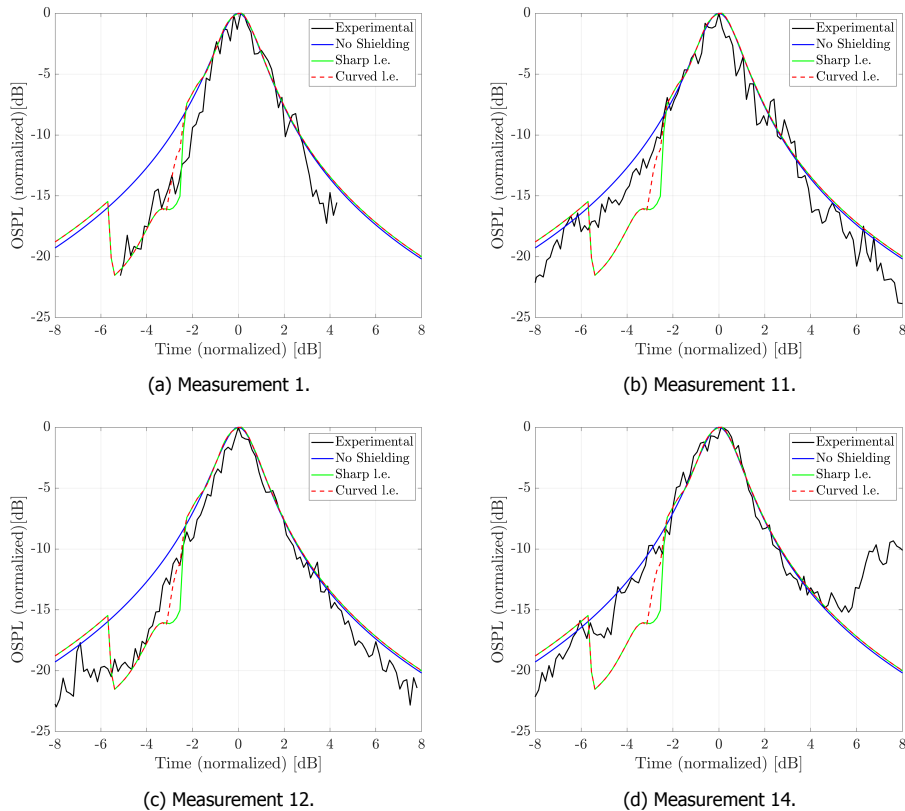


Figure 3.8: Experimental and predicted OSPL for different flyover measurements of the F70.

The experimental OSPL curve of the remaining 16 flyovers recorded can be found in Appendix E. Note that not all flyovers presented noise shielding and some do not even coincide with the predicted OSPL curve of the unshielded noise source. This can be attributed to external noise sources present during the flyover, as the measurement location is close to a highway. It is also important to note that the values of noise shielding are present from 5 s to 2.5 s before the overhead time, i.e., the sound level is not as high as when the aircraft is over the acoustic array, and other noise sources can have a strong interference. A total of 7 flyovers do not present noise shielding.

The predictions can be improved by considering a more realistic landing trajectory, for instance with a constant descent angle of 3° , typical of a landing trajectory (and including a curved leading edge).

Figure 3.9 is a summary of all the 20 flyovers of the F70. The average noise shielding value between 2.5 to 5 s before the flyover is calculated for each measurement. In this plot a value 0 dB means that no noise shielding was found for the

flyover. The dashed green line represents the average value of noise shielding of the prediction considering no descent angle and a sharp leading edge. The dashed red line corresponds to the same prediction but considering a curved leading edge. The difference between these two lines is small, because the creeping rays do not have a great influence for an observer aligned with the landing trajectory as seen in Figure 3.8 and Figure 3.6b. An additional prediction is presented, considering a descent angle of 3° with a curved leading edge, in pink.

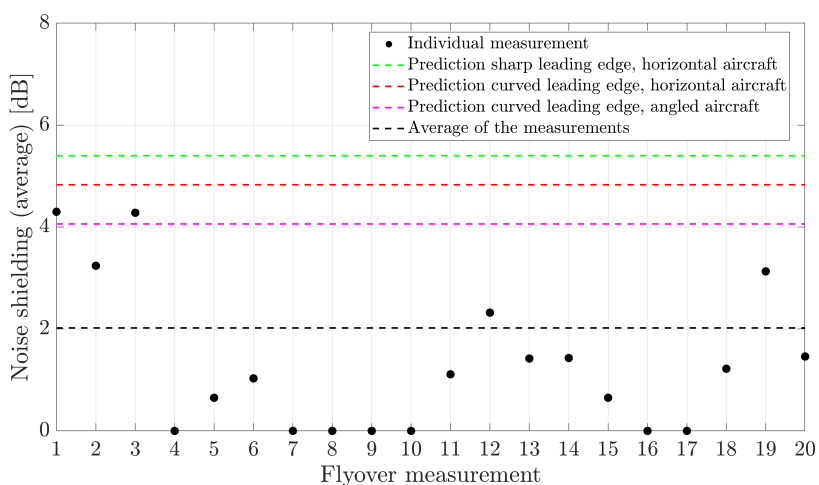


Figure 3.9: Experimental average values of noise shielding for different flyover measurements (black dots) and predicted values considering different approximations (coloured dashed lines).

The experimental values of noise shielding oscillate, which can be attributed to the flight and engine settings and the quality of the measurements (presence of external noise sources). The average value of shielding of all the F70 flyovers is 2.4 dB, indicated by the dotted black line. Not considering the aircraft attitude clearly leads to an overprediction of the noise shielding values, of approximately 3 dB. This deviation decreases to 2 dB when considering a more realistic position of the aircraft in relation to the observer.

The analysis of noise shielding of the F70 under operating conditions indicates that the simplifications of the aircraft geometry, trajectory and source position have to be carefully considered. The experimental analysis for the F70 is especially particularly challenging because the engines are positioned in the rear fuselage, resulting in low values of noise shielding. Measuring aircraft noise under operational conditions also implies that external sources can affect the noise shielding values. The next section explores the effect different assumptions can have in predictions of noise shielding, and gives recommendations for obtaining results as accurate as possible without a drastic increase of the computational time.

3.4. Discussion of the assumptions

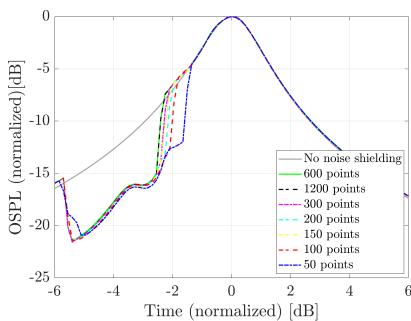
The predictions of noise shielding require a number of inputs that approximate the aircraft geometry, the noise source and the flight settings. The results of noise shielding presented in the previous section were obtained using the approximations with the best trade-off between accuracy and computational time.

The discretization of the aircraft contour that divides the shadow and light region, i.e., the observers with and without noise shielding, respectively, influences the results and has to be carefully considered. A convergence analysis of the results with the number of points of the contour is therefore an important first step towards accurate analyses.

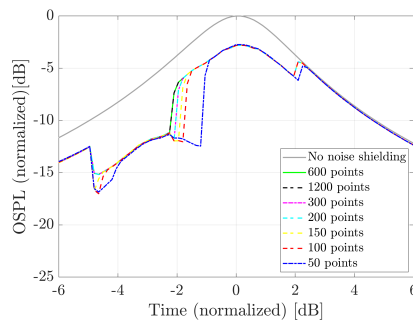
In noise shielding predictions, the required number of points or panels increases with the frequency of the noise source, a fact that is common to the BEM, ESM, Ray-tracing and the Kirchhoff Integral method. This is the reason why some noise shielding methods become too computational expensive for large objects (as the case of an aircraft) when considering a high-frequency noise source.

For the convergence analysis of the contour discretization, the noise spectrum and flight conditions (aircraft velocity, height and attitude) were fixed, and the number of points of the contour was varied from 50 to 1200.

Figure 3.10a shows the OSPL values calculated for a F70 flyover considering different contour discretizations. In this section all predictions consider a sharp leading edge, as it is the baseline case, and the least computationally expensive. In this prediction the aircraft is aligned with the observer position, similarly to the plots presented in the previous section. The noise shielding values (corresponding to the time interval where the coloured curves do not match with the grey curve) change with the contour discretization. The OSPL curves converge for a contour discretization of 600 points.



(a) Observer aligned with the flight path.



(b) Observer 100 m sideways relative to the flight path.

Figure 3.10: Predictions of OSPL (normalized) during a F70 flyover for different discretizations of the contour separating the light-shadow regions.

This convergence was also verified for other observer positions, as an example, Figure 3.10b shows the results for an observer located 100 m sideways of the aircraft

landing trajectory. Although the numerical solution converges only for a contour discretization of 600 points, it is arguable whether 200 or 300 points are already sufficient for accurate predictions, as the difference between the OSPL curves is negligible.

Figure 3.11 shows the influence of the contour discretization on plot contours of noise shielding. The plot of Figure 3.11a was obtained considering a contour discretization of 200 points, with the flight conditions and number of observers of Figure 3.6a, presented before. The two plots are similar, but Figure 3.11a shows a less smooth contour with some abrupt variations in noise shielding (dark blue points), which leads to less accurate results. The same plot is represented in Figure 3.11b considering a contour with 100 points, and also in this case the noise shielding results differ from Figure 3.6a and will conduct to erroneous conclusions. Even though the 200 and 100 points contour discretizations resulted in similar values of noise shielding in Figure 3.10 compared with the converged solution, they are clearly not enough to obtain a correct result.

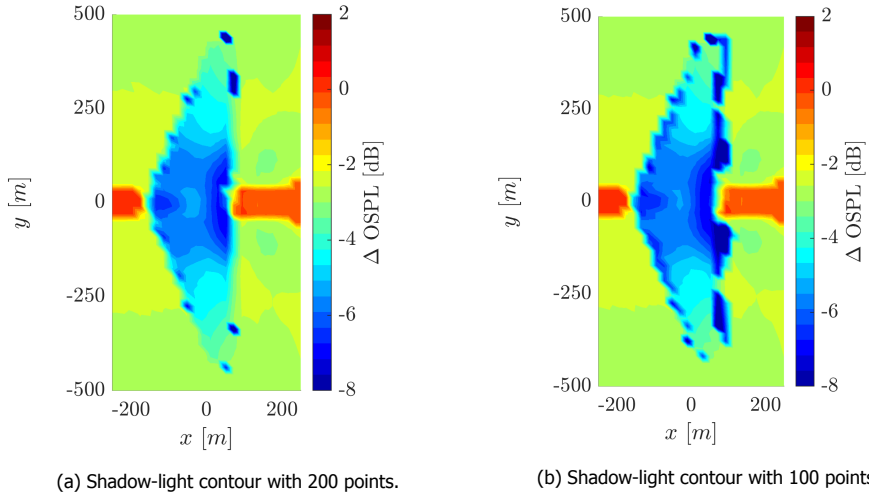


Figure 3.11: Noise shielding prediction on ground considering different contour light-shadow discretization.

Predictions considering only a few observers are not computationally expensive, even at high frequencies. However, plots with a large number of observers such as in Figure 3.11 (1500 observers) result in a long computational time. Figure 3.12 shows the computational time required for the predictions of Figure 3.11 as a function of the number of points used in the contour. The noise shielding method was implemented in MATLAB®, and the predictions were run on the same computer with a processor Intel(R) Xeon(R) CPU E5-1620 v3 and 8 Gb of installed RAM.

The computational time increases very rapidly with the number of points of the contour, and therefore the convergence study of the minimum number of points necessary for the contour is of great importance. The plots of Figure 3.11 corre-

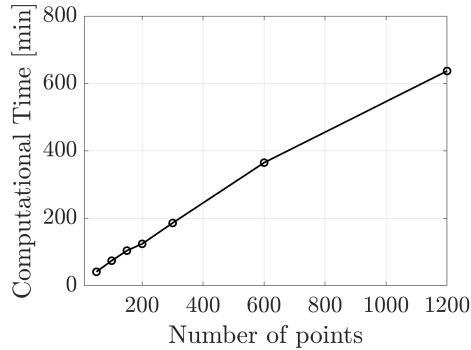


Figure 3.12: Evolution of the computational time necessary for the predictions with the increase of the shadow-light contour discretization, considering a noise spectrum divided in 1/3-octave bands and 1500 observer points.

spond to just one moment in time of the flyover of the F70. To obtain the noise shielding values on the ground it was necessary to compute 14 time steps of flight at the source (source time) to have enough points to interpolate to the observer time (accounting for the propagation time between the moving source and the observer on the ground). This means that with the contour discretization of 600 and 1200 points, each time step of the simulation took approximately 28 and 42 minutes, respectively. When simulating a complete flyover with a realistic trajectory (changing aircraft velocity, height and attitude) the time required for the predictions increases significantly and considering an unnecessary number of contour points can result in impracticable simulations.

Another input that requires particular attention is the noise spectrum of the engine. The values of noise shielding are subtracted from the Sound Pressure Level (SPL) of each frequency considered in the spectrum and then summed algorithmically to obtain the OSPL. An appropriate approximation of the engine spectrum is essential to ensure a fair comparison between predictions and experimental values of noise shielding.

The experimental spectrum was approximated as 1/3-octave bands in the predictions. The 20 flyovers of the F70 presented very similar engine noise spectra (spectra recorded at the overhead time) and therefore the same 1/3-octave bands approximation could be used for all the cases. Figure 3.13 shows the predicted values of OSPL for Measurement 1 and 15, using different frequency discretization of the noise spectra measured during these two flyovers.

The difference between using the 1/3-octave band spectrum and using smaller frequency steps is negligible for both flyovers. In addition, there is no difference in the predictions by considering the experimental noise spectrum per flyover, which shows that the average of the spectrum in 1/3-octave bands is a suitable approximation for all the 20 flyovers of the F70. This assumption not only simplifies the comparison process but also decreases the computational time. For example, sim-

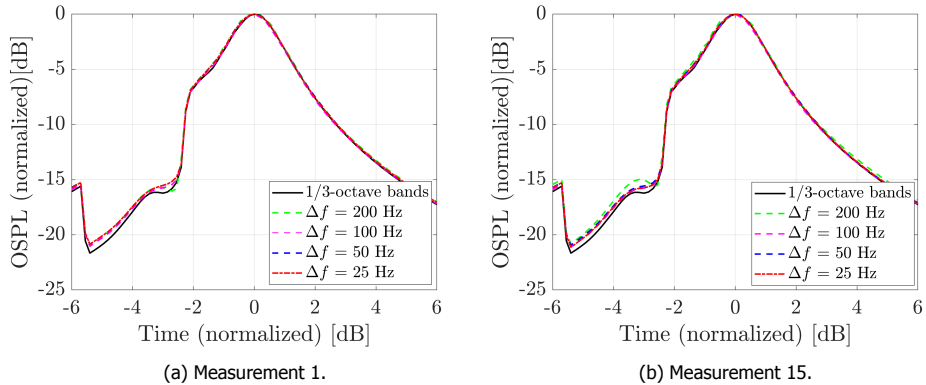


Figure 3.13: Predictions of OSPL (normalized) during two distinct F70 flyovers using different discretization of the noise spectrum measured for the corresponding flyover.

ulations considering a 100 Hz frequency step take the triple of the amount of time required for the 1/3-octave band approximation.

The noise shielding predictions presented in the previous section were obtained using the average values of aircraft velocity and height of all the 20 flyovers recorded for the F70. The values of predicted noise shielding are thus not dependent on those two parameters. However, the shape of the OSPL curve is affected by the propagation time and the Doppler effect.

The variability of the F70 height and velocity at the overhead time for the 20 flyovers recorded can be seen in Figure 3.3 . The noise shielding predictions for the F70 were repeated for some flyovers considering the measured aircraft velocity and height instead of the average values. Figure 3.14 shows the baseline prediction of the OSPL curve and 4 other predictions of OSPL using the velocity and height of the corresponding measurement. The measurements selected present the most divergent values of velocity and height compared with the average value.

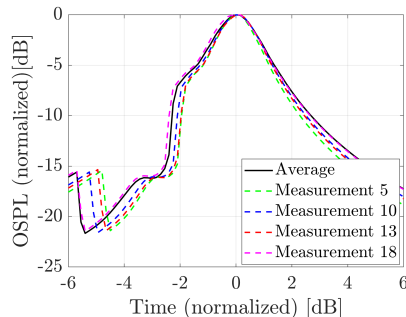


Figure 3.14: Prediction of OSPL during the F70 flyover considering different values of aircraft velocity and height.

The OSPL curve is very similar for all the cases. These small differences do not explain the shape of the curves that do not present noise shielding (see Appendix E), which therefore can be attributed to the presence of external noise sources. Similarly to what was recommended for the noise spectrum, an average value of the aircraft velocity and height can be used when the landing trajectory does not present high variability.

The calculation of the total noise shielding, i.e, including all the frequencies (Δ OSPL) is obtained using the following equation,

$$\Delta\text{OSPL} = \text{OSPL}_{\text{shielding}} - \text{OSPL}_{\text{no shielding}} \quad (3.1)$$

in which $\text{OSPL}_{\text{shielding}}$ is obtained by the summation of the sound pressure level of each frequency with the respective noise shielding value, ΔSPL , subtracted (see Equation (2.64)),

$$\text{OSPL}_{\text{shielding}} = 10 \log_{10} \left(\frac{\sum_{i=1}^N 10^{(\text{SPL}_i - \Delta\text{SPL}_i)}}{10} \right). \quad (3.2)$$

In the absence of the noise source spectrum, Equation (3.2) cannot be used. In that case it is advisable not to estimate the ΔOSPL by averaging the noise shielding contribution of all frequencies, but to show the noise shielding results separately per frequency instead. An average of the noise shielding values ΔSPL might lead to very inaccurate results. For the case of a non flat noise spectrum, as is the case of an engine, it is crucial to consider the noise spectrum when calculating the ΔOSPL . As an example, Figure 3.15 shows the averaged values of ΔSPL over the frequency during a F70 flyover. This plot is very different compared with Figure 3.6a, in which ΔOSPL was calculated using Equation (3.2).

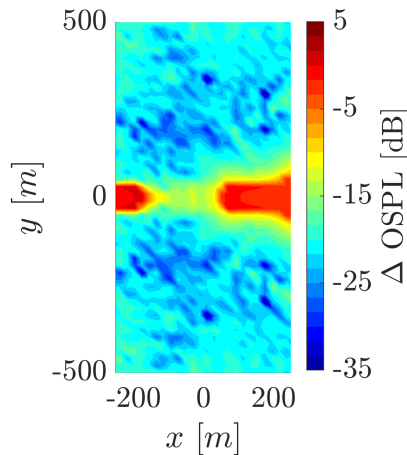


Figure 3.15: Noise shielding prediction on ground when averaging the ΔSPL values over the frequency.

4

Noise shielding of propeller noise by a wing

The shielding of a noise source is affected by its directivity. This chapter explores the differences between noise shielding of an omni-directional source (monopole directivity) and of a propeller (approximately a dipole), using experimental data and predictions. Two shielding objects are used in the experiments: a flat plate and a wing with the same dimensions. The effect of the curvature of the leading edge is assessed by comparing the noise shielding values of these two objects. Conventional beamforming is used to image the source distribution over the shielding surface. This helps to understand the noise shielding behavior for different obstacles and types of noise source. The experimental campaign of this chapter aims to determine the accuracy of the predictions and to explore possible limitations.

Parts of this chapter have been published in *The Journal of the Acoustical Society of America*, **142**, 2 (2019) [45].

4.1. Experimental setup at the anechoic room

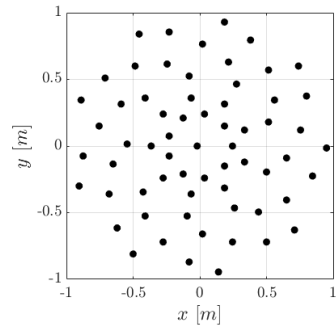
The experimental campaign took place in an anechoic facility with a vertical wind tunnel, at the Delft University of Technology. The free-field behaviour of the anechoic room follows the ISO 3745 guidelines [139] and the reverberation time is 0.25 s, equivalent to the anechoic category of ISO 3382 [140]. The vertical wind tunnel is positioned at the center of the anechoic room and has a circular shape of 60 cm and a contraction ratio of around 60:1 [141]. Ghaemi et al [142] determined a turbulent intensity below 0.5 % at the exit of the nozzle for a freestream of 10 m/s. In the experiments of this section the flow speed was set constant at the velocity of 10 m/s.

A microphone array, composed of 64 G.R.A.S. 40PH CCP free field microphones [143], was used to measure the noise. The microphones were individually calibrated with a G.R.A.S. 42AA pistonphone [144]. The 2 m by 2 m metallic structure supporting the microphones was designed to reduce acoustic reflections [145]. The Data Acquisition System (DAS) consisted of 5 National Instruments PXOe-4499 sound and vibration data acquisition modules controlled by a NI RMC-8354 controller. The uncertainty associated to the noise measurements was experimentally determined as 0.5 dB.

The microphones positions in the metallic structure follow the TU Delft Optimized Array distribution [146]. This configuration provides the best trade-off for the main lobe width and maximum sidelobe level in beamforming. Figure 4.1a shows the structure of the microphone array and Figure 4.1b illustrates in detail the microphone distribution.



(a) Microphone array used in the experiments [45].



(b) TU Delft Optimized Array distribution.

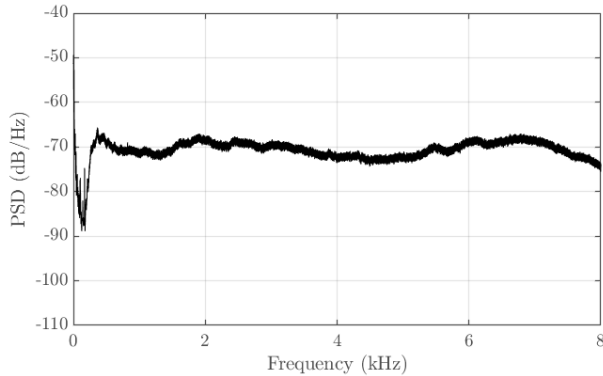
Figure 4.1: Configuration of the microphone array.

The experiments were performed with two distinct noise sources: an omnidirectional source and a small propeller. The omnidirectional source is a customized miniature sound source type QindW developed by Qsources (Figure 4.2a). This sound source is omnidirectional in the azimuthal plane, and has a flat frequency response from approximately 500 Hz to 6300 Hz (as shown in Figure 4.2b) when driven by white noise.

The second noise source used in the experiments was a three-bladed propeller



(a) QindW omnidirectional source.



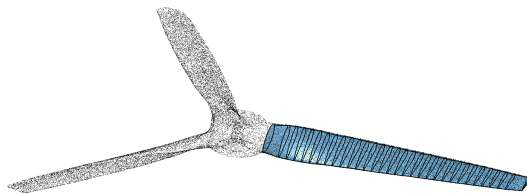
(b) Frequency response of the omnidirectional source.

Figure 4.2: Omnidirectional source used in the experiments.

Master Airscrew E-MA1260T. Figure 4.3a shows the propeller mounted with the hub and the shaft, which is inside a tube of aluminium together with the electric motor (Kontronik PYRO 700–45 Brushless). The motor is controlled with an electronic speed control using a Kontronik Jive PRO 80p HV. The propeller has a 29.6 cm diameter and its airfoil distribution along the span is illustrated in Figure 4.3b. The blade geometry was obtained using a mobile 3D scanner and then reconstructed in CATIA™.



(a) Propeller setup used in the experiments [45].



(b) 3D scan of the propeller [74].

Figure 4.3: Propeller used as a noise source in the experiments.

The wing used as an obstacle between the noise source and the microphone array has a NACA-64-8A airfoil, 123 cm of span and 24.5 cm of chord (see Figure 4.4). The side plates at the extremities of the wing were necessary to fix it without interfering with the longest edges (leading and trailing edge). The wing is positioned such that the trailing edge is the upper edge and the leading edge is the bottom edge. A flat plate of the same dimension (and with exactly the same side plates for support) is also used in the experiments as an obstacle.

The values of noise shielding were determined for different distances between the noise source, obstacle and microphone array. The experimental setup in the



Figure 4.4: Wing used as obstacle in the noise shielding measurements.

anechoic room is represented in Figure 4.5. The distances considered are relative to the source position. The microphone array is kept fixed in the anechoic room, and the noise source and shielding object are changed for the different measurements.

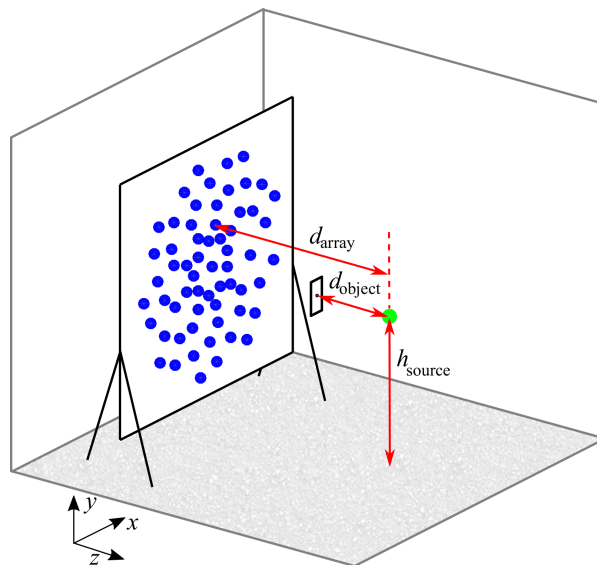


Figure 4.5: Experimental setup of a noise source shielded by an obstacle in the wind tunnel.

4.2. Noise shielding of an omni-directional noise source

The noise level variation at the microphones of the array is experimentally determined using an omni-directional source shielded by a flat plate and compared with predictions. The distance between the omni-directional source, plate and microphone array is varied and different frequency bands are considered for the comparison between experimental data and predictions.

In a second part of the experiment, the flat plate is replaced by the wing. The new values of noise shielding are compared with those obtained previously for the plate. Therefore, this experimental campaign has a two-fold objective: to validate the noise shielding tool and to assess the effect of a curved edge.

The comparison between experimental data and predictions is complemented by a visualization of the sound diffraction around the edges of the obstacle using beamforming. In the case of the predictions, the acoustic pressure calculated with the noise shielding tool was used as input in the conventional beamforming code. The comparison of experimental and predicted beamforming plots allows us to understand possible differences in the noise shielding values and/or to identify external sources in the experimental setup.

The beamforming plots of Figure 4.6 and Figure 4.7 correspond to two different cases of shielding of the omni-directional source by the flat plate, considering different distances between the source and the array (d_{array}) and the obstacle (d_{object}). Both predicted and experimental beamforming plots are shown for the two cases.

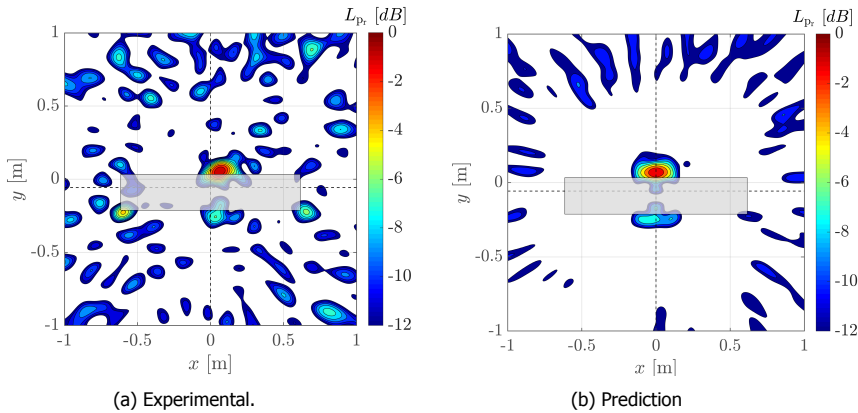


Figure 4.6: Beamforming plots for the omni-directional source shielded by a flat plate, with $d_{\text{array}}=1.81$ m and $d_{\text{object}}=0.38$ m, and a frequency of 3150 Hz. The intersection of the two dashed lines indicates the noise source position behind the plate [45].

The beamforming plots from experimental data are similar to those of the predictions, with the strongest noise source located at the upper edge of the plate, which is closer to the noise source. The predictions show less side lobes than the experimental plots, which was expected because the pressure measured at the microphones can suffer disturbances from the experimental setup and reflections in

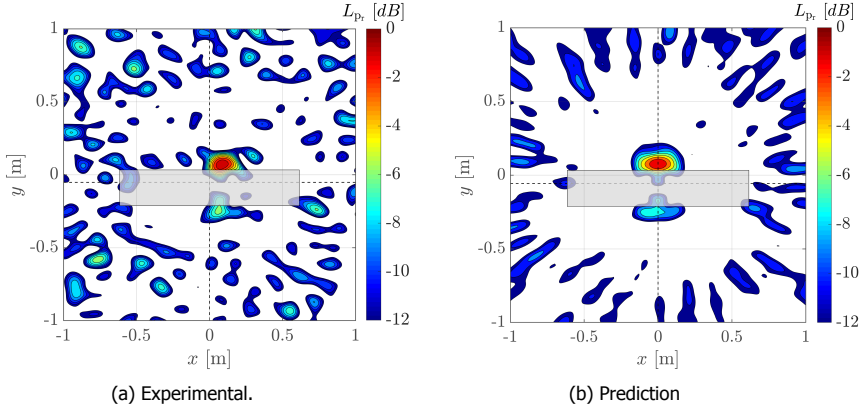


Figure 4.7: Beamforming plots for the omni-directional source shielded by a flat plate, with $d_{\text{array}}=3.40$ m and $d_{\text{object}}=0.75$ m, and a frequency of 5000 Hz. The intersection of the two dashed lines indicates the noise source position behind the plate [45].

the anechoic room. The experimental results also show that the noise source is not exactly at the center of x -axis, as intended, which shows that beamforming is also a valuable tool to identify the exact position of the noise source and so that information can be used as input in predictions.

The experiment of the omni-directional noise source shielded by the flat plate considered six different combinations of d_{array} and d_{object} , which multiplied by the 64 microphones of the array results in a large dataset of noise shielding values, too exhaustive to compare individually. Therefore, the difference between experimental values of noise shielding and predictions is shown in terms of an average absolute deviation, given by

$$\delta_s = \frac{1}{N} \sum_{n=1}^N |\Delta L_{p,\text{prediction}_n} - \Delta L_{p,\text{experimental}_n}|. \quad (4.1)$$

Here N is the total number of microphones and $\Delta L_{p,\text{prediction}}$ and $\Delta L_{p,\text{experimental}}$ are the predicted and experimental noise shielding values, respectively.

The results of the average absolute deviation δ_s considering the 1/3-octave bands with center frequency of 2000, 3150, 4000 and 5000 Hz are presented in Figure 4.8. The values of δ_s are positioned according to the distances d_{array} and d_{object} used in the measurement. Thus, one can easily identify which distances between source, obstacle and microphone array result in higher deviations between measurements and predictions.

The average deviation of Figure 4.8 is around 2-3 dB, which confirms the good agreement between experimental values of noise shielding and predictions. This is an expected result, taking into account the similarity between the beamforming plots (see Figure 4.6 and Figure 4.7).

It is important to note that the measurements with higher values of δ_s are those with the source closer to the obstacle and further away from the microphone array.

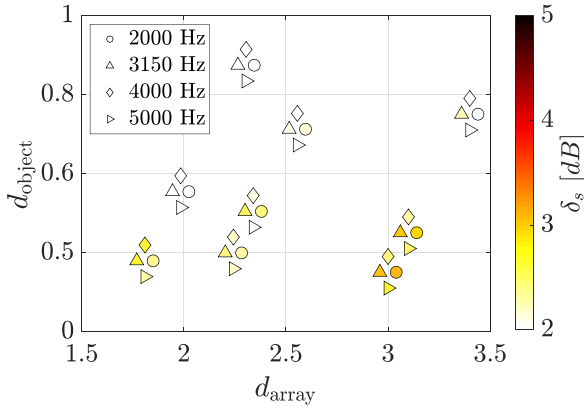


Figure 4.8: Average absolute deviation in dB between experimental results and predictions of noise shielding for the flat plate. The shape of the marker indicates the frequency considered (center frequencies of 1/3-octave bands) [45].

This can be either attributed to less accurate measurements, since the microphones are away from the noise source or to noise reflections on the wing surface, due to the small distance between the source and the plate.

The flat plate was later replaced by the wing, and the noise shielding values were measured considering the same distances d_{array} and d_{object} of the previous experiment. The values of δ_s were recalculated using the new experimental data, but the same predictions of noise shielding, i.e., for the flat plate. Figure 4.9 shows the new values of average absolute deviation, which are now very significant, with some positions where the predictions present more than 5 dB of deviation compared with the experimental values. Clearly, the curved leading edge influences the values of noise shielding, and a more adequate prediction is required. In Figure 4.10 the values of average absolute deviation were calculated with predictions that take into account the creeping rays generated by the leading edge of the wing, and the values of δ_s decreased compared with Figure 4.9.

Therefore, a curved edge has a significant effect on noise diffraction, a behaviour expected specially at high frequencies [91]. The influence of the leading edge on the noise shielding results is confirmed by the beamforming plots of Figure 4.11. Figure 4.11a shows the beamforming plot obtained for the wing and Figure 4.11b shows the exact same experiment but with the plate as the obstacle. The case of the wing shows two noise sources of the same magnitude at the trailing and leading edge, while the plate case has the strongest source located at the trailing edge as the other experimental beamforming plots shown before (Figure 4.6 and Figure 4.7).

The beamforming plot obtained using predictions with the curved leading edge, shown in Figure 4.12, presents a similar behaviour as the plot for the experimental data: two noise sources of equal strength at the trailing and leading edge of the wing.

The predictions show a good agreement with the experimental data, both in

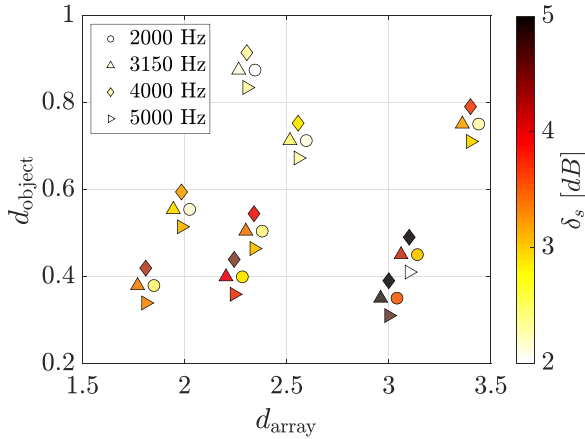


Figure 4.9: Average absolute deviation in dB between experimental results and predictions of noise shielding for the wing (considering a flat plate in the predictions). The shape of the marker indicates the frequency considered (center frequencies of 1/3-octave bands) [45].

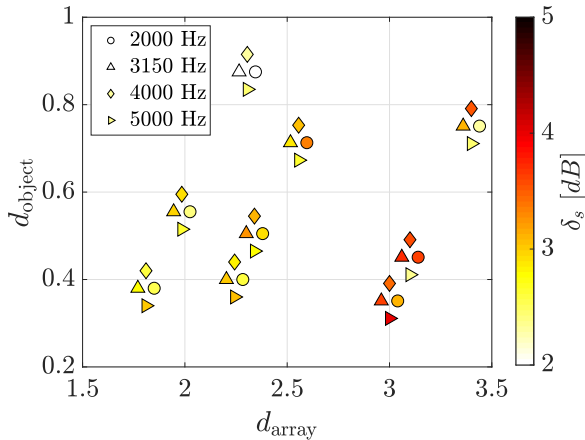


Figure 4.10: Average absolute deviation in dB between experimental results and predictions of noise shielding for the wing (considering the creeping rays generated by the leading edge). The shape of the marker indicates the frequency considered (center frequencies of 1/3-octave bands) [45].

terms of values of noise shielding and diffraction pattern at the edges of the obstacle. The effect of the curvature of the leading edge on noise shielding is evident in this experimental case. The leading edge was approximated as a half circle with a radius of 8 mm, i.e., the wing presented a very small curvature. For surfaces with more pronounced curvatures the creeping rays are expected to have an even stronger influence on the noise shielding results.

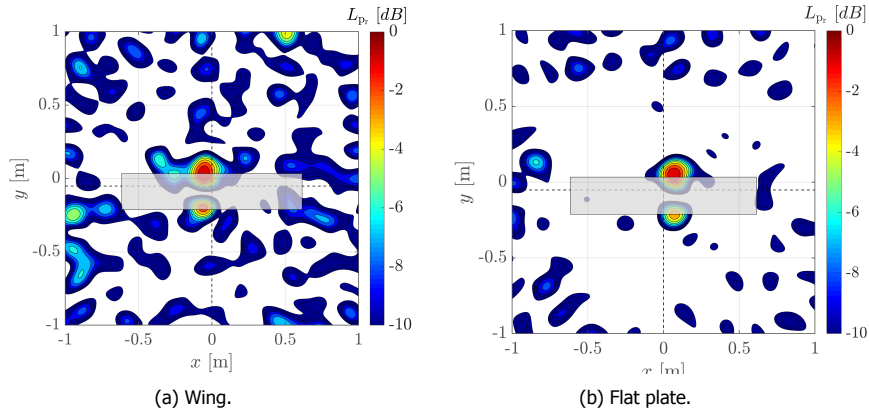


Figure 4.11: Experimental beamforming plots for a frequency of 4000 Hz, $d_{\text{array}}=3.1$ m and $d_{\text{object}}=0.45$ m [45].

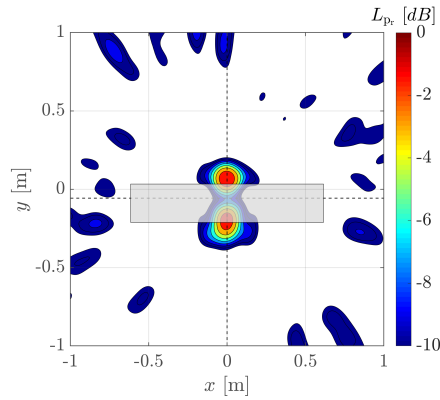


Figure 4.12: Prediction of beamforming plot for a frequency of 4000 Hz, $d_{\text{array}}=3.1$ m and $d_{\text{object}}=0.45$ m, considering a curved leading edge [45].

4.3. Noise shielding of a propeller by a wing

The shielding of propeller noise is complex when compared with the case of the omni-directional source presented in the previous section. Propellers generate distinct types of noise, as explained in Section 2.2, with monopole, dipole and quadrupole directivity. Although propeller radiation is commonly associated with a dipole directivity, due to the strong noise contribution of the thrust and torque compared with other noise sources, it is still a rough approximation.

The experimental setup used to measure the noise shielding of a propeller by a wing is illustrated in Figure 4.13. A heavy metallic structure of aluminium was used to fix the propeller to the nozzle of the wind tunnel in order to minimize vibrations that could interfere with the wake field. The structure was covered with foam to

minimize sound reflections. The presence of this structure, as well as the noise of the electric motor add noise sources to the already complex case of propeller noise.

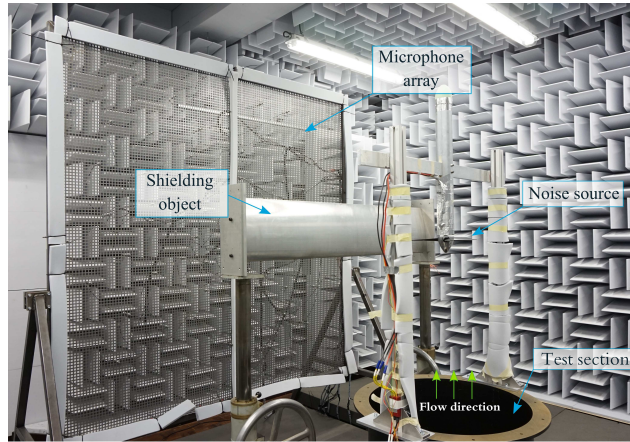


Figure 4.13: Experimental setup used to measure the shielding of propeller noise by a wing [45].

Therefore, in this experiment beamforming is not only used to understand the noise diffraction behaviour at the edges of the obstacle but also to detect possible secondary noise sources resulting from the interaction of the support structure with the flow from the wind tunnel and the flow generated by the rotation of the propeller.

The propeller is fixed at the nozzle position. Thus only the wing can be moved, which limits the number of measurements. Table 4.1 shows the relative distances between the wing, propeller and microphone array considered in the experiment, as well as the values of rotational speed set for the propeller. The measurements were first conducted with no incoming flow and then with a flow at a constant velocity of 10 m/s.

Table 4.1: Distances considered in the experiment and values of rotational speed (in RPM) of the propeller.

d_{array} [m]	1.46
d_{object} [m]	0.40
	0.54
Rotational speed [RPM]	RPM ₁ = 4400
	RPM ₂ = 7000
	RPM ₃ = 7600

A propeller operating with no incoming airflow generates a non-uniform flow, resulting in an increase of broadband noise. Nevertheless, the measurements with no incoming airflow can be used to assess the influence of the flow on shielding of propeller noise. The measurements showed very different results for the two cases: significant values of noise shielding were found for the propeller under the constant airflow, but for the propeller with no incoming airflow no noise shielding was detected, but rather an increase in noise levels.

In order to show the shielding behaviour for a wide range of frequencies, microphones at the center of the array were selected in the polar and azimuthal directions, as represented in Figure 4.14.

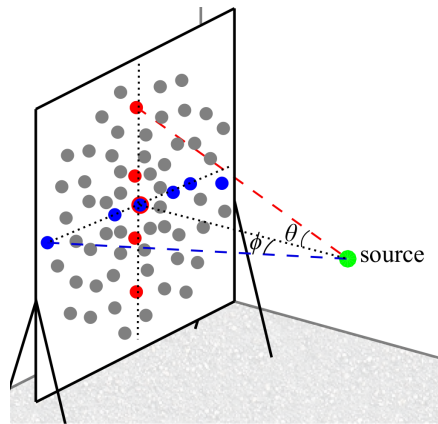


Figure 4.14: Microphones selected in the azimuth (in blue) and polar (in red) directions [45].

Figure 4.15 shows the difference in noise level measured in the azimuth direction between the unshielded and shielded propeller, for frequencies between 500 and 5000 Hz. Positive values indicate an increase of noise whereas negative values indicate the existence of noise shielding. The same plot is shown in Figure 4.16 for the microphones in the polar direction.

Both Figures 4.15 and 4.16 show positive values of ΔL_p for most frequencies, indicating that the presence of the wing is increasing the noise level at the microphone positions rather than reducing it. The frequency of 1300 Hz shows a strong reinforcement of noise, of up to 10 dB. The beamforming plot at that frequency, presented in Figure 4.17, shows a strong noise source at the top of the tube that contains the rotating shaft and the electric motor. This source is located higher than the wing so it is not efficiently shielded, and overshadows any diffraction of propeller noise that might be present at this frequency.

Figure 4.15 and Figure 4.16 indicate noise shielding at a frequency of 2660 Hz, which corresponds to the 7th harmonic of the propeller set at RPM_3 . The beamforming plot at this frequency, in Figure 4.18, shows a very different behaviour compared with Figure 4.17, with two sources located at the longest edges of the wing, indicating diffraction of propeller noise.

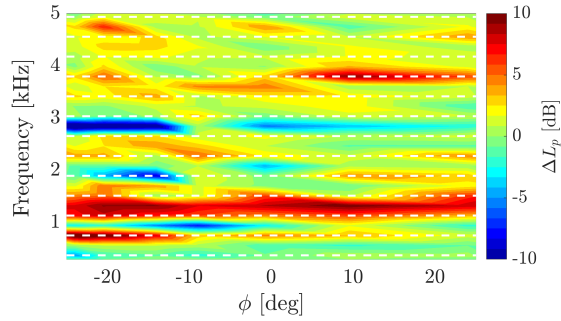


Figure 4.15: Values of noise shielding as a function of frequency and azimuth direction ϕ . The propeller is set at the highest value of rotational speed (RPM3), with no incoming airflow and $d_{\text{object}}=0.40$ m. The white dashed lines correspond to the propeller harmonics [45].

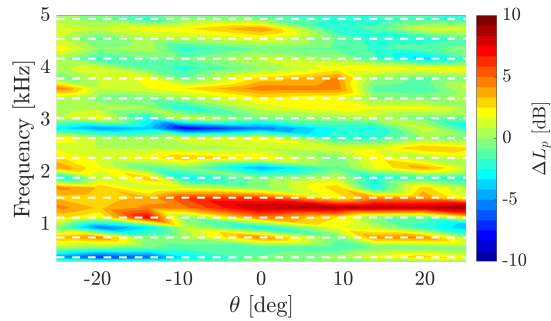


Figure 4.16: Values of noise shielding as a function of frequency and polar direction θ . The propeller is set at the highest value of rotational speed (RPM3), with no incoming airflow and $d_{\text{object}}=0.40$ m. The white dashed lines correspond to the propeller harmonics [45].

In the presence of an incoming airflow at constant speed the vortices generated at the blade tips are pushed downstream and do not interact with the propeller wake, which decreases the turbulence of the flow generated by the propeller rotation. The noise shielding results obtained in this experiment differ from those observed for the propeller with no incoming airflow.

Figure 4.19 shows the beamforming plots of the propeller alone for the frequency of 2660 Hz, with and without an incoming airflow. The noise source is located at the right side of the propeller, which is the rotation direction, in both plots. However, Figure 4.19a shows two distinct noise sources, located at the top and bottom of the propeller disk, and Figure 4.19b shows a single source. The distinct behaviour of the noise source results is reflected in the noise shielding results.

Figure 4.20 and Figure 4.21 show the values of noise shielding for the microphones selected in the polar and azimuth directions (see Figure 4.14) when the

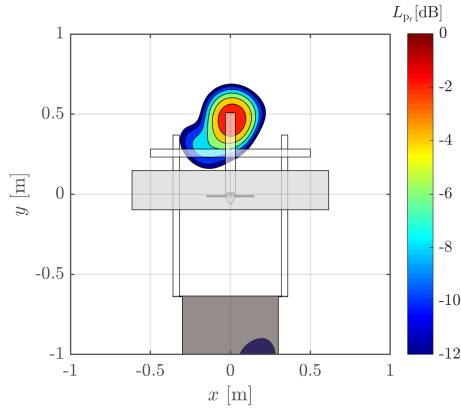


Figure 4.17: Beamforming plot for a frequency of 1300 Hz, $d_{\text{object}}=0.40$ m. The propeller is set at RPM_3 with no incoming airflow [45].

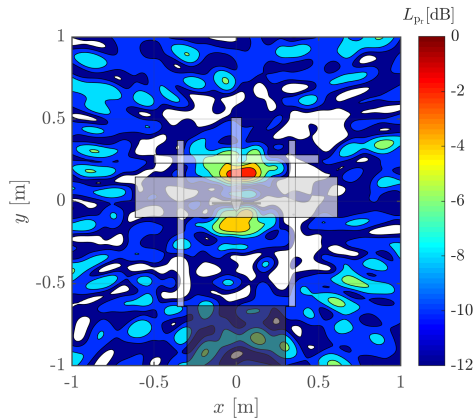


Figure 4.18: Beamforming plot for a frequency of 2660 Hz, $d_{\text{object}}=0.40$ m. The propeller is set at RPM_3 with no incoming airflow [45].

propeller is subjected to a constant incoming flow.

These two plots show noise shielding for most frequencies, unlike the case of the propeller with no incoming flow of Figure 4.15 and Figure 4.16. There is noise reinforcement for some positions and frequencies, but it is not as significant as for the propeller with no flow (notice that the maximum value in the scale of ΔL_p was adjusted). However, the values of noise shielding for the propeller are less significant than the values measured for the omnidirectional source. Consider the plots of Figure 4.22 and Figure 4.23, which are an equivalent case to the azimuth and polar plots presented for the propeller above (i.e., with the same relative distances in the experiment) but considering the omni-directional noise source. The values of

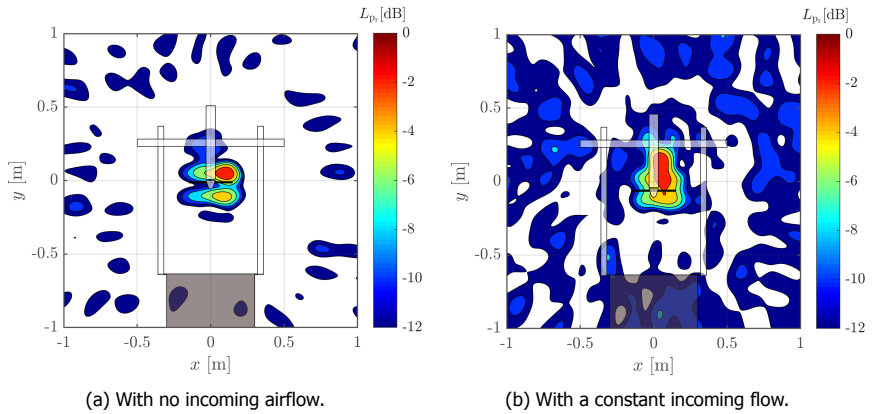


Figure 4.19: Beamforming plots of the propeller at a frequency of 2660 Hz [45].

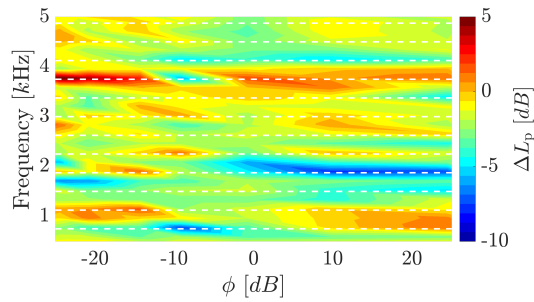


Figure 4.20: Values of noise shielding as a function of frequency and the azimuthal direction ϕ . The propeller is set at the highest value of rotational speed (RPM3), with a constant incoming airflow and $d_{\text{object}}=0.40$ m. The white dashed lines correspond to the propeller harmonics [45].

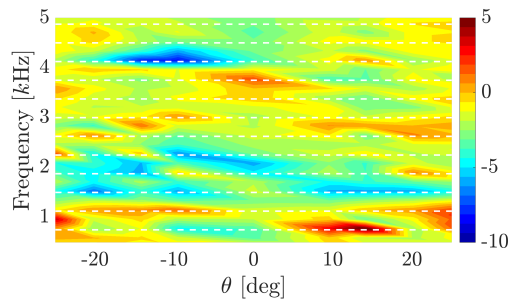


Figure 4.21: Values of noise shielding as a function of frequency and the polar direction θ . The propeller is set at the highest value of rotational speed (RPM3), with a constant incoming airflow and $d_{\text{object}}=0.40$ m. The white dashed lines correspond to the propeller harmonics [45].

noise shielding are noticeable higher for the omni-directional source, showing that it is more efficiently shielded than the propeller.

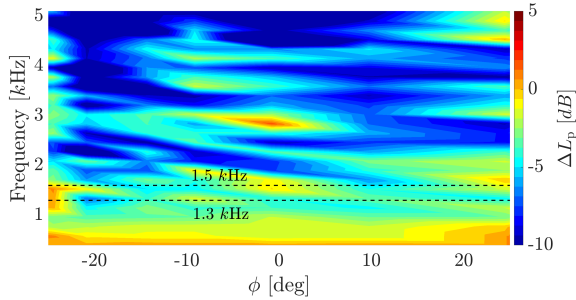


Figure 4.22: Values of noise shielding as a function of frequency and azimuthal direction ϕ , for the omni-directional source and $d_{\text{object}}=0.40$ m [45].

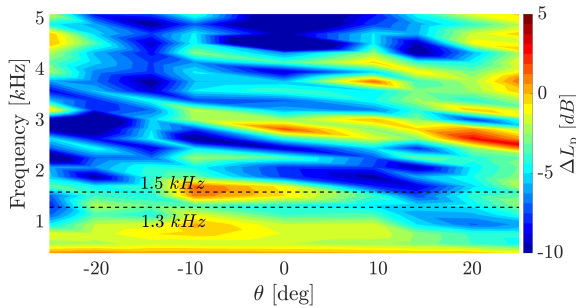


Figure 4.23: Values of noise shielding as a function of frequency and polar direction θ , for the omni-directional source and $d_{\text{object}}=0.40$ m [45].

The plots of Figure 4.22 and Figure 4.23 show significant noise reinforcement at a frequency between 13 000 –1600 Hz, also observed for the propeller under no incoming flow (see black dashed lines). The beamforming plot of Figure 4.24a, at 1300 Hz shows two sources on the leading and trailing edges of the wing, which indicates noise shielding but also the presence of external noise sources coming from the setup. Other external sources from the support structure, at different frequencies, were found. An example is illustrated in Figure 4.24b, in which two strong noise sources are located at the nozzle.

The beamforming plots for frequencies with noise shielding, e.g., at 2660 Hz, show two noise sources, located at the leading and trailing edge, as expected, indicating noise shielding (see Figure 4.25).

From the results as presented in this chapter, it is found that the method used for the predictions of shielding of an omni-directional source, presented in Section 4.2, in general, shows a good agreement with the experimental data. However,

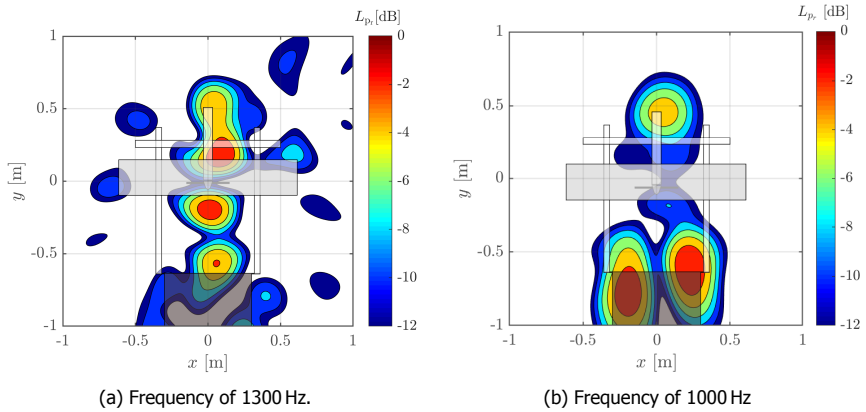


Figure 4.24: Beamforming plots of the propeller shielded by the wing. The propeller is set at RPM_3 with a constant incoming flow and $d_{\text{object}}=0.40\text{ m}$ [45].

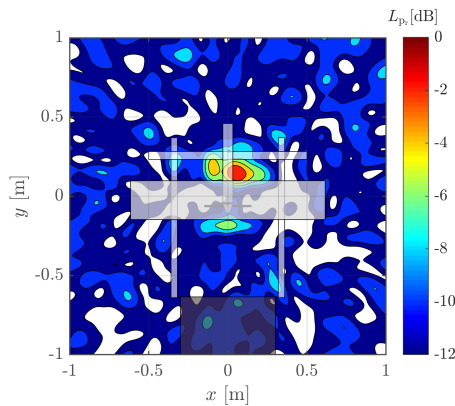


Figure 4.25: Beamforming plot for a frequency of 2660 Hz, $d_{\text{object}}=0.40\text{ m}$. The propeller is set at RPM_3 with a constant incoming flow [45].

the propeller has a different noise directivity and the predictions of noise shielding need to be adapted accordingly. Therefore, two types of source are used in the predictions besides the monopole: a dipole source and a multi-source composed by a ring of monopole sources. All predictions in this section include the creeping rays generated at the leading edge. The effect of the flow velocity is not accounted for in the noise shielding predictions (such a low velocity is not expected to affect the noise shielding values). However, it is accounted for in the beamforming plots.

The plots of Figure 4.20 and Figure 4.21 show limited noise shielding, with values less than or equal to 5 dB for most frequencies. For the other two values of rotational speed of the propeller (see Table 4.1) the values of noise shielding were even lower. It was observed that the higher values of noise shielding are at the frequencies of the harmonics. Therefore, for the comparison between experiments

and predictions, only the frequencies of the harmonics were selected.

The sound pressure level of the harmonics decreases rapidly after the 5th harmonic and harmonics higher than the 7th are hardly discernible. In addition, the lowest frequency considered for the analyses corresponds to the 3rd harmonic (roughly 1000 Hz for the three values of angular speed). Lower frequencies are not considered because external noise sources are more than or equally significant as the noise of the propeller diffracted by the wing, as seen in the beamforming plots of Figure 4.24. Therefore, only frequencies corresponding to the 3rd to the 7th harmonics are considered for the comparison, which correspond roughly to a range between 1000 and 3000 Hz.

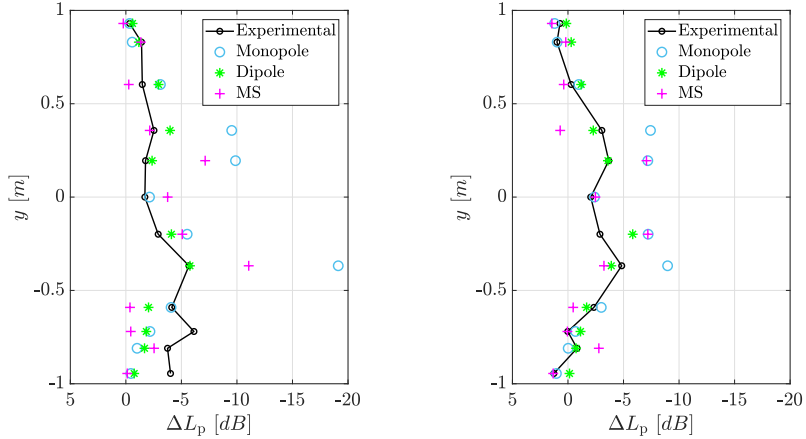
For the predictions with the multi-source, different combinations of number of monopoles N (see Equation (2.74)) and azimuthal number n were tested (see Equation (2.72)). It was found that 16 distributed monopoles and an azimuthal number $n = 20$ resulted in a stable solution (i.e., the ring of monopoles resulted in a single compact noise source) for describing a disk shaped source for the range of frequencies considered. This configuration was used for the predictions with the multi-source.

To better understand the difference in noise shielding between the three types of sources considered in the predictions, the values are plotted as a function of y . The propeller is centered at the wing in the x -axis. Since the wing covers a big extension of the array in that axis, noise shielding is expected to be approximately constant over x . The values of noise shielding are averaged over x in order to have the variation only dependent on y .

Figure 4.26a displays the averaged values (over the x -axis) of noise shielding, ΔL_p , for the 5th harmonic (with the propeller set at rotational speed RPM_3) and $d_{\text{object}} = 0.40 \text{ m}$, resulting from the measurements and model predictions, using a monopole, dipole and multi-source as source. The value predicted for the dipole directivity is not presented at $y = 0 \text{ m}$ because it is a singularity. It is clear from Figure 4.26 that the prediction with the dipole shows the best agreement with the experiments.

The dipole predictions showed the best agreement with the experimental data for all the test cases analysed. On the other hand, predictions using a monopole directivity greatly overestimate noise shielding for the propeller. Figure 4.26b shows another test case used for the comparison between experimental data and predictions, in which the dipole is clearly again the best approximation.

The monopole seems to be a good approximation for predicting the noise shielding of a propeller at $y = 0 \text{ m}$, where the dipole is not suitable. The multi-source is a better approximation than the monopole, but still results in significant deviations compared with the experiments. The deviation between experiments and predictions with the monopole and multi-source is specially high for observer positions with higher experimental values of shielding, at $y = \pm 0.2 \text{ m}$ and $y = \pm 0.4 \text{ m}$, a region where the dipole has the best agreement with the experiments.



(a) 5th harmonic of the propeller set at RPM₃ and $d_{\text{object}}=0.4$ m. (b) 4th harmonic of the propeller set at RPM₃ and $d_{\text{object}}=0.53$ m.

Figure 4.26: Experimental values of noise shielding along the y axis of the microphone array plotted against predictions using different noise source directivity [45].

4.4. Conclusions

This chapter compared predictions of noise shielding with experimental values. It was observed that the creeping rays influenced the values of noise shielding at the receivers, even for edges with a small curvature, such as the wing used in the considered set of experiments. This difference was corroborated by beamforming plots, which showed distinct noise diffraction behaviour around the edges when considering the flat plate or the wing as the obstacle.

The agreement between predictions and measurements of noise shielded by the wing improved significantly when the creeping rays were taken into consideration. Also the predicted and experimental beamforming plots became more similar.

The experimental results of noise shielding of the propeller differ greatly from the results obtained for the omni-directional source. Significant values of noise shielding are found when the propeller is under a constant incoming flow. However, such values are low when compared with the omni-directional source. Also, sound at the frequencies of the harmonics is more shielded than broadband noise.

Different types of noise source models were used in the predictions of noise shielding of the propeller: monopole, dipole, and a multi-source composed of monopoles. The dipole showed a good agreement with the experimental data, but both the monopole and the multi-sources greatly overestimated noise shielding.

Beamforming proved to be an important tool in analyzing noise shielding either by showing the diffraction on the edges of the obstacle or by detecting external noise sources.

5

Influence of noise shielding in low noise aircraft

Disruptive aircraft concepts such as the blended wing body or joined wing aircraft are expected to drastically decrease the noise impact around airports, but still require many years of research before they can be incorporated in an airline's fleet. Such designs are therefore unlikely to contribute to mid-term noise reduction goals. Tube and wing aircraft with over the wings engines are a more feasible option for the near future.

This work analyzes a low-noise version of the B747-400, in which the engines are placed above the wings in locations that maximize engine noise shielding. A multi-disciplinary procedure is used to calculate the aircraft and engine performance, the flight procedure and finally the noise impact. The noise impact is evaluated in terms of Sound Exposure Level during departure and approach.

The predictions of noise shielding use both approximations of a sharp and a curved leading edge to assess differences in the final noise impact and whether it is relevant to include the creeping rays considering the resulting increase of computational time.

This work has been published in *The Journal of Aircraft*, **57**, 6 (2020) [134].

5.1. Methodology

The premise behind the methodology used to obtain the low-noise version of the B747-400 is to reduce the noise impact on the ground by means of engine noise shielding and an adjustment of the flight procedure. This is expected to result in a reduction of the SEL along approach and departure over a wide area. Decreasing the fan noise contribution is considered as an effective approach to reduce engine noise [147, 148]. The noise shielding values are less significant for the low than the high frequency range, as experimentally observed in Section 4.3, and thus jet noise is not as efficiently shielded as fan noise. Therefore, in the low-noise aircraft analyzed in this work, the focus lies on shielding of forward and aft fan noise.

Any change to the aircraft can affect the aerodynamics and flight performance and has to be thoroughly considered. If the engine locations that maximize noise shielding have a negative influence on the flight performance, the resulting increase of drag or weight would require higher engine thrust and would possibly overshadow any benefits from shielding.

In addition, the levels of different noise sources can strongly vary for approach and landing, e.g. airframe noise can even dominate the overall aircraft noise during approach. Other noise sources than the engine are also taken into consideration in this analysis to assure realistic results.

Another important aspect to account for in the simulations is the typical distance between source and receiver during approach and departure associated with higher levels of community annoyance. These distances lie in a range between 500 and 2000 m, which means that frequency-dependant atmospheric propagation effects have a significant impact on the ground noise levels. It is not efficient to shield engine noise at frequencies that are strongly attenuated by the atmosphere and would have a low noise level at the receiver in any circumstance.

The noise assessment of a new aircraft design should be based on a multi-disciplinary process taking into account modifications to the vehicle design and the corresponding flight performance. An existing simulation framework of DLR and TU Braunschweig [147] was used to investigate and optimize the aircraft ground noise impact for approach and departure. These calculations were performed by DLR (see Section 5.5). The framework predicts the noise impact taking into account the aircraft and engine design [149, 150], a detailed flight simulation [151], the noise generated by each component [147] and the effect of engine noise shielding [44, 45]. The complete simulation process is illustrated in Figure 5.1, along with the input required for each tool and respective output. A brief explanation of each tool integrating this framework is given below.

The aircraft geometry was calculated using the *Preliminary Aircraft Design and Optimization (PrADO)* tool developed by TU Braunschweig [149]. This tool also calculates the total mass of the aircraft and its individual components, the vehicle aerodynamics and engine data. *PrADO* has a modular structure, which means that specific modules can be replaced by external numerical or experimental data. For this work, *PrADO* used an external engine performance map, calculated with the *Gas Turbine Laboratory (GTlab)* developed by the Institute of Propulsion Technology, DLR Cologne [150]. *GTlab* is a component based framework for turbo engines and

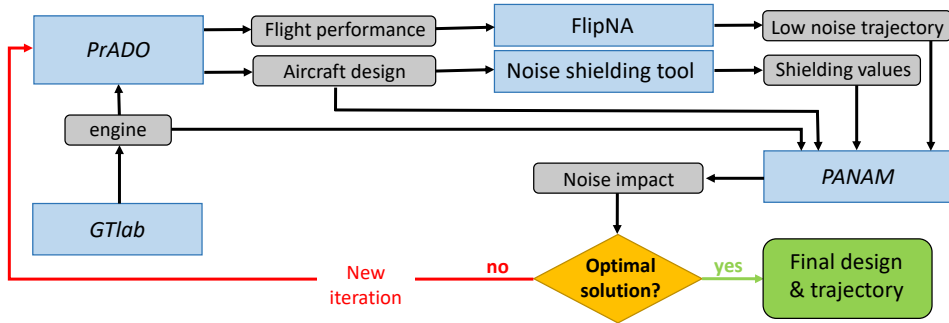


Figure 5.1: Computational framework used to evaluate the aircraft noise impact on ground.

gas turbine simulations that calculates the thermodynamics cycle for both design and off-design conditions. In addition to stationary operations, also basic transient operations can be simulated.

The flight trajectories were determined with the *Flightpaths for Noise Analysis* (FlipNA) using the aerodynamic parameters and mass of the aircraft calculated by *PrADO* and the engine performance determined by *GTlab*. A low-noise approach trajectory can be obtained by reducing the engine rotational speed and the aircraft velocity, two parameters that directly contribute to noise. Furthermore, the high lift devices and the landing gear are deployed as late as possible in order to reduce airframe noise.

The low-noise departure trajectory considers full engine power, with $N_1 = 105\%$, followed by cutback where engine speed is reduced to $N_1 = 100\%$, and this value is kept for acceleration and climb.

The noise shielding module, developed by TU Delft, uses the noise shielding method presented in Chapter 2. Fan noise is modeled as two monopoles, at the inlet and nozzle of the engine. This approach can be considered more accurate than considering a single noise source centered at the fan disk center [152]. The leading edge is modelled both as a sharp and a curved edge. Due to the large dimension of the wingspan in relation to the airfoil thickness, the wing is commonly approximated as a flat plate. This is an acceptable approximation when the radius of the curvature of the leading edge is small compared with the wavelength, but for high frequencies, the effect of the curvature affects the noise shielding values [91]. Chapter 3 and Chapter 4 showed that the creeping rays affect the noise shielding results even when the curved edge has a small radius. Nevertheless, it is difficult to predict what are the differences between those two modeling approaches of the leading edge in terms of aircraft noise impact without using the complete framework of Figure 5.1.

The noise shielding values are calculated for half-spheres centered at the noise source, with a discretization of 2° , as shown in Figure 5.2. Therefore, noise shielding

values are available for any azimuth and polar position of the observers relative to the noise source and can be directly subtracted from the values of fan noise. The half-spheres are calculated for half of the aircraft and then mirrored in order to save computational time.

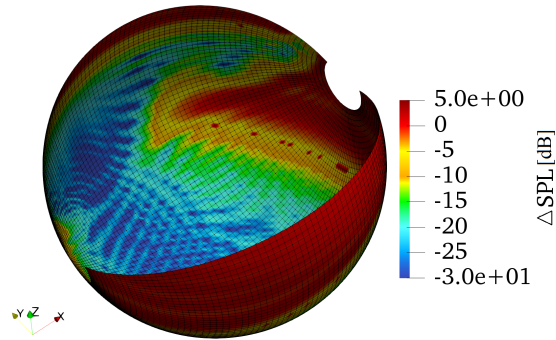


Figure 5.2: Half-spheres of noise shielding values for the frequency of 1000 Hz, with a discretization of 2° in the polar and azimuth directions.

The noise assessment was determined by the tool *Parametric Aircraft Noise Analysis Module* (PANAM). As the name indicates, it is a parametric noise prediction model that assesses the aircraft noise emission and the resultant impact on the ground. PANAM requires as input the aircraft geometry, trajectory, noise shielding values, engine deck and the observer positions. In the simulation process all engines were considered to run at the same operating point and consequently present equal noise emission. PANAM uses standard noise metrics, such as the SEL, to assess the noise impact.

The five computational tools mentioned above were integrated in an iterative process used to find the aircraft final design, approach and departure trajectories and the resulting noise impact.

5.2. Reference vehicle

The low-noise concept analyzed in this research is a variation of the B747-400 (B744). The engines were relocated above the wings in order to minimize the noise impact on ground through shielding of engine noise by the wings and fuselage. The original B744 and its low-noise version, here denominated B744_{eow} (B747-400 engines over the wings), are shown in Figure 5.3. The engines of Figure 5.3b are in a random position, as the engine locations that maximize noise shielding are determined in the next section.

The B744_{eow} presents higher values of drag than the B744, due to the new engine locations above the wings, which originate stronger wave drag. This increase of drag has consequences in the flight performance, increasing the fuel consumption and therefore leads to an excessive value of maximum take-off weight for

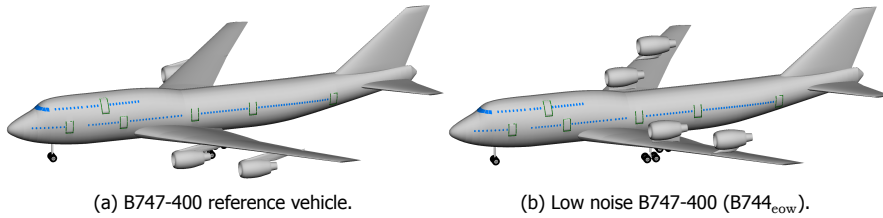


Figure 5.3: B747-400 and its low-noise version.

this design. To overcome this problem, the range of the B744_{eow} was reduced to 8100 km, whereas the original B744 has a design range of 10 600 km.

However, the noise impact of the two B744 versions is not comparable with this adjustment of the range. Another variation of the B744, denominated B744_{TR} (B744 reduced range), is calculated with *PrADO* for the comparison. The payload range chart of the B744_{eow} and B744_{TR} is shown in Figure 5.4. The range of the aircraft is not exactly the same, despite que range modification. The cruise speed was decreased from Mach 0.85 for the B744_{TR} to 0.70 for the B744_{eow} due to the drag increase. The lower cruise speed of the B744_{eow} however, is not sufficient to level the fuel consumption of the two aircraft, with an increase of 18 % for the B744_{eow} relative to the B744_{TR}.

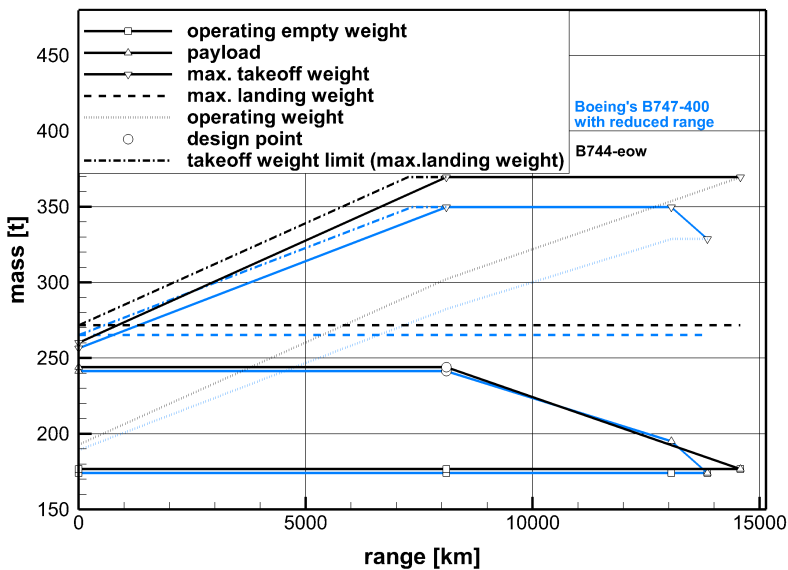


Figure 5.4: Payload range chart for the new reference vehicle B744_{TR} and its low-noise version, B744_{eow}.

Table 5.1 summarizes the design differences between the B744_{TR} and the B744_{eow}. The geometry of the B744_{TR} is the same as the original B744, but the wings of B744_{eow} needed to be slightly modified due to changes in aerodynamics. From this point forward, the B744_{TR} is the only reference vehicle considered for the comparison with the B744_{eow}.

Table 5.1: Differences in the characteristics of the B744_{TR} and B744_{eow}.

	A_{wing} [m^2]	λ_F [-]	MTOW [ton]	M_{cruise} [-]	Cruise Fuel [ton]	$E_{cruise,beg}$ [-]	Λ [deg]
B744 _{TR}	562	7.18	350	0.85	108	17.5	38.6
B744 _{eow}	580	8.00	369	0.70	125	17.0	38.9

The approach and departure trajectories for the B744_{TR} determined using the methodology presented in Section 5.1 are shown in Figure 5.5. The low-noise approach trajectory (Figure 5.5a) shows a first descent section with -2.7° , identified as segment 1 in the plot, with the engine speed set to idle and the aircraft flying at 1.3 times the stall speed. The high lift devices are deployed at point 2 to avoid acceleration and the aircraft descends with -3° . The landing gear is deployed at point 3, and the flaps are fully set. The stabilization point is reached at 300 m and the velocity and trajectory slope are kept constant. The thrust is increased to compensate the drag originated by the high lift devices and the landing gear.

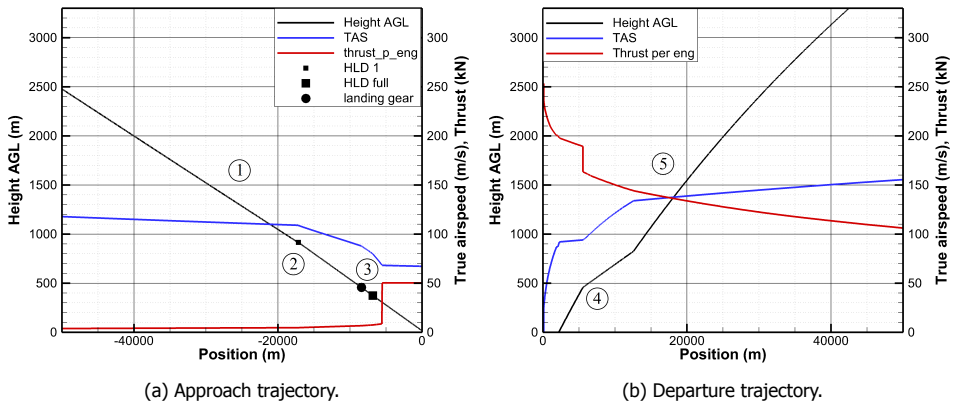


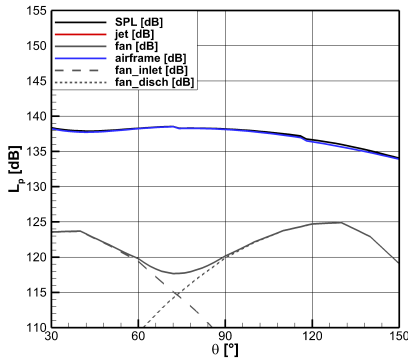
Figure 5.5: Approach and departure trajectories of the B744_{TR}.

The departure trajectory, shown in Figure 5.5b, is conducted with full thrust up to the cutback point, identified as point 4, and continues with a cutback rotational speed of $N_{1,c,b} = 100\%$. Once the airspeed reaches 130 m/s the aircraft gains

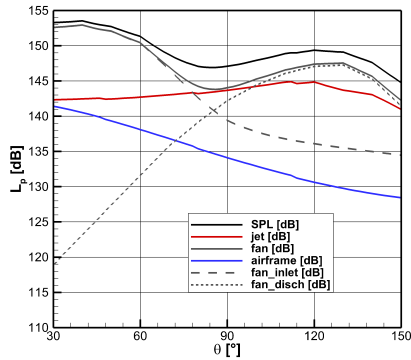
altitude on segment 5 up to cruise altitude.

The noise emission of the B744_{TR} during approach and departure was analyzed by selecting points of the trajectories that are relevant to annoyance on ground, i.e., when the aircraft is outside the airport limits but still at a low altitude. The trajectory point selected for approach was 15 km before the approach threshold. In this approach phase the aircraft altitude is 800 m, the velocity is 103 m/s, the engine is in idle at $N_1 = 35\%$ and the flaps set to 20° . The noise emission resultant from this approach point, shown in Figure 5.6a, clearly indicates that airframe is the dominant noise source for all polar directions. Fan forward and fan aft noise are, respectively, 17 dB and 10 dB below airframe noise.

The point selected from the departure trajectory was 12.5 km after break release: the aircraft is at an altitude of 820 m, its velocity is 133 m/s, $N_1 = 100\%$ and the high lift devices are not deployed. The noise emission plot for the referred departure point is shown in Figure 5.6b, and in contrast to the what was observed for approach, fan noise is now dominant. This indicates that noise emission can be significantly reduced during departure by fan noise shielding, but the effect will be negligible for approach.



(a) Noise emission of select approach point.



(b) Noise emission of select departure point.

Figure 5.6: Overall sound level for the B744_{TR} for the approach and departure conditions selected.

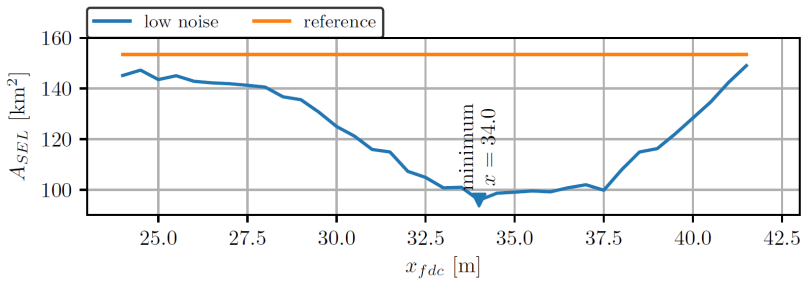
5.3. Noise assessment of the low noise aircraft

This section compares the noise impact of the B744_{TR} with the B744_{cow} for approach and departure. First, the positions of the inboard and outboard engines of the B744_{cow} were determined with the objective of maximizing noise shielding. Then the approach and departure trajectories were recalculated taking into account the new engine positions, and the noise emission was evaluated for one operating point of those trajectories. Finally, the noise impact on ground was determined and compared for the two aircraft using both sharp and curved leading edge approximations to assess the influence of the creeping rays on this low-noise design.

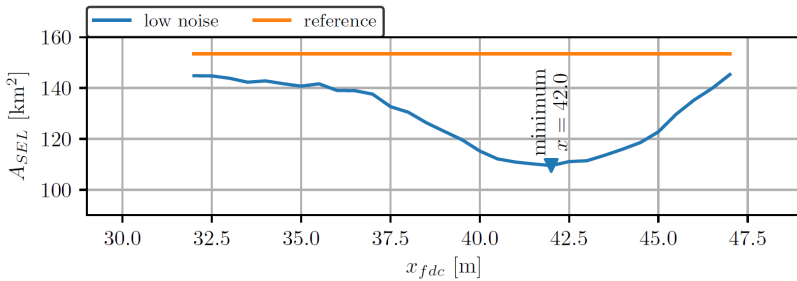
5.3.1. Optimal engine position

The engine positions that maximize noise shielding were determined individually for the inboard and outboard engines. The engine positions in the span direction are kept fixed (the same as in the B744_{TR}) and are only modified in the chord direction. The criterion used to determine the engine positions that maximize noise shielding was the 80 dB SEL contour area for departure, which is assessed for different positions of the engine relative to the nose of the aircraft (x_{fdc}).

Figure 5.7 shows the contour area of 80 dB SEL for different inboard and outboard engine positions along the chord, considering a sharp leading edge in the noise shielding predictions. The engine positions were investigated in discrete steps of 0.5 m. The orange line shows the area of the 80 dB SEL contour of the B744_{TR}, which remains constant for all x_{fdc} positions because it is not shielded.



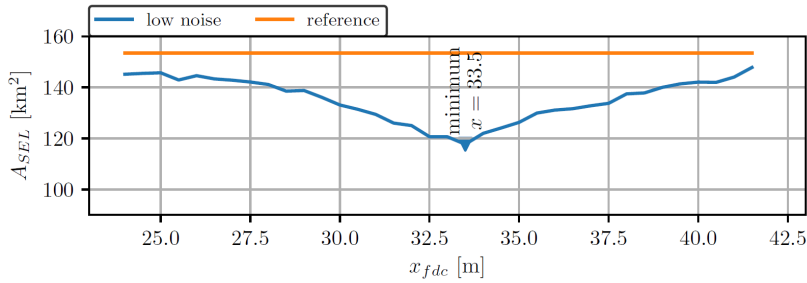
(a) Inboard engine.



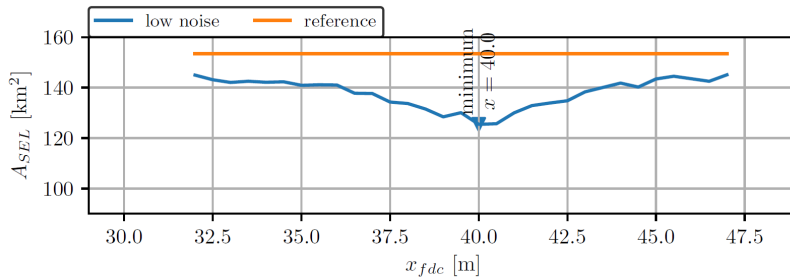
(b) Outboard engine.

Figure 5.7: SEL isocountour area of 80 dB for departure, plotted for difference values of x_{fdc} considering a sharp leading edge in the noise shielding prediction.

The same plots are shown in Figure 5.8 considering a curved leading edge in the noise shielding predictions. Figure 5.7a and Figure 5.8a indicate that the most promising position of the inboard engines is 34 m relative to the aircraft nose for a sharp leading edge, and 33.5 m for a curved leading edge. For the outboard engine, the optimal position is 42 m for a sharp leading edge and 40 m for a curved leading edge. A SEL area change of 20 % can be associated with a source noise reduction of approximately 1 dBA [153].



(a) Inboard engine.



(b) Outboard engine.

Figure 5.8: SEL isocountour area of 80 dB for departure, plotted for difference values of x_{fdc} considering a curved leading edge in the noise shielding predictions.

Figure 5.9 shows the optimal inboard and outboard engines position in the chord, for both cases of a sharp and a curved leading edge. The dimensions of the airfoil section are at scale, as well as the positions of the fan inlet and exhaust in the chord direction. The fan disk center is represented by a black cross and the fan inlet and exhaust by dots (blue for the position found considering a sharp leading edge, and black for a curved leading edge). The distance of the engine relative to the surface of the wing changes along the chord direction, which is also accounted for in this scheme.

The more the engine is centered on the wing chord, the larger is the region of observers in the shadow zone. The optimal engine positions take advantage of that in order to maximize noise shielding. The optimal engine positions considering creeping rays are slightly upstream compared to the optimal positions determined for a sharp leading edge: 0.5 m for the inboard engines and 2 m for the outboard engines. This is in agreement with experimental results of noise shielding for a NACA 0012 airfoil [154, 155]. These experiments consistently showed that a noise source located at the airfoil leading edge presented higher values of shielding than when located at the trailing edge.

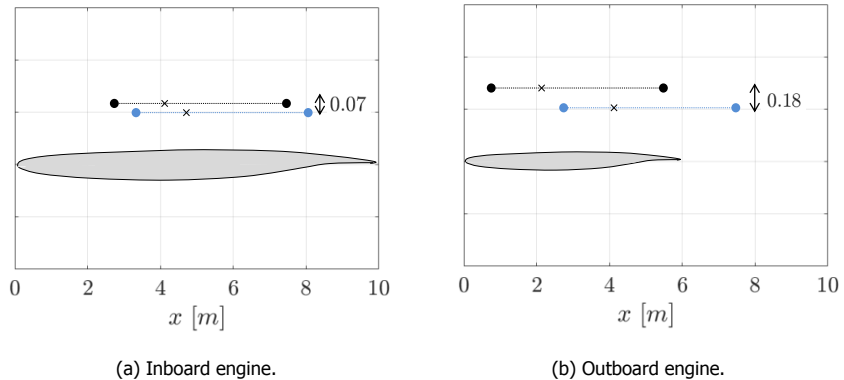


Figure 5.9: Position of the inboard and outboard engines in the chord. The engine inlet and exhaust positions are indicated in blue and black, for the sharp and curved leading edge approximations, respectively.

5.3.2. Noise impact for departure

The departure trajectory of the B744_{cow} is slightly different from the B744_{tr} due to the design differences of the two aircraft. The B744_{tr} has a better performance, because the B744_{cow} presents an increased weight due to the larger wing. The departure trajectories for the two aircraft are shown in Figure 5.10.

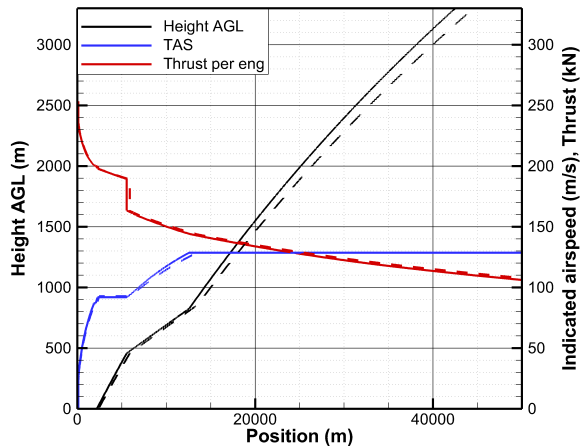


Figure 5.10: Low-noise departure trajectories for the B744_{tr} (solid lines) and the B744_{cow} (dashed lines).

The noise emission of the B744_{cow} for a representative point of the departure trajectory (equivalent to the operating point selected in Figure 5.6) is shown in Figure 5.11. The aircraft is at an altitude of 800 m, the aircraft speed is 130 m/s, $N_1 = 100\%$ and no high lift devices are deployed. The noise emission depends on

the values of noise shielding which results in two different plots, Figure 5.11a and Figure 5.11b, for predictions with a sharp and curved leading edge, respectively. The noise emission of the reference aircraft B744_{TR} is also shown in the plots, represented by a dashed black line.

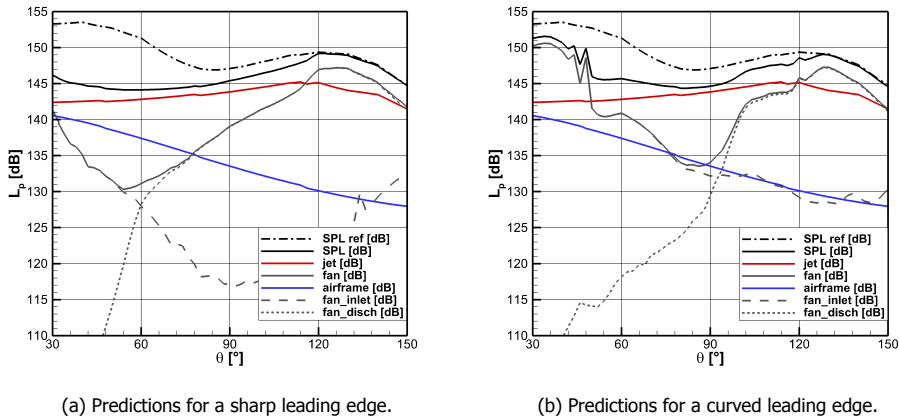


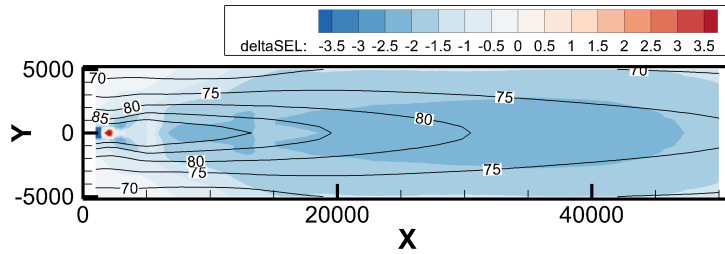
Figure 5.11: Overall sound emission of the B744_{eow} for the departure condition selected.

The difference between the total noise emission of the B744_{eow} and the reference aircraft is larger in Figure 5.11a than in Figure 5.11b, i.e., when considering a sharp leading edge. The forward and aft fan noise are also represented in the plots, showing that the forward fan noise has higher values of shielding for the sharp leading edge simulation, whereas aft fan noise presents higher values of shielding for the curved leading edge case.

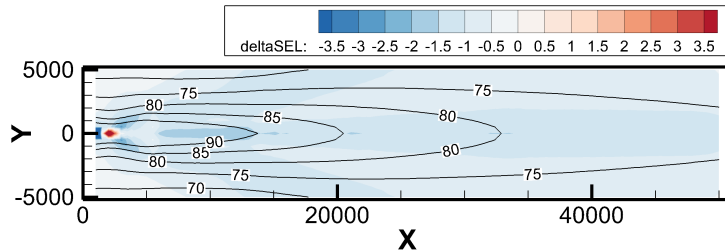
Due to the fan noise reduction, jet noise has a very relevant contribution to the total noise of the B744_{eow}, in contrast to what was observed for the B744_{TR}, in which fan noise was dominant (see Figure 5.6b).

The SEL contour areas were used to assess the ground noise impact: Figure 5.12 shows the values of SEL of the B744_{eow} relative to the B744_{TR}, i.e., negative values indicate that the B744_{eow} has lower SEL than the B744_{TR} and consequently lower noise impact. Again, predictions are presented separately for the case of a sharp and curved leading edge.

The noise reduction on ground is higher considering a sharp than a curved leading edge, for a large area of the contour. The difference becomes noticeable about 7 km behind the break release, where the engine speed is reduced to cutback rotational speed, thus jet noise is decreased and fan noise dominates. The maximum reduction in SEL was -2 dB for predictions with a sharp edge and -1.5 dB considering a curved edge. The red dots in the plots are related with the higher MTOW of the B744_{eow} which implies a longer take-off distance.



(a) SEL contour area considering a sharp leading edge in the shielding predictions.



(b) SEL contour area considering a curved leading edge in the shielding predictions.

Figure 5.12: SEL values for departure of the B744_{TR} (lines) and Δ SEL values of the B744_{eow} relative to the B744_{TR}.

5.3.3. Noise impact for landing

Similarly to what was observed for departure, also the approach trajectory of the B744_{eow} is slightly different from the B744_{TR}, as shown in Figure 5.13. The approach operating point selected for the noise assessment of the B744_{eow} is located 15 km before approach threshold (same as for the B744_{TR}). At this point of the approach trajectory the altitude of the aircraft is 800 m, the velocity 98 m/s, $N_1 = 35\%$, the position flaps are set to 15° and the Kruger flaps are set.

The noise emission of the B744_{eow} is shown in Figure 5.14, considering the two approximations of the leading edge. The total noise emission of the reference aircraft is also represented in the plots by a dashed black line. Airframe noise is dominant and fan noise does not play an important role in the total noise. Despite the reduction of fan noise due to shielding, it has no impact on the total noise. The slight noise reduction of the B744_{eow} relative to the B744_{TR} is due to the lower flight speed.

Figure 5.15 shows the ground noise impact of the B744_{eow} relative to the B744_{TR} for predictions considering both a sharp and curved leading edge. As expected, the two plots are very similar, because the fan has a negligible contribution to the total noise and therefore the role of noise shielding is not significant.

Away from touchdown, the engine is idle and the SEL reduction is attributed to the decrease in airspeed along the B744_{eow} trajectory. After the deployment of the landing gear, at approximately 6 km before touchdown the engines are spooled up

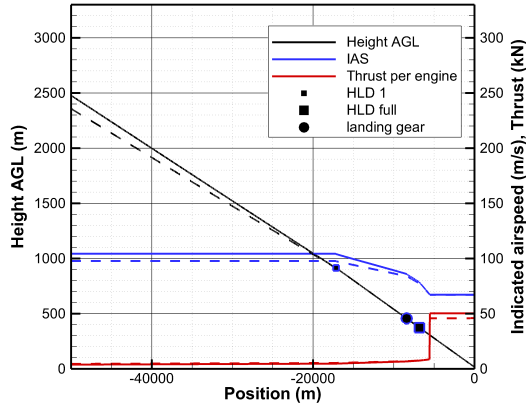
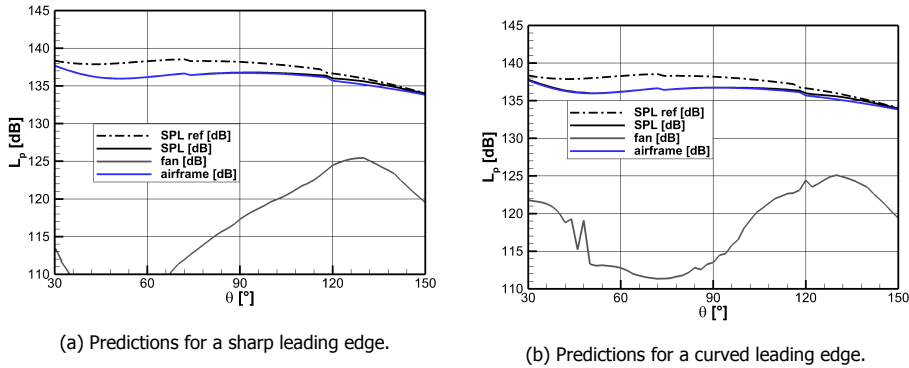


Figure 5.13: Low-noise approach trajectories for the B744_{RT} (solid lines) and the B744_{cow} (dashed lines).



(a) Predictions for a sharp leading edge.

(b) Predictions for a curved leading edge.

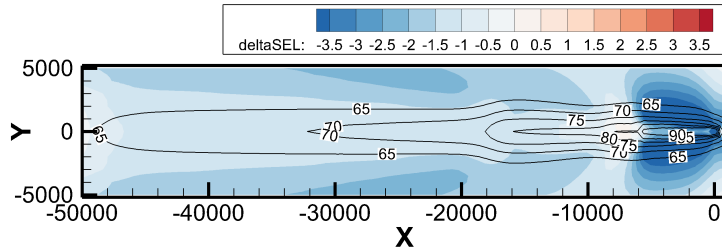
Figure 5.14: Overall sound emission of the B744_{cow} for the approach condition selected.

to compensate the drag and the fan noise becomes significant compared to airframe noise, originating a SEL reduction in both Figure 5.15a and Figure 5.15.

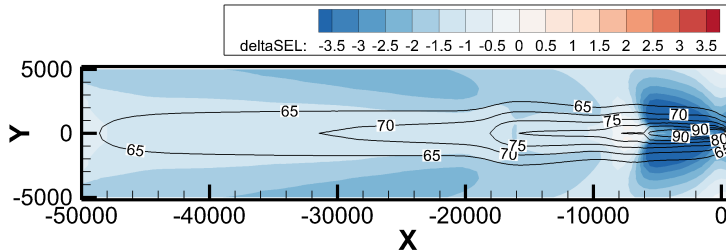
5.4. Discussion

Noise shielding can be calculated with different levels of detail and in this research work the leading edge was modelled both as a sharp and a curved edge. The shape of the leading edge influences the engine locations that maximize the shielding of fan noise and therefore has an impact on the aircraft design, performance and resulting ground noise impact.

This research was conducted with the premise of investigating the influence of the creeping rays on the design process and resulting ground noise impact using a multi-disciplinary computational framework that generates a final realistic aircraft



(a) SEL contour area considering a sharp leading edge in the shielding predictions.



(b) SEL contour area considering a curved leading edge in the shielding predictions.

Figure 5.15: SEL values for approach of the B744_{tr} (lines) and Δ SEL values of the B744_{ew} relative to the B744_{tr}.

design and flight trajectories. The adopted study case was an ongoing DLR research project, a low-noise variant of the B744 with the engines located over the wings.

The engine positions that maximize the shielding of fan noise were determined based on the area on ground with a SEL of 80 dB during departure. This is a more complex and adequate criteria than, for example, focusing on the highest values of shielding for a range of frequencies of interest (as the first harmonics of the fan), without taking into account the propagation effects on the atmosphere. Reducing the area of 80 dB SEL decreases the number of people highly annoyed in the proximity of the airport.

Relocating the engines over the wings changed the vehicle aerodynamics and performance, and the geometry of the B744_{ew} was slightly adapted (wing area and taper ratio) as well as the operational conditions (lower cruise speed and higher fuel consumption). The payload range chart had to be adjusted, as well as the departure and approach trajectories used to determine the ground noise impact. Not considering these modifications would lead to an unrealistic comparison between the B744 and its low noise version.

The optimal engine locations are different for noise predictions considering a sharp and a curved leading edge. The optimal positions of the engines are closer to the leading edge when it is modelled as curved in the predictions: the inboard engines are 0.5 m closer to the leading edge and the outboard engine 2 m, compared with the optimal positions found for the sharp leading edge approximation. This is

in agreement with experimental data found in the literature. In addition, the fan disk center is approximately centered in the chord in order to maximize the number of receiver positions in the deep shadow zone.

Fan noise is effectively shielded during departure, and the SEL values obtained for the B744_{eow} are lower than for the B744_{tr}, both considering a sharp and curved leading edge in the predictions. With the reduction of fan noise, the jet noise contribution gains importance and dominates the noise emission. For that reason the SEL could not be further decreased than 2 dB, considering a sharp leading edge, and 1.5 dB for the curved leading edge case.

For approach, the fan is not the dominant noise source and shielding has a minimum effect on the SEL contour. The value of SEL is only reduced comparatively to the reference vehicle at the final phase, when the engines are spooled up to compensate the drag. The slight decrease in SEL for the B744_{eow} compared with the reference aircraft during the entire approach trajectory is due to the reduced airspeed, not noise shielding.

This case study shows how the leading edge is modeled influences the aircraft design and noise impact. Therefore it is recommended to account for the creeping rays in aircraft with large wings and BWB configurations. For small wing areas and af-mounted engines, such as the case of the Fokker 70 analysed in Chapter 3, the effect of creeping rays is expected to be negligible.

In addition, any design change has to be carefully analyzed as it influences the aircraft performance and the final noise impact, and the shielding of fan noise is only beneficial up to the point other noise sources such as airframe and jet noise assume importance.

5.5. Acknowledgment

The author specifically acknowledges the contribution to this chapter of Mr. Marc Koch from DLR Göttingen. His contribution is comprised of: low-noise aircraft concepts and overall aircraft design (PrADO Software), engine simulation (DLR GTlab), flight simulation (DLR FlipNA), and overall aircraft noise results (DLR PANAM). All of these simulations have been performed at DLR Göttingen.

6

Sound Quality Metrics of aircraft under operating conditions

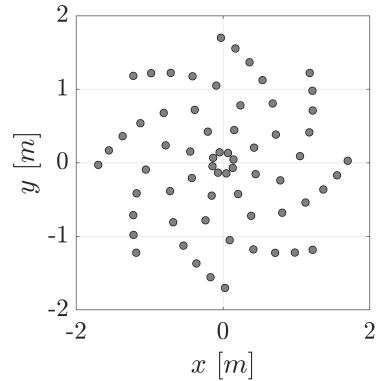
The sound quality metrics give information about the characteristics of a sound, such as the frequency content and the prominence of tones, unlike traditional noise metrics that only provide a final value of annoyance. In this chapter, the five sound quality metrics, loudness, tonality, sharpness, roughness and fluctuation strength are applied to aircraft noise. The analysis includes different aircraft types during landing and take-off. The influence of the aircraft design, propulsion system and operating conditions on the sound quality metrics is analyzed.

6.1. Experimental Setup

The experimental campaign took place at Amsterdam Schiphol Airport for four days with similar weather conditions. The meteorological data was provided by the Royal Netherlands Meteorological Institute. The measurement system (see Figure 6.1a) consists of an acoustic array of 64 microphones distributed in an underbrink spiral configuration [157] with 8 arms, as shown in Figure 6.1b. This acoustic array is an improved version of the array used in the measurements of Chapter 3.



(a) Acoustic array.



(b) Underbrink spiral microphone distribution.

Figure 6.1: Acoustic array used in the experimental campaign.

The structure of the array is 4 by 4 meters and it is covered with absorbent foam to reduce reflections. In addition, the outer microphones are at a distance of 30 cm from the edges of the array to reduce the influence of ground reflection on the measurements. All the microphones were covered with wind shields and were calibrated with a piston phone. The microphone model is the PUI AUDIO 665-POM-2735P-R from PUI Audio.

A camera is placed at the center of the array to determine the overhead time and to localize the main acoustic noise sources using beamforming. Images from the camera can be overlapped with beamforming plots, allowing the localization of the noise sources on the aircraft. Consecutive frames of the camera can also be used to estimate the height and velocity of the aircraft. The camera is a Datavision UI-1220LE model with lens Kowa LM4NCL and a frame rate of 30 Hz.

The microphones are connected to the Data Acquisition System that records the analog signals and converts them to digital signals at a sampling frequency of 50 kHz. The velocity and height of the aircraft were obtained using an ADS-B system connected to the laptop. Not all aircraft have this system on board, and in those cases the aircraft type was checked with online live flight trackers and the velocity and altitude were estimated with consecutive frames of the camera.

The acoustic array was placed close to location 18C of the Schiphol airport runways, represented in Figure 6.2. This location was chosen because of its proximity to the runway (670 m) and considerable distance from main roads, so car traffic

would not contaminate the results.



Figure 6.2: Runways of Schiphol airport, and the runway selected for the measurements (in a red circle).

The experimental campaign resulted in 141 landing measurements of 14 aircraft types, and 160 take-off measurements of 12 aircraft types. Table 6.1 shows the aircraft types recorded, ordered by their value of Maximum Take-Off Weight (MTOW), and the corresponding number of landing and take-off measurements.

Table 6.1: Landing and take-off flyovers recorded in Schiphol Airport.

Aircraft	N ^o of landings	N ^o of take-off	Aircraft	N ^o of landings	N ^o of take-off
CRJ-700	0	5	A320	13	19
CRJ-900	2	0	B737-800	41	53
ERJ-175	14	22	B737-900	4	4
F70	7	0	A321	3	5
AVRO-RJ85	3	0	A330-200	0	5
ERJ-190	22	15	B787	6	0
ERJ-195	0	4	B777-200	5	0
B737-700	15	15	B777-300	3	5
A319	3	8	Total	141	160

The models Boeing 737-800 (B737-800), Airbus A320 (A320), Embraer 190 and

195 (ERJ-190 and ERJ-195, respectively) correspond to the highest number of measurements for landing and take-off. Some aircraft types are not available for both take-off and landing, for example, the Fokker 70 (F70) and the Boeing 787 (B787).

This data set contains aircraft with very different characteristics: small aircraft with capacity for less than 100 passengers, such as the Bombardier CRJ-900 and the ERJ-190, medium-range aircraft (the B737 and the A320 series) and long-range aircraft (B777 series). The data set only contains turbofan propelled aircraft, all of them twin-engine with the exception of the AVRO RJ-85, which has 4 engines. Two of the aircraft have rear-mounted engines, the F70 and the AVRO RJ-85, and therefore engine noise is partially shielded by the wings and fuselage.

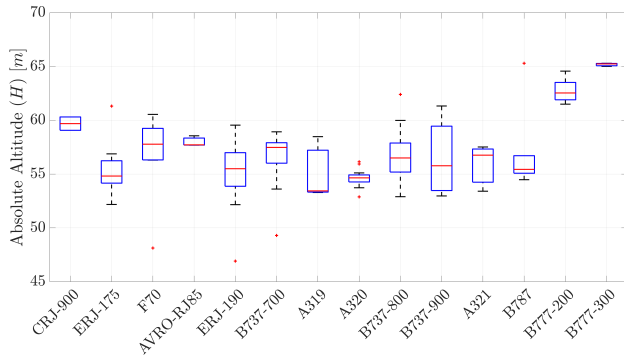
6.2. Experimental assessment of the Sound Quality metrics

The flight trajectories during landing are more regular than the ones of take-off, because all aircraft follow the Instrument Landing System (ILS). The flight trajectory and aircraft operating conditions influence the SQM measured on the ground and should be taken into account in this analysis. Figures 6.3 to 6.5 show the average and the variability of the absolute altitude (H), total ground speed (V_{Gr}) and speed of the low-pressure shaft of the fan (N_1) obtained from the spectrograms, estimated for all aircraft types, during landing and take-off. The aircraft types are presented in ascending order of their value of MTOW.

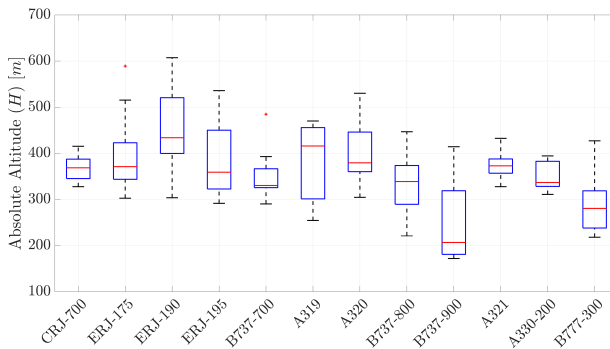
The distance between the aircraft and the microphone array is approximately ten times larger for the take-off measurements than for the landing. This difference has to be taken into consideration when analyzing the SQM, because atmospheric attenuation is distance-dependent. The variability of the height within aircraft type is also higher for the take-off measurements, which was expected, due to the more irregular flight trajectories compared with landing procedures.

The average ground speed measured for landing flyovers varies between 60-80 m/s whereas for take-off the values lie between 70-90 m/s. Values for N_1 were obtained from the spectrograms, i.e., derived from the acoustic measurements. The variability of N_1 is very significant for some aircraft during landing (e.g. the B787 and the A321), with most aircraft presenting an average value between 50-65%. The values of N_1 show less variability within the same aircraft type for take-off flyovers than for landing, with the exception of a few flyovers that show extremely low values of N_1 for take-off.

Similar plots are presented for the SQM in Figures 6.6 to 6.9. Figure 6.6 shows that loudness increases with the dimension of the aircraft, as expected, as larger surfaces generate higher levels of airframe noise, but also require more powerful engines and consequently generate higher levels of engine noise. The variability of loudness is small for landing aircraft but very significant during take-off. During landing, fan noise and airframe noise (specially landing gear noise and flap noise) have approximately the same importance. The airframe noise contribution is roughly constant because it mostly depends on the aircraft structure, flap deflection and velocity. In addition, the landing measurements were recorded with



(a) Landing.



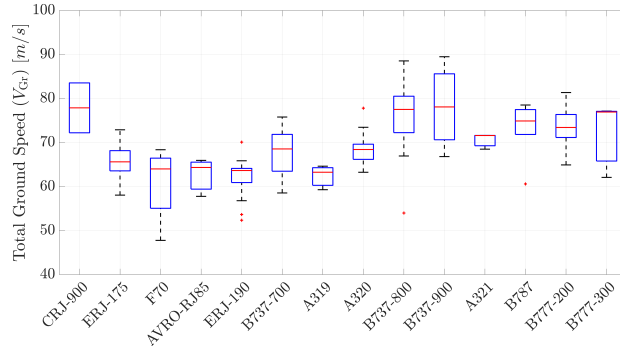
(b) Take-off.

Figure 6.3: Aircraft height for landing and take-off flyovers.

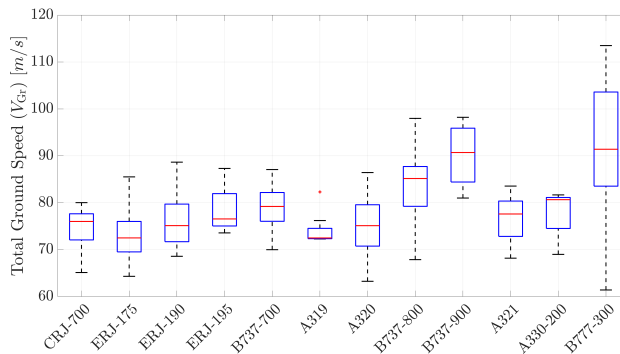
the aircraft at very similar altitudes. Both explain the low variability of loudness for landing aircraft. The two aircraft with the lowest values of loudness are the F70 and the AVRO-RJ85, for which engine noise is partially shielded by the airframe.

For the take-off measurements, however, the engines are the most important noise source, and a variation of the engine settings is reflected in the total noise. Also, the trajectories for take-off are more irregular, and these two factors result in a high variability of loudness. The average values of loudness are higher for landing than for take-off, which is contrary to what one would expect. However, the aircraft were at a higher altitude for the take-off measurements, and therefore they were perceived as less loud.

The tonality plots of Figure 6.7 show approximately the same average values for landing and take-off. The A319 and A320 stand out for their high values of tonality compared to aircraft of similar size, for instance the B737-700 and 800. Prominent tones were expected for landing due to the high contribution of fan noise, which generate strong tones at frequencies between 1000-2000 Hz. During take-off the engines are at the maximum performance and the Blade Passage Frequency (BPF) is higher than during landing, as well as its harmonics, which increases tonality.



(a) Landing.



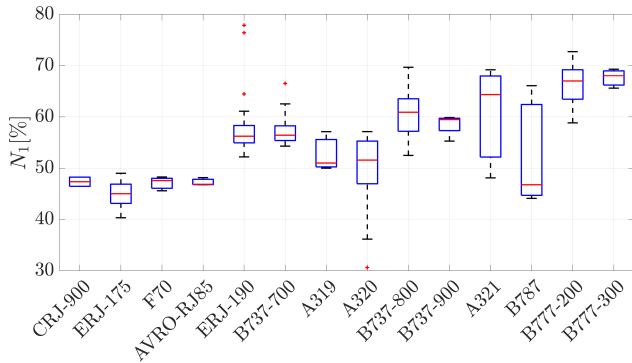
(b) Take-off.

Figure 6.4: Aircraft velocity for landing and take-off flyovers.

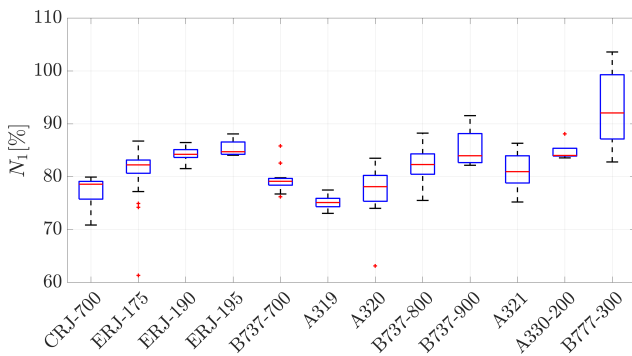
However, tones can be masked by the low frequency noise generated by the jet. In addition, tones at high frequencies are strongly attenuated by the atmosphere. Modern engines have higher values of bypass ratio (BPR) to decrease the velocity of the jet, and consequently jet noise. The BPR of the engines of the A319 and A320 is higher than 6. All the other aircraft recorded during take-off are equipped with engines with lower BPR, between 5-5.5 (except the B777-300 which is a long-range aircraft), which justifies the high value of tonality of the A319 and A320. The similar values of tonality for landing and take-off will be later investigated using spectrograms and the signal spectra.

Also the values of roughness, shown in Figure 6.8, are similar for take-off and landing. Take-off aircraft are expected to generate rougher sounds than landing, because of buzz-saw noise. Buzz-saw noise is generated when the fan tips operate at supersonic speed, generating weak shock waves spiraling upstream against the mean flow [158, 159]. This behaviour generates periodic noise, denominated buzz-saw noise tones (BSN), which decreases with frequency. Irregularities in the mean flow and spacing of shock waves make this phenomenon difficult to predict.

During landing, low-frequency noise is associated with airframe noise, which



(a) Landing.



(b) Take-off.

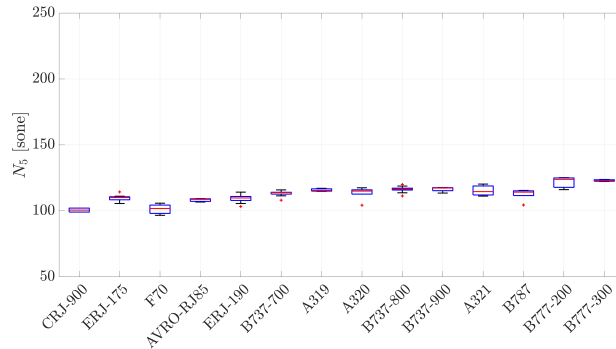
Figure 6.5: N_1 for landing and take-off flyovers.

is more dominant during this flight phase than for take-off. The increase of this metric with the MTOW values also indicates a relation with the dimensions of the aircraft. The similarity in roughness during take-off and landing will be explored further ahead in this research work.

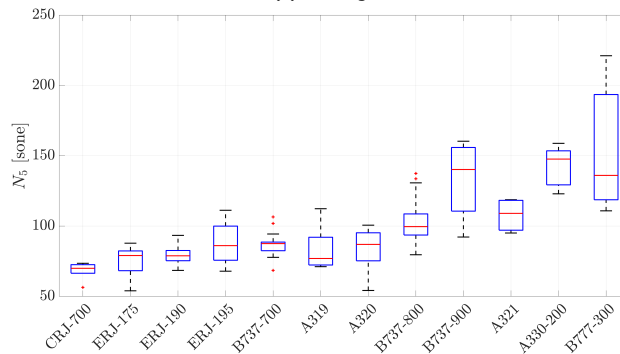
Finally, Figure 6.9 shows the values of sharpness and its variability for each aircraft type. The values are noticeable higher for landing. The sharpness values for take-off are low because jet noise masks the harmonics of fan noise. In addition, the first harmonics of fan noise, of higher frequency for take-off than for landing, are strongly attenuated by the atmosphere. The AVRO-RJ85 shows the highest value of sharpness because it is the only four-engined aircraft of the data set.

Figure 6.10 shows the spectrogram of an A320 take-off flyover, and the spectrum at overhead time. This A320 aircraft is equipped with CFM56-5A engines with 36 fan blades. The BPF of the fan and its second harmonic are clearly visible in the spectrum at 2650 Hz and 5300 Hz, respectively. Other peaks appear at lower frequencies, the buzz-saw noise tones, spaced at 74 Hz. Only the most prominent BSN tones are identified in Figure 6.10 for an easy reading.

The spectrogram and the spectrum at the overhead time for a A320 landing



(a) Landing.



(b) Take-off.

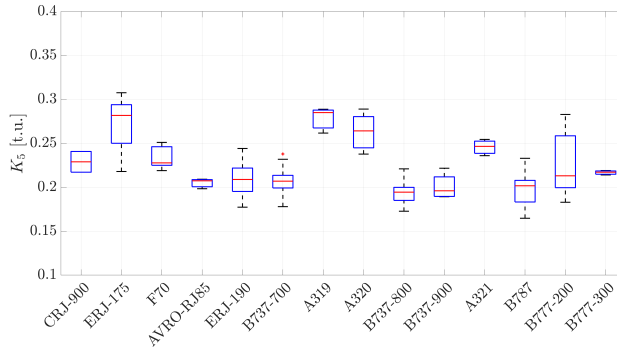
Figure 6.6: Loudness for landing and take-off flyovers.

flyover are shown in Figure 6.11. The BPF value is lower than for take-off, due to the lower rotational velocity of the fan. The first four harmonics of the fan are very clear and with a high SPL value. The spectrum of Figure 6.11b has more high frequency content than the take-off spectrum of Figure 6.10b. The aircraft altitude is lower at landing, therefore the noise is less attenuated by the atmosphere. This explains the higher values of sharpness found for landing, as mentioned before.

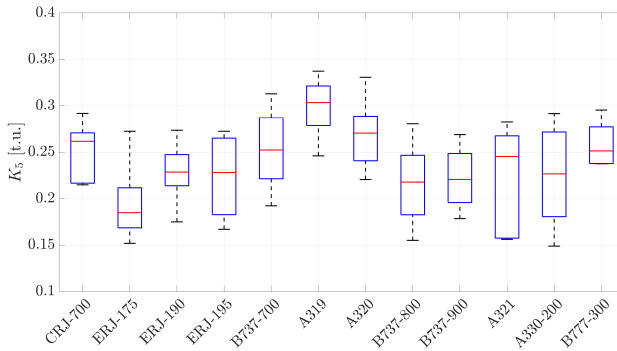
The roughness values for landing and take-off measurements are similar, and in this case we can see that the low frequency content has approximately the same SPL value for landing and take-off. Even though take-off presents buzz-saw noise, the BSN tones are not very prominent, and during landing the strong presence of low frequency airframe noise contributes to roughness, which results in similar values of this sound quality metric for these two flight phases.

The value of tonality is also identical for the landing and take-off measurements of the A320. Even though more harmonics of the fan are present during landing, take-off exhibits BSN tones and two prominent first harmonics of the fan, which balances the value of tonality for the two flight phases.

The aircraft altitude has a direct effect on sharpness and tonality because the



(a) Landing.



(b) Take-off.

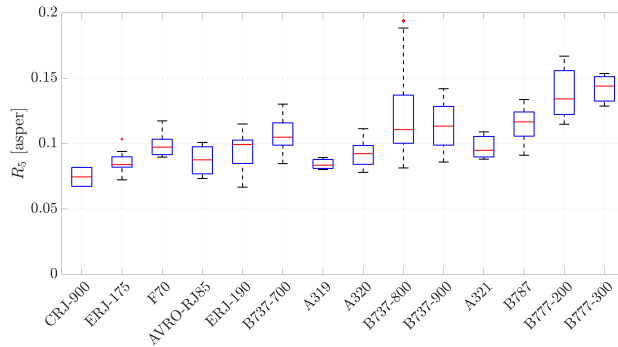
Figure 6.7: Tonality for landing and take-off flyovers.

high frequency content is attenuated by the atmosphere. High frequency noise is more relevant during take-off because of the high value of N_1 . However, the rate of climb for take-off is higher than the glide slope for landing, which means that for areas outside the airport, aircraft fly at higher altitudes for take-off, and thus high frequency content is strongly attenuated.

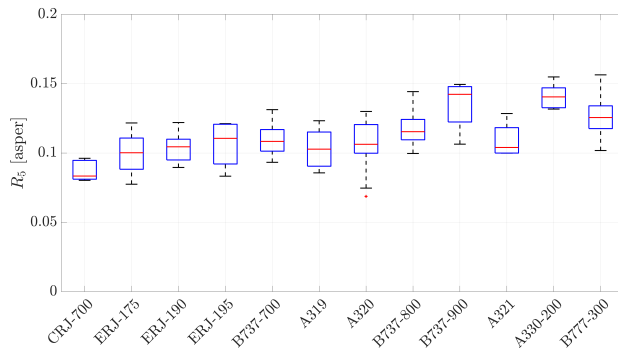
The analysis of this section shows that the SQM depend on the aircraft design, but also on the operating conditions. Neglecting the aircraft operating conditions could lead to erroneous assumptions when assessing community annoyance.

6.3. Correlation of the SQM with the aircraft design

This section investigates correlations between the SQM and characteristics of the aircraft design and the engine. Such correlations are determined separately for landing and take-off, using the average values of the SQM of each aircraft type. The best correlations are employed to find empirical expressions correlating the SQM and the aircraft design.



(a) Landing.

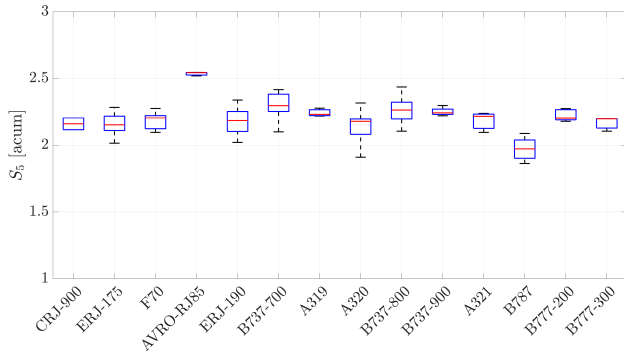


(b) Take-off.

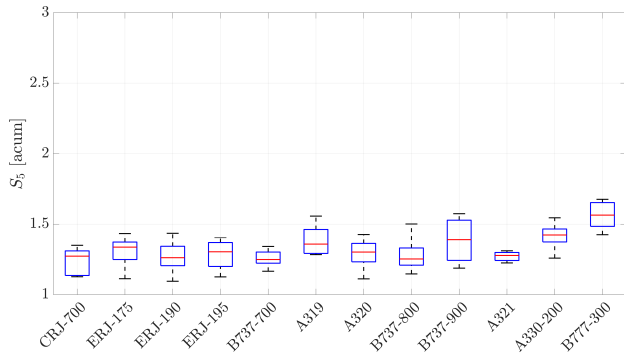
Figure 6.8: Roughness for landing and take-off flyovers.

A variety of aircraft characteristics was considered in this study. The airframe characteristics considered were the wingspan, total height and length of the aircraft, the cabin width, the MTOW, Maximum Landing Weight (MLW), the ratio flap/span of the wing, and the diameter and number of wheels in the main and nose landing gear (MLG and NLG). The engine parameters examined were the number of fan blades, the BPR, the diameter of the fan, the length of the nacelle, the maximum take-off thrust and the thrust-specific fuel consumption (TSFC).

For take-off, loudness showed a good correlation with the dimensions of the aircraft, e.g. the wing span and MTOW. Also characteristics related with the size of the engine, such as the fan diameter and maximum take-off thrust showed a significant correlation. This was expected, as the loudness of an aircraft is directly related with its dimension as seen in the previous section. Roughness also showed dependence on the aircraft dimensions, diameter of the fan and maximum take-off thrust. Sharpness, however, showed high correlations with the engine parameters such as BPR, diameter of the fan and length of the nacelle, which was expected as high frequency noise is mostly generated by the engine. No correlations were observed for tonality during take-off.



(a) Landing.



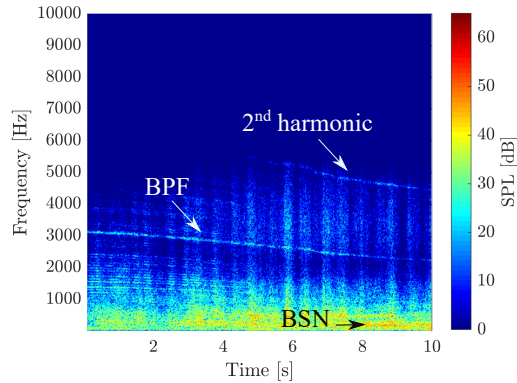
(b) Take-off.

Figure 6.9: Sharpness for landing and take-off flyovers.

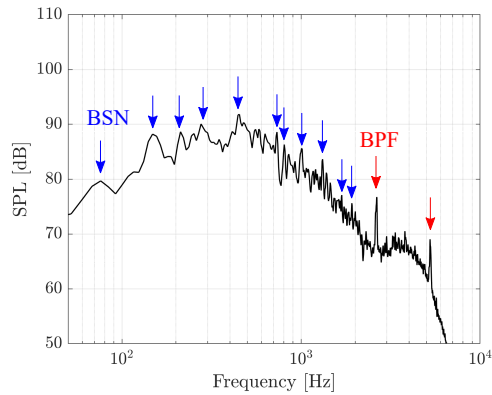
Landing, loudness and roughness presented correlations with the same parameters as take-off. However, loudness for landing also showed a high dependence on the landing gear configuration. Roughness presented high correlations with many parameters in common with take-off. Sharpness did not present any correlations and the same was observed for tonality, which was not expected due to the tonal components generated by the fan.

The aircraft characteristics showing the highest correlations with the experimental SQM values were combined in linear equations, and the coefficients were found using a multiple linear regression. These equations consider the average values of the SQM for each aircraft type, and no operational conditions were taken into consideration. Table 6.2 shows the correlation coefficients squared (R^2) and corresponding p -values obtained for the correlations of the obtained linear expressions with experimental data, for each SQM both for landing and take-off. The aircraft parameters used in the linear expressions are also presented. At this point, the coefficients are not presented because these expressions will be further improved.

The comparisons between the experimental average values and predictions for landing are shown in Figures 6.12 and 6.13. The black line indicates a correlation



(a) Spectrogram.



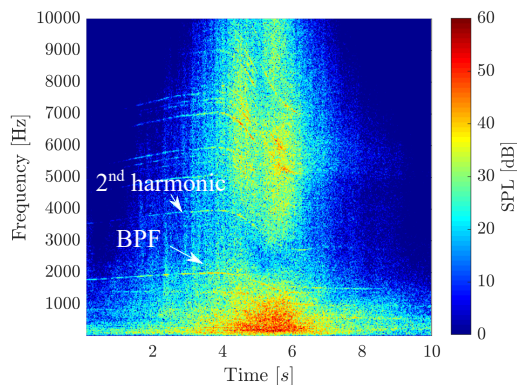
(b) Noise spectrum.

Figure 6.10: Spectrogram and spectrum at the overhead time for a take-off measurement of an A320. $N_5 = 76$ sone, $S_5 = 1.18$ acum, $K_5 = 0.32$ t.u., $R_5 = 0.10$ asper.

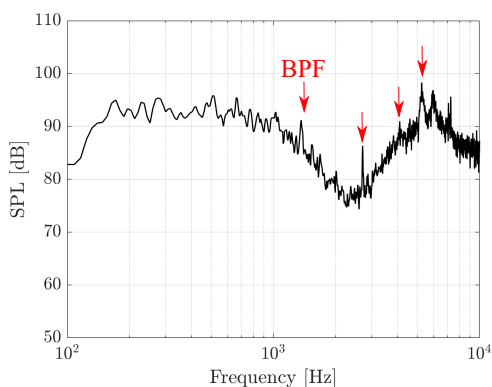
$R^2 = 1$, i.e., when the value of the predictions is the same as the experimental. The five plots show a good agreement between the average experimental values of the SQM and predictions using the empirical expressions.

6.4. Accounting for the variability of the SQM within aircraft type

The empirical expressions found for the SQM present a high correlation with the average of the experimental values for each aircraft, as seen in Table 6.2. However, as shown in Figures 6.6 to 6.9, the SQM vary within the same aircraft type, due to the operating conditions. The empirical expressions obtained in the previous section were applied to the entire data set of flyover measurements, and it was found that the values of R^2 decreased drastically, because without considering the



(a) Spectrogram.



(b) Noise spectrum.

Figure 6.11: Spectrogram and spectrum at the overhead time for a landing measurement of an A320. $N_s = 115.8$ sone, $S_s = 2.20$ acum, $K_s = 0.27$ t.u., $R_s = 0.09$ asper.

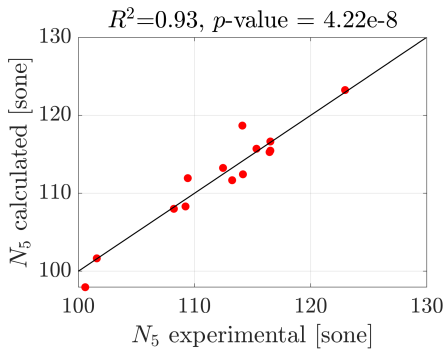
operating conditions of the aircraft, equal values of SQM were found for the same aircraft type. For instance, the R^2 value of loudness decreased from 0.95 to 0.63 for take-off and from 0.93 to 0.67 for landing. For roughness, R^2 decreased from 0.94 to 0.42 for take-off, and from 0.90 to 0.30 for landing. This demonstrates the importance of the operating conditions in aircraft annoyance.

New coefficients of the empirical expressions were found considering the entire data set of measurements and including the aircraft operating conditions. To the characteristics of the aircraft providing the best fit for each SQM, described in Table 6.2, were added variables for the aircraft velocity, altitude, and the blade passage frequency and rotational speed of the fan. A small number of random measurements were removed from the data set used to find the coefficients of the empirical expressions of the SQM in order to use them to test the final expressions.

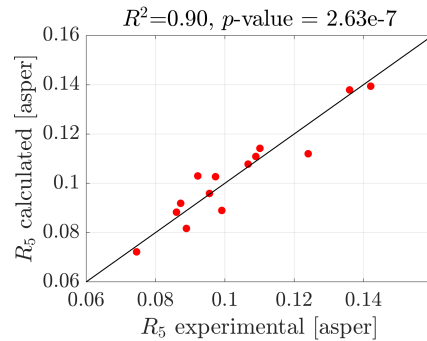
Some of the aircraft characteristics initially included in Table 6.2 did not contribute to an improved correlation with the experimental data once the operational

Table 6.2: Correlations of the empirical expressions considering the average of the SQM with experimental data.

SQM	Takeoff			Landing		
	R^2	p -value	Characteristics of the aircraft	R^2	p -value	Characteristics of the aircraft
Loudness	0.95	2.62e-8	wing span, length, cabin width, height, MTOW, fan diameter, TO-thrust.	0.93	4.22e-8	wing span, length, cabin width, MLW, BPR, nacelle length, diameter of nose and main gear tires.
Roughness	0.94	5.95e-8	wing span, length, cabin width, fan diameter, maximum take-off thrust.	0.90	2.63e-7	wing span, length, cabin width height, fan diameter, nacelle length, number of wheels and diameter of nose and main gear.
Sharpness	0.87	3.07e-6	wing span, length, cabin width, fan diameter, nacelle length, take-off thrust.			No correlations found.
Tonality			No correlations found.			No correlations found.



(a) Loudness.



(b) Roughness.

Figure 6.12: Comparison of experimental data (x -axis) with the results of the empirical expressions (y -axis) for landing. The black line corresponds to a correlation of $R^2 = 1$, i.e. when the experimental values are equal to the predicted.

conditions were included and therefore were discarded. As expected, the operating conditions with more influence on the results were the altitude of the aircraft and the rotational speed of the fan. Table 6.3 shows the coefficients of the empirical expressions found for the loudness, roughness and sharpness for take-off aircraft.

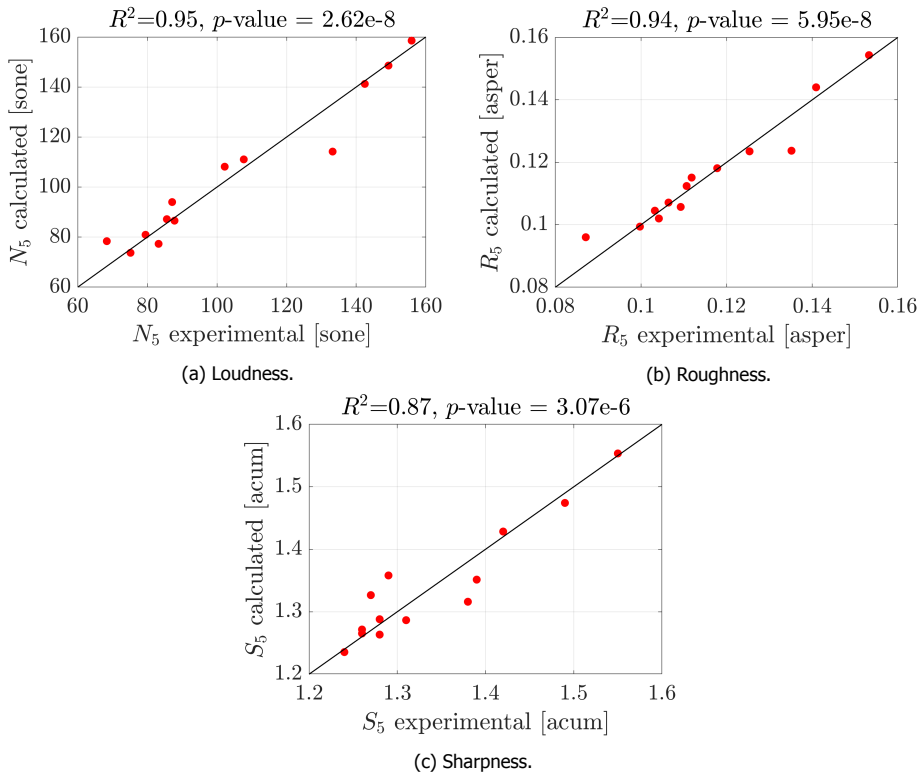


Figure 6.13: Comparison of experimental data (x -axis) with the results of the empirical expressions (y -axis) for take-off. The black line corresponds to a correlation of $R^2 = 1$, i.e. when the experimental values are equal to the predicted.

All variables considered in the expressions are in SI units. The correlations of the empirical expressions with the experimental data are shown in Figure 6.14. A good correlation was obtained for loudness, but sharpness and roughness show weaker results.

The same analysis is now presented for the landing flyovers. Despite the good correlation found for roughness with the average values of the experimental data, shown in Table 6.2, no empirical expression was able to capture the roughness variation within the same aircraft type. Also no empirical expression was found for sharpness. Despite the lack of significant correlations for tonality in Table 6.2, this changed with the introduction of the operating conditions. The fan is the most relevant source of tonal noise, therefore this result was expected. In addition, the sound pressure level of the harmonics depends on the atmospheric propagation effects and therefore on the altitude. The empirical expression for loudness continues to show a strong correlation with the experimental data when considering the entire data set, similarly to what was observed for take-off.

Table 6.4 shows the coefficients of the empirical expressions found for loudness

Table 6.3: Coefficients of the empirical expressions found for the SQM for take-off.

SQM	Altitude	N_1	Wing span	Height	Length	D_{fan}	Nacelle length	Max. TO thrust
N_5	-1.40e-1	6.14e-1	—	5.54	2.17	-2.67e+1	—	-1.29e-1
R_5	-1.00e-4	—	—	3.80e-3	—	—	—	-8.00e-3
S_5	-9.00e-4	2.40e-3	2.32e-2	—	3.00e-3	7.37e-1	1.29e-1	-9.3e-3

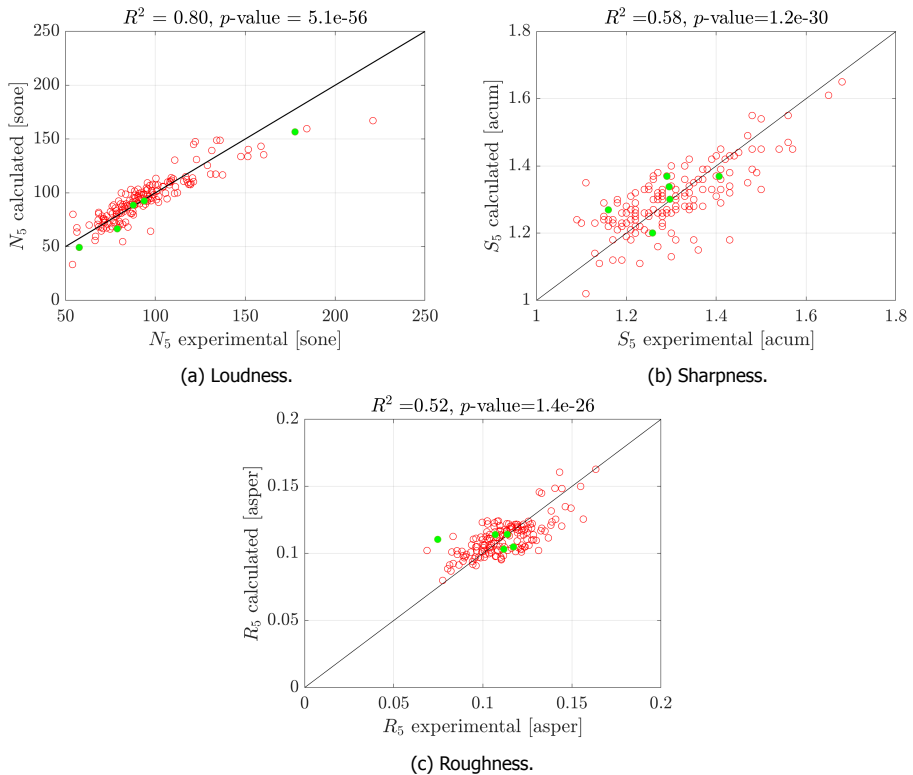


Figure 6.14: Comparison of experimental data (x -axis) with the results of the empirical expressions (y -axis) for take-off. The red circles are the experimental data used to find the coefficients of the empirical expression, whereas the green points correspond to random measurements put aside to test the empirical expressions.

and tonality for landing aircraft. The two expressions do not have parameters in common, loudness depends only on the aircraft dimensions and tonality has a close relation with the operating conditions of the fan, engine parameters and the landing gear configuration (number of wheels multiplied by their diameter ϕ).

The comparison of the experimental data points with the results obtained using the empirical expressions for landing is shown in Figure 6.15. The measurements that were randomly left out the data set used for finding the coefficients of the

Table 6.4: Coefficients of the empirical expressions found for the SQM for landing.

N_5	Wing span	Length	Cabin width	Height	Nacelle length	D_w MLG	
	-7.76	6.69e-1	4.82e+1	1.00e+1	1.05e+1	2.94e+1	
K_5	N_1	BPF	Nº fan blades	BPR	ϕ fan	Nº wheels NLG $\times D_w$	Nº wheels MLG $\times D_w$
	-3.00e-3	1.00e+4	3.40e-3	-3.60e-2	2.44e-1	-8.00e-3	-2.20e-2

empirical expressions show a reasonable agreement with the experimental results (green points).

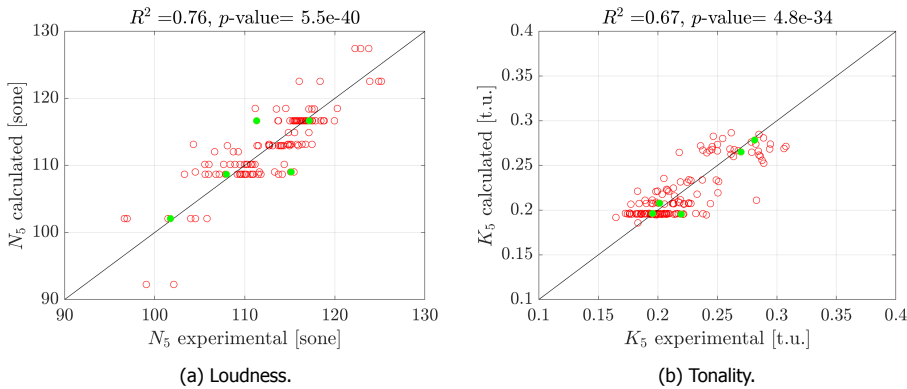


Figure 6.15: Comparison of experimental data (x -axis) with the results of the empirical expressions (y -axis) for landing. The red circles are the experimental data used to find the coefficients of the empirical expression, whereas the green points correspond to random measurements put aside to test the empirical expressions.

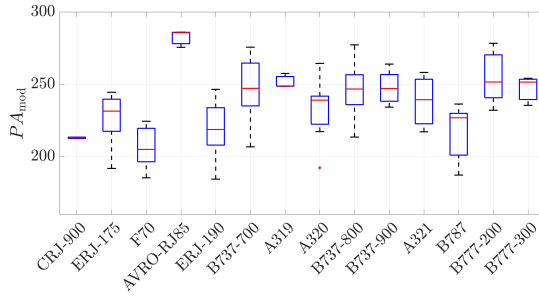
6.5. Comparison of EPNL with PA_{mod}

The SQM are combined to calculate the values of PA_{mod} for each flyover measurement. Figure 6.16 shows the PA_{mod} values for each aircraft type for landing and take-off. The values of EPNL are also included, in Figure 6.17.

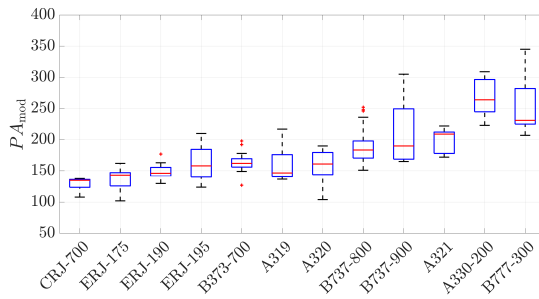
For the landing aircraft, the EPNL metric classifies the B777-series as the most annoying aircraft. However, according to PA_{mod} , the AVRO-RJ85 is perceived as more annoying than the B777. Both metrics present the lowest value for the F70, closely followed by the CRJ-900 and the ERJ-900. The two metrics show a good agreement for landing aircraft as both identify the A330-200 and the B777-300 as the noisiest aircraft and the CRJ-700 as the least annoying.

Figures 6.18 and 6.19 display the values of EPNL and PA_{mod} normalized by the maximum value, i.e. the maximum value found for all flyovers. For the purpose of a fair comparison, the EPNL values shown are in a linear scale (in sone) [43], calculated using

$$N_{\text{est}} = 2^{\frac{\text{EPNL}-40}{10}}. \quad (6.1)$$



(a) Landing.



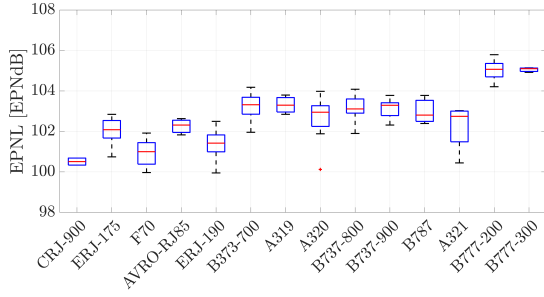
(b) Take-off.

Figure 6.16: Values of PA_{mod} for landing and take-off flyovers.

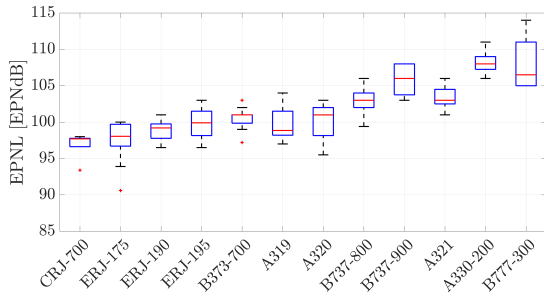
The take-off measurements show a very high correlation between the two metrics, in contrast to the landing measurements, which show substantial different results for the two metrics for some of the aircraft, e.g., the B777-series and the A319. The EPNL metrics takes into account the loudness of a sound and the presence of tones, whereas PA_{mod} also includes other sound characteristics, i.e., roughness, sharpness and fluctuation strength. One of the advantages of PA_{mod} is the independent calculation of the sound characteristics that contribute to the final value of annoyance and therefore it is easy to understand which SQM has the greatest influence.

To better understand the influence of each SQM on PA_{mod} , they were varied within the range of values found for the flyovers. The other SQM are kept constant, with the average value determined for the dataset. Figure 6.20 shows how PA_{mod} varies with the values of SQM determined for the landing and take-off flyovers. The SQM values are normalized by their maximum value so they can all be shown in the same plot.

The fluctuation strength is not represented in these plots because its contribution is not associated with aircraft noise, but with background noise. In addition, Figure 6.20b does not show the variation with sharpness, because its value is lower than 1.75 for all the take-off measurements and therefore its contribution to PA_{mod} is zero (see Section 2.5.3).



(a) Landing.



(b) Take-off.

Figure 6.17: Values of EPNL for landing and take-off flyovers.

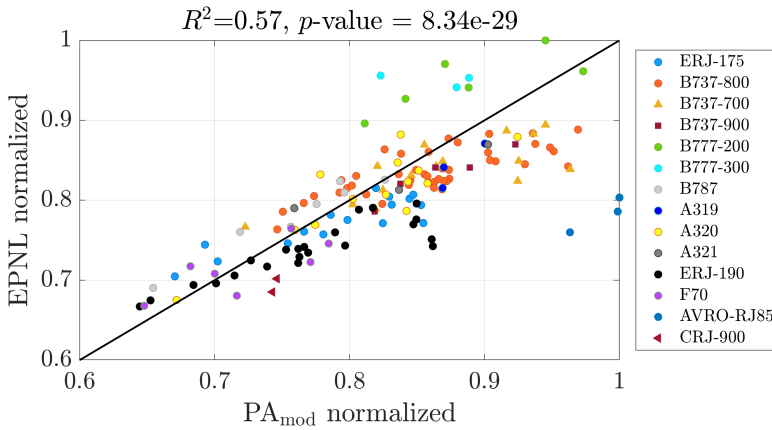


Figure 6.18: Values of EPNL and PA_{mod} for landing flyovers, normalized by the maximum value.

In Figure 6.20b only loudness has a significant impact on PA_{mod} . This explains the high correlation between PA_{mod} and EPNL for take-off, since the latter depends mostly on this sound quality metric. However, for landing, Figure 6.20a shows that

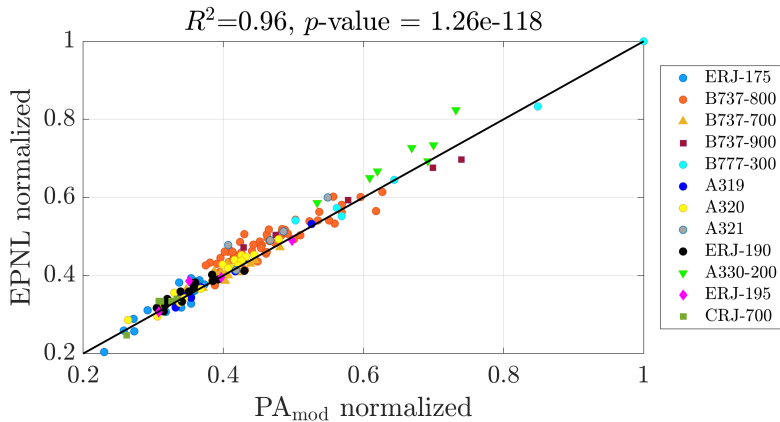


Figure 6.19: Values of EPNL and PA_{mod} for take-off flyovers, normalized by the maximum value.

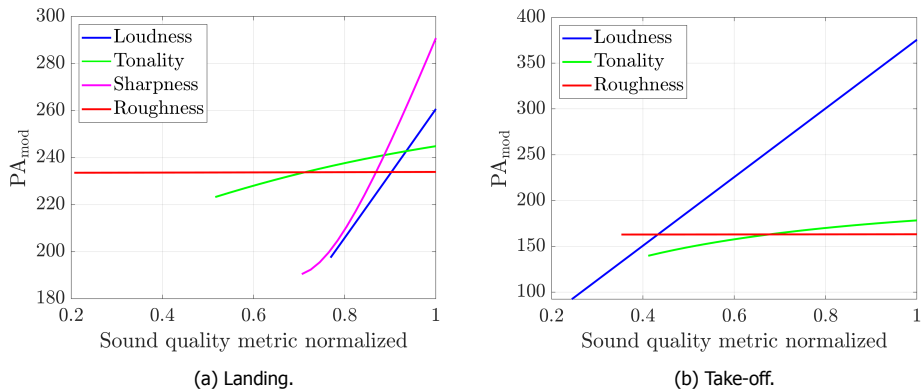


Figure 6.20: Influence of the sound quality metrics on the values of PA_{mod} within the range determined for the flyover measurements.

both loudness and sharpness have a great influence on PA_{mod} . The EPNL does not account for the effect of sharpness on annoyance, which explains the differences between the two metrics observed in Figure 6.18.

6.6. Discussion

This work analyzed the sound quality metrics and total annoyance of a large number of landing and take-off flyovers. It was observed that the sound quality metrics and the two metrics used to assess annoyance present relevant variability within the same aircraft type. This variation was associated to differences in the aircraft operating conditions.

The selected measurement location was at a distance of approximately 670 m

from the runway, representative of urban areas around airports highly affected by aircraft noise. Due to the high rate of climb of take-off trajectories compared with the glide slope during landing, for the same point on the ground, aircraft fly at very different altitudes for the two flight phases. This results in a strong attenuation of high frequency noise for take-off and consequently very low values of sharpness. Aircraft noise is expected to present higher values of sharpness for take-off than for landing, however, the flyovers analyzed highlighted the importance of considering atmospheric propagation when assessing the noise impact on ground. Also the values of roughness were expected to be higher for take-off due to the buzz-saw noise tones, but that was not verified. The noise spectrum showed that the BSN tones were not very prominent and therefore the values of roughness were similar for the landing and take-off flyovers. The average values of tonality were also very similar for landing and take-off flyovers, despite the masking effect of the fan harmonics by jet noise. Modern engines present high values of BPR, which results in a reduction of jet noise and consequently less masking of the fan harmonics.

Correlations between the average values of SQM for each aircraft type and their design and engine characteristics were investigated, resulting in empirical expressions. For landing those expressions could be determined for loudness and roughness, and for take-off were obtained expressions for loudness, roughness and sharpness. The empirical expressions showed a very high correlation with the experimental values. However, they failed capturing the variability associated to the aircraft operating conditions and new empirical expressions were obtained considering the velocity and altitude of the aircraft, and the rotational speed of the fan.

The available operating conditions were very limited, and therefore the empirical expressions resultant from this work need to be further investigated. However, this work indicates that the sound quality metrics can be associated to characteristics of the aircraft and considered in the design phase of low-noise concepts, in multi-disciplinary optimization procedures, similarly to current approaches that use the SEL or EPNL to estimate the noise impact.

The PA_{mod} is considered a good alternative to the EPNL due to the high correlation with subjective ratings of aircraft noise. In addition, the sound quality metrics provide a better description of the noise characteristics than EPNL. Nevertheless, the two noise metrics present a high correlation for the take-off measurements due to the importance of loudness during this flight phase. For landing, however, the correlation is weaker, due to the relevant contribution of sharpness to the value of PA_{mod} .

7

Engine and airframe noise during landing and take-off

The total noise emitted by an aircraft is composed of different noise generating mechanisms, which need to be determined individually. Physics based methods require detailed input data and are computationally expensive. In the design process, such detailed input is not always available. In addition, time consuming simulations are not suitable to multi-disciplinary optimization. For these reasons, empirical models are widely used to predict aircraft noise as introduced in Chapter 2. Also these models need input variables which are not always readily available. Therefore, this chapter studies the influence of the different input variables on the total noise predictions. The total noise spectrum resulting from the empirical models is compared with flyover measurements at the overhead time for three different aircraft models equipped with distinct engines.

Parts of this chapter are based on a paper currently under review [160].

7.1. Sensitivity Analysis

The parametric semi-empirical models described in Section 2.1 are of simple implementation, but although they do not require the complete aircraft model, such as high-fidelity methods do, these models still require detailed engine and airframe data as input. Most of the airframe noise input data, e.g. the wing area and span, is relatively easy to obtain. Other parameters, such as the diameter of the wheels and the length of the struts of the landing gear are not so readily available for all aircraft types but can be determined from scaled drawings and photos with sufficient accuracy.

On the contrary, the input data required for the engine noise predictions needs to be calculated for the aircraft operating conditions. In this work, the temperature, mass flow rate and pressure across the turbofan stages and jet velocities are determined using the Gas Turbine Simulation Program (GSP), which requires a complete modeling of the turbofan stages. This input is hardly available, which makes the comparison of flyover measurements with predictions for different aircraft types a time-consuming process.

This section investigates the sensitivity of the jet, fan, combustion and airframe noise to small variations of the input data. This allows us to assess which input influences predictions the most, and which parameters can be approximated without interfering with the final results. For example, for landing aircraft, flyovers measured at the same location present small changes of the flight velocity and rotational speed of the fan N_1 . Such variations in the operating conditions influence the engine data input, which might not be available for those specific flight settings. It is important to know beforehand how small differences in the operating conditions influence the predictions.

The sensitivity analysis of the semi-empirical models used in this work considers fan, jet, combustion and airframe noise separately. Take-off conditions are used to study the influence of the input data on engine noise, because this type of noise is dominant during this flight phase. The sensitivity analysis of airframe noise is made for approach conditions, when the high lift devices and landing gear are deployed. The different components of airframe noise (main and nose landing gear, flaps, slats, horizontal and vertical stabilizers) are not analyzed separately because they are all calculated with Fink's method.

This analysis is based on the A320 aircraft equipped with CFM56 engines. For the approach condition the aircraft flies roughly at an altitude of 50 m and at a velocity of 65 m/s. The rotational speed of the fan was set to $N_1 = 64\%$. For departure, the A320 is at an altitude of 400 m flying at 70 m/s with $N_1 = 84\%$. These values were based on experimental data recorded at Amsterdam Airport Schiphol, as described in Section 6.1. The noise predictions were calculated for a polar angle of 90° and an azimuthal angle of 0° , i.e., a position below the aircraft with no sideline angle.

7.1.1. Take-off

Jet Noise

The first noise component analyzed is jet noise, which requires the input data of Table 2.2. The Mach number was the first parameter modified and was varied

20% in relation to the original value. Figure 7.1 shows a variation of jet noise with this parameter of approximately 1.5 dB over the entire frequency range. Despite the small Mach variation, jet noise changes significantly. The plot of Figure 7.1 shows the importance of an accurate calculation of the aircraft velocity for jet noise prediction and indicates that its variation for the same aircraft type should be taken into consideration.

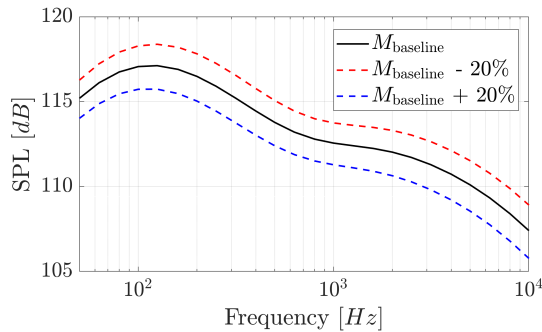


Figure 7.1: Variation of jet noise with the aircraft Mach number.

Three of the input variables of Table 2.2 are geometrical parameters: the inner and outer jet area and the length between the inner/outer jet exhaust plane. The jet areas were varied 20% in relation to the original values. These differences resulted in a maximum offset of 0.5 dB compared with the baseline prediction. This offset is not constant over the frequency range, as can be observed in Figure 7.2. The variation of length between the inner/outer jet exhaust plane is not a parameter easily found in the literature. However, it was found that its value did not influence the results even when doubled or reduced by half relative to the baseline value.

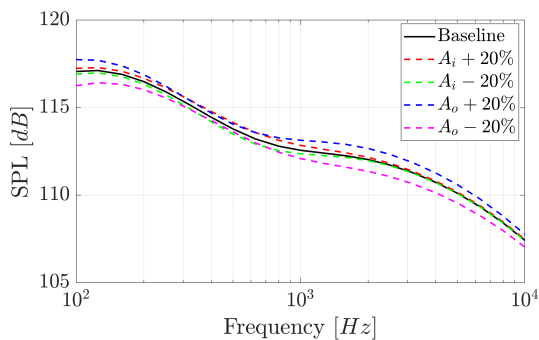


Figure 7.2: Variation of jet noise with the inner and outer jet area.

The mass flow and temperature across the fan and the jet velocity were varied

in a different manner than the geometrical parameters. The variables are selected from the engine performance deck according to slightly different operating conditions of the aircraft observed in the experimental data. The operating conditions considered for assessing the variations of the input parameters are shown in Table 7.1.

Table 7.1: Variation of the operating conditions used in the sensitivity study of the inner and outer jet temperature, mass flow rate and velocity.

	Mach	H [m]	N_1 [%]
Baseline	0.20	400	84
Other operating conditions	0.15	350	79
	0.30	600	94

The following observations can be drawn based on the three operating conditions of Table 7.1:

- For the values of the Mach number considered, the variation of the inner and outer jet mass flow rate was not significant enough to change jet noise.
- The values of the inner and outer jet mass flow rate at different aircraft altitude and fan rotational speed N_1 did not change jet noise.
- The variation of the inner and outer jet total temperature with the operating conditions of Table 7.1 was not translated in a variation of jet noise.
- The variation of the inner and outer jet velocity with the Mach number and N_1 resulted in different values of jet noise, as shown in Figure 7.3 and Figure 7.4, particularly for the latter.
- No changes were observed for the aircraft altitude variation.

This analysis shows that N_1 influences jet noise the most due to the change of the inner and outer jet velocities. When comparing flyover measurements with predictions, a small variation of the aircraft velocity of around 20 % and altitude of a few hundred meters does not justify a new simulation as jet noise is not expected to significantly change.

Fan Noise

The sensitivity study of the fan noise was performed in a similar manner as jet noise. The Mach number was changed within 20 % with no variation of fan noise. The fan diameter was also varied 20 %. This is an important parameter, because it is used to determine the rotor tip Mach and the cut-off correction. However, it was found that a variation of 20 % of the rotor diameter does not alter the fan noise values. Also the number of blades was changed from the original value of 36

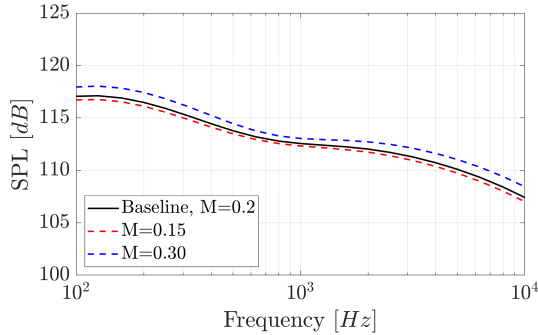


Figure 7.3: Variation of jet noise due to a different aircraft velocity, resulting in a variation of the inner and outer jet velocity.

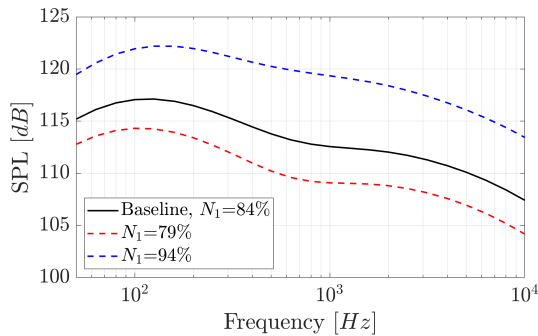


Figure 7.4: Variation of jet noise due to a different rotational speed of the fan, resulting in a variation of the inner and outer jet velocity.

to 30 and 40 without resulting in any change in the fan noise prediction, because the frequency is discretized in 1/3-octave bands and the fan BPF and harmonics remain within the same band. The number of fan rotor blades is however readily available, unlike the number of vanes, which can significantly affect fan noise when underestimated, as shown in Figure 7.5.

Another geometrical input, which similarly to the number of vanes, is difficult to find in the literature, is the rotor-stator spacing, RSS. This parameter has some influence on fan noise, as can be observed in Figure 7.6. A low value of RSS, equal to 100%, i.e. the space between the rotor and the stator is equal to the chord of the fan blades, shows a deviation of approximately 4 dB over the entire frequency range relative to the baseline value (RSS= 300%). However, for values of RSS closer to the baseline, the difference is almost negligible.

The next parameter evaluated is the BPF, which is expected to significantly influence fan noise [161]. The BPF value was varied 100 Hz and 200 Hz because this

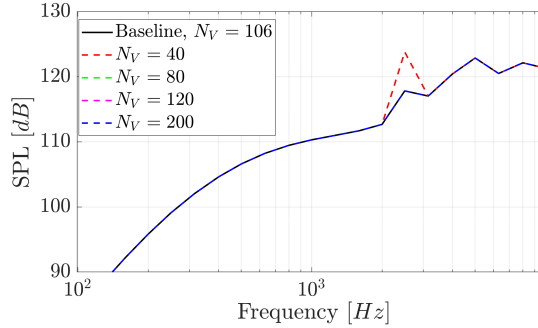


Figure 7.5: Variation of fan noise with the number of vanes, N_V .

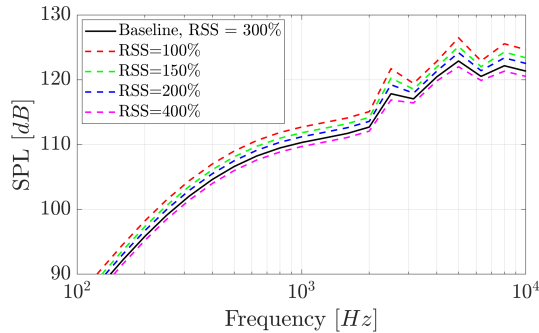


Figure 7.6: Variation of fan noise with the distance rotor-stator, RSS.

parameter can be determined from the spectrograms of experimental data with a reasonable level of accuracy, and a larger difference from the real value could hardly be estimated. The variation of fan noise with the considered values of BPF is shown in Figure 7.7. The SPL curves differ from the baseline even for this limited range of frequencies, which demonstrates the importance of this parameter.

In addition to the parameters mentioned above, the fan rotor tip Mach number at the design point, $M_{DP,t}$ was varied 20% relatively to the baseline value of 1.43, resulting in a constant offset of approximately 1 dB over the 1/3-octave bands.

The last two parameters of Table 2.1 are the temperature rise and the mass flow rate across the fan, required to calculate L_b (see Equation (2.3)). Their variation is based on the operating conditions of Table 7.1. It was found that the variation of the aircraft velocity and the consequent change in values of total temperature rise and mass flow rate did not significantly alter L_b and therefore the fan noise values. The same was observed for the variation of the aircraft altitude. However, a significant offset relative to the baseline was observed when considering different values of N_1 (see Figure 7.8).

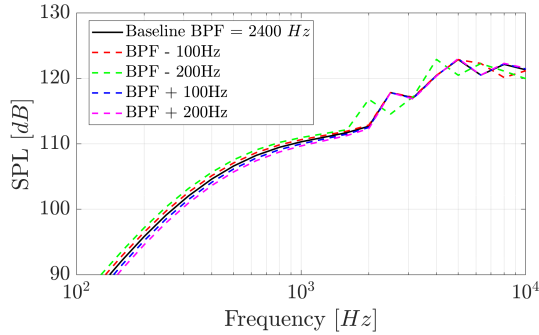


Figure 7.7: Variation of fan noise with the Blade Passage Frequency.

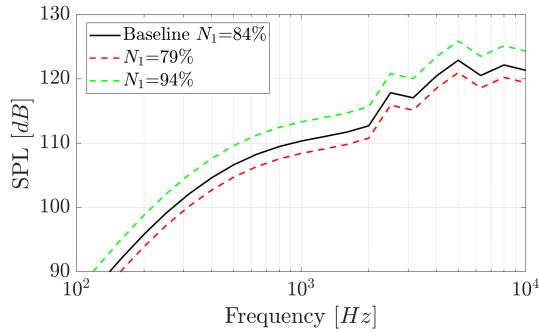


Figure 7.8: Variation of fan noise due to different values of rotational speed of the fan (N_1) resulting in a variation of L_c (a parameter in Heidmann's model dependent on the mass flow rate and temperature across the fan).

Based on this analysis, it can be concluded that the BPF and consequently the operating rotational speed of the fan, have the greatest influence on fan noise. Most geometric parameters can be approximated, with exception of the rotor stator spacing (RSS), which should be carefully considered. Small variations of the aircraft velocity and altitude for the same N_1 do not require new predictions.

Combustion Noise

Combustion noise depends on the engine performance and the parameters of Table 2.3 were changed according to the variation of the aircraft operating conditions of Table 7.1.

The total pressure and the total temperature at the inlet of the combustor, p_3 and T_3 , respectively, showed only slight variations for the different operating conditions and therefore did not influence combustion noise.

Changes of the mass flow rate at the inlet of the combustor (\dot{m}_3), considering the variation of the operating conditions of Table 7.1, resulted in a change of combustion

noise of less than 1 dB.

The total temperature at the exit of the combustor (T_4), and the total temperature at the exit of the turbine (T_8), do not change with the operating conditions because they should be at the design point of the engine. However, these parameters are not easily available and literature recommends to estimate the value at maximum take-off conditions. The component $[(T_4 - T_8)_d/T_0]^4$ of Equation (2.12), also denominated as T_{ref} in this work, has a great influence on combustion noise. Figure 7.9 shows that a 10% variation of this term results in an offset of approximately 2 dB over the 1/3-octave bands. If T_{ref} is calculated for the take-off condition of the baseline case, and not for the maximum take-off condition of the engine deck, the offset increases to almost 4 dB.

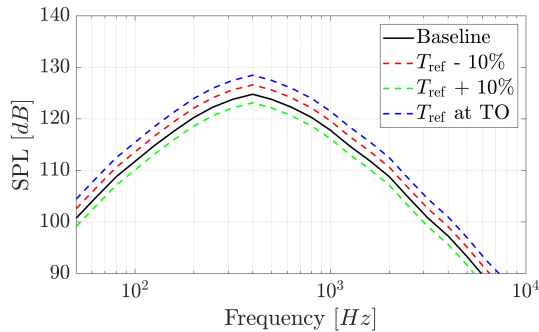


Figure 7.9: Variation of combustion noise considering different values of T_{ref} .

7.1.2. Approach

The baseline case considered for the sensitivity analysis of airframe noise is an approach flight condition with the aircraft at an altitude of 50 m, $M = 0.19$ and $N_1 = 64\%$. The landing gear is deployed, as well as the slats, and the flaps are set at a deflection angle of 30° .

Airframe noise presents a large variation with the aircraft velocity, as shown in Figure 7.10. A increase of 20% in the Mach number resulted a in difference of almost 4 dB constant over the frequency range, and a decrease of 20% led to values of airframe noise 6 dB inferior to the baseline case.

Flap noise is considered an important component of airframe noise during approach. It was observed that a change of the flap deflection angle from the initial value of 30° to 15° resulted in a maximum variation of 2 dB compared with the baseline case. Therefore, a small difference of the flap deflection is not expected to change significantly airframe noise predictions. This is important for the comparison with flyover measurements because the deflection angle is not available and needs to be approximated for typical approach conditions. A 20% variation of the flap area or span did not significantly affect airframe noise, and the difference relative to the baseline case was only noticeable at high frequencies, where fan noise

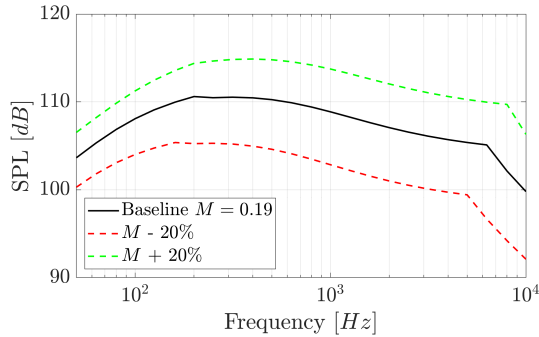


Figure 7.10: Variation of airframe noise with the aircraft velocity.

becomes more importance than airframe noise. The number of flap slots, however, has a significant influence on airframe noise (see Figure 7.11).

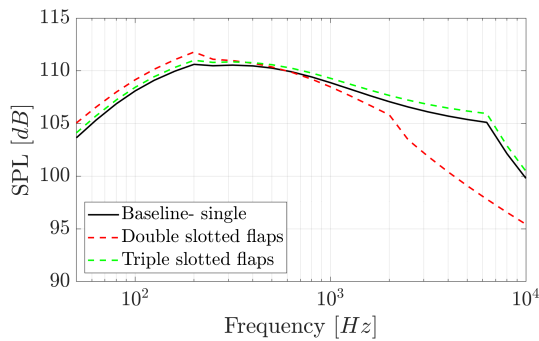


Figure 7.11: Variation of airframe noise with the number of flap slots.

A variation of 20% of the wing area and span did not result in a change of airframe noise. The same was observed for a 20% variation of the horizontal and vertical tail area and span.

The landing gear noise is calculated using the length of the struts and the wheel diameter. The number of boogies and wheels can be easily determined using pictures of the aircraft, as well as the length of the struts and wheels diameter. A variation of 20% in the length of the strut of the main and nose landing gear did not change the airframe noise spectrum. The diameter of the wheels of the main landing gear was the parameter that most influenced airframe noise, even though the difference relative to the baseline was less than 1 dB for the entire frequency range. A variation of 20% of the wheels diameter of the nose landing gear did not result in a change of airframe noise.

7.1.3. Summary

This analysis revealed which parameters have more influence on noise predictions based on the semi-empirical models used in this work. It was shown that slight changes in the aircraft operating conditions did not significantly change all the engine input data required for the predictions and some geometrical parameters can be approximated without affecting the noise spectrum. This is particularly relevant in the comparison of these models with flyover measurements, in which some parameters need to be approximated.

Jet noise (as determined by Stone's model) depends mostly on the aircraft velocity and rotational speed of the fan. Parameters dependent on the operating conditions were found to have no influence in jet noise for the three take-off conditions of Table 7.1, with exception of the inner and outer jet velocity. Geometrical parameters were found to have a small influence on jet noise when deviating 20 % from the real value (maximum offset of 0.5 dB).

Fan noise (calculated with Heidmann's model) is affected by geometrical parameters, namely the number of blades, vanes and the distance rotor-stator. The rotational speed of the fan directly affects fan noise, as expected, because it determines the frequencies of the harmonics. However, this parameter can be accurately estimated from the flyover measurements. The rotational speed of the fan also affects the mass flow rate and temperature across the fan, which influence the values of fan noise.

Combustion noise did not present changes for the operating conditions of Table 7.1. However, a wrong estimate of the parameter T_{ref} (which depends on the temperature difference between the exit of the combustor and the turbine) affects combustion noise. This parameter should be determined at the design point of the engine, but when these conditions are not available, can be calculated for the maximum take-off condition.

Airframe noise showed variations with the aircraft velocity and the number of flap slots. Other geometrical parameters only have an impact on airframe noise when using gross approximations (deviating more than 20 % from the correct dimensions).

7.2. Comparison of semi-empirical noise models with flyover data

This section compares measurements of aircraft noise during landing and approach with the semi-empirical models described in Section 2.1. The flyover measurements were recorded at Amsterdam Airport Schiphol using an acoustic array. The measuring system and the location of the measurements are described in Section 6.1.

The aircraft Airbus A319, A320, A330-200 and Boeing B777-300 were selected for this comparison due to the availability of the input data required for the engine noise predictions. The comparison is made for a polar angle of 90° and azimuthal angle of 0°, which corresponds to the overhead time of the aircraft relative to the acoustic array. This is the instant at which the aircraft is closer to the array and its relative position can be determined with highest accuracy.

Figure 7.12 shows the variation of the OSPL measured for the flyovers of the same aircraft type. These values are determined at the source location, i.e., the values measured at the array were propagated back to the aircraft location considering spherical spreading and atmospheric absorption. The A330 is not shown for approach because no measurements were available.

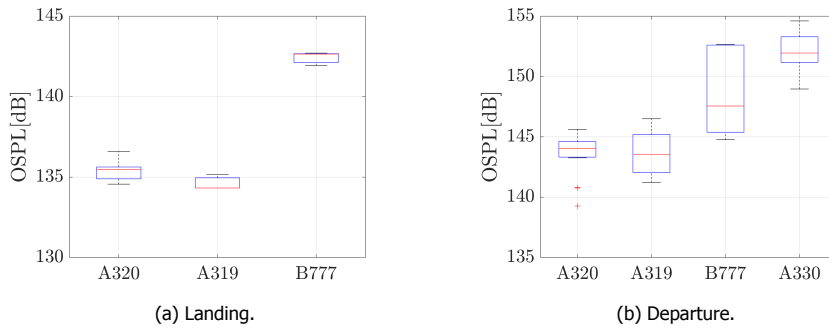


Figure 7.12: Variation of the OSPL at the aircraft location for each aircraft type.

The variation of the OSPL is clearly higher for departure than for landing, as expected, because landing aircraft must follow the Instrument Landing system, which results in very regular trajectories. Therefore, all landing aircraft were centered at the acoustic array whereas some departure flyovers were very misaligned. The values of OSPL were obtained using a time interval of 0.1 s and averaged over the 8 microphones at the center of the array (see Figure 6.1b).

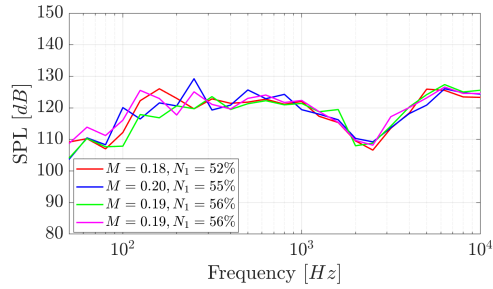
The noise spectrums of different flyover measurements of the A320 are shown in Figure 7.13, both for approach and departure. These plots show the corresponding aircraft velocity and the rotating speed of the fan of each flyover. For landing, the noise spectra of the different flyovers do not show significant variation. The noise spectra for departure flyovers however, present more variability and significant differences at high frequencies. It was observed that the take-off flyovers centered on the array (green, light blue and pink spectra of Figure 7.13b) presented higher frequency content than when misaligned (red and blue spectra).

Also the noise spectra for landing A319 flyovers showed less variability than for take-off, as shown in Figure 7.14. The same trend was observed for the B777 (see Figure 7.15).

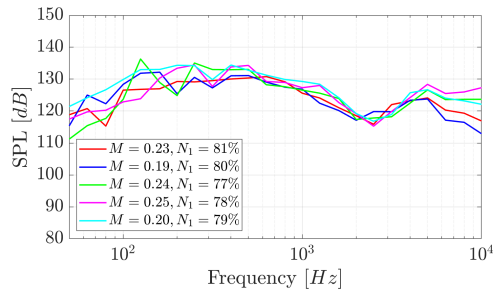
The take-off noise spectra of the A320 and the A319 indicate that low-frequency noise presents higher sound pressure levels than high-frequency noise, i.e. jet and combustion noise are dominant. Such difference is not so evident for the B777. However, considering that the three aircraft types are equipped with modern turbofan engine with high values of BPR, jet noise is not expected to play a dominant role during take-off.

The noise spectra for landing aircraft show similar values of sound pressure levels for high and low frequencies, but

slightly higher for values above 3000 Hz. The low sound pressure level values



(a) Landing.



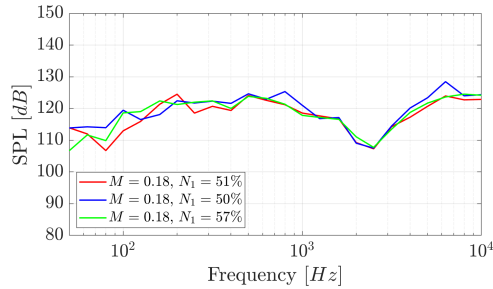
(b) Departure.

Figure 7.13: Measured noise spectrum (in 1/3-octave bands) of A320 flyovers.

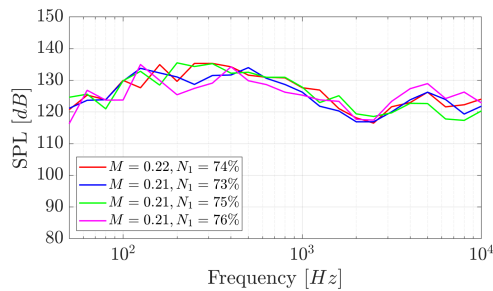
between 1600 Hz to 3150 Hz observed for the A319 and A320 seem to indicate the presence of lining treatment of the engine ducts because the CFM56 typically presents a BPF value in this frequency range.

The A319 and the A320 are equipped with the same engine, and except for the fuselage length, have similar airframe dimensions. Figure 7.16 shows the noise spectra obtained for different A320 (in grey) and A319 flyovers (in red) during landing and take-off. The A319 and A320 spectrums are similar and the small differences cannot be attributed to differences in the aircraft design because the same range of variability is observed for flyovers of the same aircraft type. These results were expected considering the sensitivity analysis of the previous section, which showed the low sensitivity of airframe noise to slight variations of the fuselage dimensions.

The following subsections compare the experimental and predicted noise spectra of the A320, A330 and B777 aircraft. The semi-empirical predictions use the average values of altitude, N_1 and aircraft velocity measured for the landing and take-off flyovers of each aircraft type. These predictions combined the different noise components at the source position, assuming a unit sphere with a radius of 1 m.



(a) Landing.



(b) Departure.

Figure 7.14: Measured noise spectrum (in 1/3-octave bands) of A319 flyovers.

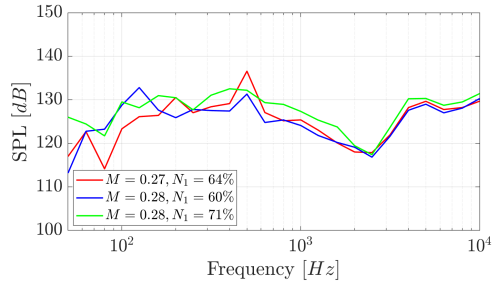
7.2.1. Airbus A320

The polar plots of Figure 7.17 show the OSPL values of the different noise components, predicted for the A320 during landing and take-off (considering an azimuthal angle of 0°).

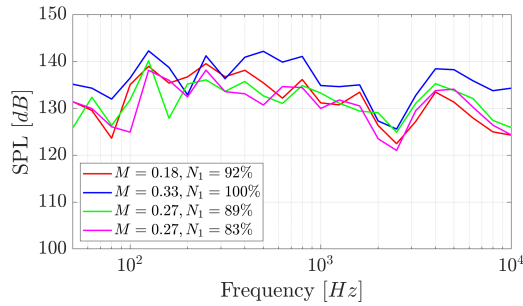
The polar OSPL plot for landing A320 (Figure 7.17a) shows a negligible contribution of the jet to the total noise. Fan and combustion noise are dominant for polar angles higher than 60° and airframe noise is predominant for polar angles inferior to 60° .

For departure, according to Figure 7.17b, fan and combustion noise are dominant for most observer polar positions, but jet noise has an important contribution to the total noise. In addition, airframe noise is negligible compared to other noise sources. The relative importance of the different noise components predicted by the semi-empirical methods are in line with what is theoretically expected - predominance of engine noise for take-off and a more balanced contribution of engine and airframe noise for landing.

Figure 7.18 and Figure 7.19 compare the predicted spectrum of the A320 with results obtained from different measurements, considering a receiver at $\theta=90^\circ$ and $\phi=0^\circ$, i.e., in agreement with the position of the acoustic array. For this position, the predicted OSPL for landing and take-off was 130.6 dB and 136.4 dB, respectively. The average experimental value determined for landing was 135.5 dB, whereas for take-off the OSPL value increased to 144dB.

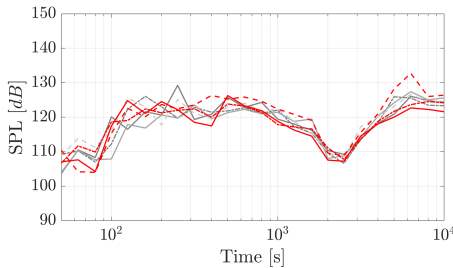


(a) Landing.

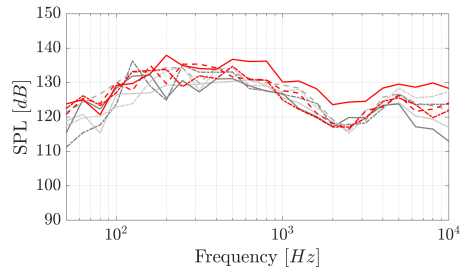


(b) Departure.

Figure 7.15: Measured noise spectrum (in 1/3-octave bands) of B777 flyovers.



(a) Landing.

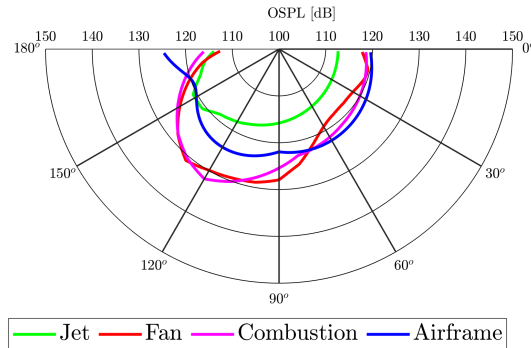


(b) Departure.

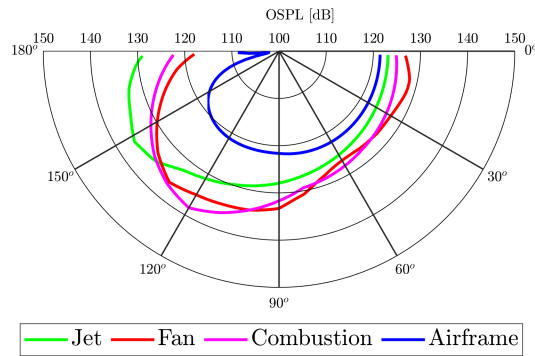
Figure 7.16: Noise spectrum (in 1/3-octave bands) of A320 (in grey) and A319 (in red) aircraft of different flyover measurements.

The landing prediction shows lower values of SPL than those measured for the entire frequency range except for frequencies between 2000–3150 Hz. The low frequencies up to 2000 Hz have a deviation of approximately 5 dB. The same SPL difference is found for frequencies higher than 3150 Hz, in a spectral region associated with fan noise.

The comparison between the experimental noise spectrum of the A320 with predictions for take-off, shown in Figure 7.19 shows a good agreement for the



(a) Landing.



(b) Departure.

Figure 7.17: Values of OSPL predicted for the A320 over different polar angles and azimuth angle $\phi = 0^\circ$.

high frequency range, where fan noise is dominant. The liners were approximated using typical values found in the literature [64], which according to Figure 7.18 and Figure 7.19, led to an overestimation of the fan noise suppression. For the low-frequency range, the total noise predicted is approximately 10 dB lower than the experimental.

One suggestion for this discrepancy of SPL between the experimental and predicted noise spectrum at low frequencies is that it can be associated with jet-installation noise. Recent work used high-fidelity methods to investigate this effect and it was found that high values of low-frequency noise amplification can occur in the far-field [162]. This installation effect is more evident for observers perpendicular to the engine, i.e. at $\theta=90^\circ$, as shown in Figure 7.20, resulting in an increase of

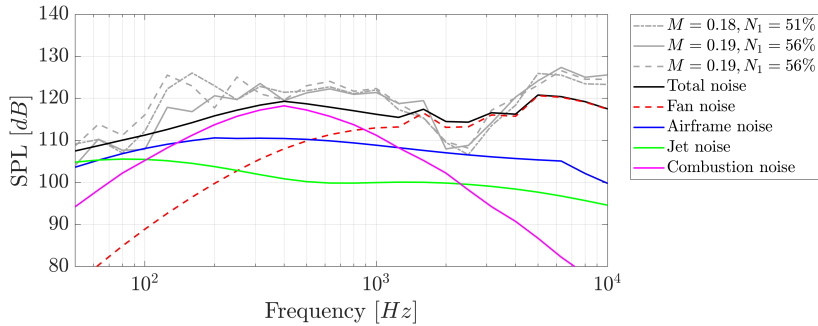


Figure 7.18: Comparison of the A320 noise spectrum (in 1/3-octave bands) of landing flyover measurements with predictions.

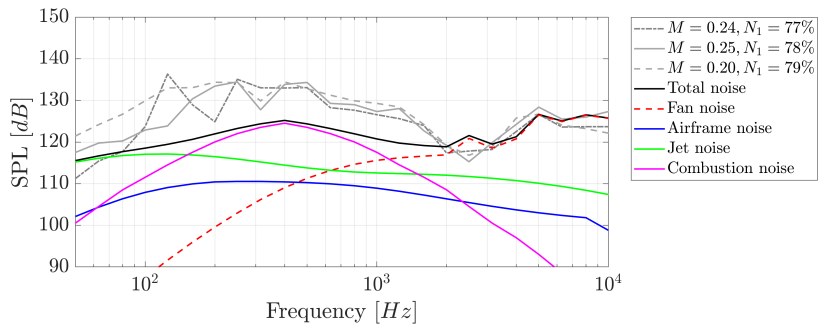


Figure 7.19: Comparison of the A320 noise spectrum (in 1/3-octave bands) of departure flyover measurements with predictions.

OSPL up to 5 dB. The noise spectra of Figure 7.18 and Figure 7.19 were measured at the acoustic array location and propagated back to the source, and this far field installation effect might therefore be present at the source position.

7.2.2. Boeing B777

The polar plots of the predicted OSPL obtained for the B777, shown in Figure 7.21, present some differences compared to the A320 polar plot, in particular the predominant role of airframe noise during landing. The comparison between the predicted and the measured noise spectrum is illustrated in Figure 7.22 and Figure 7.23 for approach and departure, respectively.

The average experimental OSPL value determined for approach was 142 dB, approximately 4 dB higher than the predicted value of 138 dB. A similar discrepancy was also observed for the A320. The experimental noise spectrum shows a good agreement with the prediction for the low frequency range up to 1600 Hz, but the high frequencies are underestimated, clearly due to low predicted values of fan

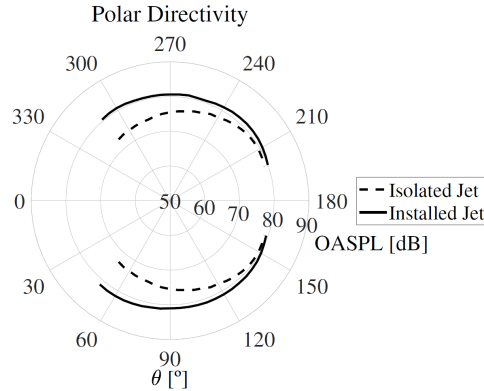


Figure 7.20: Polar directivity of the isolated and installed jet for a distance equal to four times the nozzle exit diameter [162].

noise.

The average experimental OSPL of the B777 determined for take-off was 148 dB. This value is higher than the predicted value of 142.5 dB, similarly to what was observed for the A320. The agreement between the experimental and measured noise spectrum is reasonable for high frequencies. There is evidence of jet noise installation effects at the low frequencies, but the offset is smaller than for the A320. However, for the A320, jet noise assumes almost the same importance as fan and combustion noise, which is not the case for the B777, which has a higher contribution of fan and combustion than jet noise.

7.2.3. Airbus A330

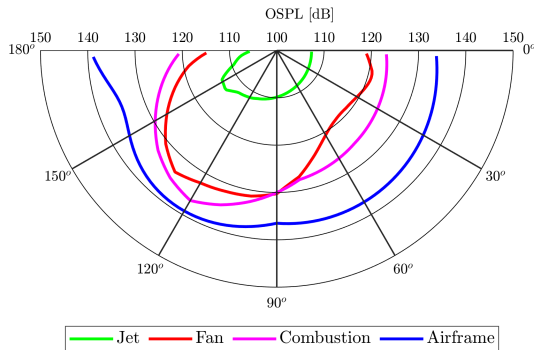
The A330 is the last case analyzed. The OSPL polar plot for the approach condition is shown in Figure 7.24. This plot shows more similarities with the A320 than with the B777, due to the predominance of airframe noise for polar angles lower than 90° whereas for the B777 this type of noise is dominant at any polar position.

The predicted OSPL value was 144.4 dB, while the measured value was 152.9 dB. Figure 7.25 shows the measured and predicted noise spectrum of the A330 for take-off. The difference between the predicted and measured OSPL is in line with the values also observed for the A320 and B777.

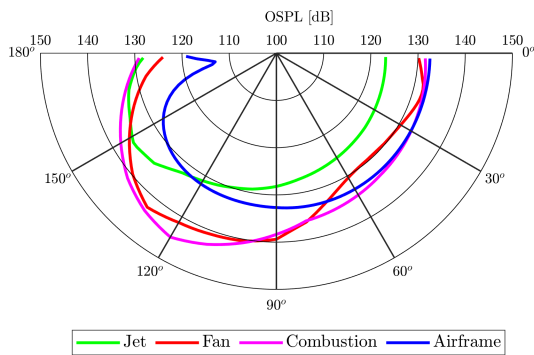
The predicted noise spectrum for take-off shows a good agreement with the measurements for high frequencies. The low frequency range presents a significant offset, similarly to what was observed for the A320 and B777.

7.2.4. Summary

The three aircraft analyzed consistently showed similar deviations between predictions and semi-empirical methods at a polar angle of 90° and azimuthal angle of 0°, as summarized in Table 7.2. According to the sensitivity analysis of Section 7.1,



(a) Landing.



(b) Departure.

Figure 7.21: Values of OSPL predicted for the B777 over different polar angles and azimuth angle $\phi = 0^\circ$.

these deviations are not related with approximations of the aircraft operating conditions, as small differences in the aircraft altitude, velocity and rotational speed of the fan are not expected to significantly affect the noise spectrum. Also the small variability observed in the measured noise spectra of the three aircraft (Figures 7.13 to 7.15) indicates that the differences between experiments and predictions are not related with deviations of the operating conditions.

The predicted and measured noise spectra showed a good agreement at low frequencies for landing. Airframe noise has an important contribution during this flight phase and jet noise presents very low values and therefore the jet installation effects are not so evident as during take-off. For high frequencies, however, the measured and predicted spectra present significant differences during landing

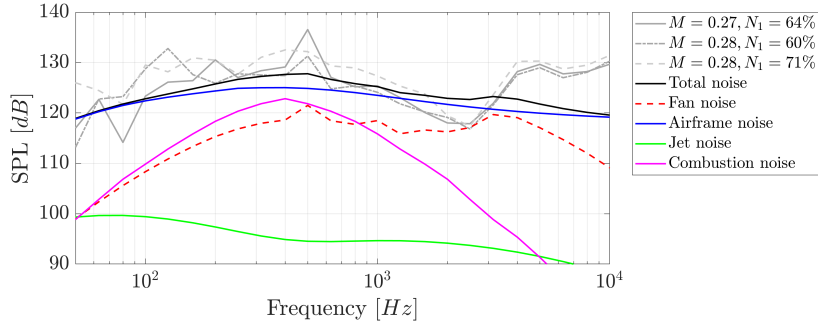


Figure 7.22: Comparison of the B777 noise spectrum (in 1/3-octave bands) between measurements with predictions for approach.

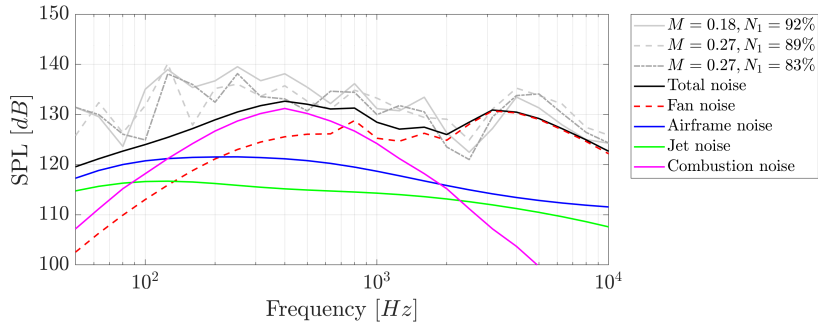


Figure 7.23: Comparison of the B777 noise spectrum (in 1/3-octave bands) between measurements with predictions for departure.

for the three aircraft analyzed. The frequency range between 1600–3150 Hz is overpredicted due to approximations of the liner dimensions and the higher 1/3-octaves bands are underpredicted, indicating that the higher harmonics of the fan are underestimated.

For departure, however, it was found a good match between predictions and measurements at the high frequency range. This indicates that only the first harmonics of the BPF are correctly predicted by the semi-empirical model. The BPF has a higher value for take-off and therefore the first harmonics are located at higher frequencies. For landing, the BPF is lower and consequently the harmonics located at high frequencies are higher than the 4th harmonic.

The case of the B777 supports that the higher harmonics are being underpredicted by the model. The predicted noise spectrum for this aircraft presented the lowest agreement with the measurements. The B777 is equipped with two GE90-115B engines, which have 22 fan blades and a maximum rotational speed of 2602 RPM. At full power the BPF is therefore approximately 950 Hz. At take-

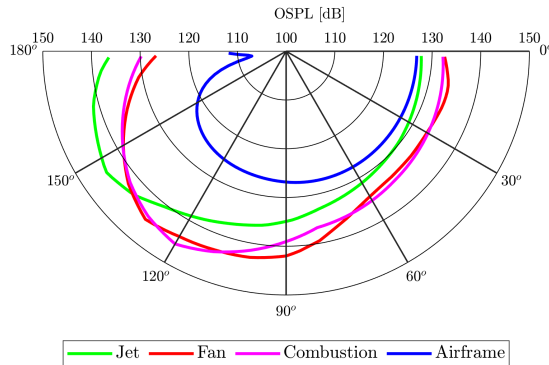


Figure 7.24: Values of OSPL predicted for the A330 over different polar angles and azimuth angle $\phi = 0^\circ$ during approach.

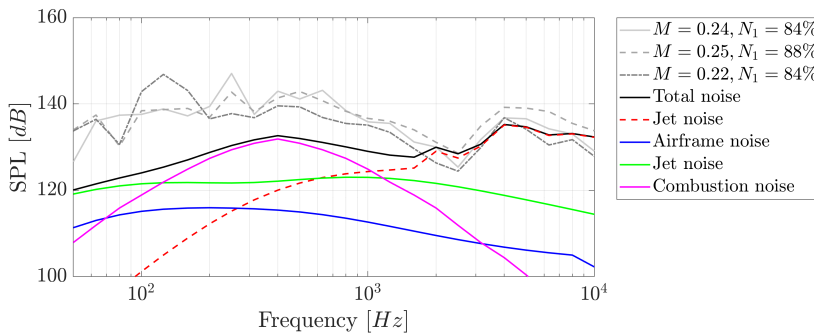


Figure 7.25: Comparison of the A330 noise spectrum (in 1/3-octave bands) between measurements with predictions for departure.

off, considering $N_1 = 90\%$, the 5th harmonic is located at the center frequency of 4000 Hz. It is visible that the prediction for this aircraft at take-off does not match the experimental results so well as the A320 and A330, which have BPF values around 2850 Hz and 1960 Hz, respectively. For landing, considering $N_1 = 60\%$, the BPF of the B777 is 572 Hz, and consequently the harmonics up to the 5th are in the low and mid frequency range.

This analysis showed that the semi-empirical methods can provide a good agreement with experimental data for take-off if jet noise installation effects are taken into consideration. Research on this topic indicates a SPL deviation up to 10 dB in the far field for low frequencies in relation to an isolated jet [48]. The empirical models could be adjusted based on the findings of these high-fidelity predictions.

Table 7.2: Measured and predicted values of OSPL for the A320, B777 and A330 at a polar angle of 90° and azimuthal angle of 0°.

	Airbus A320		Boeing B777		Airbus A330
	Landing	Take-off	Landing	Take-off	Take-off
Predicted	130.6	136.4	138.0	142.5	144.4
Measured	135.5	144.0	142.0	148.0	152.9

For landing, the experimental noise spectrum is in agreement with the prediction only for low frequencies. The results indicate that fan noise is underestimated for low values of BPF.

8

Summary and Outlook

8.1. Summary

This thesis has analyzed different aspects relevant to future low-noise aircraft. The shielding of engine noise, particularly of fan noise, by the airframe is a key factor for future designs. This topic was explored in two of the objectives of this work:

- 1. Development and validation of a noise shielding prediction tool suitable to be used for low-noise aircraft concepts, i.e., accurate, flexible and time-efficient.**
- 2. Explore the potential of a low-noise version of the B747-400 aircraft, with over the wing engines.**

An approach based on the Kirchhoff integral method and the Modified Theory of Physical Optics was considered to have the best trade-off between accuracy, flexibility and computational time relative to other noise shielding computation methods. This trade-off was presented in Chapter 2, as well as the detailed formulation of the selected approach. The implementation of this method, which considers a monopole source shielded by a sharp-edged obstacle, was validated with literature results.

An experimental campaign, analyzed in Chapter 4, studied the noise shielding of an omni-directional source and a propeller by a wing and a flat plate with the same dimensions. The experiments took place in an anechoic vertical wind tunnel in order to minimize external noise sources and reflections.

The experimental and predicted values of noise shielding were in close agreement for the case of an omni-directional source shielded by a flat plate (maximum deviation of 3 dB). The beamforming plots confirmed the agreement between predictions and experimental data as similar noise diffraction patterns were observed at the edges of the obstacle.

A second experiment considered an omni-directional noise source shielded by a wing. It was observed that the leading edge significantly affected noise shielding,

due to the presence of creeping rays. In addition, the noise diffraction patterns around the wing observed in the beamforming plots, differ from those found for the flat plate, considering the same relative positions of the obstacle, noise source and microphone array. Based on these results, the prediction method was extended to include the effect of the creeping rays.

The next experiment assessed the noise shielding of a propeller by a wing. The experimental values of noise shielding were significantly reduced compared with the case of the omni-directional source. In addition, the values of noise shielding were higher at the frequencies of the harmonics, indicating that tonal noise is more efficiently shielded than broadband noise.

Beamforming was used to identify external noise sources originating from the experimental setup that could interfere with the values of noise shielding. Thus, frequencies affected by the presence of external noise sources were not used in this analysis of noise shielding of a propeller.

Propellers are complex noise sources due to the different mechanisms of noise generation. This research work found that the agreement between experimental and predicted values of noise shielding at the frequencies of the harmonics improves when approximating the directivity of the propeller as a dipole - the monopole and the multi-source approximations did not provide realistic values of noise shielding for a propeller.

The noise shielding tool was applied to the case of an operating aircraft in Chapter 3. Landing flyovers measurements of the aircraft Fokker 70 were used for the comparison between predicted and experimental values of noise shielding. The aircraft geometry, velocity, altitude and attitude were approximated. The measured noise spectrum at the overhead time was used to simulate the engine, and propagation effects were also taken into consideration. The measured curve of Overall Sound Pressure Level presented variations for the different flyovers, a fact attributed to external noise sources since the aircraft operating conditions were similar for all the measurements. As a consequence, not all Fokker 70 flyovers presented noise shielding and the experimental value estimated was not constant for all the flyovers. The determined average experimental value of noise shielding was 2 dB, whereas predictions indicated a value of 4 dB. The predicted value was obtained considering the curvature of the leading edge and using a realistic aircraft attitude in relation to the array.

Shielding of engine noise is an essential characteristic for low-noise aircraft concepts. Such concepts are not necessarily disruptive compared with conventional designs, such as the Blended Wing Body. A low-noise alternative of the Boeing 747-400, with the engines located over the wings, has been explored in this thesis. The noise shielding tool was incorporated in an existing computational framework of DLR, in order to determine optimal engine positions that maximize engine noise shielding and therefore minimize the noise footprint on the ground. The different engine locations affect the aerodynamics and flight performance, and therefore any resulting modifications to the aircraft design were taken into consideration in this analysis. The leading edge was simulated both as a sharp and a curved edge in order to assess differences, not only in the final noise impact, but also in the optimal

engine positions.

It was found that the optimal engine positions were different when considering a sharp or a curved leading edge. This result reinforces the importance of the creeping rays in noise shielding results, also observed in the wind-tunnel experiments. The resultant Sound Exposure Level on the ground for take-off was also different for the two leading edge approximations, with higher values for the sharp leading edge. For approach, the two cases resulted in similar Sound Exposure Level contours because the engine contribution to the total noise is not as relevant as for take-off.

Psychoacoustic annoyance metrics are increasingly seen as an alternative to traditional metrics in the assessment of aircraft annoyance, as they show a better agreement with psychoacoustic surveys. A third objective of this thesis investigated the hypothesis of correlating parameters of the aircraft design with sound quality metrics (loudness, tonality, sharpness and roughness):

3. Investigate the suitability of psychoacoustics metrics (using flyover measurements) in the design of new aircraft.

This investigation was based on a large set of flyover measurements of different aircraft types during landing and take-off. The acoustic array was located a few hundred meters from the airport, i.e., in a location representative of communities highly affected by aircraft noise.

It was observed that the sound quality metrics presented some variation for the same aircraft type, due to slight differences of the operating conditions. Aircraft noise was expected to present higher values of sharpness for take-off than for landing, but the opposite was observed, due to atmospheric attenuation. The value of roughness was also expected to be high during take-off aircraft, due to buzz-saw noise tones, which was contradicted by the experimental data. In addition, tonality, which is associated with fan noise, presented similar average values for the same aircraft type during take-off and landing. Fan noise is expected to be more prominent during landing, because it is partially masked by jet noise during take-off, however, modern turbofan engines present high values of bypass ratio, which results in a decrease of jet noise and consequently of the masking effect of the fan harmonics.

The sound quality metrics were found to have strong correlations with many aircraft design parameters. Such correlations were used to find empirical expressions for the sound quality metrics. Empirical expressions for take-off aircraft could be found for loudness, roughness and sharpness. For landing, empirical expressions were found only for loudness and tonality. The introduction of the operating conditions in the empirical expressions, such as the aircraft altitude, velocity and the rotational speed of the fan increased the agreement between experimental data and predictions.

This study indicates that the sound quality metrics and consequently psychoacoustic annoyance metrics can be used in multi-disciplinary computational frameworks to estimate the ground noise impact. The empirical expressions correlating

the aircraft design and operating conditions with the sound quality metrics showed encouraging results, taking into account the limited number of available operating conditions.

The last objective of this thesis analyzed whether widely used parametric semi-empirical methods are accurate enough to estimate aircraft noise and capture the noise variability observed in flyover measurements:

4. Comparison of flyover measurements with engine and airframe noise predictions using parametric semi-empirical methods. The limitations of such methods are assessed and a sensitivity analysis is performed to understand which parameters might be neglected or approximated when not available.

The different engine noise components (fan, jet, combustion) and airframe noise were analyzed separately. The input required for the airframe noise predictions is often available as it is mainly related with the aircraft dimensions. The input necessary for the engine noise predictions, however, require simulations of the engine performance for the operating conditions of the aircraft. Such simulations require detailed engine information, which is not always made available by the manufacturers. The sensitivity analysis of engine noise showed which variables have a greater influence on predictions, and which parameters can be approximated. It was also found that the variability of the noise spectra experimentally observed for flyovers of the same aircraft with slightly different operating conditions cannot be reproduced by the empirical models.

The predicted noise spectra for take-off aircraft were in agreement with the experimental spectra for high frequencies (from the 1/3-octave band of 3150 Hz), a range associated with fan noise. However, the low frequencies of the noise spectrum up to 2000 Hz are underpredicted. This resulted in an Overall Sound Pressure Level deviation between experimental data and predictions of approximately 7.5 dB for the Airbus 320, 8.5 dB for the Airbus 330 and 5.5 dB for the Boeing 777. These values are in line with high-fidelity predictions of jet installation noise.

The noise predictions for landing aircraft were also underpredicted for low frequencies, but the difference is lower than the value observed for take-off. This is a consequence of the reduced contribution of the jet to the total noise. In contrast to what was observed for take-off, the high frequencies are underpredicted for landing. It was observed that fan noise predictions could only estimate with accuracy the first five harmonics of the fan, which poses a problem for predictions of engine noise during landing. This resulted in an Overall Sound Pressure Level deviation between experiments and predictions of approximately 5 dB for the Airbus 320 and of 4 dB for the Boeing 777.

8.2. Outlook

The experiments and predictions carried out under Objectives 1 and 2 showed the complexity of engine noise shielding for aircraft under operating conditions. After reviewing the main results, the following recommendations can be made:

- The aircraft geometry should not be approximated by sharp edges before assessing the impact of the creeping rays on the noise shielding results. It is recommended to calculate the values of noise shielding for a few observer positions in the polar and azimuthal directions (to avoid excessively long computation times) for both the simplified (sharp-edged) and the original (with round edges) geometries and assess differences.
- According to the experimental results, tonal noise is more efficiently shielded than broadband noise. Therefore, in typical aircraft equipped with turbofan engines, shielding of fan noise results in a decrease of the ground noise level. However, other engine noise sources such as the jet and the combustor will not benefit from it. This should be taken into account when selecting the engine location.
- The impact of engine noise shielding can only be completely assessed when considering all the noise sources onboard and the aircraft trajectory. This was observed in the analysis of the low-noise version of the Boeing 747-400. Although significant fan noise shielding values were estimated for the approach condition, the noise impact on ground did not change because the fan contribution to the total noise was not as relevant as during departure.
- An insufficient discretization of the contour shadow-light of the aircraft results in erroneous noise shielding predictions. The number of points necessary to ensure an accurate prediction increases with the frequency, therefore the convergence study of the solution must consider the highest frequency of the noise source.
- The variation of velocity and altitude of the same aircraft type experimentally observed for the flyovers do not have a significant effect on the noise shielding results. Therefore, for the comparison between measurements of aircraft flyovers and predictions of noise shielding it is recommended the use of average values in order to simplify the process.

The empirical expressions correlating the sound quality metrics with the aircraft geometry and operating conditions, obtained under Objective 3, should be further investigated. The following steps are recommended as future work:

- Use of a larger dataset of flyovers measured at different locations in the vicinity of airports.
- Include other parameters dependent on the operating conditions, e.g. the flap deflection angle and the exhaust jet velocity.

The comparison between noise predictions and aircraft flyover data, carried out under Objective 4, suggests that the semi-empirical noise models can be further improved. Future work should focus on the following aspects:

- Installation effects are not included in the semi-empirical noise models. The analysis of Chapter 7 indicates that the engine noise prediction can be improved by taking jet installation noise into account, for instance by the means of an empirical constant dependent on the jet velocity.
- Harmonics higher than the fifth were underestimated by Heidmann's model. The empirical expressions for the fan inlet and outlet tones are linear equations that decrease with the number of the harmonic. This empirical expression can be adjusted for the higher harmonics using experimental data of engines with low values of maximum rotational speed of the fan (e.g. the GE90 family).

A

Appendix A - Green's function

The Green's functions in two and three dimensions, are expressed by Equation (A.1) and Equation (A.2), respectively,

$$G(\mathbf{p}, \mathbf{q}) = \frac{i}{4} H_0^{(1)}(kr) \quad (\text{A.1})$$

$$G(\mathbf{p}, \mathbf{q}) = \frac{1}{4\pi} \frac{e^{ikr}}{r}. \quad (\text{A.2})$$

The function $H_0^{(1)}$ is the spherical Hankel function of the first kind of order zero. These two equations are valid when $k \in \mathbb{C} \setminus \{0\}$. For the special case of $k = 0$ the Green's functions are given by Equation (A.3) and Equation (A.4), in two-dimensions and three-dimensions, respectively,

$$G_0(\mathbf{p}, \mathbf{q}) = -\frac{1}{2\pi} \log r, \quad (\text{A.3})$$

$$G_0(\mathbf{p}, \mathbf{q}) = \frac{1}{4\pi} \frac{1}{r}. \quad (\text{A.4})$$

B

Appendix B - Method of the stationary phase

Consider the notation introduced by Lummer [102] to express the discretization of the diffraction problem,

$$\mathbf{y}_0 = \mathbf{y} - s\mathbf{e} \quad (\text{B.1})$$

$$\mathbf{a} = \mathbf{y}_0 - \mathbf{x}_s \quad (\text{B.2})$$

$$\mathbf{b} = \mathbf{y}_0 - \mathbf{x}_s \quad (\text{B.3})$$

$$\mathbf{u} = \mathbf{a} \times \mathbf{b} \quad (\text{B.4})$$

$$\mathbf{v} = \mathbf{e} \times (\mathbf{a} - \mathbf{b}) \quad (\text{B.5})$$

$$\mathbf{a}^2 = \mathbf{a} \cdot \mathbf{a} \quad (\text{B.6})$$

$$\mathbf{b}^2 = \mathbf{b} \cdot \mathbf{b} \quad (\text{B.7})$$

$$\alpha = \mathbf{a} \cdot \mathbf{e} \quad (\text{B.8})$$

$$\beta = \mathbf{b} \cdot \mathbf{e} \quad (\text{B.9})$$

$$\gamma = \mathbf{a} \cdot \mathbf{b} \quad (\text{B.10})$$

$$\boldsymbol{\omega} = \mathbf{a} \times \mathbf{e} \quad (\text{B.11})$$

$$\mathbf{z} = \mathbf{v} + \mathbf{w} \quad (\text{B.12})$$

$$\boldsymbol{\rho} = \mathbf{a} + s\mathbf{e} \quad (\text{B.13})$$

$$\mathbf{r} = \mathbf{b} + s\mathbf{e} \quad (\text{B.14})$$

$$\boldsymbol{\rho}^2 = \mathbf{a}^2 + 2\alpha s + s^2 \quad (\text{B.15})$$

$$\mathbf{r}^2 = \mathbf{b}^2 + 2\beta s + s^2 \quad (\text{B.16})$$

$$\boldsymbol{\rho} \cdot \mathbf{r} = \gamma + (\alpha + \beta)s + s^2 \quad (\text{B.17})$$

$$(\boldsymbol{\rho} \times \mathbf{r}) \cdot d\mathbf{s} = (\mathbf{a} \times \mathbf{b}) \cdot \mathbf{e} ds \quad (\text{B.18})$$

$$\cos(\theta_s(s)) = \frac{a_x + se_x}{\rho(s)} \quad (\text{B.19})$$

The curvilinear abscissa of the stationary phase s^* is given by,

$$s^* = -\frac{|\boldsymbol{\omega}|\beta + |\mathbf{z}|\alpha}{|\boldsymbol{\omega}| + |\mathbf{z}|}. \quad (\text{B.20})$$

If the phase function $g(s)$ does not have any stationary phase points inside the segment Γ , the asymptotic expansion can be obtained by integration by parts as expressed in Equation (B.21),

$$I_\Gamma = \frac{1}{ik} \left[\frac{A_f(s_b)}{g'(s_b)} e^{ikg(s_b)} - \frac{A_f(s_a)}{g'(s_a)} e^{ikg(s_a)} \right] + O(k^{-1}). \quad (\text{B.21})$$

In this situation the integral is governed by its end points contribution. However, if g has one stationary point lying on Γ at s^* such that $g'(s^*) = 0$ and $g''(s^*) \neq 0$, the integral is governed by the stationary point contribution, and Equation (2.55) can be expressed as,

$$I_\Gamma = \frac{e^{i\frac{\pi}{4}}}{2} A_f(s^*) \sqrt{\frac{\pi}{kg''(s^*)}} e^{ikg(s^*)} + O(k^{-1/2}). \quad (\text{B.22})$$

The first and second derivatives of the phase function g can be defined as,

$$\begin{aligned} g'(s) &= \frac{dg}{ds} = \frac{d}{ds} (|\mathbf{r}(s)| + |\boldsymbol{\rho}(s)|) = \frac{1}{2|\mathbf{r}|} \frac{d}{ds} \mathbf{r}^2 + \frac{1}{2|\boldsymbol{\rho}|} \frac{d}{ds} \boldsymbol{\rho}^2 \\ &= \frac{\alpha + s}{|\boldsymbol{\rho}|} + \frac{\beta + s}{|\mathbf{r}|}, \end{aligned} \quad (\text{B.23})$$

$$\begin{aligned} g''(s) &= \frac{d}{ds} \left(\frac{\alpha + s}{|\boldsymbol{\rho}|} + \frac{\beta + s}{|\mathbf{r}|} \right) = \frac{|\boldsymbol{\rho}| - \frac{(\alpha+s)^2}{|\boldsymbol{\rho}|}}{\boldsymbol{\rho}^2} + \frac{|\mathbf{r}| - \frac{(\beta+s)^2}{|\mathbf{r}|}}{|\mathbf{r}|^2} \\ &= \frac{1}{|\mathbf{r}|} + \frac{1}{|\boldsymbol{\rho}|} - \frac{(\alpha + s)^2}{|\boldsymbol{\rho}|^3} - \frac{(\beta + s)^2}{|\mathbf{r}|^3}. \end{aligned} \quad (\text{B.24})$$

C

Appendix C - Evaluation of the line segment in the uniform theory of diffraction

Consider the diffraction integral of Equation (2.55) and the fundamental property of the Fresnel integral,

$$F[x] = U(-x) + \text{sign}(x)F[|x|], \quad (\text{C.1})$$

where U is the unit step function such as $U(-x) = 1$ if $x \leq 0$ and $U(-x) = 0$ if $x > 0$ and $\text{sign}(x) > 0$ if $x \geq 0$ and $\text{sign}(x) < 0$ if $x < 0$.

With a change of variable, the Fresnel integral becomes Eq.2.57, where t_d is the detour parameter, $t_d(s) = \epsilon_t(s)\sqrt{k|g(s^*) - g(s)|}$ with the shadow indicator $\epsilon_t(s) = 1$ if $s - s^* \geq 0$ and $\epsilon_t(s) = -1$ if $s - s^* < 0$. $E(s) = \frac{A_f(s)}{h(s)}$, and

$$h(s) = \begin{cases} k \frac{g'(s)}{2t_d(s)}, & \text{if } s \neq s^* \\ \sqrt{\frac{kg''(s^*)}{2}}, & \text{if } s = s^*. \end{cases} \quad (\text{C.2})$$

Therefore, the diffraction integral can be expressed as

$$\begin{aligned} I_\Gamma &= \int_{s_a}^{s_b} A_f(s) e^{ikg(s)} ds \\ &= \int_{s_a}^{\infty} A_f(s) e^{ikg(s)} ds - \int_{s_b}^{\infty} A_f(s) e^{ikg(s)} ds, \end{aligned} \quad (\text{C.3})$$

which results in the final expression of Eq.2.61.

D

Appendix D - Determination of the tone correction for the Tone Corrected Perceived Noise Level

The first step necessary for the PNL calculation is the determination of the slope of the spectrum in 1/3-octave bands,

$$\begin{aligned} s(3, k) &= \text{no value} \\ s(i, k) &= \text{SPL}(i, k) - \text{SPL}(i - 1, k), \quad i = 4, 5, \dots, 24 \end{aligned} \quad (\text{D.1})$$

where s is the slope in decibels, i is the 1/3-octave band considered and k is the index of the time step.

The next step identifies which values of s have a change of value greater than 5 dB, according to

$$|\Delta s(i, k)| = |s(i, k) - s(i - 1, k)| > 5 \text{ dB}. \quad (\text{D.2})$$

Then, three conditions need to be verified for the selected slope values s :

- If $s(i, k)$ is positive and greater than the previous slope $s(i - 1, k)$, the $\text{SPL}(i, k)$ values are selected;
- If $s(i, k)$ is zero or negative and $s(i - 1, k)$ is positive, then $\text{SPL}(i - 1, k)$ is selected;

- If none of the conditions above is verified, no $SPL(i, k)$ nor $SPL(i - 1, k)$ are selected.

In the next step the adjusted values of $SPL(i, k)$ ($SPL'(i, k)$), are obtained following the procedure described below:

- For the non selected $SPL(i, k)$, the value is not adjusted, i.e., $SPL'(i, k) = SPL(i, k)$;
- For the selected $SPL(i, k)$, $SPL'(i, k)$ is given by

$$SPL'(i, k) = \frac{1}{2} [SPL(i - 1, k) + SPL(i + 1, k)];$$

- If the $SPL(i, k)$ of the 24th 1/3-octave band is selected then,

$$SPL'(24, k) = SPL(23, k) + s(23, k).$$

The slope is then recalculated (s'), including an imaginary 25th 1/3-octave band:

$$\begin{aligned} s'(3, k) &= s'(4, k) \\ s'(i, k) &= SPL'(i, k) + SPL'(i - 1, k), \quad i = 4, 5, \dots, 24 \\ s'(25, k) &= SPL'(24, k). \end{aligned} \tag{D.3}$$

$$\tag{D.4}$$

In a next step, the average of three adjacent slopes s' is calculated for $i=3$ to 23,

$$\bar{s}(i, k) = \frac{1}{3} [s'(i, k) + s'(i + 1, k) + s'(i + 2, k)], \tag{D.5}$$

and the final values of sound pressure level, SPL'' , are calculated using the following expressions:

$$\begin{aligned} SPL''(3, k) &= SPL(3) \\ SPL''(i, k) &= SPL''(i - 1, k) + \bar{s}(i - 1, k), \quad i = 4, 5, \dots, 24. \end{aligned} \tag{D.6}$$

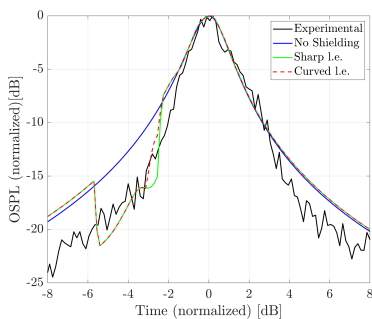
The difference between the original value of SPL and SPL'' for each 1/3-octave and time step, $F_t(i, k)$, is used to calculate the correction value C using the relations of Table D.1.

Table D.1: Tone correction factor C , according to the band frequency and protrusion of the level.

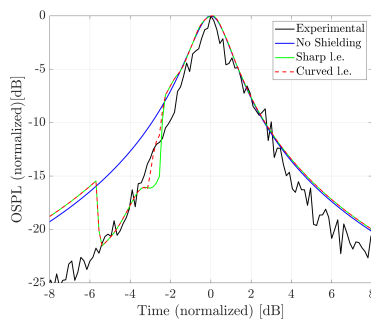
Frequency f [Hz]	F_t [dB]	C [dB]
$f \leq f < 500$	$1.5 \leq F_t < 3$	$F_t/3 - 0.5$
	$3 \leq F_t < 20$	$F_t/6$
	$20 \leq F_t$	3.333
$500 \leq f \leq 5\,000$	$1.5 \leq F_t < 3$	$2F_t/3 - 1$
	$3 \leq F_t < 20$	$F_t/3$
	$20 \leq F_t$	6.667
$5\,000 < f \leq 10\,000$	$1.5 \leq F_t < 3$	$F_t/3 - 0.5$
	$3 \leq F_t < 20$	$F_t/6$
	$20 \leq F_t$	3.333

E

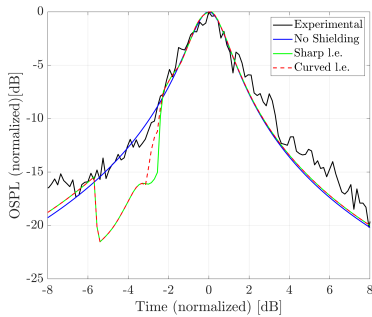
Appendix E - Flyover measurements of the F70 compared with predictions



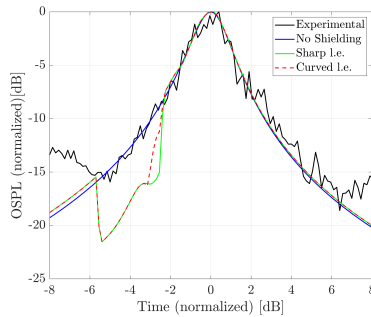
(a) Measurement 2.



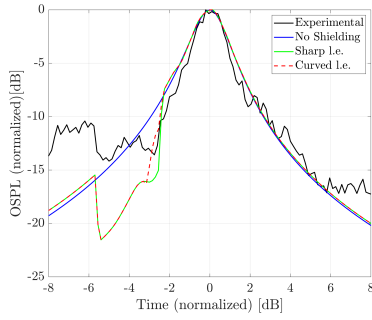
(b) Measurement 3.



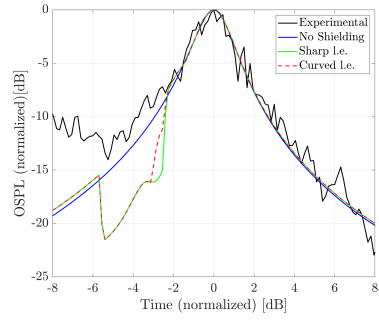
(c) Measurement 4.



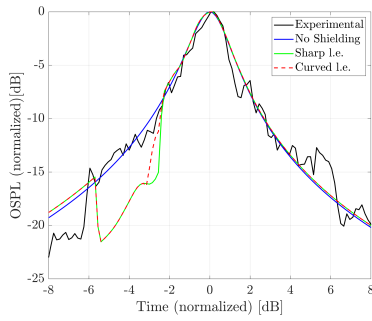
(d) Measurement 5.



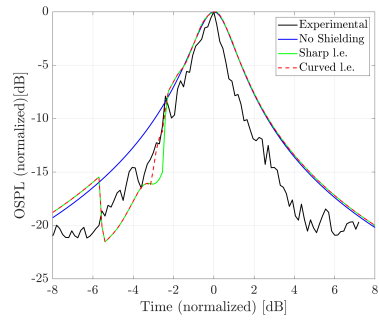
(e) Measurement 6.



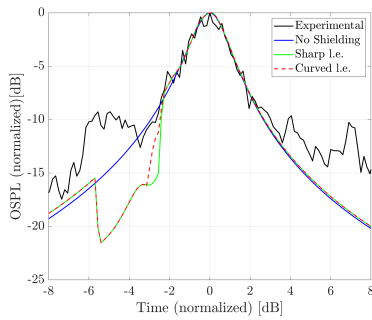
(f) Measurement 7.



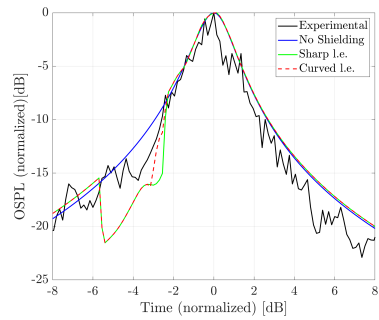
(g) Measurement 8.



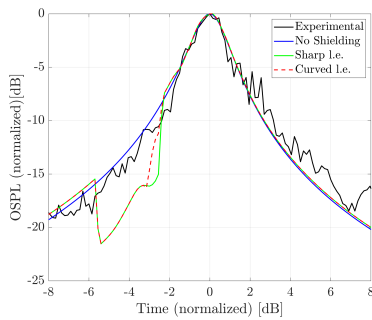
(h) Measurement 9.



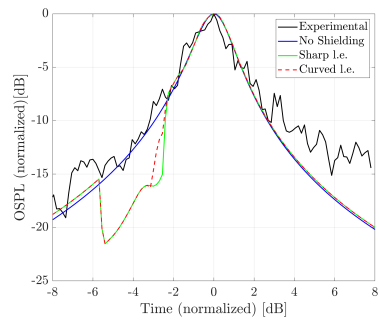
(i) Measurement 10.



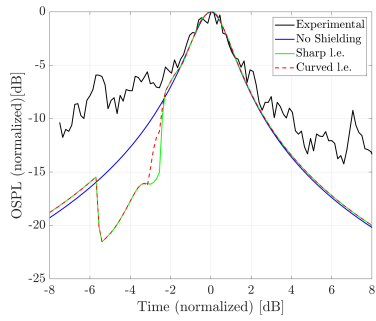
(j) Measurement 13.



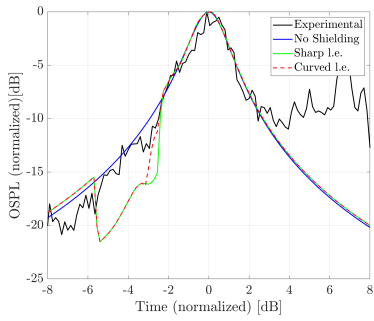
(k) Measurement 15.



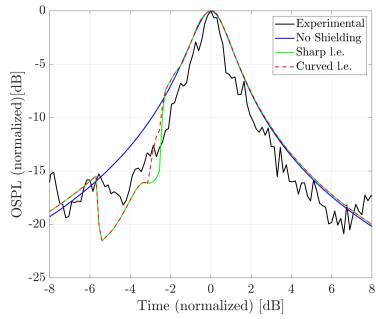
(l) Measurement 16.



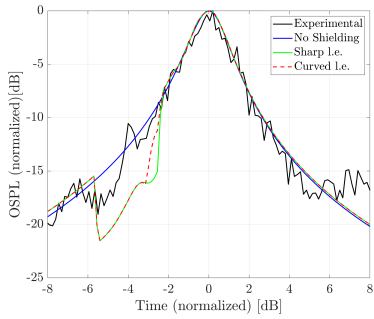
(m) Measurement 17.



(n) Measurement 18.



(o) Measurement 19.



(p) Measurement 20.

Figure E.1: Experimental and predicted OSPL for different flyover measurements of the F70.

References

- [1] ICAO Environmental Unit in collaboration with FCM Communications Inc, *ICAO Environmental Report*, (2007).
- [2] European Union Aviation Safety Agency (EASA), *European Aviation Environmental Report*, (2019).
- [3] Federal Aviation Administration (FAA), *FAA Aerospace Forecast – Fiscal Years 2019-2039*, (2019).
- [4] E. Ahyudanari, *Airport Location Of City Center And Its Contribution To Air Quality*, *Geographia Technica* **14**, 176 (2019).
- [5] M. Taptich, A. Horvath, and M. Chester, *Worldwide Greenhouse Gas Reduction Potentials in Transportation by 2050: World GHG Reduction Potentials in Transport, 2050*, *Journal of Industrial Ecology* **20**, 329 (2016).
- [6] M. Basner, M. Witte, and S. McGuire, *Aircraft Noise Effects on Sleep—Results of a Pilot Study Near Philadelphia International Airport*, *International Journal of Environmental Research and Public Health* **16**, 3178 (2019).
- [7] M. Rojek, M. Rajzer, W. Wojciechowska, T. Drozd, P. Skalski, T. Pizon, A. Januszewicz, and D. Czarnecka, *Relationship among long-term aircraft noise exposure, blood pressure profile, and arterial stiffness*, *Journal of hypertension* **37**, 1350 (2019).
- [8] T. Münzel, M. Sørensen, F. Schmidt, E. Schmidt, S. Steven, S. Kröller-Schön, and S. Daiber, *The Adverse Effects of Environmental Noise Exposure on Oxidative Stress and Cardiovascular Risk*, *Antioxidants & Redox Signaling* **28**, 873 (2018).
- [9] F. Gelderblom, T. Gjestland, S. Fidell, and B. Berry, *On the Stability of Community Tolerance for Aircraft Noise*, *Acta Acustica united with Acustica* **103**, 17 (2017).
- [10] P. Brooker, *Do people react more strongly to aircraft noise today than in the past?* *Applied Acoustics* **70**, 747 (2009).
- [11] Advisory Council for Aeronautics Research in Europe (ACARE), *Acare strategic research agenda issue 1*, (2002).
- [12] The International Civil Aviation Organization (ICAO), *The International Civil Aviation Organization (ICAO)*, (2008).

- [13] C. Hall, *Low noise engine design for the Silent Aircraft Initiative*, The Aeronautical Journal **113**, 599 (2009).
- [14] I. Hughes and A. Dowling, *The absorption of sound by perforated linings*, Journal of Fluid Mechanics **218**, 299 (1990).
- [15] G. Lilley, *The Prediction Of Airframe Noise And Comparison With Experiment*, Journal of Sound and Vibration **239**, 849 (2001).
- [16] W. Dobrzynski, *Almost 40 Years of Airframe Noise Research: What Did We Achieve?* Journal of Aircraft **47**, 353 (2010).
- [17] D. Angland, X. Zhang, and N. Molin, *Measurements of Flow Around a Flap Side Edge with Porous Edge Treatment*, AIAA Journal **47**, 1660 (2009).
- [18] W. Dobrzynski, B. Gehlhar, and H. Buchholz, *Model and full scale high-lift wing wind tunnel experiments dedicated to airframe noise reduction*, Aerospace science and technology **5**.
- [19] K. Yamamoto, K. Hayama, T. Kumada, and K. Hayashi, *A flight demonstration for airframe noise reduction technology*, CEAS Aeronautical Journal **10**, 77 (2019).
- [20] M. Zhang, A. Filippone, and N. Bojdo, *Multi-objective optimisation of aircraft departure trajectories*, Aerospace Science and Technology **79**, 37 (2018).
- [21] R. Hogenhuis, S. Hebly, and H. Visser, *Optimization of area navigation noise abatement approach trajectories*, Proceedings of the Institution of Mechanical Engineers, Part G: Journal of Aerospace Engineering **225**, 513 (2011).
- [22] K. White, M. Arntzen, F. Walker, F. Waiyaki, M. Meeter, and A. Bronkhorst, *Noise annoyance caused by continuous descent approaches compared to regular descent procedures*, Applied Acoustics **125**, 194 (2017).
- [23] M. Braakenburg, S. Hartjes, H. Visser, and S. Hebli, *Development of a Multi-Event Trajectory Optimization Tool for Noise-Optimized Approach Route Design*, in *11th AIAA Aviation Technology, Integration, and Operations (ATIO) Conference, September 20-22, Virginia Beach, VA* (2011) AIAA paper 2011-6929.
- [24] P. Okonkwo and H. Smith, *Review of evolving trends in blended wing body aircraft design*, Progress in Aerospace Sciences **82**, 1 (2016).
- [25] Y. Katsurayama and T. Imamura, *Numerical Simulation of Engine Noise Shielding around Blended Wing Body Aircraft*, Transactions Of The Japan Society For Aeronautical And Space Sciences **58**, 83 (2015).
- [26] A. Morris, P. Arendsen, G. LaRocca, M. Laban, R. Voss, and H. Hönlinger, *Mob-a european project on multidisciplinary design optimisation*, in *24th ICAS congress, Yokohama, Japan* (2004).

- [27] S. Mistry, *A novel Airframe Design Methodology for silent aircraft*, PhD thesis (2008).
- [28] C. Werner-Westphal, W. Heinze, and P. Horst, *Multidisciplinary Integrated Preliminary Design Applied to Unconventional Aircraft Configurations*, *Journal of Aircraft* **45**, 581 (2008).
- [29] DLR, <https://event.dlr.de/en/ila2018/dlr-lna-modell/>, Accessed in October 2019.
- [30] L. Bertsch, W. Heinze, and M. Lummer, *Application of an Aircraft Design-To-Noise Simulation Process*, in *14th AIAA Aviation Technology, Integration, and Operations Conference, June 16-20, Atlanta, GA (2014)* AIAA paper 2014-2169.
- [31] H. Fastl and E. Zwicker, *Psychoacoustics: facts and models*, 3rd ed., Springer series in information sciences No. 22 (Springer, Berlin ; New York, 2007).
- [32] L. Cattafesta, C. Bahr, and J. Mathew, *Fundamentals of Wind-Tunnel Design*, in *Encyclopedia of Aerospace Engineering*, edited by R. Blockley and W. Shyy (John Wiley & Sons, Ltd, Chichester, UK, 2010).
- [33] E. Duell, J. Yen, S. Arnette, and J. Walter, *Recent Advances in Large Scale Aeroacoustic Wind Tunnels*, in *8th AIAA/CEAS Aeroacoustics Conference & Exhibit, June 17-19, Breckenridge, Colorado (2002)* AIAA paper 2002-2503.
- [34] S. Lele and J. Nichols, *A second golden age of aeroacoustics?* *Philosophical Transactions of the Royal Society A: Mathematical, Physical and Engineering Sciences* **372** (2014).
- [35] M. Lighthill, *On sound generated aerodynamically I. General theory*, *Proceedings of the Royal Society of London. Series A, Mathematical and Physical Sciences* **211** (1952).
- [36] T. Colonius and S. Sanjiva, *Computational aeroacoustics: progress on nonlinear problems of sound generation*, *Progress in Aerospace Sciences* **40**, 345 (2014).
- [37] European Civil Aviation Conference (ECAC), *CEAC Doc. 29. Report on Standard method of Computing Noise Contours around Civil Airports*, (2005).
- [38] L. Bertsch, S. Guerin, G. Looye, and M. Pott-Pollenske, *The Parametric Aircraft Noise Analysis Module - Status overview and recent*, in *17th AIAA/CEAS Aeroacoustics Conference (32nd AIAA Aeroacoustics Conference), June 5-8, Portland, Oregon (2011)* AIAA paper 2011-2855.
- [39] W. Zorunski, *Aircraft noise prediction program theoretical manual, part 1*, (1982), NASA Technical Memorandum 83199.

- [40] W. Zorumski, *Aircraft noise prediction program theoretical manual, part 2*, (1982).
- [41] CANSO (Civil Air Navigation Services Organization), *Managing the Impacts of Aviation Noise, A Guide for Airport Operators and Air Navigation Service Providers*, (2015).
- [42] T. Colonius and S. Sanjiva, *Concepts of perceived noisiness, their implementation and application*, *Journal of the Acoustical Society of America* **43**, 344 (1967).
- [43] S. More, *Aircraft Noise Characteristics and Metrics*, PhD thesis (2011).
- [44] A. Vieira, M. Snellen, and D. Simons, *Assessing the shielding of engine noise by the wings for current aircraft using model predictions and measurements*, *The Journal of the Acoustical Society of America* **143**, 388 (2018).
- [45] A. Vieira, M. Snellen, A. Malgoezar, R. Merino-Martínez, and D. Simons, *Analysis of shielding of propeller noise using beamforming and predictions*, *The Journal of the Acoustical Society of America* **146** (2019).
- [46] D. Braga, *Fan noise prediction of aero-engines based on a modal approach in the presence of acoustic treatment and inviscid sheared flows*, PhD thesis (2019).
- [47] L. Bertsch, D. Simons, and M. Snellen, *Aircraft Noise: The major sources, modelling capabilities, and reduction possibilities*, (2015), technical Report.
- [48] L. Rego, F. Avallone, D. Ragni, and D. Casalino, *Jet-installation noise and near-field characteristics of jet-surface interaction*, *Journal of Fluid Mechanics* **895** (2020), <https://doi.org/10.1017/jfm.2020.294>.
- [49] S. Pietrzko and R. Bütikofer, *FLULA - Swiss Aircraft Noise Prediction Program*, in *Acoustics 2002 - Innovation in Acoustics and Vibration, 13-15 November, Adelaide, Australia* (2002).
- [50] R. Gillian, *Aircraft Noise Prediction Program User's Manual*, (1982), NASA Technical Memorandum 84486.
- [51] M. Fink, *Airframe Noise Prediction Method*, *FAA Research*, (1977), Report, FAA-RD-77-29.
- [52] J. Stone, D. Groesbeck, and C. Zola, *Conventional profile coaxial jet noise prediction*, *AIAA Journal* **21** (1983).
- [53] M. Heidmann, *Interim prediction method for fan and compressor source noise*, (1977), NASA Technical Report TMX-71763.

- [54] J. Bridges and A. Khavaran, *Assessment of Current Jet Noise Prediction Capabilities*, in *14th AIAA/CEAS Aeroacoustics Conference, 5-7 May, Vancouver, British Columbia, Canada* (Vancouver, British Columbia, Canada, 2008) AIAA paper 2008-2933.
- [55] L. Lopes and C. Burley, *Anopp2 user's manual*, (2016), NASA Technical Memorandum 2016-219342.
- [56] L. Lopes and C. Burley, *Design of the Next Generation Aircraft Noise Prediction Program: ANOPP2*, in *17th AIAA/CEAS Aeroacoustics Conference, 5-8 June, Portland, Oregon* (2011) AIAA paper 2011-2854.
- [57] W. Dobrzynski and M. Pott-Pollenske, *Slat noise source studies for farfield noise prediction*, in *7th AIAA/CEAS Aeroacoustics Conference, 28-30 May, Maastricht, Netherlands* (Maastricht, Netherlands, 2001) AIAA paper 2001-2158.
- [58] W. Dobrzynski, L. Chow, A. Boillot, O. Dereure, and N. Molin, *Experimental Assessment of Low Noise Landing Gear Component Design*, in *15th AIAA/CEAS Aeroacoustics Conference, 11-13 May, Miami, Florida, USA* (2009) AIAA paper 2009-3276.
- [59] J. Emmerling, S. Kazin, and R. Matta, *Core engine noise control program. Vol 3: Prediction methods, suppl. 1: Extension of prediction methods*, (1976), Technical Report FAA-RD-74-125, FAA.
- [60] P. Ho and V. Doyle, *Combustion noise prediction update*, in *5th AIAA Aeroacoustics conference, 12-14 May, Seattle, WA, U.S.A.* (1979).
- [61] GSP Development Team, *GSP 11 user manual*, (2016).
- [62] <https://www.flight-mechanic.com/exhaust-systems-with-turbocharger-part-one>, Accessed in May 2020.
- [63] J. Tyler and T. Sofrin, *Axial flow compressor noise studies*, SAE transactions **70** (1962).
- [64] K. Kontos, R. Kraft, and P. Gliebe, *Improved Nasa ANOPP noise prediction computer code for advanced subsonic propulsion systems. Volume 2: Fan suppression model development*, (1996), NASA Technical Report CR-202309.
- [65] M. Lighthill, *On sound generated aerodynamically i. general theory*, Proceedings of the Royal Society of London. Series A, Mathematical and Physical Sciences **211** (1952).
- [66] M. Lighthill, *On sound generated aerodynamically ii. turbulence as a source of sound*, Proceedings of the Royal Society of London. Series A, Mathematical and Physical Sciences **222** (1954).

- [67] N. Curle, *The influence of solid boundaries upon aerodynamic sound*, Proceedings of the Royal Society of London. Series A, Mathematical and Physical Sciences **231** (1955).
- [68] J. Ffowcs-Williams and D. Hawkings, *Sound generation by turbulence and surfaces in arbitrary motion*, Philosophical transactions of the Royal Society of London **264** (1969).
- [69] J. Stone, E. Krejsa, B. Clark, and J. Berton, *Jet noise modeling for suppressed and unsuppressed aircraft in simulated flight*, (2006), NASA Technical Memorandum 2009-215524.
- [70] D. Simons, M. Snellen, R. Merino-Martínez, and A. Malgoezar, *Noise breakdown of landing aircraft using a microphone array and an airframe noise model*, in *Internoise, Hong Kong* (2017).
- [71] S. Wagner, G. Guidati, and B. Bareiss, *Wind Turbine Noise* (Springer, 1996).
- [72] M. Guynn, J. Berton, E. Hendricks, D. Thurman, M. Tong, and W. Haller, *Initial Assessment of Open Rotor Propulsion Applied to an Advanced Single-Aisle Aircraft*, in *11th AIAA Aviation Technology, Integration, and Operations (ATIO), 20-22 September, Virginia Beach, VA* (2011).
- [73] S. Yilmaz, D. Erdem, and M. Kavsaoğlu, *Effects of Duct Shape on a Ducted Propeller Performance*, in *51st AIAA Aerospace Sciences Meeting including the New Horizons Forum and Aerospace Exposition, 7-10 January, Grapevine, Texas* (2013).
- [74] A. Malgoezar, A. Vieira, M. Snellen, D. Simons, and L. Veldhuis, *Experimental characterization of noise radiation from a ducted propeller of an unmanned aerial vehicle*, *International Journal of Aeroacoustics* **18** (2019).
- [75] M. Hoogreef, R. de Vries, and L. Veldhuis, *Conceptual Assessment of Hybrid Electric Aircraft with Distributed Propulsion and Boosted Turbofan*, in *AIAA Scitech 2019 Forum, 7-11 January, San Diego, California* (2019).
- [76] J. Bonet, H. Schellenger, B. Rawdon, K. Elmer, S. Wakayama, D. Brown, and Y. Guo, *Environmentally responsible aviation (ERA) Project -N+2 Advanced Vehicle Concepts Study and Conceptual Design of Subscale Test Vehicle (STV)*, (2011), final Report NASA/CR—2011–216519.
- [77] <https://www.hyundai.com/worldwide/en/company/news/newsroom/news/-0000016369>, Accessed in June 2020.
- [78] J. Made and D. Kurtz, *A Review of Aerodynamic Noise From Propellers, Rotors, and Liff Fans*, (1970), NASA Technical Report 32-1462.
- [79] L. Gutin, *On the sound field of a rotating propeller*, (1948), NASA Technical Memorandum No. 1195.

- [80] M. Lighthill, *On Sound Generated Aerodynamically. I. General Theory*, Proceedings of the Royal Society of London A **211**, 564 (1952).
- [81] S. Rienstra and A. Hirschberg, *An introduction to acoustics* (Technische Universiteit Eindhoven, 2004).
- [82] J. Strutt, *The Theory of Sound*, Cambridge Library Collection - Physical Sciences, Vol. 1 (Cambridge University Press, 1976).
- [83] D. Russell, J. Titlow, and Y. Bemmen, *Acoustic monopoles, dipoles, and quadrupoles: An experiment revisited*, American Journal of Physics **67**, 660 (1999).
- [84] Z. Maekawa, *Noise reduction by screens*, Applied acoustics **1**, 157 (1968).
- [85] U. Kurze and G. Anderson, *Sound attenuation by barriers*, Applied Acoustics **4**, 35 (1971).
- [86] K. Kontos, B. Janardan, and P. Gliebe, *Improved NASA-ANOPP noise prediction computer code for advanced subsonic propulsion systems, volume 1: ANOPP evaluation and fan noise model improvement*, (1996), NASA Contractor Report 195480.
- [87] S. Kirkup, *The Boundary Element Method in Acoustics*, Journal of Computational Acoustics **8**, 257 (2007).
- [88] A. Burton, *The Solution of Helmholtz Equation in Exterior Domains using Integral Equations* (NPL Report NAC30, National Physical Laboratory, 1973).
- [89] D. Lee, *Review: The Use of Equivalent Source Method in Computational Acoustics*, Journal of Computational Acoustics **25** (2017).
- [90] A. Tinetti and M. Dunn, *The fast scattering code (FSC): Validation studies and program guidelines*, (2011), NASA, Contractor report CR-2011-217158.
- [91] J. Keller, *Geometrical theory of diffraction*, Journal of the Optical Society of America **52**, 116 (1962).
- [92] A. Agarwal, A. Dowling, H. Shin, W. Graham, and S. Sefi, *A Ray Tracing Approach to Calculate Acoustic Shielding by the Silent Aircraft Airframe*, in *12th AIAA/CEAS Aeroacoustics Conference (27th AIAA Aeroacoustics Conference), May 8-10, Cambridge, Massachusetts* (2006) AIAA paper 2006-2618.
- [93] D. Colas and Z. Spakovszky, *A turbomachinery noise shielding framework based on the modified theory of physical optics*, in *19th AIAA/CEAS Aeroacoustics Conference, 27-29 May, Berlin, Germany* (2013) AIAA paper 2013-2136.
- [94] C. Schultheisz, *Numerical solution of the Huygens–Fresnel–Kirchhoff diffraction of spherical waves by a circular aperture*, Journal of the Optical Society of America A **11**, 774 (1994).

- [95] Y. Umul, *Modified diffraction theory of Kirchhoff*, Journal of the Optical Society of America A **25**, 1850 (2008).
- [96] K. Miyamoto and E. Wolf, *Generalizaion of the Maggi-Rubinowicz theory of the boundary diffraction wave - Part i*, Journal of the Optical Society of America **52**, 615 (1962).
- [97] R. Lewis and J. Boersma, *Uniform Asymptotic Theory of Edge Diffraction*, Journal of Mathematical Physics **10**, 2291 (1969).
- [98] A. Sommerfeld, *Mathematical Theory of Diffraction. In: Mathematical Theory of Diffraction. Progress in Mathematical Physics*, Springer series in information sciences (Birkhäuser, Boston, MA, 2004).
- [99] J. Jiménez and E. Hita, *Babinet's Principle in Scalar Theory of Diffraction*, Optical Review **8** (2001).
- [100] F. Leppington, *Curvature Effects in the Diffraction of Short Waves into a Shadow*, Aeronautical Research Council, Department of Mathematics, Imperial College (1970).
- [101] P. Pathak, W. Burnside, and R. Marhefka, *A uniform GTD analysis of the scattering of electromagnetic waves by a smooth convex surface*, (1979), Electroscience Laboratory, Ohio State University, Technical Report No. 784583-4.
- [102] M. Lummer, *Maggi-Rubinowicz Diffraction Correction for Ray-Tracing Calculations of Engine Noise Shielding*, in *14th AIAA/CEAS Aeroacoustics Conference (29th AIAA Aeroacoustics Conference)*, 5-7 May, Vancouver, British Columbia, Canada (2008) AIAA paper 2008-3050.
- [103] D. Colas, *A Diffraction Integral Based Turbomachinery Noise Shielding Method*, MSc thesis, Massachusetts Institute Of Technology (2011).
- [104] A. Vieira, M. Snellen, and D. Simons, *Assessment of Engine Noise Shielding by the Wings of Current Turbofan Aircraft*, in *The 24th International Congress on Sound and Vibration, 23-27 July, London, UK (2017)*.
- [105] D. Johnson and D. Dudgeon, *Array Signal Processing: Concepts and Techniques* (Prentice Hall, Englewood Cliffs, 1993).
- [106] *On the estimation of spectra by means of non-linear functions of the covariance matrix*, **28**, <https://doi.org/10.1111/j.1365-246X.1972.tb06146.x>.
- [107] R. Dougherty, *Functional Beamforming*, Proceedings of the 5th Berlin Beamforming Conference ().
- [108] R. Dougherty, *Functional Beamforming for Aeroacoustic Source Distributions*, in *20th AIAA/CEAS Aeroacoustics Conference, 16-20 June, Atlanta, GA (2014)*.

- [109] P. Sijtsma, *CLEAN Based on Spatial Source Coherence*, International Journal of Aeroacoustics **6**, 347 (2007).
- [110] T. Brooks and W. Humphreys, *A deconvolution approach for the mapping of acoustic sources (DAMAS) determined from phased microphone arrays*, Journal of Sound and Vibration **294**, 856 (2006).
- [111] T. Brooks and W. Humphreys, *Three-dimensional applications of DAMAS methodology for aeroacoustic noise source definition*, in *11th AIAA/CEAS Aeroacoustics Conference, 23-25 May, Monterey, California (2005)* AIAA paper 2005-2960.
- [112] E. Sarradj, *Three-dimensional acoustic source mapping with different beam-forming steering vector formulations*, Advances in Acoustics and Vibration **2012** (2012).
- [113] L. Rayleigh, *XXXI. Investigations in optics, with special reference to the spectroscopy*, The London, Edinburgh, and Dublin Philosophical Magazine and Journal of Science **8**, 261 (1879).
- [114] S. Stevens, *The measurement of loudness*, The Journal of the Acoustical Society of America **27** (1955).
- [115] S. Stevens, *Calculation of the loudness of complex noise*, The Journal of the Acoustical Society of America **28** (1956).
- [116] S. Stevens, *Procedure for calculating loudness: Mark vi*, The Journal of the Acoustical Society of America **33** (1961).
- [117] Z. Zhang and M. Shrestha, *Sound Quality User-defined Cursor Reading Control -Tonality Metric*, Tech. Rep. (Brüel & Kjær, 2003).
- [118] R. Bennett and K. Pearsons, *Handbook of Aircraft Noise Metrics*, Tech. Rep. (1981) NASA Contractor Report 3406.
- [119] E. Zwicker, H. Fastl, U. Widmann, K. Kurakata, S. Kuwano, and S. Namba, *Program for calculating loudness according to din 45631 (iso 532b)*, The Journal Of The Acoustical Society Of Japan **12** (1991).
- [120] K. Kryter, *Concepts of Perceived Noisiness, Their Implementation and Application*, The Journal of the Acoustical Society of America **43** (1968).
- [121] C. Powell and J. Fields, *Human Response to aircraft noise*, Tech. Rep. (NASA, 1991).
- [122] A. Sahai, *Consideration of Aircraft Noise Annoyance during Conceptual Aircraft Design*, PhD thesis, RWTH Aachen University (2016).
- [123] K. Kryter, *Judges noisiness of a band of random noise containing an audible pure tone*, The Journal of the Acoustical Society of America **38** (1965).

- [124] *ISO 532-1:2017(E) - Acoustics – Method for calculating loudness – Zwicker method*, (2017).
- [125] E. Terhardt, *Calculating virtual pitch*, *Hearing Research* **1** (1979).
- [126] W. Aures, *Berechnungsverfahren für den sensorischen wohlklang beliebiger schallsignale*, *Acta Acustica united with Acustica* **59** (1985).
- [127] E. Terhardt, G. Stoll, and M. Seewann, *Algorithm for extraction of pitch and pitch salience from complex tonal signals*, *The Journal of the Acoustical Society of America* **71** (1982).
- [128] G. von Bismarck, *Sharpness as an attribute of the timbre of steady sounds*, *Acta Acustica united with Acustica* **30** (1974).
- [129] W. Aures, *A procedure for calculating auditory roughness*, *Acustica* **58** (1985).
- [130] P. Daniel and R. Weber, *Psychoacoustical Roughness: Implementation of an Optimized Model*, *Acta Acustica united with Acustica* **83** (1997).
- [131] A. Osses Vecchi, R. García León, and A. Kohlrausch, *Modelling the sensation of fluctuation strength*, in *22nd International Congress on Acoustics: Acoustics for the 21st Century* (2016).
- [132] J. Angerer, D. McCurdy, and R. Erickson, *Development of an annoyance model based upon elementary auditory sensations for steady-state aircraft interior noise containing tonal components*, *NASA Technical Memorandum* 104147.
- [133] K. M. Västfjäll, D., *Emotion in Product Sound Design*, in *Proceedings of Journées Design Sonore, March 20-21, Paris* (2002).
- [134] A. Vieira, M. Koch, L. Bertsch, M. Snellen, and D. Simons, *Simulation Methodologies of Engine Noise Shielding by Wings Within Conceptual Aircraft Design*, *Journal of Aircraft* **57** (2020).
- [135] <https://en.ids-imaging.com/store/ui-1220le-rev-2.html>, Accessed in December 2019.
- [136] <http://www.puiaudio.com/product-detail.aspx?categoryId=4&partnumber=POM-2735P-R>, Accessed in December 2019.
- [137] R. van der Groot, J. Hendriks, K. Scheper, G. Hermans, W. van der Wal, and D. Simons, *A low cost, high resolution acoustic camera with a flexible microphone configuration*, in *Berlin Beamforming Conference* (2012).
- [138] G. Howell, A. Bradley, M. McCormick, and J. Brown, *De-Dopplerization and acoustic imaging of aircraft flyover noise measurements*, *Journal of Sound and Vibration* **105**, 151 (1986).

- [139] *ISO norm 3745 - Acoustics - Determination of sound power levels and sound energy levels of noise sources using sound pressure - Precision methods for anechoic rooms and hemi-anechoic rooms, Tech. Rep. 3 (International Organization for Standardization), (2012).*
- [140] *ISO norm 33382 - Acoustics - Measurements of room acoustics parameters, Tech. Rep. 1 (International Organization for Standardization), (2012).*
- [141] C. Arce León, R. Merino-Martínez, R. Ragni, F. Avallone, and M. Snellen, *Boundary layer characterization and acoustic measurements of flow-aligned trailing edge serrations*, *Experiments in Fluids* **57** (2016).
- [142] S. Ghaemi, D. Ragni, and F. Scarano, *PIV-based pressure fluctuations in the turbulent boundary layer*, *Experiments in Fluids* **53**, 1823 (2012).
- [143] G.R.A.S. Sound & Vibration 40 PH CCP Freefield array microphone, Accessed in February 2020.
- [144] G.R.A.S. Pistonphone, *G.R.A.S. Sound & Vibration - 42AA Pistonphone class 1*, Accessed in February 2020.
- [145] C. Vlemmix, *Acoustic Array Design: The design of a reconfigurable phased microphone array for aeroacoustic wind tunnel measurements*, (2017).
- [146] A. Luesutthiviboon, S. and Malgoezar, M. Snellen, and D. Simons, *Improving source discrimination performance by using an optimized array and adaptive high-resolution clean-sc beamforming*, in *Berlin Beamforming Conference 2018* (2018).
- [147] L. Bertsch, *Noise Prediction Within Conceptual Aircraft Design*, PhD thesis, Göttingen (2013).
- [148] A. Agarwal and A. Dowling, *The calculation of acoustic shielding of engine noise by the silent aircraft airframe*, in *11th AIAA/CEAS Aeroacoustics Conference, May 23-25, Monterey, California* (2005) AIAA paper 2005-2996.
- [149] W. Heinze, *Ein Beitrag zur quantitativen Analyse der technischen und wirtschaftlichen Auslegungsgrenzen verschiedener Flugzeugkonzepte für den Transport grosser Nutzlasten*, Tech. Rep. ZLR-Forschungsbericht 94-01 (1994).
- [150] R. Becker, F. Wolters, M. Nauroz, and T. Otten, *Development of a Gas Turbine Performance Code and its Application to Preliminary Engine Design*, in *Deutscher Luft- und Raumfahrtkongress* (Bremen, Germany, 2011).
- [151] J. Blinstrub, *Immission-Based Noise Reduction within Conceptual Aircraft Design*, PhD thesis, Göttingen (2019).
- [152] M. Koch and L. Bertsch, *Engine noise source placement for shielding calculation*, in *Inter-Noise* (Madrid, Spain, 2019).

- [153] M. Smith, *Aircraft noise* (Cambridge University Press, 1989).
- [154] F. Hutcheson, C. Bahr, and R. Thomas, *Experimental Study of Noise Shielding by a NACA 0012 Airfoil*, in *2018 AIAA/CEAS Aeroacoustics Conference*, June 25-29, Atlanta, Georgia (2018).
- [155] K. Rossignol and J. Delfs, *Analysis of the Noise Shielding Characteristics of a NACA0012 2D Wing*, in *22nd AIAA/CEAS Aeroacoustics Conference*, 30 May - 1 June, Lyon, France (2006).
- [156] A. Vieira, M. Snellen, and D. Simons, *Experimental Assessment of Sound Quality Metrics for Takeoff and Landing Aircraft*, *AIAA Journal* **59** (2020).
- [157] R. Dougherty, *Spiral-shaped array for broadband imaging*, us5838284a, ().
- [158] A. McAlpine and M. Fisher, *The effect of acoustic lining on "buzz-saw" noise generated by an aero-engine*, in *7th AIAA/CEAS Aeroacoustics Conference*, 28-30 May, Maastricht, Netherlands (2001) AIAA paper 2001-2201.
- [159] S. Uellenberg, *Buzzsaw noise predictions for modern turbofans*, in *10th AIAA/CEAS Aeroacoustics Conference*, 10-12 May, Manchester, Great Britain (2004) AIAA paper 2004-3000.
- [160] *Comparison of semi-empirical noise models with flyover measurements of operating aircraft*, Currently under review in the *Journal of Aircraft*.
- [161] D. Simons, M. Snellen, B. van Midden, M. Arntzen, and D. Bergmans, *Assessment of Noise Level Variations of Aircraft Flyovers Using Acoustic Arrays*, *Journal of Aircraft* **52** (2015).
- [162] L. Rego, F. Avallone, D. Ragni, and D. Casalino, *Noise Amplification Effects due to Jet-Surface Interaction*, in *AIAA Scitech 2019 Forum*, 7-11 January, San Diego, California (San Diego, California USA, 2019).

Acknowledgements

These four years of PhD project were an unique experience and I would like to express my gratitude to those who supported me in this challenging but rewarding journey.

Firstly I would like to thank my promotors, Prof. dr. Dick Simons and Prof. dr. ir. Mirjam Snellen, for giving me the opportunity to be part of this research group. You trusted me as an independent researcher and questioned my work in a constructive way. Thanks for your advice and support. I sincerely appreciate your enthusiasm and positivity, which always led to fruitful discussions.

I would like to acknowledge the dedication of all the committee members of my Ph.D. defense. Thank you for your valuable comments and for attending my defense.

I would like to express my gratitude to Dr. ir. Lothar Bertsch, for encouraging my collaboration with DLR and Marc Koch. Marc, thank you for the effort you put into this joint project and the endless hours of simulations at DLR.

ANCE has a great work atmosphere, and my colleagues made every coffee and lunch break the perfect moment to relax and also to learn something new from all the different backgrounds and cultures. Big thanks to Tannaz, Timo and Leo - we started the PhD roughly at the same time and I feel we went through this long process together, sharing many doubts and thoughts. A special thanks to my office mate Colin, always available for a coffee and a true brewing expert. Thanks also to Anwar, for being such a fun company during the long hours we spent at the wind tunnel. This list is not complete without mentioning Feijia, Roberto, Salil, Alejandro and Bieke - I greatly appreciated being surrounded by such interesting and caring colleagues.

I would like to extend my sincere gratitude to Lisette, our group secretary. You take a personal interest in every PhD student arriving and you are essential for the cohesion of the group. I learned a lot from your stories and experiences.

Particularly important to me during this time was my good friend Alice. Thank you for your constant support and our long conversations over great coffee and cake. Our quest for the best coffee place in Delft was a success but your cheesecake is still the best by far.

Many thanks to my old friend Nuno, always available for some relaxing nonsense chit-chat but also serious theoretical discussions. I hope to receive an invitation for your Ph.D. defense soon!

Thanks also to Xavier, who challenged me to evolve at both professional and personal level. You were a great friend during these last four years and the perfect host of Rotterdam- you have a true talent to find the best spots.

I am also grateful to Marisa and her precious advice. Your professional excellence and integrity inspire me as a researcher, yet you have a lovely down-to-earth

personality, which is a rare combination, and I really enjoyed having you around.

My success would have not been possible without the encouragement of my parents, Ana Maria and José Aníbal. Thank you for trusting my capacities (sometimes maybe too much) and being always there for me. I am also very grateful for having a sister as fun and talented as Susana, who designed the cover of this thesis. Travelling with you is always an adventure due to your unique trouble magnet nature, but I really used those times to relax from my research work.

Last, but not least I want to thank my boyfriend Roberto for the continuous support and countless trips to the Netherlands, spending most of his days of holidays at home while I was working. Our many trips were truly fun and I always came back to Delft full of energy and research ideas. Now I am counting on you for my next challenge!

Curriculum Vitæ

Ana Elisa ALVES VIEIRA

03-08-1989 Born in Viana do Castelo, Portugal.

Education

1995–1998 Grammar School,
Escola básica do primeiro ciclo de Fontão, Ponte de Lima, Portugal.

1999–2006 Grammar School and High School,
Agrupamento de Escolas de Arga e Lima, Viana do Castelo, Portugal.

2007–2012 Bachelor and Master of Science in Aerospace Engineering,
Technical University of Lisbon (IST), Lisbon, Portugal.
Thesis: Helicopter Rotor Noise: Development of an
Acoustic Software Tool.

2016–2020 Doctor of Philosophy (Ph.D.) in Aeroacoustics,
Faculty of Aerospace Engineering,
Delft University of Technology, Delft, The Netherlands.
Thesis: Improving capabilities in modeling aircraft noise
sources
Promotors: Prof. dr. D.G. Simons and Prof. dr. ir. M. Snellen

Professional Experience

2013 Software Engineer,
EDISOFT, Lisbon, Portugal.

2014-2015 Research Engineer in Aeroacoustics,
CEIIA, Oporto, Portugal.

Awards

2014 EREA Young Researchers Science Slam 2014,
Brussels, Belgium.

List of Publications

Peer-reviewed journal articles

5. **A. Vieira**, M. Snellen, D.G. Simons, *Experimental Assessment of Sound Quality Metrics for Take-off and Landing Aircraft*, AIAA Journal **58**, 1 (2020).
4. **A. Vieira**, M. Koch, L. Berstch, M. Snellen, D.G. Simons, *Simulation Methodologies of Engine Noise Shielding by Wings Within Conceptual Aircraft Design*, Journal of Aircraft **57**, 6 (2020).
3. **A. Vieira**, M. Snellen, A. Malgoezar, R. Merino-Martinez, D.G. Simons, *Analysis of shielding of propeller noise using beamforming and predictions*, The Journal of the Acoustical Society of America **146**, 2 (2019).
2. A. Malgoezar, **A. Vieira**, M. Snellen, D.G. Simons, L. M. Veldhuis, *Experimental characterization of noise radiation from a ducted propeller of an unmanned aerial vehicle*, International Journal of Aeroacoustics **18**, 4 (2019).
1. **A. Vieira**, M. Snellen, D.G. Simons, *Assessing the shielding of engine noise by the wings for current aircraft using model predictions and measurements*, The Journal of the Acoustical Society of America **143**,1 (2018).

Conference papers

5. **A. Vieira**, U. Mehmood, R. Merino-Martinez, M. Snellen, D.G. Simons, *Variability of Sound Quality Metrics for Different Aircraft Types During Landing and Take-Off*, 25th AIAA/CEAS Aeroacoustics Conference, Delft, The Netherlands (2019).
4. R. Merino-Martinez, **A. Vieira**, M. Snellen, D.G. Simons, *Sound quality metrics applied to aircraft components under operational conditions using a microphone array*, 25th AIAA/CEAS Aeroacoustics Conference, Delft, The Netherlands (2019).
3. **A. Vieira**, A. Malgoezar, M. Snellen, D.G. Simons, *Experimental study of shielding of propeller noise by a wing and comparison with model predictions*, Euronoise 2018 Conference, Crete, Greece (2018).
2. **A. Vieira**, M. Snellen, D.G. Simons, *Assessment of Engine Noise Shielding by the Wings of Current Turbofan Aircraft*, The 24th International Congress on Sound and Vibration, London, UK (2017).
1. **A. Vieira**, L. Cruz, F. Lau, J. Mortagua, R. Santos, *A New Computational Framework for UAV Quadrotor Noise Prediction*, 5th CEAS Air & Space conference, Delft, The Netherlands (2015).